

THE UNIVERSITY OF MICHIGAN  
College of Engineering  
Department of Nuclear Engineering  
Cavitation and Multiphase Flow Laboratory

Report No. 03371-2-T  
08466-7-T

A HIGH SPEED PHOTOGRAPHIC STUDY OF CAVITATION  
BUBBLE COLLAPSE

by

Charles Lee Kling

Approved by: F. G. Hammitt

Financial Support Provided by:

National Science Foundation  
Grant No. GK 730

and

Army Research Office  
Grant No. DAHOC4 67 0007

March 1970





## ABSTRACT

### A HIGH SPEED PHOTOGRAPHIC STUDY OF CAVITATION BUBBLE COLLAPSE

by

Charles Lee Kling

Chairman: Frederick G. Hammitt

Cavitation is the growth of voids in a local low pressure region of a fluid followed by their collapse as they move into a higher pressure region of the fluid. If these voids collapse with the proper relationship to a nearby solid surface, actual material damage will occur on the surface in the form of pits or erosion. The objective of this investigation is to determine the relationship between the form taken by the collapse of a cavitation bubble moving near a solid surface and damage to that solid surface.

In order to study cavitation bubble collapse in an environment closely related to engineering systems, a flowing system was used utilizing the water tunnel facility of the Cavitation and Multi-phase Flow Laboratory of the University of Michigan. Both natural and spark induced cavitation bubbles were studied in two-dimensional venturis incorporated in the water tunnel facility. Various high speed photographic systems were used to directly observe the collapse mode of the cavitation bubbles and the effect of this collapse upon a nearby solid surface. The damage produced by the collapsing bubbles and by the impact of high speed water jets was studied in detail using a metallographic camera.

The movement of a collapsing bubble, collapsing with spherical symmetry toward a solid wall was analyzed assuming a potential flow field, and using the method of images, programmed on an analog computer. The theoretical results correlate very well with the

experimental measurements.

The present observations show:

1. A cavitation bubble moving parallel to a solid surface begins to migrate toward the surface as the bubble begins to collapse, i. e., the distance between the bubble centroid and the surface decreases due to the attraction of the solid surface.

2. As the cavitation bubble decreases in size, the velocity of the centroid toward the surface increases.

3. As the cavitation bubble approaches minimum volume, the bubble becomes flattened in a direction parallel to the wall with the surface furthest from the wall penetrating the bubble and forming a high speed jet which impinges upon the surface of the wall.

4. This impinging jet, at least in the cases observed, produces the characteristic pits of cavitation damage.

Photographic results of natural cavitation bubbles show the initial migration toward the wall, the initial deformation of the bubble, and in some instances, the remains of a jet which has struck the surface. For spark induced bubbles, the collapse could be followed photographically in much greater detail so that the formation of the jet could be observed quite clearly.

The results of the photomicrographs show a large number of similarities among pits produced by collapsing natural and spark induced cavitation bubbles and high speed liquid jet impact.

## ACKNOWLEDGEMENTS

The careful guidance and assistance provided by Professor Frederick G. Hammitt, Assistant Professor Louis P. Solomon and the other members of the Doctoral Committee are gratefully appreciated.

Personal financial support has been provided by the Atomic Energy Commission and the National Defense Education Act Title IV Fellowships. Project financial support has been provided by the National Science Foundation, Grant GK-730 and the Army Research Office Grant DAHCO4 67 0007.

As with any experimental thesis a large number of people have given their time and thoughts to the solution of many of the problems which have arisen. Almost everyone in the Automotive Laboratory Instrument Shop headed by Edward Rupke, Supervisor, and William Rekewitz, Foreman, has at some time been of direct help in the fabrication of the laboratory equipment. Paul Herman of the Michigan Memorial Phoenix Project Electronic Shop aided in the design and fabrication of the electronic circuits. Help in maintaining and operating laboratory equipment was provided by Edward E. Timm and Terry M. Mitchell, while Hassan M. Mostafa, Darrel O. Rogers, and Richard Getz acted as darkroom assistants in the processing of the photographic materials. Darrel O. Rogers and Virginia M. Wild also deserve thanks for their help in preparing the final draft of the manuscript. To all these people and many others, the author wishes to extend his sincere thanks.

Finally, the author would like to thank his wife, Bobbie, and daughter Kristen, who have provided shelter and comfort throughout this entire educational experience.



Dedicated to the memory

of my father,

DEATH OF THE FATHER

---

## TABLE OF CONTENTS

ACKNOWLEDGEMENTS . . . . .	ii
DEDICATION . . . . .	iii
LIST OF FIGURES . . . . .	vi
LIST OF TABLES . . . . .	xiv
NOMENCLATURE . . . . .	xv
I. INTRODUCTION . . . . .	1
A. Motivation . . . . .	1
B. Objective . . . . .	1
C. Historical Background . . . . .	2
D. Problem Statement . . . . .	5
II. EXPERIMENTAL EQUIPMENT . . . . .	11
A. High Speed Water Tunnel . . . . .	11
B. Plexiglas Two-Dimensional Venturi . . . . .	13
C. Aluminum Two-Dimensional Venturi . . . . .	18
D. Static Underwater Spark Chamber . . . . .	29
E. Gas-Gun Momentum-Exchange Device . . . . .	29
F. Aluminum Coatings . . . . .	35
III. PHOTOGRAPHIC SYSTEMS . . . . .	37
A. Fastax Camera and E. G. and G. Stroboscopic Light Source . . . . .	37
B. Dynafax Camera and Xenon Arc Light Source . . . . .	40
C. Cranz-Schardin Photographic System . . . . .	43
D. Beckman and Whitley Model 330 Camera . . . . .	54
E. Other Photographic Equipment . . . . .	58
IV. RESEARCH INVESTIGATIONS AND PROCEDURES . . . . .	59
A. Bubble Generation Using the Underwater Spark . . . . .	59
B. Equations Governing Bubble Collapse . . . . .	64
C. Analysis of the Photographic Results . . . . .	75
V. DISCUSSION OF RESULTS . . . . .	82
A. Plexiglas Two-Dimensional Venturi . . . . .	82
B. High Speed Liquid Jet Impact . . . . .	98
C. Static Underwater Spark Chamber . . . . .	106
D. The Two-Dimensional Aluminum Venturi . . . . .	113
VI. CONCLUSIONS . . . . .	186

REFERENCES .....	189
------------------	-----

APPENDIX

A. Scientific High Speed Photography .....	193
B. Analog Program .....	204
C. Fortran Listing of Digital Computer Program ..	208

## LIST OF FIGURES

Figure		Page
1.1	Monroe Jet Formation from Detonation of a Shaped Charge . . . . .	6
2.1	Schematic Diagram of High Velocity Water Loop . . . . .	12
2.2	Schematic of Plexiglas Two-Dimension Venturi Without Wedge of Spoiler . . . . .	15
2.3	Flow Separation Caused by Uneven Flow at the Tip of the Wedge . . . . .	16
2.4	Modified Plexiglas Venturi Including Wedge and Spoiler (Quarter Size) . . . . .	17
2.5	Imperfections in Plexiglas Which Appear When Focused Back Lighting is Used . . . . .	19
2.6	Schematic Diagram of Original and Modified Flow Path for the Aluminum Two-Dimensional Venturi Including Wedge and Spoilers (Approximately Half Size). . . . .	21
2.7	Assembled Aluminum Two-Dimensional Venturi Including Spark Bubble Generator (Approximately Quarter Size) . . . . .	22
2.8	Aluminum Two-Dimensional Venturi Assembled with Pressure Tap Plates (Approximately Quarter Size) . . . . .	23
2.9	Schematic Diagram of Pressure Tap Position in Aluminum Two-Dimensional Venturi . . . . .	24
2.10	Natural Cavitation Bubble Detector (Approximately Full Size) . . . . .	26
2.11	Schematic Diagram of Underwater Spark Bubble Generator Circuit . . . . .	28
2.12	Static Underwater Spark Bubble Chamber (Approximately 2/3 Size). . . . .	30
2.13	Gas Gun Momentum Exchange Facility Including Target and Velocity Measuring Device (Approximately Quarter Size) . . . . .	32
2.14	Water Cavity of Gas Gun Momentum Exchange Facility (Approximately Double Size) . . . . .	33
2.15	Dual Beam Velocity Measuring Device (Approximately Half Size) . . . . .	34



Figure	Page
3.1 Schematic Arrangement of Plexiglas Venturi, Fastax Camera, and Strobe Light . . . . .	39
3.2 Schematic Arrangement of Aluminum Venturi, Dynafax Camera, and Xenon Arc Lamp . . . . .	42
3.3 Granz-Schardin Photographic System Including Delay Network and High Voltage Supply . . . . .	45
3.4 Schematic Diagram of Cranz-Schardin Photographic System . . . . .	46
3.5 Compact, Triggerable Air Gap, Spark Light Source . . . . .	47
3.6 Schematic Diagram of Spark Light Source . . . . .	47
3.7 Schematic Diagram of Delay Network . . . . .	49
3.8 Schematic Diagram of Trigger Circuit . . . . .	51
3.9 Rear View of Iron Box with Back Panel Removed Showing Position of Light Sources and Trigger Circuits . . . . .	52
3.10 Experimental Arrangement of Model 330 Camera and Aluminum Venturi . . . . .	55
4.1 Representative Flow Patterns for Sinks Used in "Method of Images" . . . . .	67
4.2 Theoretical Solution of Bubble Collapse Far From a Solid Surface with Various Internal Gas Contents . . . . .	70
4.3a Normalized Radius vs. Normalized Time for a Fixed Initial Wall Distance ( $b_o = 1.3$ ) and a Variable Internal Gas Content . . . . .	71
4.3b Normalized Wall Distance vs. Normalized Time for a Fixed Initial Wall Distance ( $b_o = 1.3$ ) and a Variable Internal Gas Content . . . . .	72
4.4a Normalized Radius vs. Normalized Time for a Fixed Internal Gas Content ( $Q/\Delta P = 0.040$ ) and a Variable Initial Wall Distance . . . . .	73
4.4b Normalized Wall Distance vs. Normalized Time for a Fixed Internal Gas Content ( $Q/\Delta P = 0.040$ ) and a Variable Initial Wall Distance . . . . .	74
4.5 Measurements Taken From the Projected Image of a Cavitation Bubble and Typical Datum Lines . . . . .	77

Figure		Page
4.6	Diagram of Axis of Rotation for Bubbles with an Assumed Ellipsoid Shape . . . . .	78
4.7	Typical Values of Eccentricity, $\epsilon$ , and a Visual Representation of the Associated Bubble Deformation . . . . .	80
5.1	Fastax High Speed Photographs Using Diffuse Back Lighting, 7200 Frames/Second, 1.0 $\mu$ s Exposure/Frame Flow Left to Right, Fluid Velocity 27.7 m/s, Air Content 1.3%, Scale Length (Arrow) 0.52 cm . . . . .	83
5.2	Orientation of Flattened Side of Bubble vs. Distance From Tip of Wedge and Relation to Constante Pressure Lines . . . . .	87
5.3	Fastax High Speed Photographs Using Diffuse Back Lighting and Showing the Poor Resolution of the Fastax System. Scale Length (Arrow) 0.52 cm . . . . .	89
5.4	Fastax High Speed Photographs Using Diffuse Back Lighting and Showing the Remains of a High Speed Jet Striking the Wedge During Cavitation Bubble Rebound . . . . .	90
5.5	Dynafax High Speed Photographs Using Diffuse Back Lighting, 12,500 Frames/Second, 1.0 $\mu$ s Exposure/Frame, Fluid Velocity 34.2 m/s, Right to Left, Air Content 1.2%, Magnification 2.0 . . . . .	91
5.6a	Normalized Radius vs. Normalized Time for the Natural Cavitation Bubble Reaching the Tip of the Wedge in Frame 2 of Figure 5.5 . . . . .	96
5.6b	Normalized Wall Distance vs. Normalized Time for the Natural Cavitation Bubble Reaching the Tip of the Wedge in Frame 2 of Figure 5.5 . . . . .	97
5.7a	Normalized Radius vs. Normalized Time for the Natural Cavitation Bubble Impinging Upon the Tip of the Wedge in Frame 5 of Figure 5.5 . . . . .	99
5.7b	Normalized Wall Distance vs. Normalized Time for the Natural Cavitation Bubble Impinging upon the Tip of the Wedge in Frame 5 of Figure 5.5 . . . . .	100
5.8	Spark Camera Photographs Using Focused Back Lighting and Showing a Water Jet Impacting on a Plexiglas Specimen. Time Measured from First Frame, 0.22 $\mu$ s Exposure/Frame, Scale Length, 0.5 cm . . . . .	102

Figure	Page
5.9	Model of Material Failure During High Speed Liquid Jet Impact. Axial Deformations are Greatly Exaggerated . . . 104
5.10	Pit Produced in Plexiglas by Impact of High Speed Liquid Jet. Proficorder Graduations: 660 $\mu$ Horizontal, 0.635 $\mu$ Verticle . . . . . 105
5.11	Pit Produced in 1100-0 Aluminum by Impact of High Speed Liquid Jet. Proficorder Graduations: 600 $\mu$ Horizontal, 0.635 $\mu$ Verticle . . . . . 105
5.12	Pit Produced in Aluminum Lighting Sheet by Impact of High Speed Water Jet. Proficorder Graduations: 600 $\mu$ Horizontal, 2.54 $\mu$ Verticle . . . . . 105
5.13	Dynafax High Speed Photographs of Spark Bubble Collapse in the Static Underwater Spark Bubble Chamber. Diffuse Back Lighting Time Measured from First Frame, 1.05 $\mu$ s Exposure/Frame, Magnification 2.5. Air Content 2.2% . . . . . 108
5.14	Normalized Radius vs. Normalized Time for the Spark Generated Cavitation Bubble Shown in Figure 5.13 . . . . . 112
5.15	Dynafax High Speed Photographs of Natural Cavitation Bubble Collapse in the Unmodified Aluminum Two-Dimensional Venturi. Focused Back Lighting, Time Measured from First Frame, 1.0 $\mu$ s Expsoure/Frame, Fluid Flow Magnification 2.2. Air Content 0.9% . 115
5.16a	Normalized Radius vs. Normalized Time for the Natural Cavitation Bubble Shown in Figure 5.15 . . . . . 118
5.16b	Normalized Wall Distance vs. Normalized Time for the Natural Cavitation Bubble Shown in Figure 5.15 . . . . 119
5.17	Typical Axial Pressure Profiles for the Modified Aluminum Two-Dimensional Venturi with and without the Wedge in Place . . . . . 120
5.18	Dynafax High Speed Photographs of a Natural Cavitation Bubble Collapse in the Modified Sluminum Two-Dimensional Venturi. Focused Back Lighting; Time Measured from First Frame, 1.0 $\mu$ s Exposure/Frame, Fluid Flow 24.2 m/s Left to Right, Magnification, 2.3. Air Content 1.0%. 123
5.19a	Normalized Radius vs. Normalized Time for the Natural Cavitation Bubble Shown in Figure 5.18 . . . . . 126

Figure	Page
5.19b	Normalized Wall Distance vs. Normalized Time for the Natural Cavitation Bubble Shown in Figure 5.18 . . . . . 127
5.20	Dynafax High Speed Photographs of a Natural Cavitation Bubble Impinging on the Wedge in the Modified Aluminum Two-Dimensional Venturi. Focused Back Lighting, Time Measured from First Frame, Fluid Flow 24.2 m/s, Left to Right, Magnification 2.3. Air Content 1.0% . . . . . 128
5.21	Photomicrographs of Natural Cavitation Pits Produced on the 50 $\mu$ , 1100-0 Aluminum Sheet. All Pits are Shown on the Same Scale . . . . . 131
5.22	Model 330 High Speed Photographs of a Spark Induced Cavitation Bubble Collapsing in the Modified Aluminum Two-Dimensional Venturi Without the Wedge Present. Diffuse Back Lighting, Time Measured from First Frame, 2.0 $\mu$ s Exposure/Frame, Fluid Flow 24.7 m/s Left to Right, Magnification 6.1. Air Content 0.7% . . . 133
5.23	Normalized Radius vs. Normalized Time for the Spark Induced Cavitation Bubble Shown in Figure 5.22 . . . . . 136
5.24	Model 330 High Speed Photographs of a Spark Induced Cavitation Bubble Collapsing in the Modified Aluminum Two-Dimensional Venturi. Diffuse Back Lighting, Time Measured from First Frame, 0.8 $\mu$ s Exposure per Frame, Fluid Velocity 26.7 m/s, Right to Left, Initial Wall Distance, $b_o = 1.62$ , Magnification 5.0. Air Content 0.8% . . . . . 138
5.25a	Normalized Radius vs. Normalized Time for the Spark Induced Cavitation Bubble Shown in Figure 5.24 . . 141
5.25b	Normalized Wall Distance vs. Normalized Time for the Spark Induced Cavitation Bubble Shown in Figure 5.24 . . . . . 142
5.26	Model 330 High Speed Photographs of a Spark Induced Cavitation Bubble Collapsing in the Modified Aluminum Two-Dimensional Venturi. Diffuse Back Lighting, Time Measured from First Frame, 4.0 $\mu$ s Exposure/Frame, Fluid Velocity 27.1 m/s, Left to Right, Initial Wall Distance, $b_o = 1.40$ , Magnification, 7.0. Air Content 0.7% . . . . . 143

Figure	Page
5.27a	Normalized Radius vs. Normalized Time for the Spark Induced Cavitation Bubble Shown in Figure 5.26 . . . . . 147
5.27b	Normalized Wall Distance vs. Normalized Time for the Spark Induced Cavitation Bubble Shown in Figure 5.26 . . 148
5.28	Model 330 High Speed Photographs of a Spark Induced Cavitation Bubble Collapsing in the Modified Aluminum Two-Dimensional Venturi. Focused Front Lighting, Time Measured from First Frame, 2.6 $\mu$ s Exposure/Frame, Fluid Velocity 20.1 m/s, Left to Right, Initial Wall Distance, $b_0 = 1.21$ , Magnification 8.0. Air Content 0.7% . . . . . 149
5.29a	Normalized Radius vs. Normalized Time for the Spark Induced Cavitation Bubble Shown in Figure 5.28 . . . . . 152
5.29b	Normalized Wall Distance vs. Normalized Time for the Spark Induced Cavitation Bubble Shown in Figure 5.28 . . . . . 153
5.30	Model 330 High Speed Photographs of a Spark Induced Cavitation Bubble Collapsing in the Modified Aluminum Two-Dimensional Venturi. Diffuse Back Lighting, Time Measured From the First Frame, 1.8 $\mu$ s Exposure/Frame, Fluid Velocity 26.7 m/s Right to Left, Initial Wall Distance, $b_0 = 1.14$ , Magnification 6.0. Air Content 0.6% . . . . . 154
5.31a	Normalized Radius vs. Normalized Time for the Spark Induced Cavitation Bubble Shown in Figure 5.30. . . 157
5.31b	Normalized Wall Distance vs. Normalized Time for the Spark Induced Cavitation Bubble Shown in Figure 5.30 . . 158
5.32	Model 330 High Speed Photographs of a Spark Induced Cavitation Bubble Collapsing in the Modified Aluminum Two-Dimensional Venturi. Diffuse Back Lighting, Time Measured from the First Frame, 6.2 $\mu$ s Exposure/Frame, Fluid Velocity 26.7 m/s Right to Left, Initial Wall Distance, $b_0 = 0.94$ , Magnification 5.5. Air Content 0.6% . . . . . 159
5.33a	Normalized Radius vs. Normalized Time for the Spark Induced Cavitation Bubble Shown in Figure 5.32 . . . . . 161
5.33b	Normalized Wall Distance vs. Normalized Time for the Spark Induced Cavitation Bubble Shown in Figure 5.32 . . . . . 162

Figure	Page
5.34	Model 330 High Speed Photographs of a Spark Induced Cavitation Bubble Collapsing in the Modified Aluminum Two-Dimensional Venturi. Diffuse Back Lighting, Time Measured from the First Frame, 5.0 $\mu$ s Exposure/Frame, Fluid Velocity 24.7 m/s Left to Right, Initial Wall Distance, $b_0 = 0.0$ , Magnification 6.2. Air Content 0.7% . . . . . 163
5.35a	Normalized Radius vs. Normalized Time for the Spark Induced Cavitation Bubble Shown in Figure 5.34 . . . . . 165
5.36a	Enlargement of Frame 4 of Bubble 5.30. Magnification 30 . . . . . 171
5.36b	Enlargement of Frame 5 of Bubble 5.30 Taken 3.6 $\mu$ s after Frame 4 and Showing a Jet Moving Through the Interior of the Bubble. Magnification 30 . . . . . 172
5.37	Outlines of the Spark Induced Cavitation Bubble 5.30 at Various Stages of Collapse Showing the Mode of Deformation . . . . . 173
5.38	Outlines of the Spark Induced Cavitation Bubble 5.30 at Various Stages of Rebound Showing the Bubble Impinging on the Nearby Solid Surface . . . . . 174
5.39	Model 330 High Speed Photographs of Spark Induced Cavitation Bubble Breaking up in the Modified Aluminum Two-Dimensional Venturi. Diffuse Back Lighting, Time Measured from First Frame, 5.1 $\mu$ s Exposure/Frame, Fluid Velocity 24.7 m/s Left to Right, Initial Wall Distance, $b_0 = 1.35$ , Magnification 7.5. Air Content 0.6% . . . . . 175
5.40	Photomicrographs of the Damage Produced on the 50 $\mu$ Thick Aluminum Foil During the Collapse and Rebound of (a) Bubble 5.28 and (b) Bubble 5.30. Scale as Shown . . . . . 179
5.41	Photomicrographs of the Damage Produced on the 50 $\mu$ Thick Aluminum Foil by the Initiating Spark of (a) Bubble 5.28 and (b) Bubble 5.30 . . . . . 181
5.42	Photomicrograph and Accompanying Proficorder Trace of Damage Produced on the 0.5 mm Thick Aluminum Sheet by the Collapse and Rebound of one of 50 Spark Induced Cavitation Bubbles Collapsing with an Initial Normalized Wall Distance, $b_0$ , of 1.15. Scale Divisions 66.0 $\mu$ Horizontal, 0.635 $\mu$ Vertical . . . . . 184

Figure		Page
5.43	Photomicrograph of Damage Produced on the 0.5 mm Thick Aluminum Sheet by the Initiating Spark of a Spark Induced Cavitation Bubble with an Initial Normalized Wall Distance, $b_o$ , of 1.15 . . . . .	184

## LIST OF TABLES

Table		Page
2.1	Mechanical Properties of Aluminum Coatings . . . . .	36
4.1	Energy and Pressure Calculations for the Underwater Spark Bubble Generator . . . . .	62
4.2	Typical Results from the Digital Computer Program . . . . .	81
5.1	Comparison of the Average Horizontal Slip Velocity and the Instantaneous Horizontal Slip Velocity at Minimum Volume for Spark Induced Cavitation Bubbles . . . . .	168
5.2	Spark Generated Cavitation Bubble Parameters . . . . .	182



## NOMENCLATURE

Symbol	Description	Units
A	Effective aperture	
a	Time magnification factor	
B	Blur	m
b	Distance between bubble centroid and wall (normalized)	m
$b_o$	Initial wall distance (normalized)	m
b	Bubble centroid velocity (normalized)	$m s^{-1}$
b	Bubble centroid acceleration (normalized)	$m s^{-2}$
C	Circle of confusion set equal to (film resolution) <sup>-1</sup>	m
c	Speed of sound in water (1500)	$m s^{-1}$
D	Depth of field	m
d	Diameter of lens aperture	m
$E_f$	Energy of gas formation	$j (mole)^{-1}$
$E_{in}$	Energy dissipated in gas formation	j
$E_p$	Potential energy	j
$E_s$	Energy dissipated in water by spark	j
F	Framing rate	$s^{-1}$
$F_R$	Force vector along r coordinate	$kg m s^{-2}$
f	Focal length	m
$f_e$	Effective focal length	m
I	Current	amp
L	Resolution of film-camera system	$m^{-1}$
$M_v$	Virtual mass	kg

$M_{vo}$	Initial virtual mass	kg
$m$	Magnification ( $\frac{\text{image}}{\text{object}}$ )	
$N$	Total frames per sequence	
$P$	Pressure inside bubble	atm
$P_o$	Pressure inside bubble for $R=R_o$	atm
$P_r$	Pressure at $r$ coordinate	atm
$P_{wh}$	Water hammer pressure	atm
$P_\infty$	Pressure at $\infty$ distance from bubble	atm
$P_v$	Virtual momentum of bubble	$\text{kg m s}^{-1}$
$\Delta P$	Difference between $P_\infty$ and partial pressure inside bubble	atm
$Q$	Partial pressure inside bubble for $R=R_m$	atm
$R$	Bubble wall position (normalized)	m
$R_m$	Maximum bubble radius	m
$R_o$	Minimum bubble radius	M
$R$	Bubble wall velocity	$\text{m s}^{-1}$
$R$	Bubble wall acceleration	$\text{m s}^{-2}$
$R_{1,2,3,4}$	Resistances	ohms
$RC$	Delayed constant of capacitor circuit	s
$r$	Radial Coordinate	m
$T$	Kinetic energy	j
$T_g$	Ambient temperature	$^{\circ}\text{C}$
$t$	Exposure time	s
$t_n$	Time normalization factor	s
$t_w$	Writing time	s
$V$	Voltage	volt
$V_o$	Initial voltage	volt

$V_{pg}$	Volume of permanent gas	ml
$V_m$	Maximum velocity of object being photographed	$m s^{-1}$
$V_s$	Slip velocity	$m s^{-1}$
$V_{so}$	Initial slip velocity	$m s^{-1}$
$v$	Jet velocity	$m s^{-1}$
$w$	Decay constant	$s^{-1}$
$X$	Semi-major axis	m
$x$	Object distance from lens	m
$Y$	Semi-minor axis	m
$\Delta$	Relative aperture	
$\epsilon$	Eccentricity	
$\varphi$	Velocity potential	$m^2 s^{-1}$
$\rho$	Density	$kg m^{-3}$
$\theta$	Angle between velocity vector of object and film plane	radians



## CHAPTER I

### INTRODUCTION

#### A. Motivation

Cavitation is the formation of voids in a fluid when the local pressure becomes sufficiently less than the vapor pressure of the fluid for a period sufficiently long enough for the voids to grow. The void will then collapse after it moves into a region where the local pressure is greater than the vapor pressure. These voids may be discrete vapor bubbles, cavities which are attached to submerged bodies, or a combination of both. Cavitation is easily detected visually in a transparent fluid by the appearance of a "cloud" in the cavitation region, (i. e. , an apparently frothy region) or acoustically, due to a sound generation in a region where the voids collapse. Although cavitation may be beneficial in cleaning surfaces, actual damage to the material may be observed.

Even though cavitation has been the subject of scientific study for over 100 years the basic mechanisms of cavitation, especially in relation to the damage produced on solid surfaces, is still open to question. This investigation is a fundamental study of the cause of cavitation damage, and attempts to clarify the controversy through direct observation. Although other factors, such as corrosion or fatigue failure, may contribute to cavitation damage, the factor stressed in this investigation will be mechanical damage due to the collapse of a single bubble.

#### B. Objective

The objective of this investigation is to experimentally study the collapse modes of vapor-gas bubbles moving near a solid surface and to determine what, if any, aspects of this collapse

cause damage to the solid surface. The damage produced by collapsing cavitation bubbles will be compared with similar damage produced by the impingement of high speed water jets. "Scientific photography" was used in the investigation to directly observe the collapse of cavitation bubbles, the impingement of high speed water jets, and the damage produced on solid surfaces by these mechanisms. The purpose of scientific photography is to broaden the interpretative powers of the human eye by time magnification or reduction and increased spatial resolution. High speed photographic systems were used for the motion study of cavitation bubble collapse and liquid jet impingement, while a metallographic camera was used for the detailed study of damage produced. A more detailed discussion of the purposes and pertinent parameters of scientific high speed photography is given in Appendix A.

### C. Historical Background

Euler<sup>(1)</sup> in 1754 was perhaps the first to suggest the possibility of the formation of voids in local low pressure regions of hydrodynamic machinery. Probably the first analysis of bubble dynamics related to this phenomena is that of Besant<sup>(2)</sup> in 1859. The same results were obtained by Lord Rayleigh's investigation<sup>(3)</sup> in 1917 of the spherical collapse of an empty cavity initially at rest in an inviscid, incompressible fluid. These results show that as the volume of the bubble approaches zero, the bubble wall velocity and the fluid pressure in the vicinity of the bubble approach infinity. Rayleigh's investigation also provided for the inclusion of a permanent gas within the bubble which would eventually arrest the bubble motion. Depending upon the amount of gas in the bubble, very high collapse velocities and fluid pressures could still be obtained, showing a potential for producing damage if these velocities and pressures could be applied upon a solid surface. Some of the first photographs

of cavitation were made by Sir Charles Parsons during experiments started in 1895<sup>(4)</sup>. From photographs of the cavitation occurring on a model ship propeller, Parsons concluded that the damage was mechanical in nature.

In the 1940's much significant work was done in the field of bubble dynamics. Cole<sup>(5)</sup> presents both the compressible and incompressible fluid flow equations related to the bubble dynamics of underwater explosions. He also describes approximations for the shock wave produced upon initiation of the bubble, and using the method of images, he develops differential equations describing the effect of a solid boundary or a free surface on the dynamics of a spherically pulsating bubble. Several techniques for experimentally measuring the underwater explosion bubble are discussed. The results show that the bubble follows incompressible theory closely throughout most of the bubble lifetime.

A review of current ideas and investigations related to cavitation and the damage it produces is given by Hammitt<sup>(6)</sup> and others. The more recent investigations on the dynamics of spherically symmetric bubbles<sup>(7, 8, 9, etc.)</sup> have included the effects of viscosity, surface tension, and condensation rates of internal vapor. The effect of heat transfer on the collapse of a bubble, which becomes more important as the fluid approaches saturation temperature, has also been studied<sup>(10, 11)</sup>. One important result of these investigations shows that for a stationary bubble, the pressure in the surrounding fluid at a distance equal to the initial radius of the bubble does not reach a value sufficient to explain observed pits in strong materials during the collapse of the bubble.<sup>(8, 9)</sup>

The pressure produced upon rebound depends upon the assumed gas content of the bubble. Conditions with very low internal gas can be postulated where damaging potential pressures are

produced upon rebound. Theoretical results<sup>(12)</sup> show that the collapse of a bubble is an unstable process so that any asymmetries in bubble shape are amplified as the bubble collapses. The damaging potential of a collapsing bubble would be greatly increased if migration toward a solid surface occurred during collapse and rebound. Many investigations<sup>(13, 14, 15)</sup> have considered the effect of a nearby solid surface and have shown that migration does indeed occur; however, the proximity of the wall not only has a retarding effect upon the bubble collapse, but it also produces an asymmetry which may effect bubble shape. Photographic investigations to support the spherically symmetric collapse theories are generally conducted far from a solid surface and even in gravity free conditions<sup>(11, 18)</sup> in an attempt to conserve spherical symmetry.

Photographic investigations of typical cavitation environments<sup>(19, 20)</sup> have shown cavitation damage to be quite similar to damage produced by the impingement of high speed water jets. In addition, between  $10^4$  to  $10^{10}$  cavitation bubbles are observed to collapse adjacent to a solid surface for each damage crater produced.<sup>(20, 21)</sup> Therefore, bubbles are subject to some highly selective conditions which must be met in order to produce damage. Several studies<sup>(22, 23, 24, 25)</sup> have been conducted to determine what effect a solid surface has on the collapse of attached or nearby bubbles in a static fluid. This study differs basically from these in using a flowing system (venturi) more typical of actual engineering applications. The general result of these studies shows the formation of a jet produced by the deformation of the wall of the bubble. This jet penetrates the bubble or attached cavity and strikes the surface, in some cases producing damage. Other mechanisms have also been proposed to describe the formation of this jet. Kozirev<sup>(26)</sup> concluded from a high speed motion picture analysis of highly asymmetric cavitation clouds

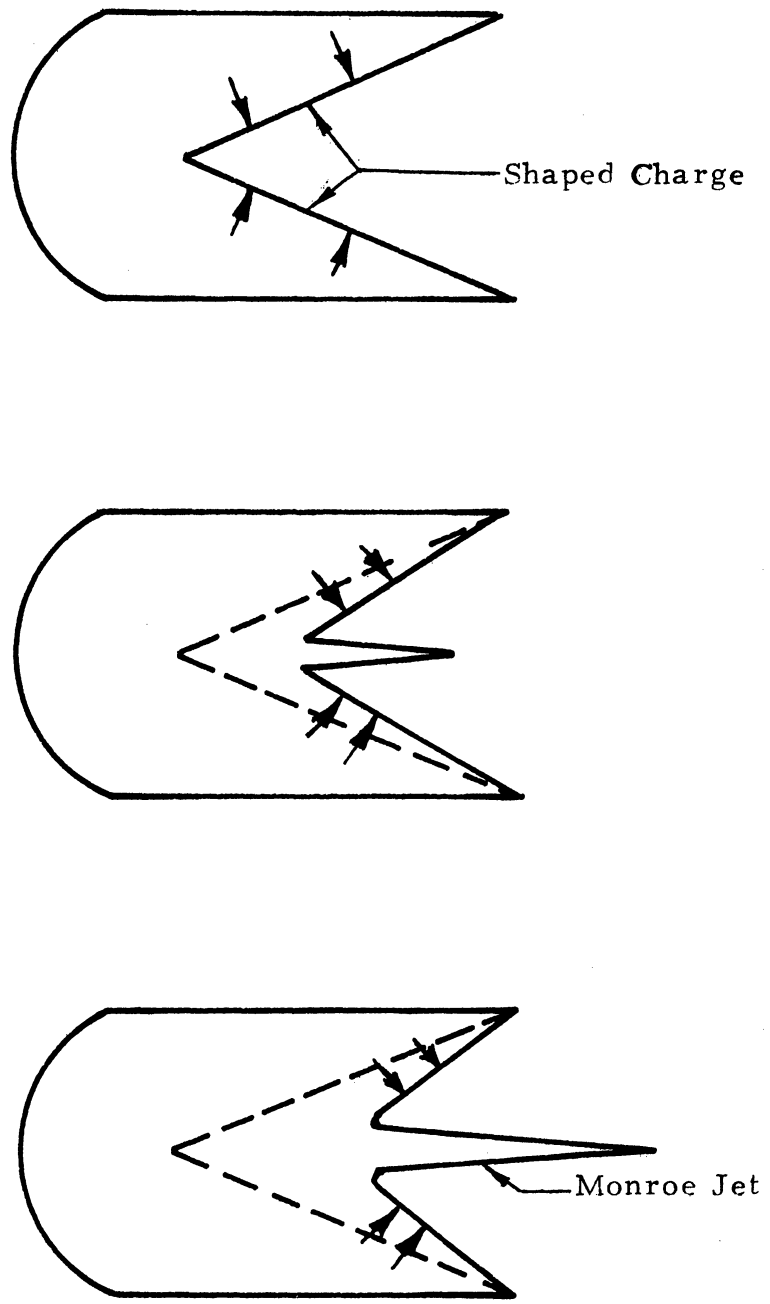


that Monroe jets were produced at discontinuities of the asymmetric shapes. A Monroe jet (Figure 1.1) is produced by the "shaped charge" effect of an explosion or a cavity collapse. If spherical symmetry and bubble motion with respect to the fluid (possibly produced by the attraction of the solid surface) are assumed, conservation of momentum demands that the translatory velocity of the bubble increases rapidly as its volume decreases. (24, 27)

Theoretical investigations of bubble collapse near a solid surface (22, 25, 28) have used perturbation theory to account for the asymmetries produced by the wall and by the non-spherical shape of the bubble. Unfortunately, perturbation solutions are not valid for large asymmetries which eventually develop, so that only the initial stages of bubble collapse may be followed with confidence in this manner. A two-dimensional solution of the fluid flow equation is under development at this laboratory (29) which will hopefully be able to follow the bubble collapse through a much larger volume reduction with the resulting larger asymmetries, and similar work is in progress at California Institute of Technology (30).

#### D. Problem Statement

Low density natural cavitation clouds and isolated artificially produced bubbles were studied using ultra-high speed photography as they grew and collapsed near a solid boundary in a flowing system. The photographs were analysed and compared with a theoretical analysis of the spherically symmetric collapse of a bubble near a solid surface using the method of images. The damage produced by the collapse of the artificially produced cavitation bubbles on selected target materials was compared with the damage produced by the impact of high speed water jets and by the impingement of spherical shock waves, produced by the electric spark used



3000

Figure 1.1 Monroe Jet Formation from Detonation of a Shaped Charge

to generate some of the bubbles.

The flowing system used in this investigation utilized two-dimensional venturis incorporated in the water tunnel facility of the Cavitation and Multiphase Flow Laboratory of the University of Michigan. For the particular two-dimensional venturis used in this investigation, direct observation showed that incipient cavitation began for flow velocities in the venturi throat ranging between 20 m/s and 30 m/s, depending upon the ambient pressure in the water tunnel facility. At these velocities, assuming the camera is perpendicular to the direction of flow and the magnification between the object and image is approximately 0.5, eq. A-4\* gives an exposure time of less than  $2\mu\text{s}$ , if blurring due to simple object translation is to be less than the resolution of the camera. Because the bubble wall also moves with respect to the centroid of the bubble a still shorter exposure time would be required to "stop" the bubble wall motion. If the cavitation cloud in the venturi throat is set at an optimum density for photographic investigation, it appears to end 2 cm to 3 cm downstream of the throat. From this distance of travel and the known velocity, a good approximation of the total collapse time for an incipient cavitation bubble is calculated to be approximately 1 ms. The minimum framing rate is then easily determined from the minimum number of pictures of a single bubble collapse required (i. e., if only 10 pictures per bubble were required the minimum framing rate would be  $10^4$  frames/second). However, previous experimental evidence has shown that the damage produced by a cavitation bubble occurs over a time scale of only a few microseconds, so that if this damaging process is to be photographed, the framing rate should be of the order of  $10^6$  frames/second. At this framing rate approximately 1,000 pictures

---

\*Equations referred to in this section are found in Appendix A.

per photographic sequence would be needed in order to follow the bubble through its entire collapse sequence, including a detailed observation of the production of damage. Since no camera available today could meet these requirements, a compromise had to be made between the framing rate and coverage of the bubble collapse mode. The entire collapse mode could be covered with a framing rate lower than  $10^6$  frames/second with only a probability of one or two frames being taken during the damage portion of the bubble collapse, or a camera system capable of  $10^6$  frames/second could be used and only a small segment of the bubble collapse would be detailed. For the latter case, either a detector would be required so that the bubble would be photographed only during its damaging stage, or several sequences could be taken, with the probability that one of these sequences would show a bubble during the damaging phase of its collapse. Ideally the depth of field for the study of incipient cavitation should include the width of the throat section of the venturi (1.27 cm for the aluminum 2-dimensional venturi) so that any bubble photographed in the throat section would be in focus. Solving eq. A-5 for the relative aperture required to achieve a given depth of field results in

$$N = \frac{M^2 D}{Z_c(M+1)} \quad 1-1$$

For all the cameras used in this investigation except the Beckman and Whitley Model 330 Camera, the initial camera aperture and achievable magnifications produced a depth of field which included the entire width of the venturi. For the Beckman and Whitley Model 330 Camera, the ideal relative aperture is 28. This value was approached by the addition of light stops which were placed in front of the camera lens. Since increasing the relative aperture of the camera objective also increases the effective aperture of the

camera system, a higher speed film was required to achieve the same image density for a given light intensity.

For studies of spark generated bubbles the requirements of the photographic system are simplified. Bubbles similar in size and lifetime to incipient cavitation bubbles can be produced at a prescribed point in time and space through the use of a spark gap. The bubble generator circuit was designed for precise control of the energy input used to generate a bubble. Therefore, nearly identical bubbles could be generated repeatedly. Their lifetime could be accurately determined by using a camera with a writing time equal to or greater than the lifetime of the bubble. The camera could then be used with a much higher framing rate, and therefore much shorter writing time, to photograph only the damaging portion of the bubble collapse, with the delay time between the initial and damage portion of the bubble lifetime determined by the previous photographic sequence. Since the induced bubbles were produced at a precise point in space, and traveled in a direction along the focal plane of the camera, the depth of field required is only the maximum radius of the bubble (about 0.4cm.). For this depth of field, no additional light stops were required even for the Beckman and Whitley Model 330 camera.

The impacts of high speed water jets striking a solid surface were also photographically studied because of the similarity in damage produced by cavitation and jet impact. A gas-gun momentum-exchange device was used to produce high-speed water jets with a diameter near 0.18 cm, and a velocity up to 700 m/s. Since the jets traveled only 1 cm before striking the target and the damage was produced on a time scale of microseconds, a camera with a framing rate of  $\sim 10^6$  frames/second is required to take several photographs of the jet as it impacts the surface and produces damage. The impact

damage pits were then compared with cavitation damage pits.  
They are found to be of very similar nature.

## CHAPTER II

### EXPERIMENTAL EQUIPMENT

Cavitation has been investigated and photographed in many different types of machinery where rotation, vibration, constriction or obstruction of the flow causes local pressure to drop below the minimum required to suppress cavitation. Because this study is primarily interested in the possibility of material damage produced by the collapse of a single bubble, the facilities used must be capable of producing cavitation fields ranging from single, isolated bubbles to bubble clouds in which the bubble density is low enough so that the growth and collapse of an individual bubble is not masked by the other bubbles in the cloud.

#### A. High Speed Water Tunnel

The facilities used for the investigation of cavitation at the University of Michigan have been described in several reports. (9, 20, 31) One of these facilities, the high-speed water tunnel was used for this investigation. The high-speed water tunnel (Fig. 2.1) is a closed system consisting of four experimental loops. A variable speed centrifugal pump provides the water flow to the high pressure tank. The water flows through any or all of the experimental loops to the low pressure tank, then back to the pump completing the circuit. Experiments are conducted by placing venturis in the experimental loops. Each loop is provided with an orifice plate and differential manometer for the monitoring of the flow rate. For the experiments of this investigation, three of the experimental loops were closed and a two dimensional venturi was placed in the fourth loop. The reference pressure in the loop is maintained by regulating the

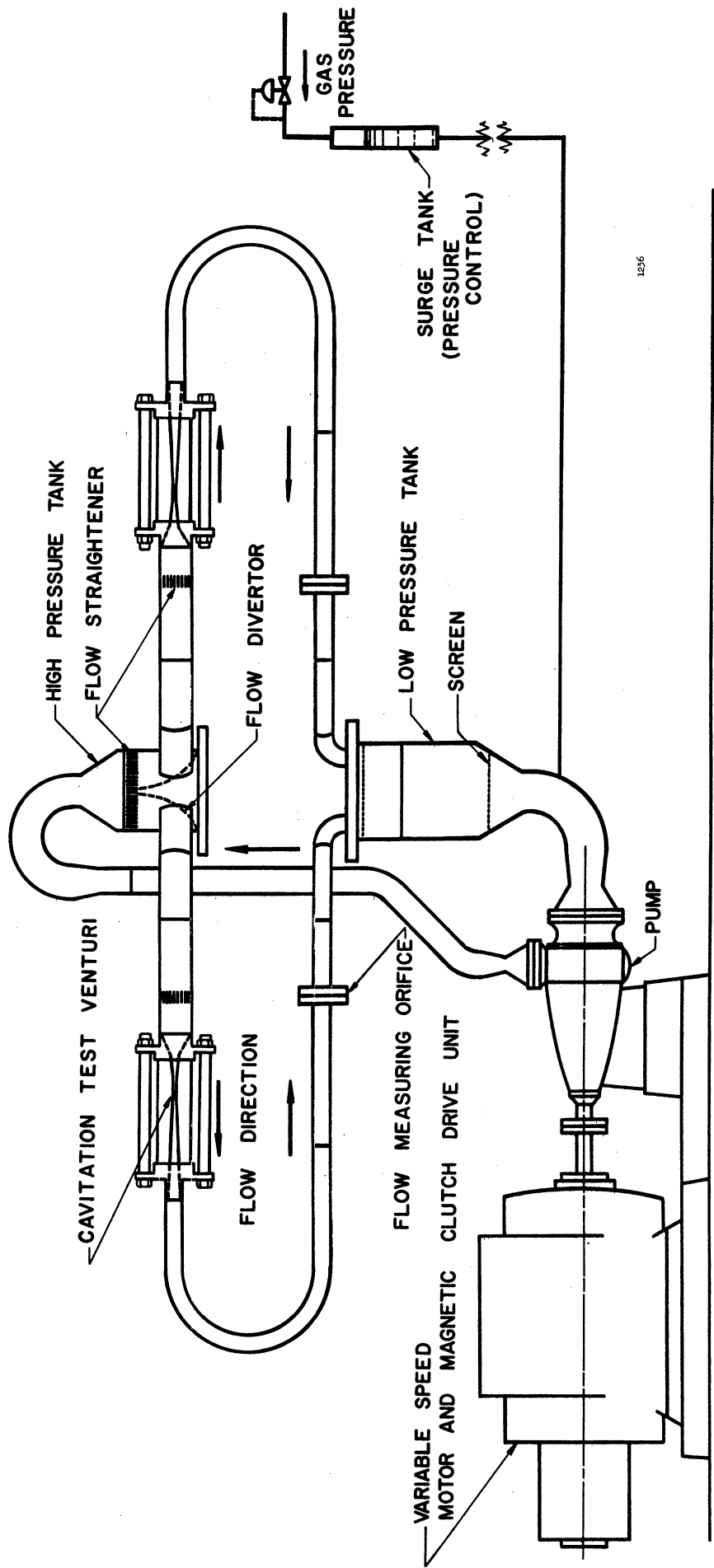


Figure 2.1 Schematic Diagram of High Velocity Water Loop



air pressure in a surge tank which is connected to the low pressure tank of the loop through a by-pass loop. This by-pass loop also contains a deionizer, a filter, and a cold-water deaerator for regulation of the air content. The air content of the water can be varied from saturated (approximately 2.2 volume percent air at room temperature and atmospheric pressure) to a minimum of  $\approx 0.5$  volume percent.

The type and extent of cavitation produced in the experimental venturis of this facility are governed by four variable parameters: flow rate, pressure, temperature and air content. The flow rate is determined by pump speed and may be monitored by the orifice plate and differential manometer included in each loop. The overall pressure level depends upon the pressure in the surge tank (connected to the low pressure tank). The temperature is generally maintained constant by the use of cooling coils in the low pressure tank to remove the pump work energy. Finally, the air content was regulated by the water flow through the deaerator tank. The best photographic conditions for natural cavitation were produced by setting the pump speed and pressure to the desired extent of cavitation, and then varying the air content to produce the proper bubble size distribution in the bubble cloud. For the investigation using spark-produced bubbles, pump speed and pressure were set so that cavitation was just suppressed in the venturi. Air content was also held to a minimum so that the number of nuclei that could cause cavitation bubbles would be as small as possible.

#### B. Plexiglas Two-Dimensional Venturi

Optical distortion of the bubble photographs was held to a minimum by use of two-dimensional venturis which have a rectangular cross section at every axial position. Preliminary

photographic studies used a modified version of the plexiglas two-dimensional venturi described in Ref. 9. The original venturi (Fig. 2.2) consisted of four pieces of plexiglas clamped between two cast aluminum end pieces which mated the venturi to the pipes of the test loop in the water tunnel. One side of the venturi was tapped for pressure profile readings. The rectangular cross section of this venturi has a constant edge of 7.6 cm. and the diffuser and nozzle sections had an included angle of 6 degrees so the venturi was symmetric about the throat region which could be varied in cross-section from 0.32 cm. x 7.6 cm. to 2.22 cm. x 7.6 cm. Several modifications were made to this venturi in order to facilitate the study of cavitation bubble collapse near a solid surface. First, the throat width was set at a constant 0.63 cm. and the four pieces of the venturi were glued together in order to eliminate leakage problems. Next, a new side plate was fabricated to allow partial disassembly without the removal of the cast aluminum end pieces. Finally, a stainless steel wedge was introduced into the diffuser section of the venturi, perpendicular to the constant 7.6 cm. dimension of the rectangular cross section. The wedge extended from 0.95 cm. to about 15 cm. downstream of the exit of the throat and was tapered to fit the sides of the diffuser. In initial tests, flow problems inherent in the venturi caused flow separation at the tip of the wedge (Fig. 2.3). However, providing the wedge with a variable angle of attack and a downstream spoiler equalized the flow around the tip of the wedge and eliminated separation, providing streamlines that were parallel to at least one side of the wedge. Fig. 2.4 is a photograph of the modified venturi in position for the photographic study. This plexiglas venturi gave satisfactory results for photographic studies using diffuse back lighting. However, when focused back lighting was used (as would be required for

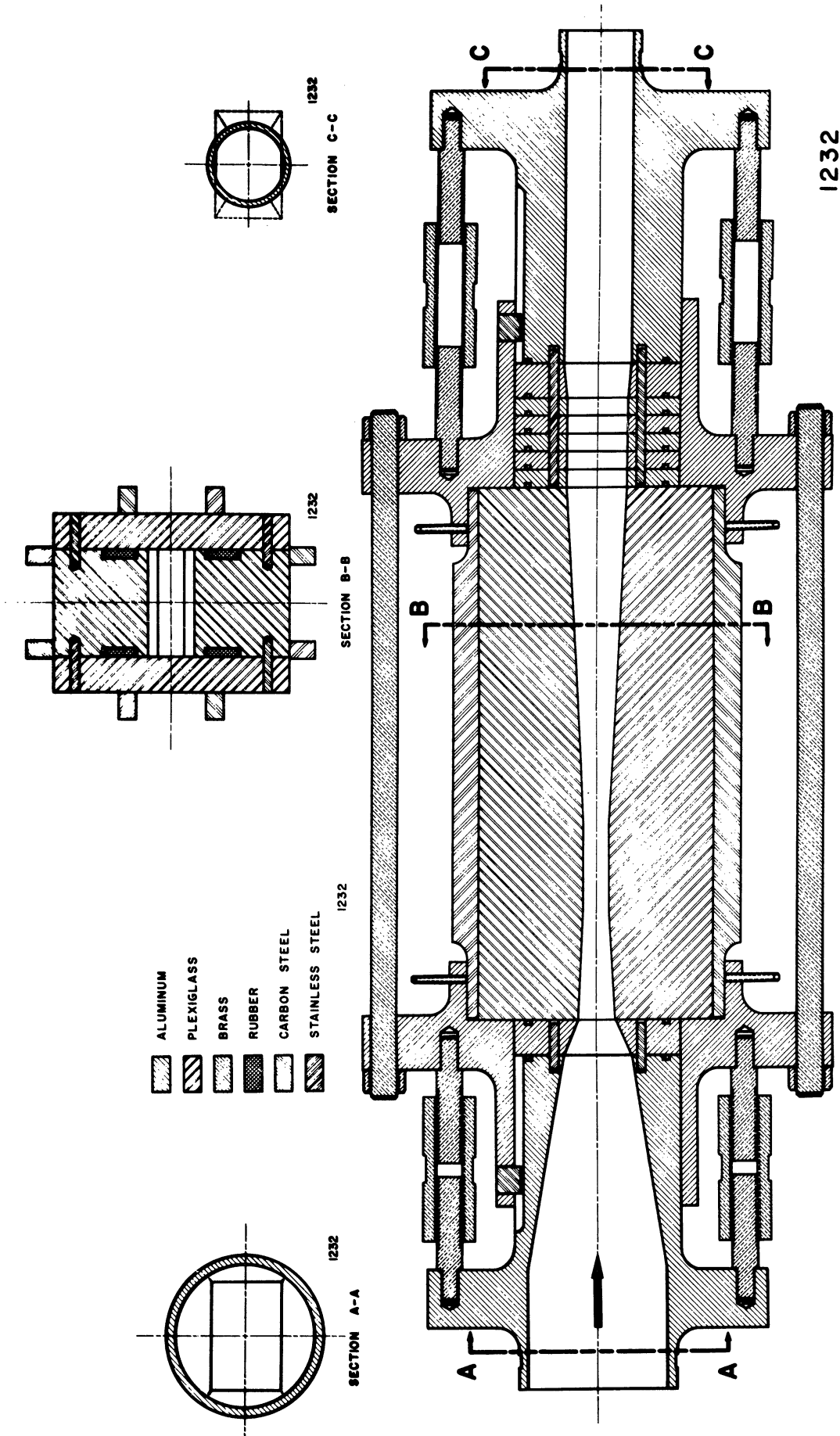


Figure 2.2 Schematic of Plexiglas Two-Dimension Venturi Without Wedge or Spoiler

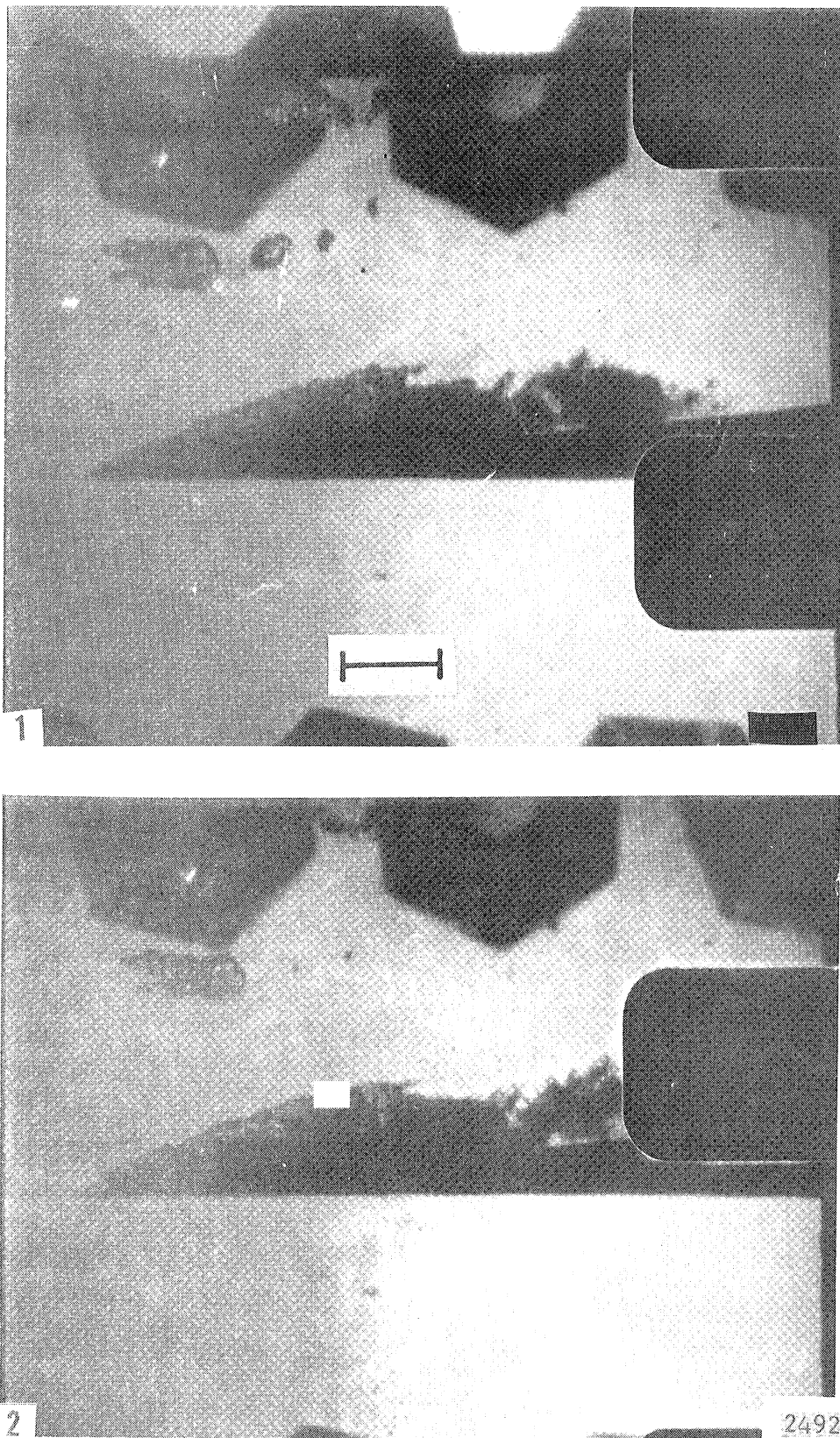


Figure 2.3 Flow Separation Caused by Uneven Flow at the Tip of the Wedge

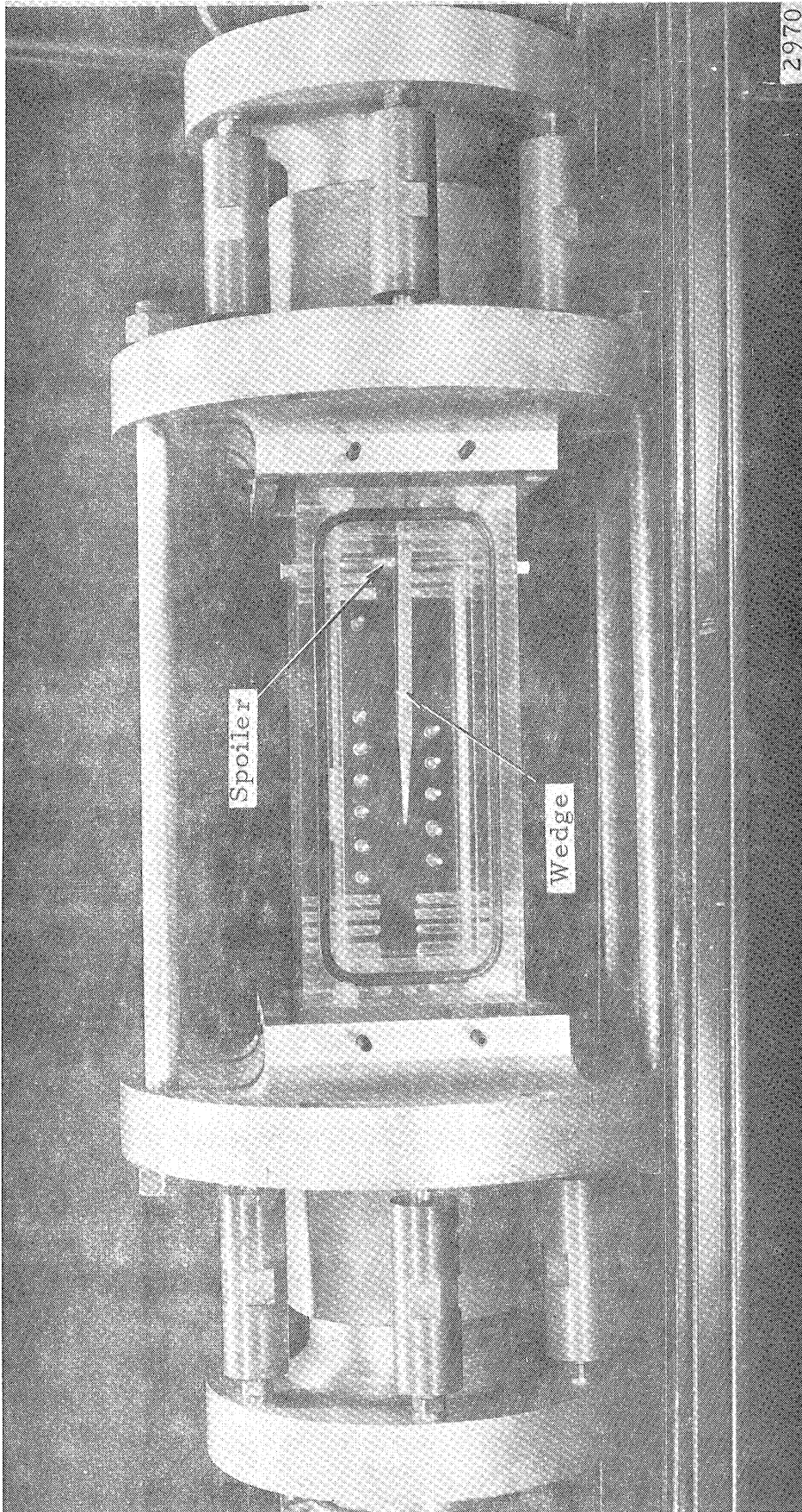


Figure 2.4 Modified Plexiglas Venturi Including Wedge and Spoiler (Quarter Size)



shadowgraph or Schlieren work) small cracks in the sides of the venturi, plus a total of 15 cm of plexiglas in the optical path, caused the optical distortion shown in Fig. 2.5. These cracks, which show up as lines in the figure, could not be removed by polishing, and the uneven lighting was caused by variation in the thickness of the plexiglas.

### C. Aluminum Two-Dimensional Venturi

A second two-dimensional venturi was constructed to eliminate the optical problems encountered with the two-dimensional plexiglas venturi. This second venturi was constructed of four pieces of aluminum bolted together. Provision was made for flat glass or plexiglas plates to be incorporated in the sides. It was designed with the constant dimension of the rectangular cross section parallel to the light beam used for photographing bubbles. In this way, the light beam passed through a constant thickness of glass and water and, with proper alignment, the beam was perpendicular to each interface. A stainless steel wedge was designed which bisected the angle of the diffuser and was capable of being moved in the axial direction as required. This design provided two identical flow paths which were symmetric with the axis of the wedge. Flow control was aided by the use of downstream "spoilers" on either side of the wedge allowing for precise equalization of the flow at the tip of the wedge. The venturi was initially designed with a throat cross-section of 1.27 cm x 1.27 x 5.08 cm long, and a  $12^\circ$  included diffuser angle, with the hope of preventing separation at the wall by proper positioning of the wedge. Initial high-speed photographs showed that separation could not be prevented by the wedge. With the wedge leading edge at the throat exit, cavitation initiated at its tip causing separation on both sides of the wedge and, with the wedge slightly withdrawn from the throat exit, separation occurred

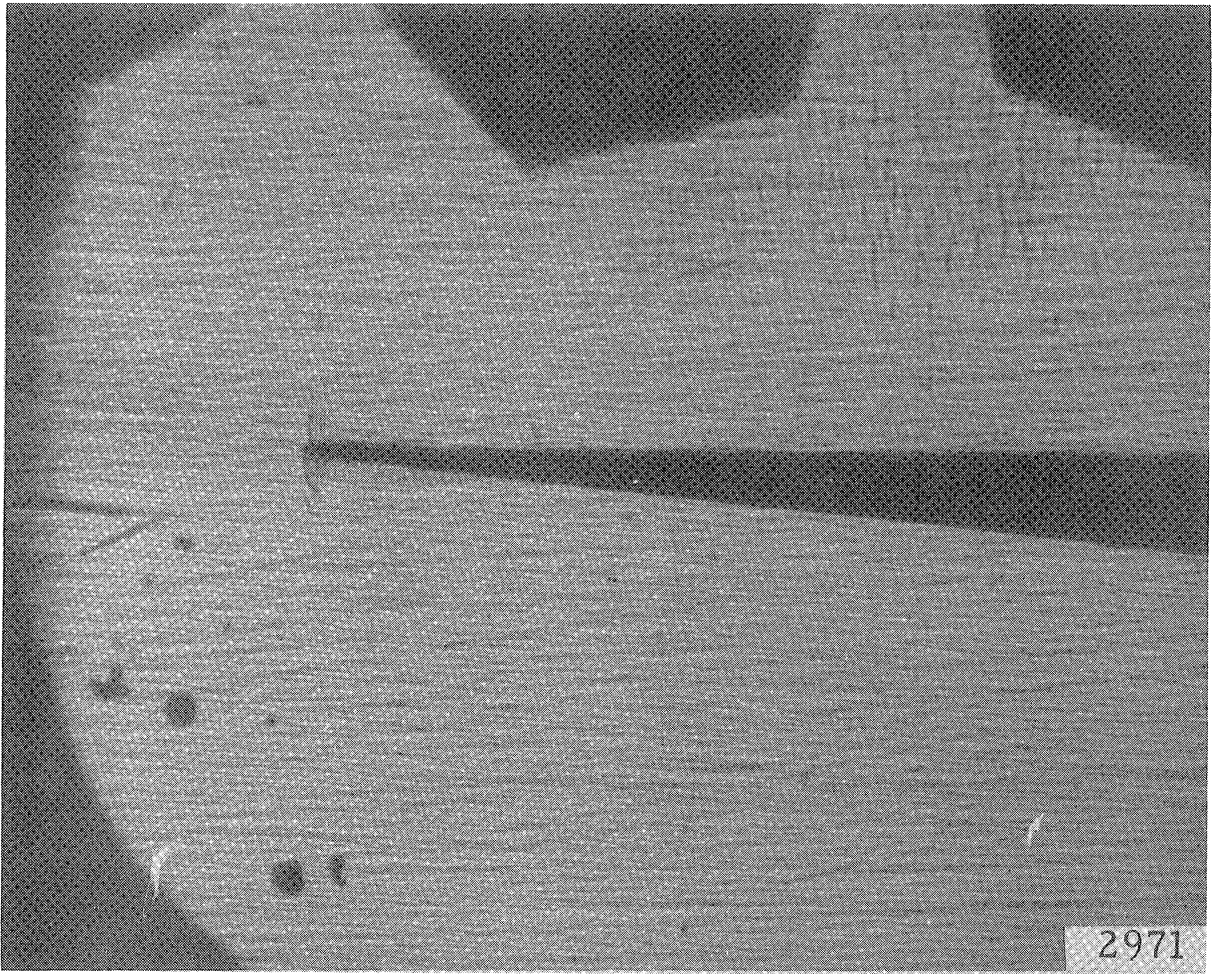


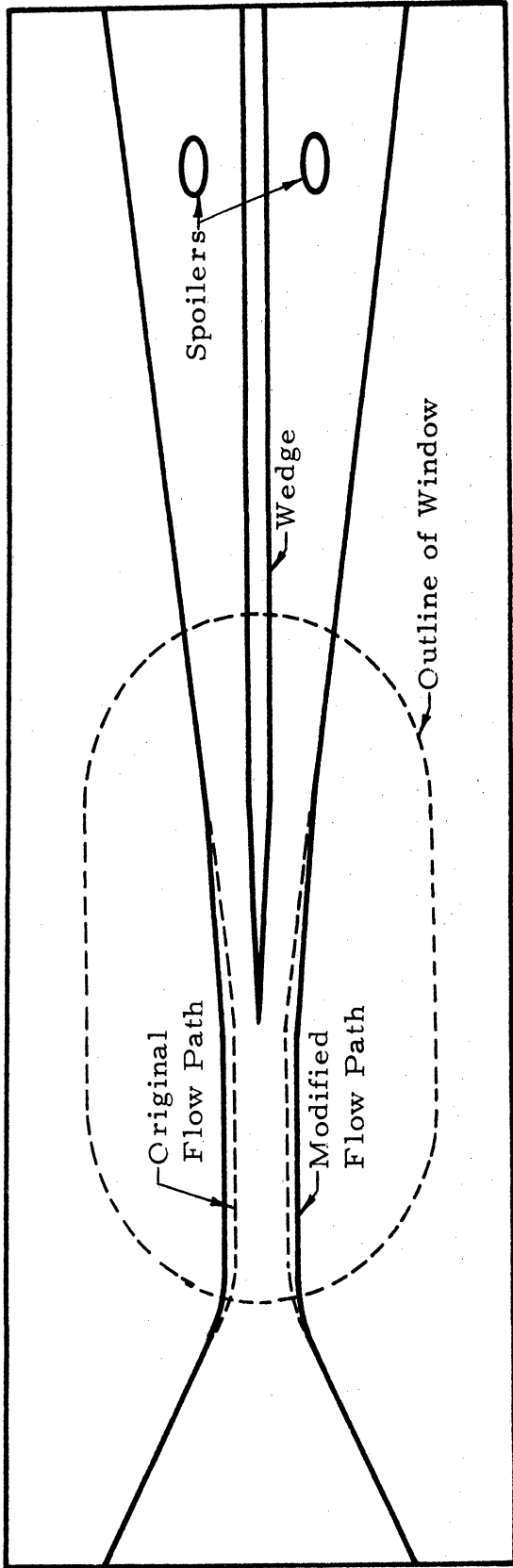
Figure 2.5 Imperfections in Plexiglas Which Appear When Focused Back Lighting is Used

along the walls. Also, because the diffuser and the wedge diverged at different included angles ( $12^\circ$  for the diffuser vs.  $7^\circ$  for the wedge) streamlines in the flow were not parallel to the wedge, adding additional complication to the analysis. These problems were reduced by modification of the venturi so that a short section of the diffuser had an initial included angle of  $7^\circ$  which coincided with the included angle of the wedge; thereby, eliminating separation and producing streamlines parallel to the wedge and diffuser wall. These modifications increased the throat dimensions to 1.59 cm high x 1.27 cm wide x 5.0 cm long, while the diffuser diverged at an initial angle of  $7^\circ$  for 5.0 cm downstream of the throat exit and at an angle of  $12^\circ$  thereafter. A schematic representation of the flow path is shown in Fig. 2.6. The assembled venturi (Fig. 2.7) was clamped between the same aluminum end pieces used for the plexiglas venturi.

Axial pressure profiles in the venturi were made with an additional side plate and a special plexiglas plate both containing pressure taps. A pressure profile was made by operating the venturi under the identical conditions of a photographic run with one side plate and the opposite glass plate replaced by the tapped plates (Fig. 2.8). Pressure readings were then taken at each tap. A plot of these pressures vs. the positions of the taps (Fig. 2.9) gave the pressure profile in the venturi.

The optical windows in the sides of the venturi were 17.2 cm long x 8.9 cm wide x 0.79 cm thick and extended beyond either side of the throat. For all the photographic investigations of natural cavitation and some of the spark-induced bubble investigations, surplus low cost, flat, coated glass windows were used, producing photographs with little distortion and light loss. For spark-induced bubble investigations, these glass plates were provided with





2972

Figure 2.6 Schematic Diagram of Original and Modified Flow Path for the Aluminum Two-Dimensional Venturi Including Wedge and Spoilers (Approximately Half Size)

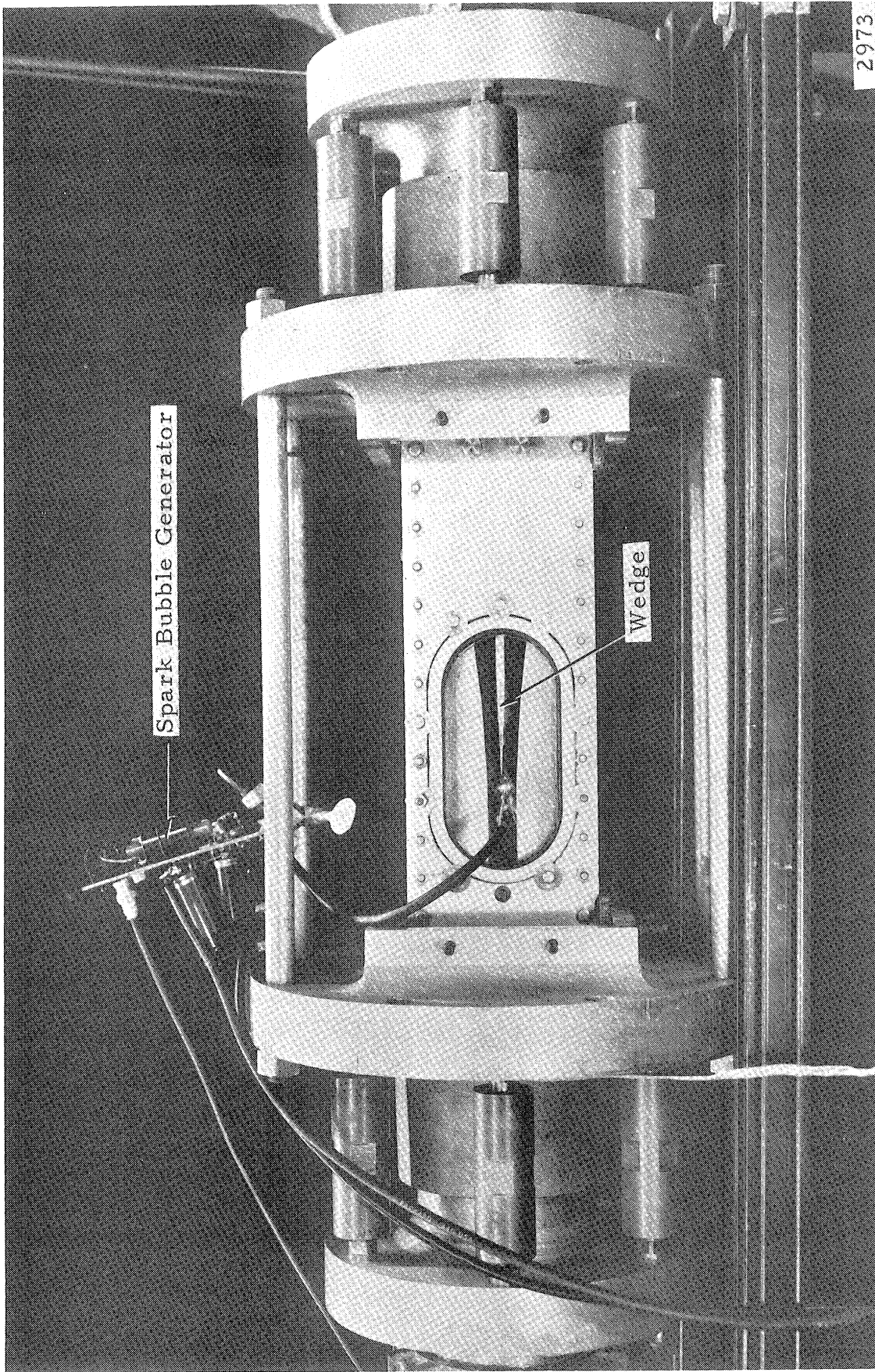


Figure 2.7 Assembled Aluminum Two-Dimensional Venturi Including Spark Bubble Generator (Approximately Quarter Size)

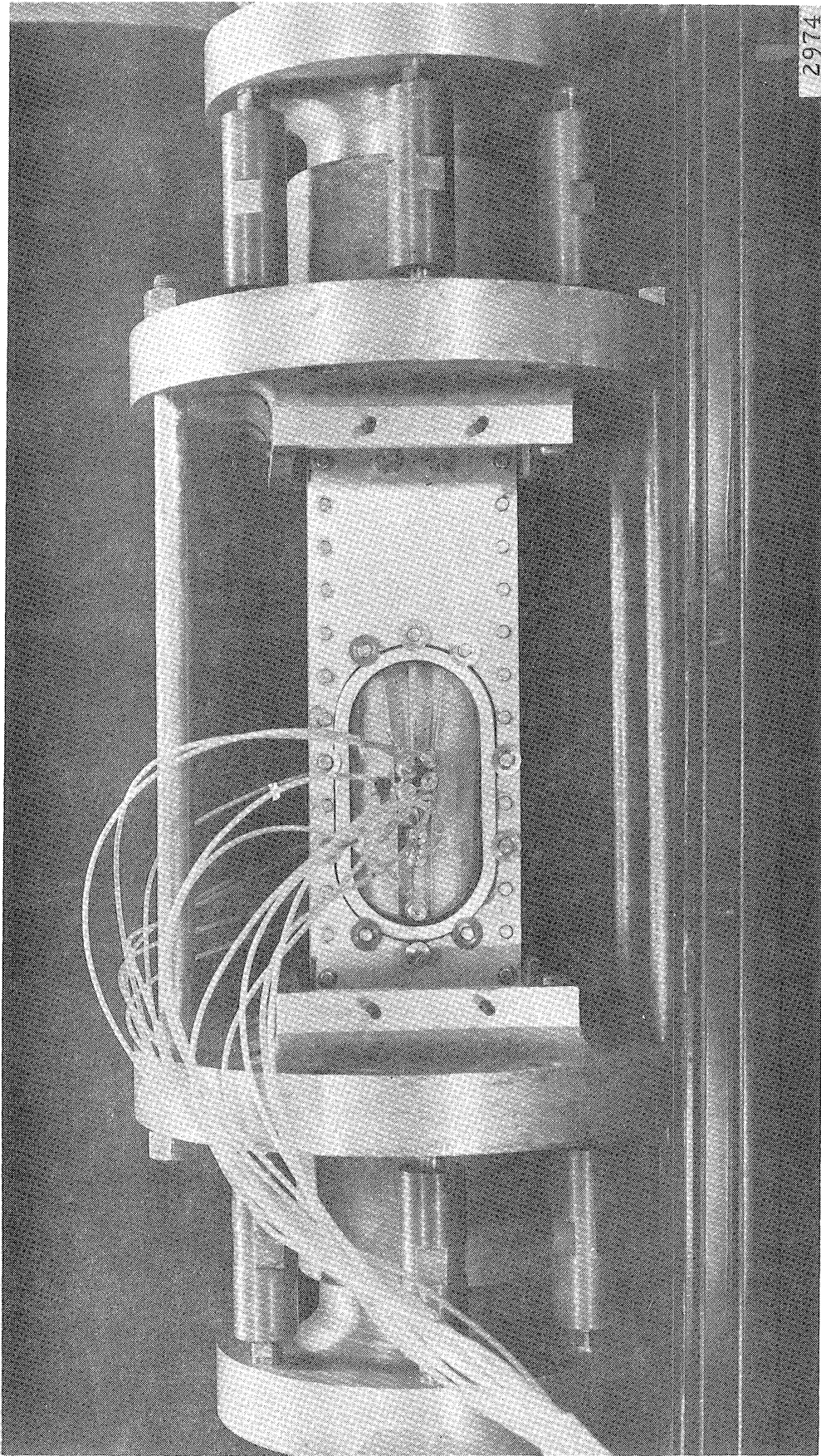
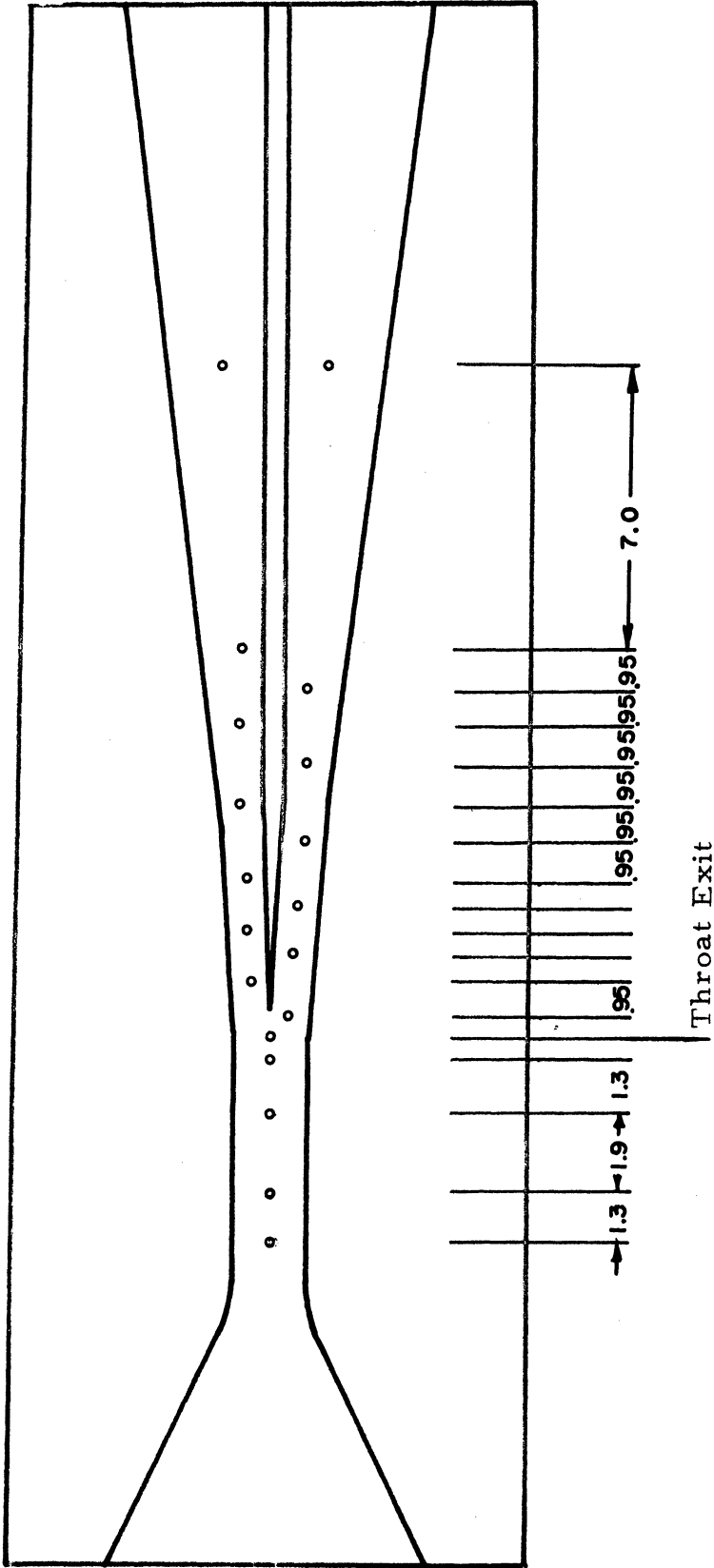


Figure 2.8 Aluminum Two-Dimensional Venturi Assembled  
With Pressure Tap Plates (Approximately  
Quarter Size)



Dimensions in cm.  
All undimensioned spaces 0.64 cm

2975

Figure 2.9 Schematic Diagram of Pressure Tap Position  
in Aluminum Two-Dimensional Venturi



ultrasonically drilled holes to accommodate the spark electrodes. However, the shock wave produced by the initial spark coupled with the clamping stresses in the glass plates caused severe breakage problems. Plexiglas plates of the same dimensions, offering much less distortion than the 15 cm thickness of the original plexiglas venturi, were then constructed. These plates were drilled to accommodate the spark electrodes and eliminated the breakage problems. The spark electrodes consist of 0.075 cm hardened steel needles ground to a streamlined shape in the direction of flow.

An attempt was made to produce a natural cavitation bubble detector to be used with the Beckman and Whitley Model 330 camera. Such a detector is required because of the short writing time (40  $\mu$ s to 1000  $\mu$ s) of the camera. Therefore, the probability of photographing a randomly-occurring cavitation bubble in the critical phase of its collapse is very small. The detector (Fig. 2.10) uses a light-beam photodiode arrangement to detect the bubble. When a bubble in the correct position breaks the light beam the signal from the photodiode triggers the delay network which, after a specified delay, fires the photographic sequence of the Model 330 camera. Although the detector greatly reduced the random probability of photographing a natural cavitation bubble, the variations of bubble size and shape were so great that all the photographs produced were of irregularly shaped bubbles or of cavitation bubbles that were not near their critical collapse stage.

In order to have some control over the size and position of cavitation bubbles in the two-dimensional aluminum venturi, several methods of bubble generation (natural cavitation, gas bubble injection, spark bubble generation, laser nucleation of bubbles, etc.) were studied. Of these, the spark bubble-generator provided the

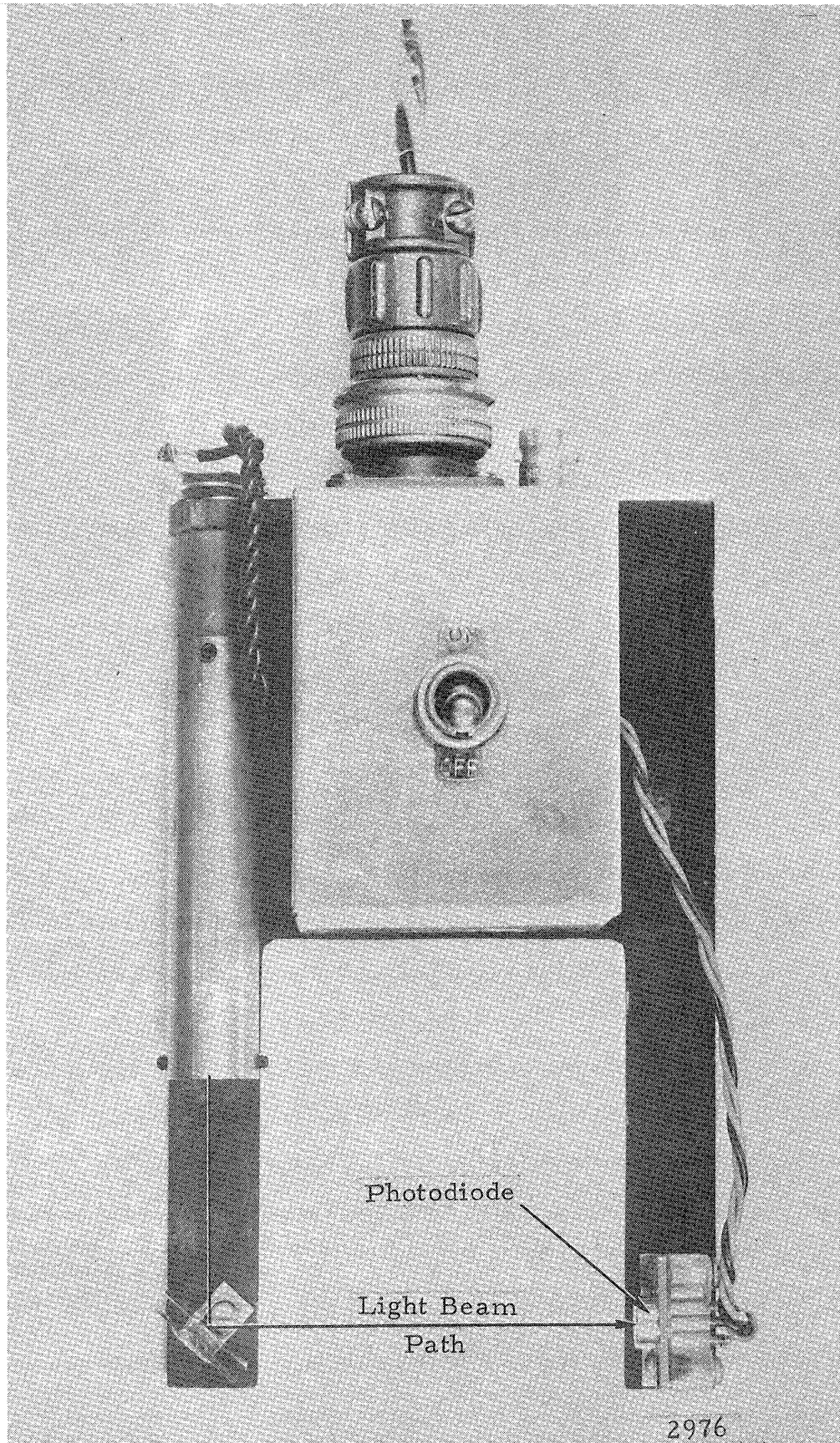


Figure 2.10 Natural Cavitation Bubble Detector (Approximately Full Size)

simplest device which allowed precise control of bubble size, bubble position, and time of initiation. The spark bubble-generator circuit shown schematically in Fig. 2.11 was used in spark-induced bubble investigations in both the venturi and spark chamber to be discussed later. A spark-induced bubble was generated by first charging the energy storage capacitor to a high voltage ranging between 7 and 12 kilovolts. A trigger pulse from the camera circuit to the silicon-controlled rectifier discharged the  $1.0 \mu\text{F}$  capacitor across the primary of a trigger transformer producing the trigger pulse (24 kV peak and  $10 \mu\text{s}$  pulse width). This trigger pulse breaks down the gap between the trigger electrode and the center electrode. The energy storage capacitor then discharges across the damping resistor,  $R_1$ , the hold-off gap, and the underwater gap producing the bubble. The time delay between the trigger pulse and the energy storage capacitor's discharge is about  $5 \mu\text{s}$  and the pulse width of the discharge of the energy storage capacitor is of the order of  $1 \mu\text{s}$ . For a given venturi throat pressure, the bubble size is dependent upon the energy delivered to the underwater spark gap. This energy is governed by the magnitude of the energy storage capacitor, the charging voltage, the magnitude of the damping resistor and the size of the underwater gap relative to the hold-off gap. Slight variations in these parameters from generation of one bubble to the next, produced about 10% variation in bubble lifetimes. The energy deposited in the water is determined by the simultaneous measurement, using a dual trace oscilloscope, of the voltages across the inductionless shunt resistor,  $R_2$ , and the voltage divider resistors,  $R_3$  and  $R_4$ .

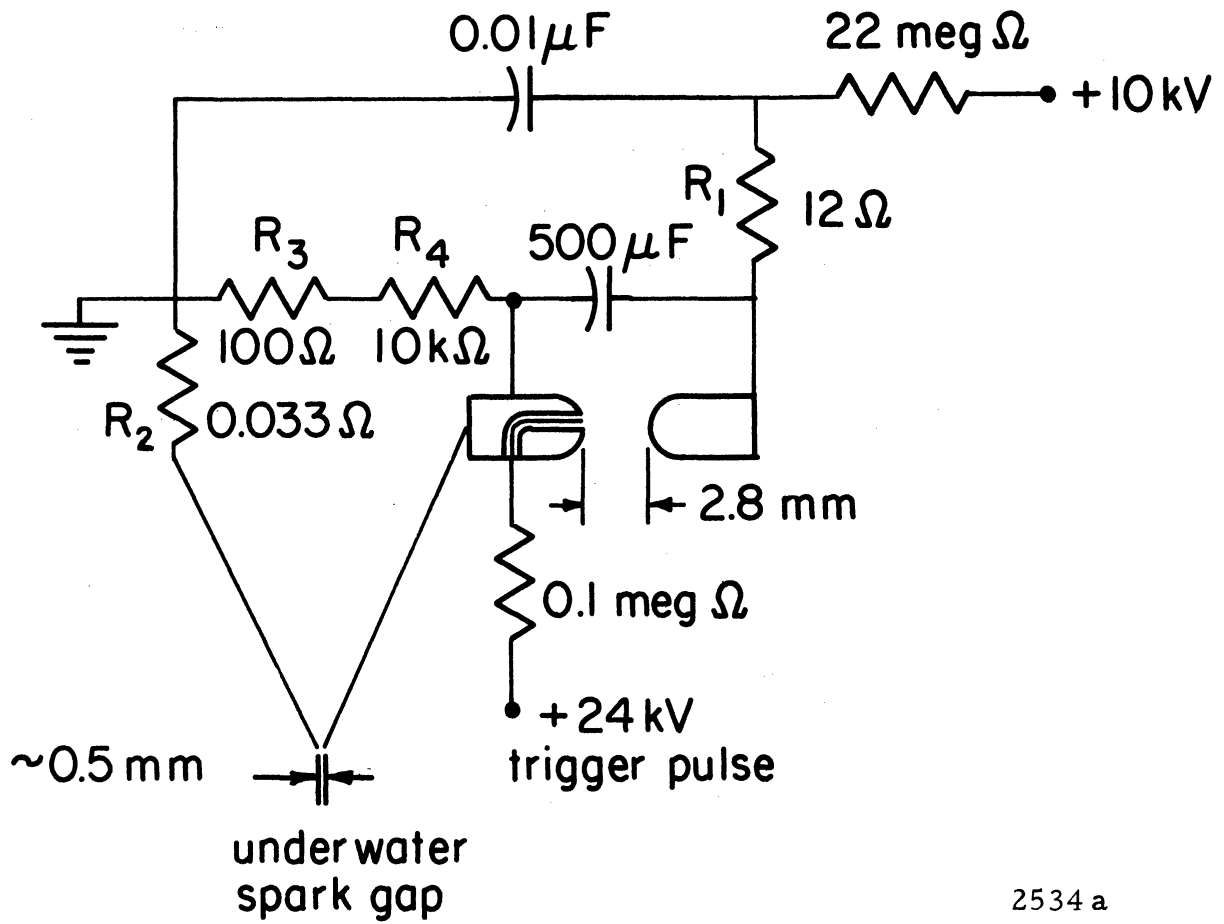


Figure 2.11 Schematic Diagram of Underwater Spark Bubble Generator Circuit



#### D. Static Underwater Spark Chamber

A preliminary investigation of the energy required to produce a spark-induced bubble of any required size in a prescribed pressure field was performed using a static underwater spark chamber. The spark chamber was constructed of 0.16 cm thick aluminum forming a box with internal dimensions of 7 cm thick x 15 cm wide x 20 cm in height. Plate glass windows 1.27 cm thick attached and sealed with silicon rubber gaskets, covered 7 cm x 5 cm holes in the sides of the box. The box also contained penetrations for the electrodes, a vacuum pump, and a pressure gage. These penetrations were also sealed with silicon rubber. Electrodes made of 0.16 cm needle-pointed stainless steel rods entered at the top of the box and were bent at a  $90^\circ$  angle to bring the tips into close proximity. The same spark bubble-generator circuit as described for the two-dimensional venturis was used in this investigation. Fig. 2.12 shows the spark chamber and spark bubble generator circuit. Photographic investigations were made varying the pressure from atmospheric down to approximately vapor pressure inside the chamber. The input energy of the spark bubble-generator circuit was varied from 0.05 joules to 5.0 joules. The results of this investigation aided in the determination of the parameters for the charging voltage, energy storage capacitors, damping resistors, and relative spark-gap distances used in the spark bubble-generator circuit for the two-dimensional venturis.

#### E. Gas-Gun Momentum-Exchange Device

A photographic investigation of high-speed water jets impacting on solid specimens was conducted in order to determine what characteristics of jet impact caused them to produce damage similar to that produced by cavitation bubble collapse. The gas-gun momentum-exchange device (more fully described

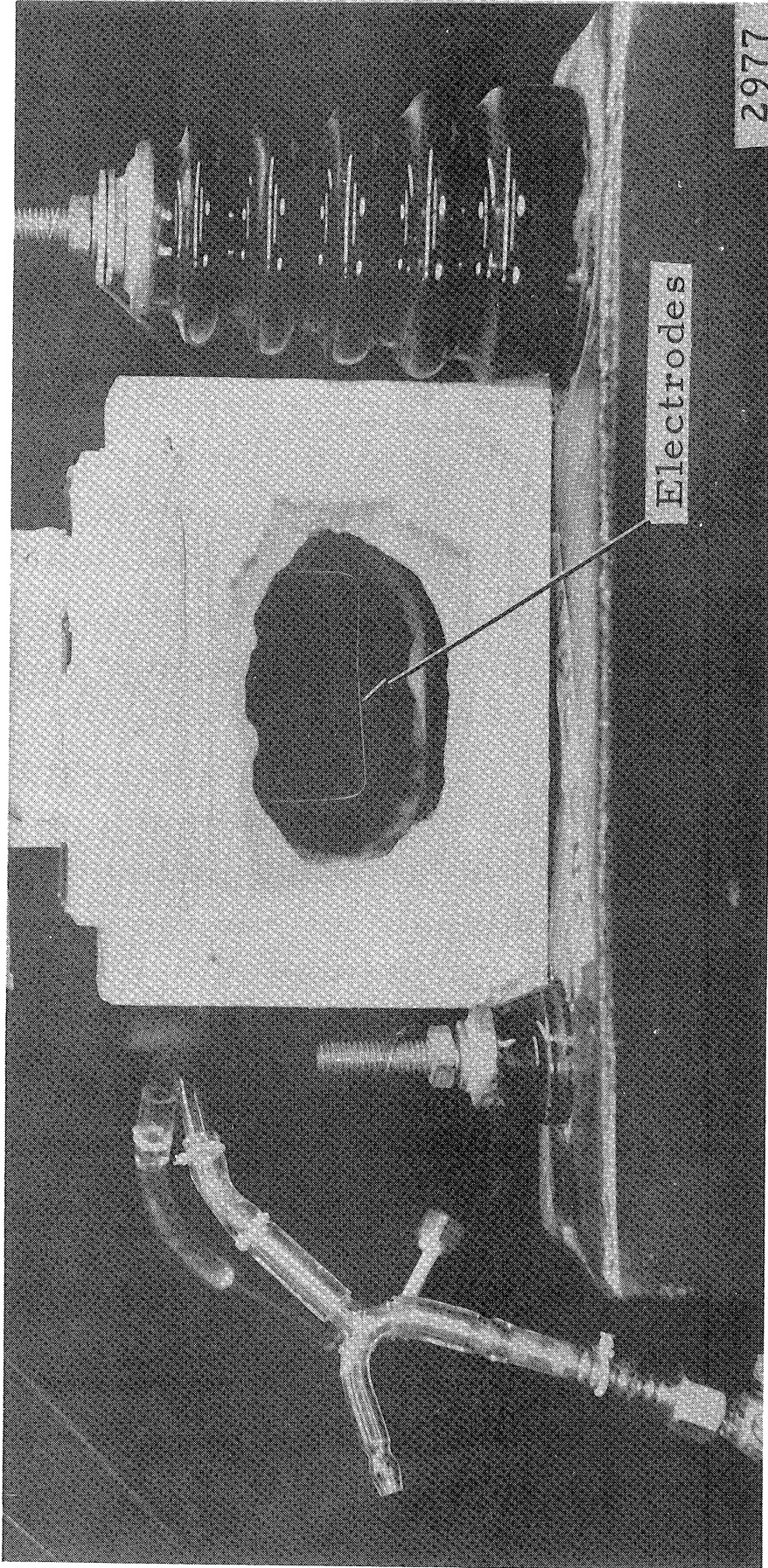


Figure 2.12 Static Underwater Spark Bubble Chamber  
(Approximately 2/3 Size)

in Ref. 32) was used to produce these high-speed water jets. The device (Fig. 2.13) used a 22 caliber (0.56 cm bore) gas gun originally designed to use CO<sub>2</sub> cartridges as a propellant but modified to use nitrogen from high-pressure tanks. The rifle fires a lead pellet into a lead impact disc at the rear of a small cavity (Fig. 2.14) containing water. The water cavity has an initial diameter of 0.61 cm and converges to form a nozzle with an exit diameter of 0.18 cm. The impact disc which is struck by the lead pellet is free to move axially in the chamber and results in a highly efficient exchange of momentum between the lead pellet and the water in the chamber. The movement of the impact disc produces a high pressure pulse in the water chamber resulting in a water jet or slug being forced through the nozzle at a very high velocity. The water jet is directed against a target specimen which is held 1 cm from the exit of the chamber. The most efficient transfer of energy between the pellet and the water in the chamber was obtained when the impact disc was made of thin sheet lead. Previous experimentation determined that the most damaging jets were produced by a maximum gas gun chamber pressure (25 atm.), which produced a pellet velocity of 140 m/s and resulted in a jet velocity of 670 m/s. Since this investigation is concerned with the similarity between cavitation bubble collapse and jet impact damage, only these most damaging jets were studied. Previous estimates indicate that this is the correct order of magnitude for the velocity. <sup>(33)</sup>

The velocity of either the pellet or the water jet were measured using a double-light beam photodiode device (Fig. 2.16). When the pellet or water jet breaks the first beam, the sweep of an oscilloscope is triggered. This sweep registers the time of flight between the two beams. An oscilloscope camera is used to permanently record the sweep trace. This device determined that with the same gas gun chamber pressure (25 atm.) the water jet velocity varied less than ten percent from 670 m/s.

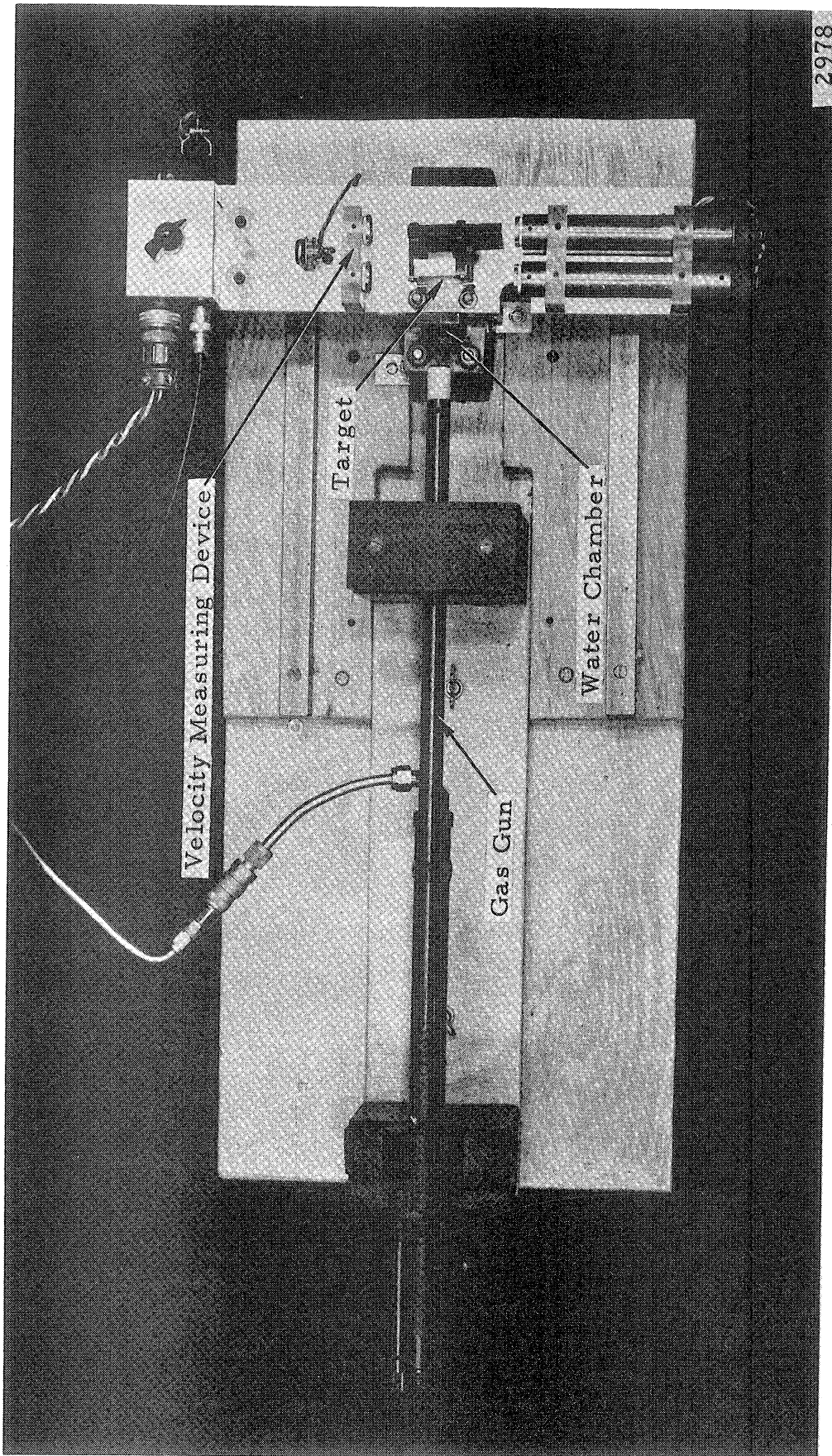
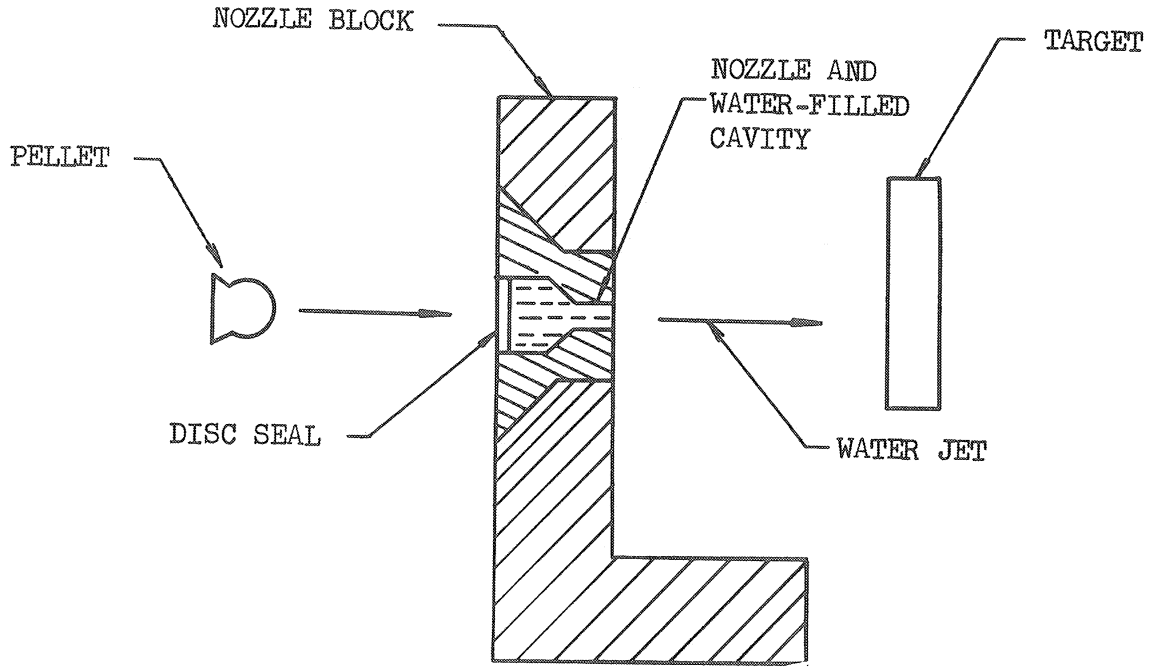


Figure 2.13 Gas Gun Momentum Exchange Facility Including Target and Velocity Measuring Device (Approximately Quarter Size)





2384



Figure 2.14 Water Cavity of Gas Gun Momentum Exchange Facility (Approximately Double Size)

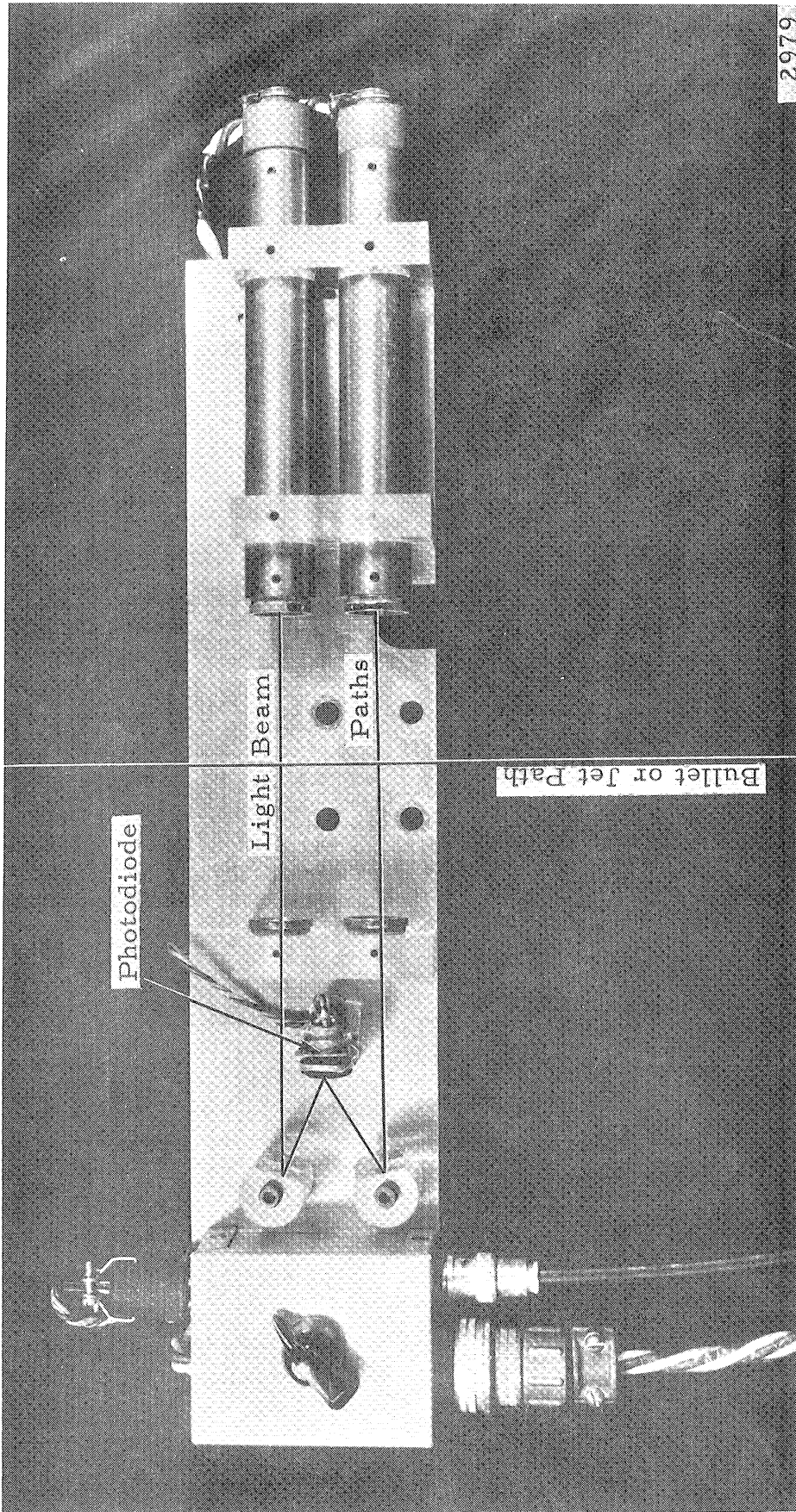


Figure 2.15 Dual Beam Velocity Measuring Device (Approximately Half Size)

## F. Aluminum Coatings

Two aluminum coatings were used to cover the surfaces impacted by high speed water jets and cavitation bubbles. Mechanical properties of the two types of aluminum used are presented in Table 2.1. The most easily damaged of these coatings is a highly polished 50  $\mu$  thick aluminum foil (1100-0) with an adhesive backing. This foil could be easily applied and removed. Because of its initial high polish, any deformation due even to a single impact could easily be detected. A second stronger aluminum was also used. This coating was fabricated from 0.50 mm aluminum lighting which also had a highly polished surface. Individual damage pits on this coating were harder to obtain because of the increased hardness of the aluminum, and also its increased thickness, so that the adhesive backing had little effect on the formation of the crater. Photomicrographs were made of the damage pits produced by high speed water jets, natural cavitation bubbles, and spark induced shock waves and cavitation bubbles. A striking similarity in the craters thus produced was then noted. For the thicker aluminum coating, proficordor traces were made in order to obtain shape information for the craters produced.

TABLE 2.1

## Mechanical Properties of Aluminum Coatings

Type of Aluminum	Thickness mm	Ultimate Strength atm	Yield Strength atm	Elongation %
1100-0	0.050	800	240	20
Specular Lighting Sheet	0.50	1700	1500	5



## CHAPTER III

### PHOTOGRAPHIC SYSTEMS

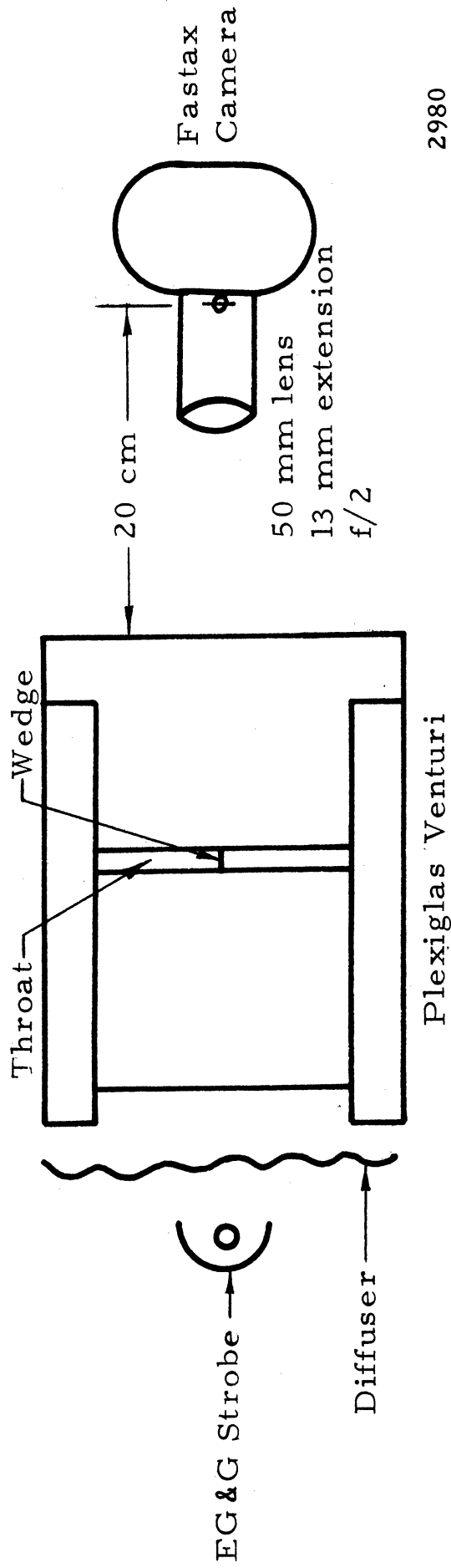
The photographic equipment described here was used to study the collapse of cavitation bubbles near a solid surface in order to determine how such bubble collapse damages the surface. An ideal photographic apparatus would follow a cavitation bubble from its inception through at least the first minimum collapse point with a framing rate and spatial resolution great enough to determine all aspects of the bubble collapse (i. e., bubble size, shape, collapse rate, etc.). Bubbles studied in this investigation have maximum diameters ranging from 0.5 mm to 20 mm, while the damage area they produce ranges from 0.01 mm to 0.1 mm (10 to 100  $\mu$ ) in diameter. The lifetime of these bubbles varies from a minimum of 0.2 ms for some spark-induced cavitation bubbles produced in the aluminum two-dimensional venturi to a maximum of  $\sim 3$  ms for spark bubbles produced in the spark chamber facility; the damage is produced by the bubbles in a time span of a few microseconds. Therefore, the ideal photographic system would have a framing rate of at least  $10^6$  frames/sec., a writing time of at least 1.0 ms and a spatial resolution to cover a range from several mm to a few microns on the same frame. No single system presently available in this laboratory meets all of these criteria. However, several different systems were used each of which met several of the above requirements; taking the systems as a whole, all of the above requirements were met or exceeded.

#### A. The Fastax Camera and the E. G. and G. Stroboscopic Light Source

In the Fastax WF-1 camera, film is transported continuously past the aperture while a rotating prism, geared to film motion, produces an image which is stationary with respect to the film.

Individual frames which are 16 mm x 8 mm constitute the 100 ft. roll of film which is used. A Wollensac Goose control regulates the amount of power delivered to the camera motors. These motors continuously accelerate the film, which is initially at rest, through the camera with the maximum acceleration determined by the yield stress of the film. Because of this acceleration, the framing rate of the camera continuously changes and the maximum framing rate is obtained only near the end of the spool of film. The exact framing rate is determined with the aid of marks placed along the edge of the film by a 60 Hz timing light. An E. G. and G. Stroboscopic light source which produces high intensity 1.2  $\mu$ s duration light pulses at a maximum rate of 7,000 flashes/sec. was used to reduce the exposure time per frame. The flash rate of the light source was synchronized to the camera by the use of a timing signal produced by the rotating prism in the Fastax camera. Since the Fastax camera has a rated top speed of about 14,000 frames/sec., the system was limited by the flash rate of the light source.

All of the photographic studies using the Fastax camera were made using the plexiglas two-dimensional venturi with the stainless steel wedge in place.(Fig. 3.1). The camera, loaded with a 100 ft. roll of Tri-X reversal film, was focused on a 1.5 cm x 3.0 cm field of view while the light source and light diffuser were placed to produce diffuse backlighting of the cavitation bubbles in the throat and diffuser of the venturi. The camera controls were set to trigger the light source only during the last 1/3 of the film when the camera had accelerated to near the maximum framing rate. A photographic run was made when the pump rpm, loop surge tank pressure and air content were set for a cavitation condition such that a few large bubbles were always in the throat and diffuser of the two-dimensional venturi. After each run, the film was processed commercially. The



2980

Figure 3.1 Schematic Arrangement of Pexiglas Venturi, Fastax Camera, and Strobe Light

film was first analysed by using a 16 mm projector, followed by a frame by frame analysis using a microfilm reader. The major advantages of this system are the large number of frames per run ( $\sim 10^3$ ), the long writing time ( $\sim 0.2$  sec.), and the short exposure time ( $1.2 \mu\text{s}$ ). This allowed a study of randomly occurring natural cavitation bubbles. The major disadvantages are the relatively low framing rate (less than 10 frames per bubble lifetime), the possibility of only one frame during the critical damage-producing phase of bubble collapse, and a relatively low resolution (due to the small frame size) so that little detail of the bubble shape could be determined for the few frames showing bubbles near their minimum collapse volumes.

#### B. Dynafax Camera and Xenon Arc Light Source

The Beckman and Whitley Dynafax Camera is a continuous access camera utilizing both film transport and a rotating mirror, to produce a high framing rate (26,000 frames/sec. maximum) and a short exposure time ( $1.0 \mu\text{s}$  minimum). A single sequence of photographs produces up to 224 16 mm frames placed in two rows on a short strip of 35 mm film which rests on the inside of a rotating drum. Each row contains only the even numbered or the odd numbered frames and the rows are displaced with respect to each other by 14.5 frames so that adjacent frames are not side by side. Therefore, some care must be exercised in reading the films in order to keep the proper sequential relationships. A rotating mirror compensates for the movement of the drum, and optical diamond stops of various size are used to control the exposure time per frame. Once the camera is brought up to speed for the required framing rate, the capping shutter of the camera is opened. The ambient light on the object being photographed is generally not strong enough to expose the film over a period of several seconds so that the exposure of the film is actually controlled by the

duration of a high-intensity light source. The light source used with this camera is a Kemlite Xenon arc lamp with a power supply built in the Michigan Memorial Phoenix Project Electronic Shop. The maximum output of this light source is 1,000 joules and the duration is variable from 0.2 ms to 12.0 ms. For photographic investigations using the Dynafax camera, the duration was set to 8.5 ms which is the writing time of the camera at its maximum framing rate.

The Dynafax camera was used for photographic investigation using both the two-dimensional venturis and the spark chamber. Both diffused and focused backlighting were used depending on the type of picture and the light intensity required. A general schematic of the experimental setup is shown in Fig. 3.2. For photographic investigation using the two-dimensional venturis, the camera was focused on the throat and diffuser sections with the proper light source behind the venturis. Next, the flow conditions in the venturi were set to produce a low density cavitation cloud. Then the camera, loaded with film, was brought up to the correct framing rate and stabilized. Finally, the capping shutter was opened and the light source triggered. After the rotating drum of the camera coasted to a stop, the film was removed and developed in the dark room facilities of the Cavitation and Multiphase Flow Laboratory of the University of Michigan. For photographic investigations using the underwater spark bubble chamber, the only changes in the experimental procedure were to replace the two-dimensional venturi with the spark chamber, to charge the energy storage capacitor before starting the camera, and to delay the trigger pulse to the spark generator circuit until the Xenon arc light source had reached its maximum illumination. Developed films were first analysed frame by frame using a microfilm reader. Later the film was

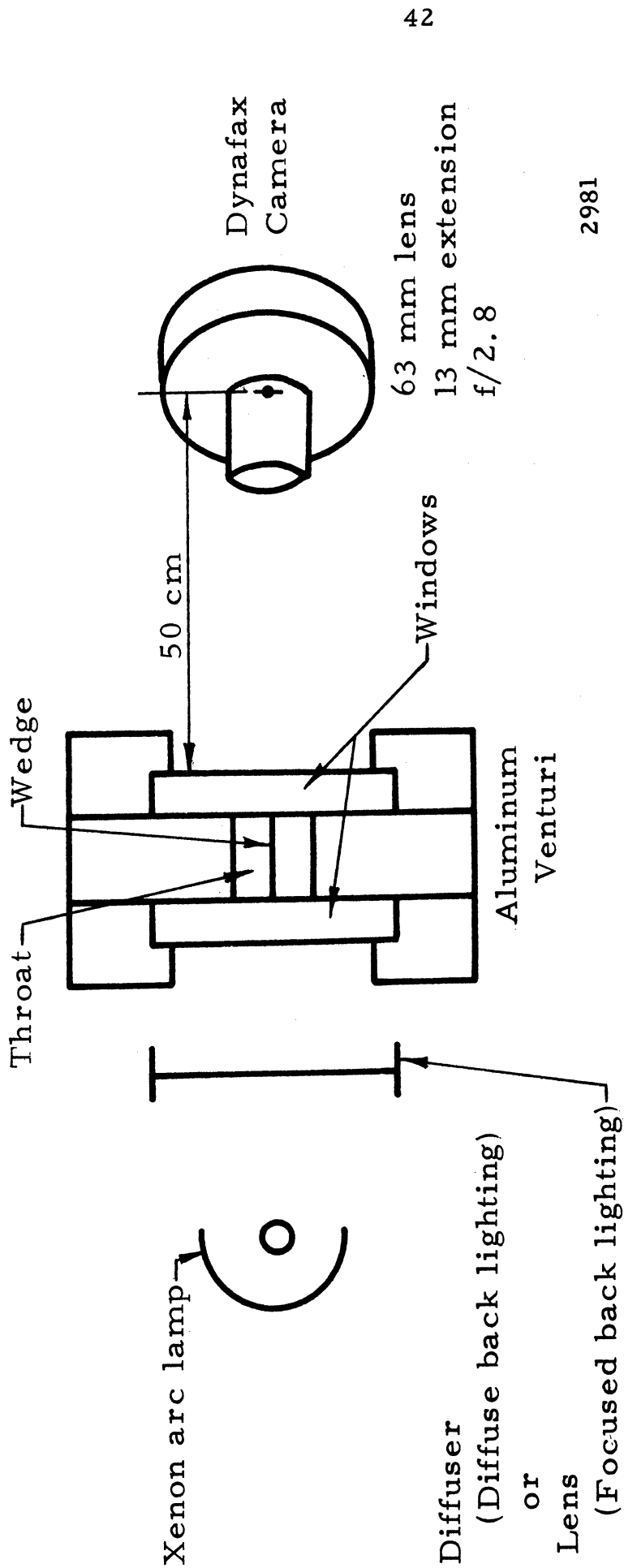


Figure 3.2 Schematic Arrangement of Aluminum Venturi, Dynafax Camera, and Xenon Arc Lamp

rephotographed in proper sequence for motion picture analysis.

The framing rates available with the Dynafax camera allowed a single bubble to be photographed up to 50 times during its lifetime. Generally one frame contained information about the critical damaging phase of the bubble collapse. Although the total number of frames per sequence is much less than the number produced by the Fastax camera, the minimum writing time of the Dynafax camera is still considerably greater than a single bubble lifetime. Unfortunately the frame size of the Dynafax film is nearly the same as the frame size of the Fastax; therefore, the resolutions are approximately equal, so that bubble definition near minimum collapse volume is relatively poor. Also, because of the peculiar optics associated with the diamond optical stops, the camera employs a system utilizing very poor light economy for the short exposure stops. Thus the high intensity Xenon arc light source must be used with this camera, and focused back-lighting, which results in less detail of the bubble shape, is sometimes required.

### C. Cranz-Schardin Photographic System

In order to obtain a photographic system with extremely high spatial resolution and a framing rate up to  $10^6$  frames/second, a Cranz-Schardin photographic system was designed and constructed using the electronic and instrument shop facilities of this laboratory. All of the frames with the continuous access Cranz-Schardin photographic system are produced on a single sheet of film which remains stationary during the photographic sequence. Each frame is made by utilizing a separate short duration high intensity spark light source and a separate camera lens. The light sources are triggered at the framing rate required, with the theoretical maximum framing rate equal to the reciprocal of the pulse duration of a single light

source, but practically limited to the reliability of the trigger circuit. The total number of frames taken during one photographic sequence is limited by the number of images which can be placed on one sheet of film and the physical size of the system components. The major advantages of this system are its extremely high spatial resolution, simplicity of design and operation, and low cost. The major parts of the system (Fig. 3.3, 3.4) are the light sources, the trigger electronics, the field optics, the camera, and the optical bench.

Compact light sources (Fig. 3.5) which are an integral part of the camera are triggerable air-gap sparks with a light output great enough to expose 400 ASA film and a light duration of 0.22 microseconds. This value is the pulse width at half maximum intensity as measured with an RCA 7102 photomultiplier. Plexiglas plates, a brass bus-bar and a bakelite strip make up the body of the light source while the major electrodes are fabricated of mild steel. The two outer electrodes are threaded to facilitate easy adjustment of the gap distances, and the center electrode is drilled to accommodate a concentric trigger electrode of insulated number 14 wire.

The operation of the light source is most easily understood by the use of a schematic (Fig. 3.6). The 0.01  $\mu$ F capacitor is charged to 10 kilovolts, and the larger gap is set just wider than the breakdown distance. When the trigger pulse (with a 24 kilovolt peak and a 10  $\mu$ s pulse width) breaks down the gap between the trigger electrode and the center electrode, the 0.01  $\mu$ F capacitor discharges across both the large and small gaps and the damping resistor within a few tenths of a microsecond. The damping resistor allows the 0.01  $\mu$ F capacitor to discharge completely in the first half cycle so that successive light pulses are eliminated.



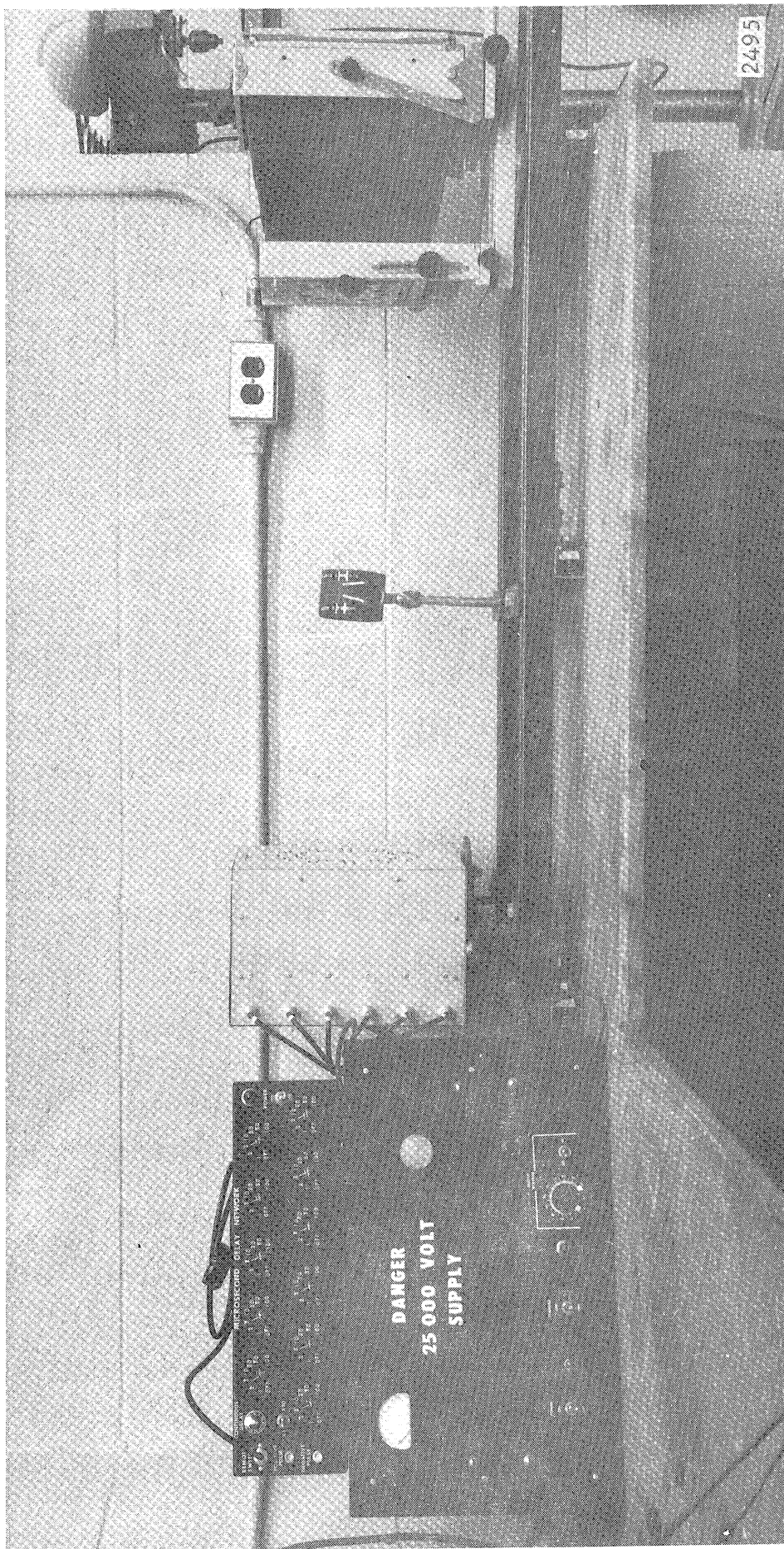


Figure 3.3 Cranz-Schardin Photographic System Including Delay Network and High Voltage Supply

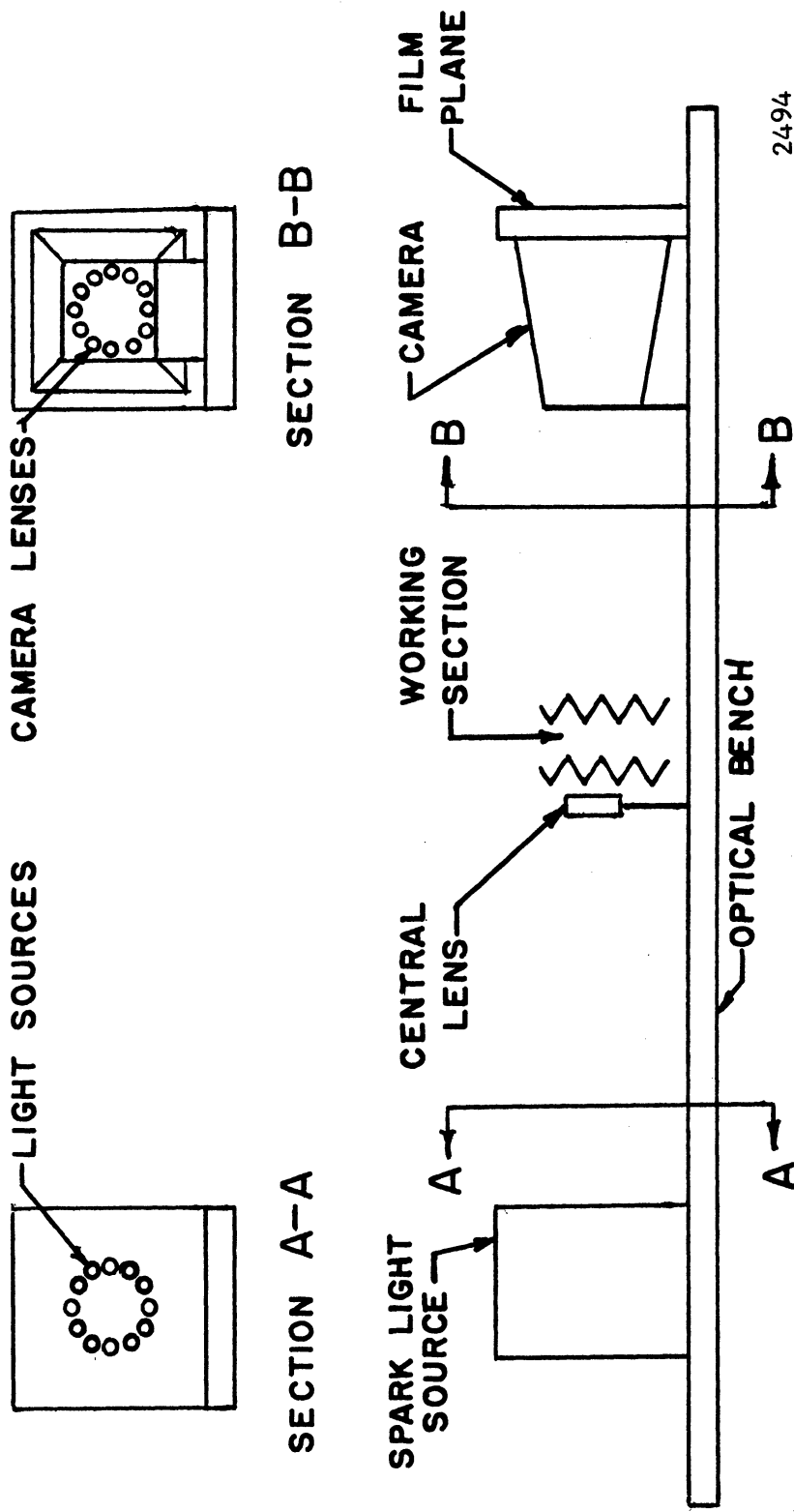


Figure 3.4 Schematic Diagram of Cranz-Schardin Photographic System

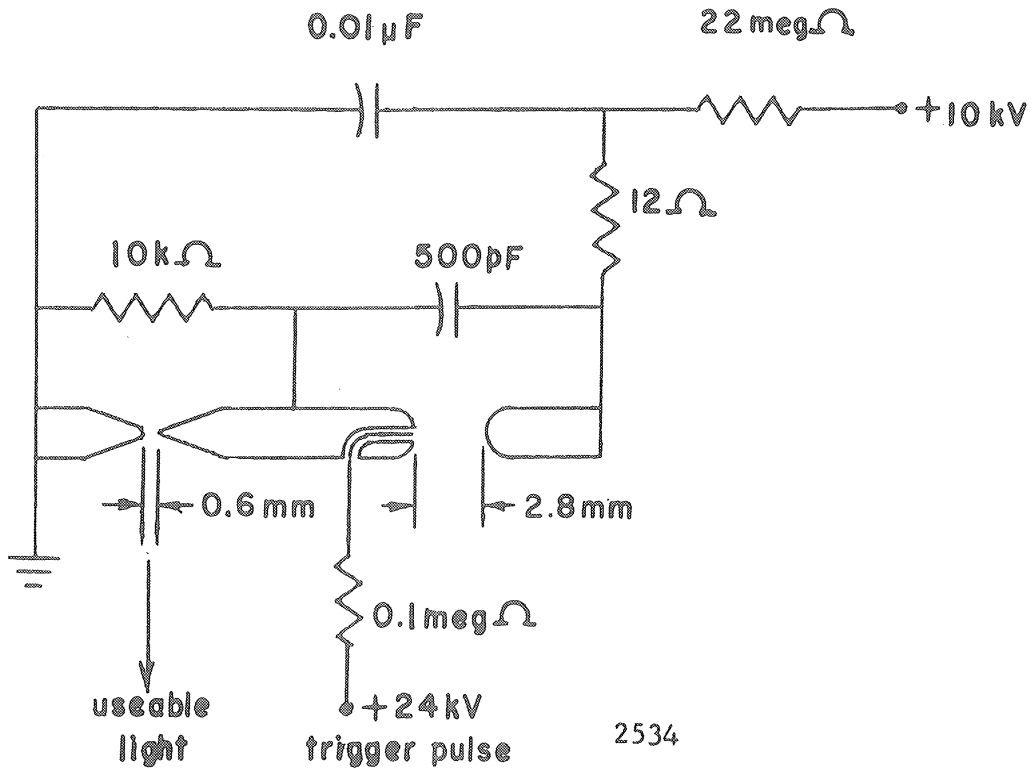


Figure 3.6 Schematic Diagram of Spark Light Source

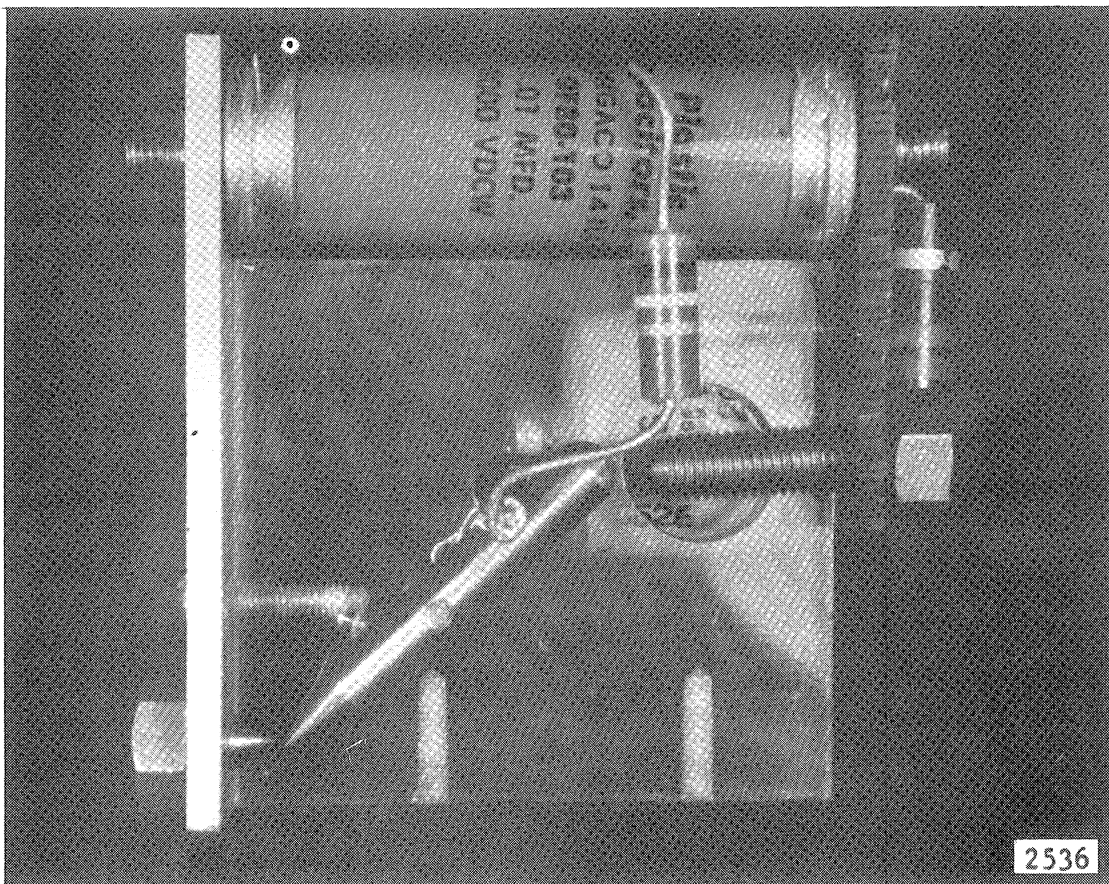
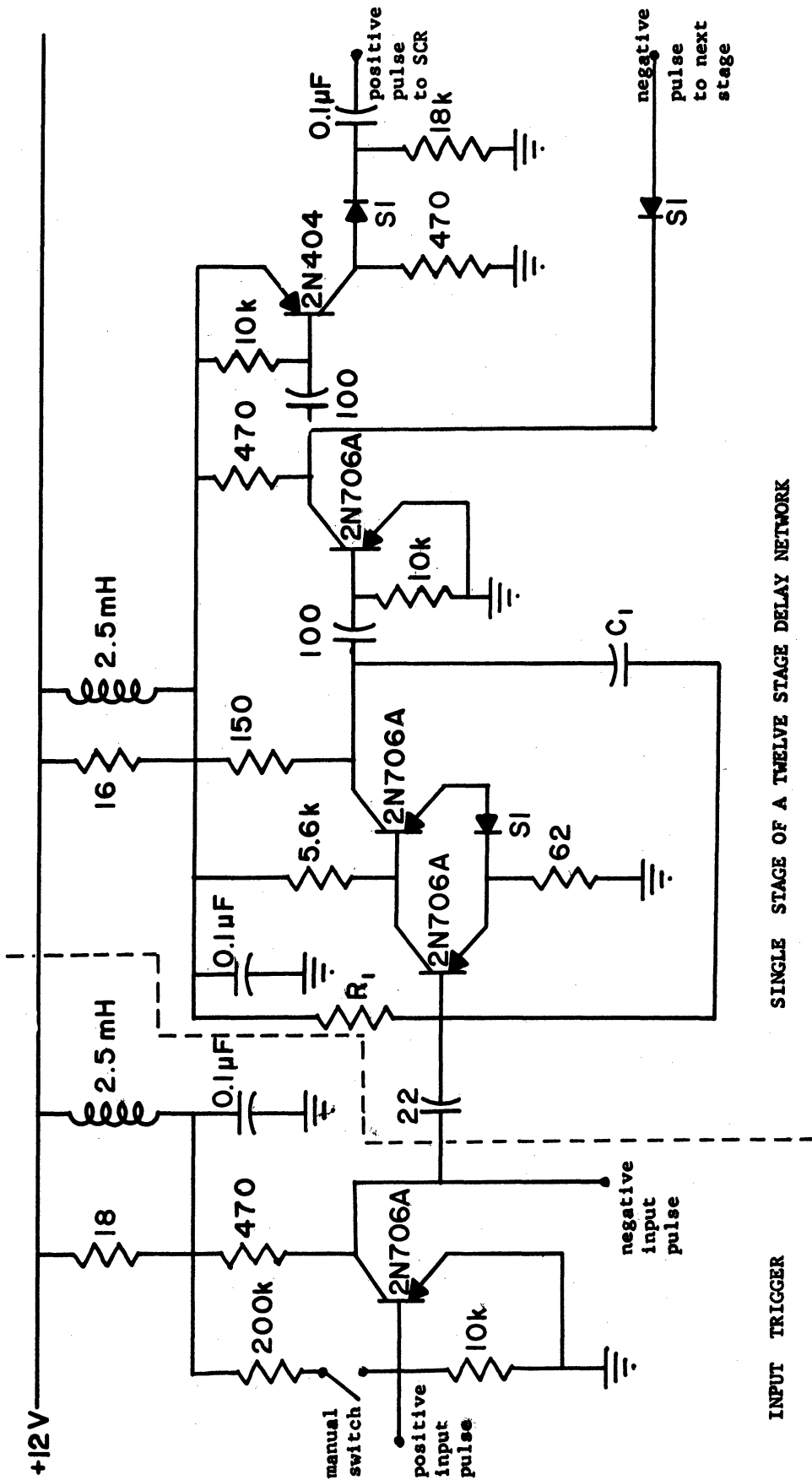


Figure 3.5 Compact, Triggerable Air Gap, Spark Light Source

The 500 pF 20 kilovolt capacitor aids in the initial breakdown of the larger gap. The smaller gap is used as the light source, and may be masked if a point light source is required. Twelve of these light sources are mounted on a 5.5 cm radius in an iron box (used to reduce electromagnetic radiation of a minimum). For compactness a 0.01  $\mu$ F capacitor having a rating of only 8 kilovolts is used. However, only one capacitor breakdown has occurred over a lifetime of approximately  $10^3$  discharges. The "jitter time" due to gap breakdown is reduced to a minimum by using the above mentioned concentric trigger electrode which allows the larger gap to be as small as possible.

A solid-state delay network was designed and constructed to produce trigger pulses with 1  $\mu$ s to 100  $\mu$ s delays (i. e.,  $10^4$  to  $10^6$  effective framing rate) for the light sources. A study of the schematic (Fig. 3.7) shows that provision is made for either a positive pulse, negative pulse, or a closed contact switch to initiate the delay network. A monostable vibrator with an adjustable RC delay forms the main component of each delay stage. The square wave output of each monostable vibrator is differentiated to produce a negative pulse with the proper delay. This pulse is amplified and then inverted. The amplified pulse triggers the next delay stage, and the inverted pulse is used to fire a silicon-controlled rectifier. The initial delay stage used a precision 10-turn resistor (+ 1%) to obtain a continuously-variable delay from 5 to  $10^3$   $\mu$ s. Each succeeding pulse may be delayed in steps of 1, 2, 10, 20, 50, and 100  $\mu$ s. The RC delays for these stages use precision resistors and padders (adjustable capacitors) to compensate for variation in self-capacitances. Variations in the time delay from one stage to the next are thus reduced to less than + 3%. Isolation filters are used for each stage of the network in order to reduce feedback and pre-ignition. Also, extreme care has been



SINGLE STAGE OF A TWELVE STAGE DELAY NETWORK

Resistances in OHMS  
 Capacitances in pF unless indicated  
 Delay given by approximately  $0.7R_1C_1$

2537

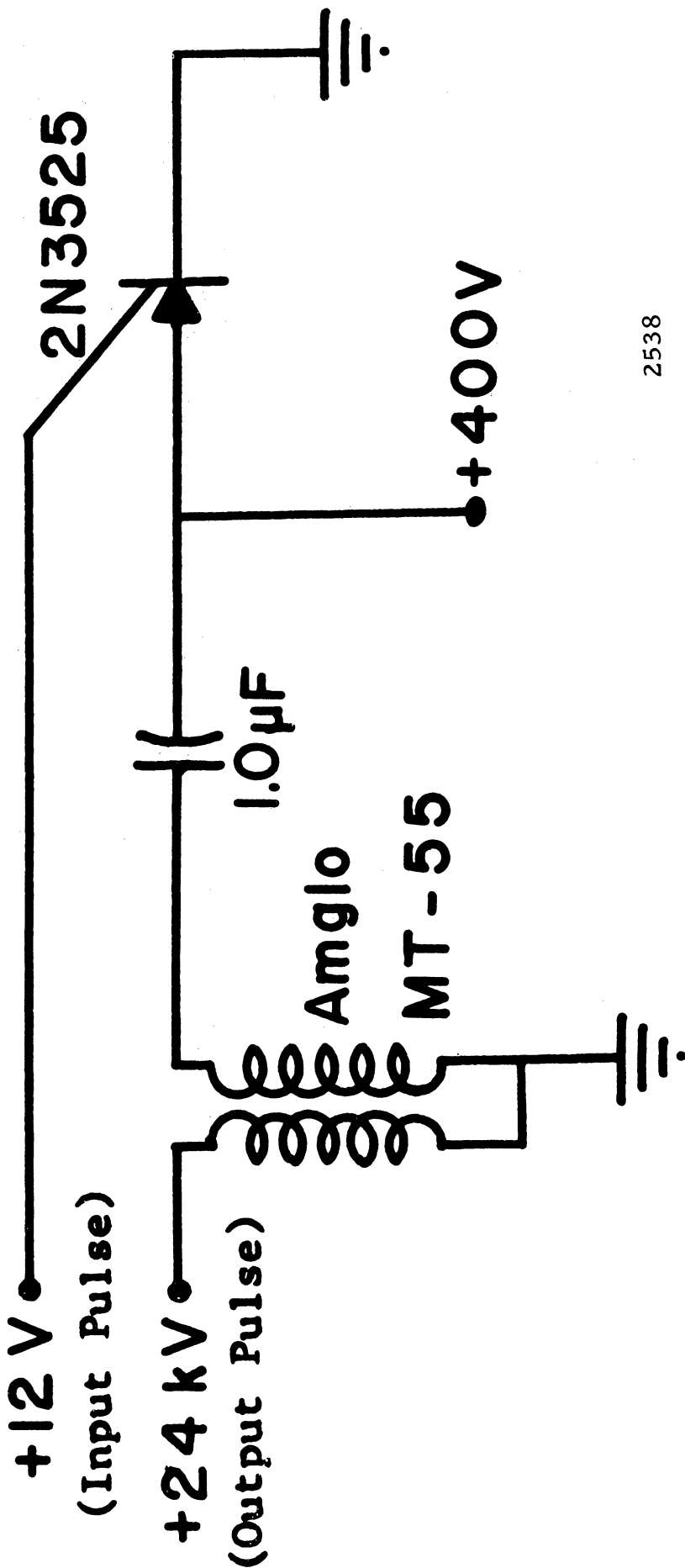
Figure 3.7 Schematic Diagram of Delay Network

exercised in grounding all components and shielding all pulse-carrying wires so that feedback is reduced.

When an inverted positive pulse fires a silicon-controlled rectifier (SCR), a 1.0  $\mu\text{F}$  capacitor discharges across the primary of a trigger transformer producing the trigger pulse (Fig. 3.8). All of the trigger components (including the SCR, 1.0  $\mu\text{F}$  capacitor, and trigger transformer) are mounted in the same iron box as the spark sources (Fig. 3.9). In this way high-voltage wiring and electromagnetic radiation are minimized. Since the network uses high-speed transistors, the major source of time "jitter" for the light sources (which totals 0.25  $\mu\text{s}$ ) is due to the variable breakdown time of the spark gaps.

The light from each spark source is focused onto a separate camera lens by a field lens. When the 12 camera lenses are mounted on the same 5.5 cm radius as are the light sources, the correct field lens imaging is obtained by making the distances between the light sources and the field lens, and between the field lens and the camera lens, equal to twice the focal length of the field lens. For working section diameters up to 15 cm, low cost acromatic field lenses of various focal lengths are easily available. A long focal length field lens provides nearly parallel light through the working section, thus allowing the possible use of shadowgraph or Schlieren methods to measure density gradients in the working section.

The camera for this photographic system is a converted 20.3 cm x 25.4 cm (8 in. x 10 in.) portrait camera. The lens plate of the camera holds 12 acromatic lenses. These lenses, as mentioned earlier, are mounted on a 5.5 cm radius and have an image of the light sources focused on them. In turn, these lenses focus the working section on the film plane. Thus, all the light from each of the spark sources that passes through the field lens,



2538

Figure 3.8 Schematic Diagram of Trigger Circuit



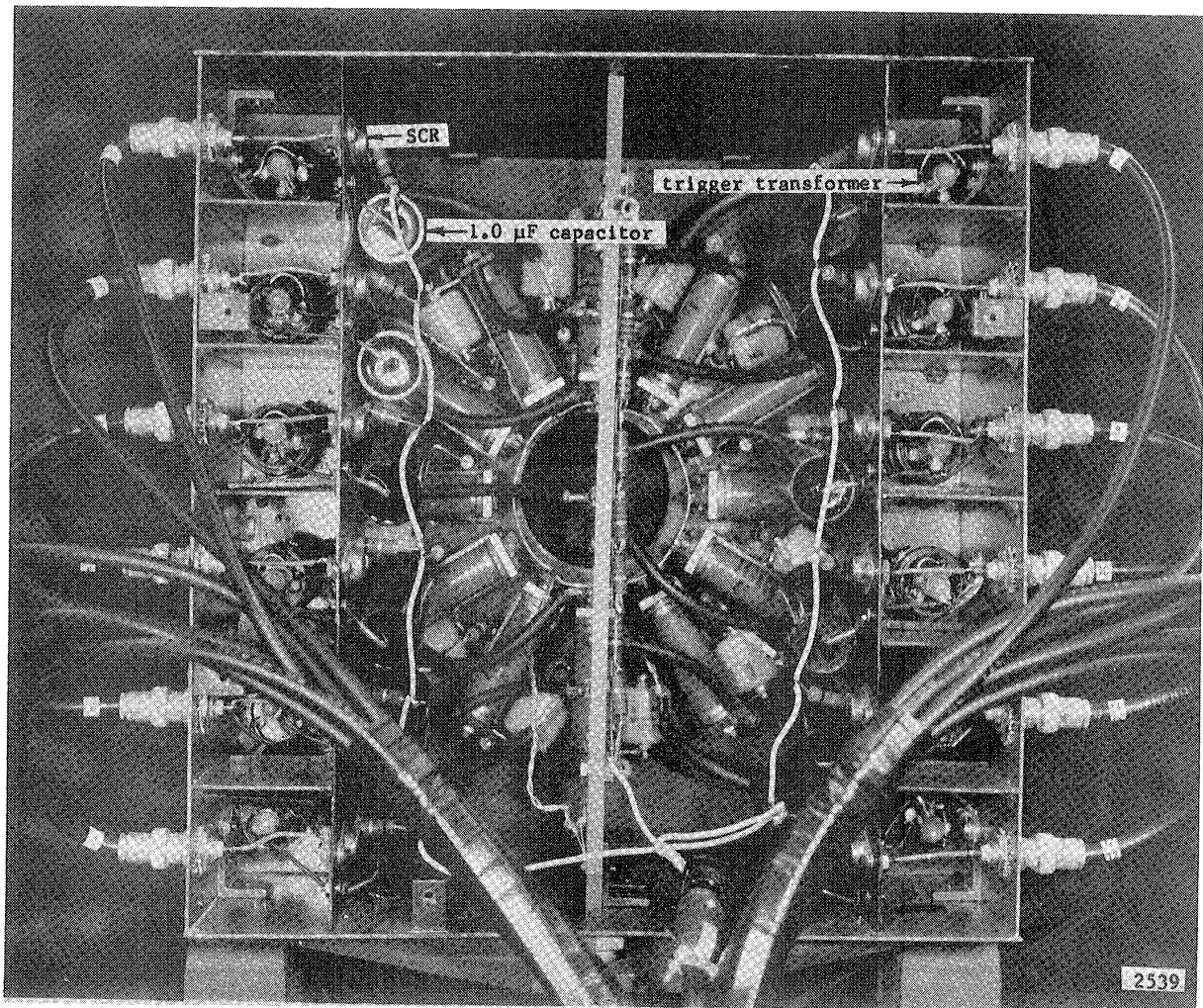


Figure 3.9 Rear View of Iron Box with Back Panel Removed Showing Position of Light Sources and Trigger Circuits



is used to produce an image of the working section of the film. The resulting circle of 12 images, each up to 3 cm in diameter, are on a radius slightly greater than the radius of the camera lens.

All of the components are mounted on a rigid platform. This "optical bench" is designed to be rigid enough to reduce relative movement of the photographic components to less than 0.01 cm so that effective Schlieren work is possible. The optical bench for this system is fabricated of heavy-duty Unistrut components well cross-braced to insure rigidity.

Once the photographic system had been constructed it proved easy to align and operate. First, all optical components were mounted in their approximate positions on the optical bench. Then, using a low power continuous light source placed behind the spark sources, focusing of the spark sources on the camera lens and of the working section on the film plane was done by direct visual means. Once the system had been aligned only periodic checks were required to insure that proper focusing was maintained.

Unless a fast capping shutter is used over the camera lens, operation of the system must take place in subdued light to avoid film exposure by extraneous light. The operating procedure is as follows:

1. The film is loaded into the camera.
2. The desired delay sequence is set on the delay network.
3. The high-voltage supply is activated (3 sec. delay required for spark capacitors to charge to 10 kilovolts).
4. The capping shutter is opened.
5. The delay network is triggered either manually or by electronic coupling to the event being photographed.

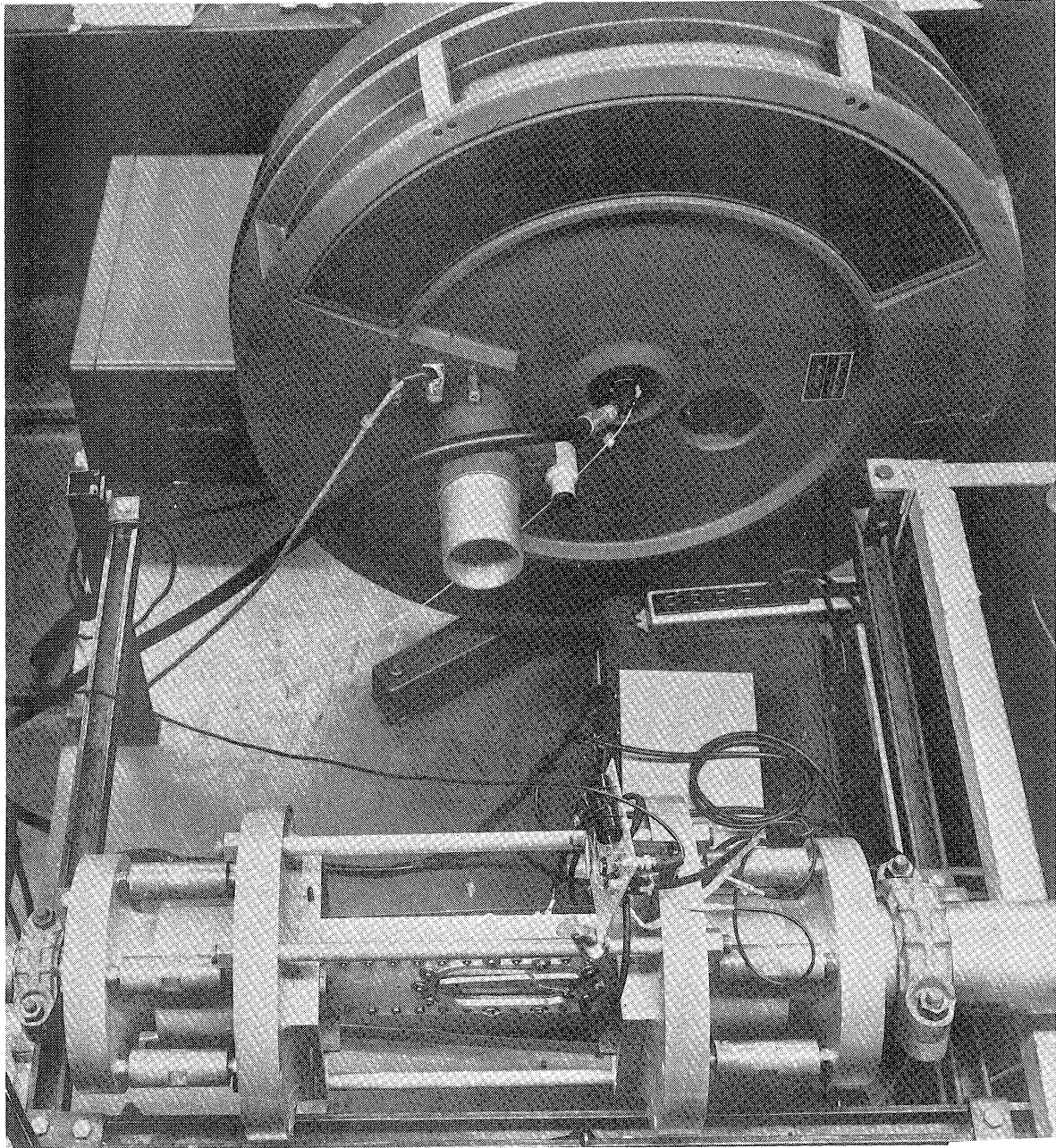
6. The capping shutter is closed.
7. The high voltage is turned off and the exposed film sheet removed.
8. The film sheet is developed and analyzed in the darkroom facilities of the Cavitation and Multiphase Flow Laboratory.

This photographic system was used for investigation of the gas-gun momentum exchange device. With the gas-gun momentum exchange device, the delay network was coupled electronically to the gun by the use of a simple aluminum foil trigger which made contact as the lead pellet struck the impact disc at the rear of the water chamber.

The Cranz-Schardin system may be used on any non-luminous object which may be photographed using focused back-lighting. The system has a constant very short duration exposure time per frame and produces negative images with a very high degree of spatial resolution. The major problems inherent in the system are the variable perspective of each frame for which account must be taken if quantitative spatial data is to be obtained, and the low number of frames per sequence (12 in this case). Because this system has continuous access and variable times between frames are possible, the second problem may be partially overcome by triggering the system during the critical stage of the event being photographed and spacing the frames to best advantage. Another major advantage of the system is its low material cost which, for the unit described, was approximately \$1,000.

#### D. Beckman and Whitley Model 330 Camera

The Beckman and Whitley 330 (Fig. 3.10) is an ultra-high speed continuous access simultaneous streak and framing camera. Using a gas driven turbine with a maximum speed of 8,333 rps the camera takes up to 80 pictures per photographic sequence at a



2575

Figure 3.10 Experimental Arrangement of Model 330 Camera,  
and Aluminum Venturi

rate ranging from  $10^4$  to  $2 \times 10^6$  frames/second. The 16 mm x 25 mm frames are placed in two groups of 40 frames each on 35 mm film which is held stationary in a film track. The streak portion of the camera removes an 0.1 mm slit from the image, and sweeps this slit around a separate film track at a maximum rate of 10.6 mm/ $\mu$ s.

The light beam which enters through the objective lens is immediately reflected at an angle to match the mechanical offset of the film tracks. The streak slit is removed from the light beam and relayed directly to the streak film track with an internal magnification of two. The remaining beam is relayed to a beam splitter which produces two separate beams that are relayed to the rotating mirror in paths that are  $180^\circ$  apart. From the rotating mirror the light beams are reflected to two banks of spherical mirrors, 40 per bank, that focus the light beams on the film track, producing one image for each spherical mirror. The three-sided rotating mirror and banks of spherical mirrors are designed so that as the rotating mirror sweeps one light beam past the last mirror of one bank, another side of the rotating mirror starts sweeping the other light beam past the first mirror of the other bank. As with other high-speed cameras the mechanical capping shutter of this camera remains open for a period of time which is long compared to the writing time of the camera; therefore the effective shuttering is controlled by the duration of the high intensity light pulse used to photograph the event under investigation. Several different light sources were used to utilize the full capacity of this camera. The Kemlite Xenon-Arc light (described in the Dynafax section) was used with this camera for writing times with a duration greater than 300  $\mu$ s. The light source supplied with the camera, a Beckman and Whitley model 1005, is a Xenon Arc

light source utilizing a delay line to produce a square wave pulse of a maximum 40  $\mu$ s duration; therefore, this light source could only be used for the maximum framing rate of the camera. To use the camera at framing rates with writing times between 40 microseconds and 300 microseconds, a Cordin Model 450 light source with a duration varying from 40  $\mu$ s to 400  $\mu$ s was employed. This light source also uses a Xenon arc flash lamp and a capacitor discharge circuit to produce a light pulse that is continuously variable.

A separate camera control operated the capping shutter, produced a firing pulse when the shutter was open, regulated the air flow to the turbine, and monitored the turbine speed. The firing pulse went to a delay network which triggered the Xenon-Arc light source with proper relationship to the event being photographed. A 100 ft. standard spool is used as a film reservoir for the framing portion of the camera and a special cassette is used to remove the film from the camera. For the streak portion, a special cassette is used, which both loads and unloads the film from the camera. Once the exposed film was removed, it was developed and analyzed in the darkroom facilities of the Cavitation and Multiphase Flow Laboratory. Films from the framing portion of the camera were analyzed frame by frame using a film strip projector, and then rephotographed onto 16 mm film for motion picture analysis. The camera utilizes a reflex viewer which, when used properly with the capping shutter, does not expose the film during the focusing process.

Attempts were made to study natural cavitation using the aluminum two-dimensional venturi. Flow conditions were set in the venturi so that a low density cavitation cloud always existed in the throat and diffuser section, and the bubble detector was

set to detect bubbles leaving the throat close to the wedge. The Xenon Arc light source was then triggered by the delay network after the turbine speed had been stabilized and the capping shutter opened. The two-dimensional aluminum venturi was also used for investigation of spark-induced bubbles. For this case, the firing pulse triggers the spark bubble generator circuit and the delay network, which in turn triggers the Xenon arc light source during the proper phase of the spark bubble growth or collapse.

#### E. Other Photographic Equipment

A Bausch and Lomb metallographic camera with a polaroid film attachment was used for detailed studies of the damage pits produced by various incipient cavitation, spark-induced bubbles, and high-speed water jets. Photomicrographs with a magnification up to 1000 x were used to study the damage pits formed on soft aluminum and plexiglas. Some photographic studies of the overall damage produced on a specimen by the collapse of many cavitation bubbles in which the magnification was approximately 10X were made using a 10.2 cm x 12.7 cm (4 in. x 5 in.) press camera. This press camera with a polaroid adaptor was also used in conjunction with a General Radio Strobo-tack to produce single short-duration (1.2  $\mu$ s exposure) photographs of the throat and diffuser section of the two-dimensional venturis in order to determine the flow conditions which would provide the correct cavitation bubble density for high speed photographic investigations.

## CHAPTER IV

### RESEARCH INVESTIGATIONS AND PROCEDURES

#### A. Bubble Generation Using the Underwater Spark

The underwater spark is a process by which electrical energy is converted into a small volume plasma which may have a temperature up to 20,000<sup>(34)</sup>°K and a pressure up to 10<sup>4</sup> atmospheres. This plasma may be studied for a short time or it may be used as a photographic light source, a sound source, or a pressure pulse source. When the trigger pulse breaks down the hold-off gap of the spark generation network shown in Fig. 2.11, the voltage imposed across the underwater spark gap quickly rises toward the charging voltage. This underwater spark gap then breaks down in less than one microsecond due either to the local heating of the electrolyte forming gas followed by gaseous breakdown, or to the breakdown of existing microbubbles. As the spark grows between the electrodes, energy is absorbed in the plasma at a rate depending upon the power input and the inertia of the water. Eventually due to a decrease in the voltage and an increase in the ionization, temperature, and pressure of the plasma; the spark is extinguished. The energy is initially stored in the plasma in the form of dissociation, excitation, ionization, and kinetic energy of the constituent particles. While the heated spark plasma tends to expand, the mechanical inertia of the water confines this expansion. Mechanical work, light radiation, thermal radiation, and thermal conduction from the surface dissipate the energy from the plasma at a rate generally much slower than the rate of energy input from the spark. Since water is compressible, the high pressure of the hot gas changes the density of the water near the interface of the plasma and the

water. This high pressure also results in a pressure wave which radiates outward in the form of a shock wave. The energy radiated in this shock wave (between 20% to 50% of the initial energy) depends mainly on the relative size of the spark plasma bubble compared to the final size of the bubble produced and to a lesser degree upon the rate of energy input to the spark.<sup>(35)</sup> The propagation velocity of the shock wave quickly approaches the sonic velocity of water (under normal conditions approximately 1500 meters per second) while viscous and geometric attenuation of the shock wave allow it to be treated as an acoustic wave after traveling only a short distance from the spark. After emission of the shock wave, the pressure in the gas sphere is greatly reduced. Even though this pressure is still well above hydrostatic, the following growth of the bubble may be considered to occur in an incompressible fluid. Radial flow around the bubble is due to the difference between internal and hydrostatic pressures and to the after-flow due to the emission of the shock wave. Due to inertia, outward motion of the fluid continues after the internal pressure drops below the hydrostatic pressure until this pressure defect stops the outward bubble wall motion. Then bubble collapse starts, again forced by the differential between hydrostatic pressure and gaseous pressure within the bubble, until the internal gas is compressed sufficiently to halt the inward flow. Velocities and pressures during this inward flow may become high enough so that water compressibility must again be considered. Secondary pressure pulses or shock waves may also be produced. The spark bubble may rebound and collapse several times before dissipation effects cause its final disappearance.

Total energy dissipated in the spark,  $E_s$ , is determined using the relation:

$$E_s = \int_0^{\infty} VI dt$$



where  $V$  = voltage across spark (volts)

$I$  = current through spark (amps) 4.1

$V$  and  $I$  are measured simultaneously using resistors  $R_2$ ,  $R_3$ , and  $R_4$  of the spark generator circuit. The resistor  $R_2$ , an inductionless shunt resistor with a value of 0.033 ohms, is used to determine the current,  $I = \frac{V_2}{R_2}$ .  $R_3$  and  $R_4$  form a one hundred to one voltage divider circuit to measure the voltage,  $V$ . For a typical damping resistor (100 ohms) and charging voltage (10kV) self-inductance may be neglected and the discharge circuit is a simple RC circuit; therefore, the displayed voltages across resistors  $R_2$  and  $R_3$  may be approximated by an exponential. Using this approximation (4.1) becomes:

$$E_s = \frac{100 V_{o2} V_{o4}}{2wR_2} \quad 4.2$$

where  $I = \frac{V_2}{R_2} = \frac{V_{o2}}{R_2} e^{-wt}$

$w$  = exponential decay constant

Results of the measurements taken show (Table 4.1) that depending upon the damping resistor and to a smaller degree on the relative sizes of the hold-off gap versus the water gap, only 0.5% to 12% the total energy stored in the capacitor is actually dissipated in the water to produce the spark bubble. For these measurements which were correlated with photographs of spark bubbles, the maximum potential energy of the bubble,  $E_p$ , is given by:

$$E_p = \frac{4}{3} \pi R_m^3 \Delta P$$

$R_m$  = maximum bubble radius 4.3

$\Delta P$  = difference between partial gas pressure and hydrostatic pressure

TABLE 4.1  
Energy and Pressure Calculations for the  
Under-water Spark Bubble Generator

Bubble	1	2	3	4	5	6	7	8
Air Gap (mm)	3.0	3.0	3.0	3.0	3.0	2.8	2.8	2.8
Under water Gap (mm)	1.0	1.0	0.5	0.5	0.5	1.3	1.0	0.7
Damping resistor (ohms)	0	0	0	22	510	0	22	22
Capacitor energy (J) (.5CV <sup>2</sup> )	0.415	0.500	0.500	0.245	0.500	1.500	0.186	0.245
Energy deposited in water (J)	0.0327	0.0295	0.0210	0.0081	0.0031	0.1785	0.0125	0.0134
Percentage	7.87	5.90	4.28	3.32	0.611	11.9	6.73	5.47
Bubble potential energy (J)	0.0113	0.0136	0.0089	0.0034	0.0013	0.0899	0.0057	0.0058
Percentage	2.48	2.72	1.78	1.37	0.268	5.99	3.08	2.39
Ambient pressure (atm)	3.27	1.18	1.18	1.08	1.16	0.303	0.815	1.67
Partial pressure at (atm) $R = R_{\max}$ (Eq. 4.4) due to permanent gas	0.0623	0.0222	0.0179	0.0169	0.0171	0.0086	0.0157	0.0228
Partial pressure (atm) at $R = R_{\max}$ (Eq. 4.22)	0.124	0.0453	0.0486	0.0328	0.0218	0.0104	0.0325	0.0621

$E_p$  varies between 0.50 and 0.30 of the energy dissipated in the water (Table 4.1). Therefore 0.50 to 0.70 of the energy is dissipated by thermal radiation and conduction, by the production of a pressure or shock wave, and by the formation of permanent gas.

A rough estimate of the maximum amount of permanent gas formed during the spark discharge can be made from the following assumptions:

1. Permanent gas is formed by the dissociation of water into hydrogen and oxygen gas with no recombination into water.

2. About 0.50 of the spark energy dissipated in the water goes into gas formation. <sup>(35)</sup>

3. The final temperature of the gas is in equilibrium with the water conditions around the electrodes. With these assumptions, the partial pressure of the permanent gas,  $Q$  (atm), is given by:

$$Q = 0.1025 \frac{E_{in} T_g}{R^3}$$

4.4

where  $E_{in}$  = energy dissipated in gas formation

$R$  = bubble maximum radius (mm).

$T_g$  = ambient fluid temperature

$P_\infty$  = ambient fluid pressure

For typical bubbles the partial pressure of the permanent gas is approximately half of the total partial pressure (eq. 4.22) at maximum volume (Table 4.1). This partial pressure of permanent gas, which is the same order of magnitude as the water vapor pressure (0.025 atm), is about  $10^3$  times the partial pressure expected from the naturally occurring gas nuclei present in the water tunnel facility. <sup>(36)</sup> This

estimate of the permanent gas is quite high due to the assumptions made (i. e. , a large percentage of the hydrogen and oxygen gas may recombine though no recombination was assumed). However, the possibility of a substantial amount of permanent gas formation is shown, and a large amount of water vapor is also formed which conceivably may not recondense rapidly enough during bubble collapse to prevent retardation of this collapse. If so, the damage potential of the bubble could be greatly reduced compared to a "natural" cavitation bubble. Therefore the damage potential of the spark generated bubble could be much less than that of a natural cavitation bubble which collapses in the same hydrostatic pressure and contains little or no permanent gas.

#### B. Equations Governing Bubble Collapse

One of the first solutions for the collapse of a cavitation bubble was presented by Lord Rayleigh in 1917<sup>(3)</sup>. He assumed the spherically symmetric collapse of an empty bubble initially at rest in an infinite, inviscid fluid. The resulting equation for the bubble wall motion,

$$\dot{R}^2 = \frac{2}{3} \frac{\Delta P}{\rho} \left( \frac{R_m^3}{R^3} - 1 \right) \quad 4.5$$

where  $R$  = bubble wall radius

$R_m$  = initial wall radius

$\dot{R}$  = bubble wall velocity

$\rho$  = fluid density

$\Delta P$  = difference between pressure at  $\infty$  and pressure inside bubble,

shows that as the bubble radius approaches zero, the wall velocity approaches infinity. A solution of this equation to give the pressure in the fluid can be obtained.

$$P(r) - P_{\infty}(r) = \Delta P \left\{ \frac{R_m^3}{R^2 r} - \frac{R_m^3 R}{r^4} - \frac{4}{3} \frac{R}{r} + \frac{1}{3} \frac{R^4}{r^4} \right\} \quad 4.6$$

$R, R_m$  = bubble wall radius  
 $r$  = radial coordinate to fluid position where pressure occurs.

This relation shows that as the radius of the bubble approaches zero the pressure approaches infinity in the vicinity of the bubble wall. Therefore, there is a large potential for damage if this high pressure were applied to a surface.

Further theoretical investigations of spherically symmetric bubble collapse which include compressibility, viscosity, surface tension, internal vapor or gas show that at a distance from the center of the bubble equal to the radius of the bubble, the pressure during collapse is not sufficient to cause the observed damage, while the pressure from the rebound is marginally adequate<sup>(8,9)</sup>. Therefore, unless significant migration of the bubble toward the surface occurs during the collapse the pressure due to spherically symmetric collapse and rebound is probably not sufficient to cause the damage observed to very strong materials.

It is obvious that a bubble must collapse in the vicinity of a surface in order to produce damage on that surface. Also it should be recognized that a bubble collapsing near a solid surface will have a strongly asymmetric condition imposed upon it by the presence of the surface. This is certain to strongly affect the spherical nature of the collapse as has been shown theoretically.<sup>(28,30)</sup> A detailed analysis of the change in the collapse mode of the bubble in the presence of the surface is beyond the scope of this work. However, a more simplified derivation will be presented in order to show the first order effect of the adjacent surface on the migration and collapse of the bubble.

This derivation incorporating the method of images follows the development of Cole<sup>(5)</sup> and Korovkin<sup>(15)</sup>. The motion of the bubble collapse is assumed to be spherically symmetric taking

place in an irrotational, incompressible, inviscid fluid. The radial collapse motion is represented by a simple radial source, and the translational motion of the bubble centroid by a superimposed dipole source. By reflecting an image of the bubble source across the rigid surface (Figure 4.1) the flow at the boundary is parallel to the rigid surface, satisfying the wall boundary conditions. The boundary condition of no flow across the surface of the bubble must also be met. For a bubble far from the surface where the flow due to the image source is nearly equal at all points over the bubble surface, this condition may be met by a simple translation of the bubble centroid which is provided by the superposition of a dipole source and an identical reflected image. For a bubble close to a rigid surface, additional sources and sinks are placed inside the bubble to provide a higher order correction for fluid flow across the surface of the bubble. Because of the approximate nature of this solution only the first order effect will be considered.

The general equations to be satisfied are:

$$\frac{d}{dt} \frac{\partial T}{\partial \dot{R}} - \frac{\partial T}{\partial R} = F_R \quad 4.7$$

$$\frac{d}{dt} \frac{\partial T}{\partial \dot{b}} - \frac{\partial T}{\partial b} = 0 \quad 4.8$$

where

- $R$  = radial position of bubble wall
- $\dot{R}$  = radial velocity of bubble wall
- $b$  = distance between bubble centroid and rigid surface
- $\dot{b}$  = bubble centroid velocity toward rigid surface
- $T$  = kinetic energy
- $F_R$  =  $4 \pi R^2 \left[ -\Delta P + Q \left( \frac{R_m}{R} \right)^3 \right]$  = force acting along the R coordinate

where

- $\Delta P$  = difference between pressure at  $\infty$  and the vapor pressure in bubble
- $Q$  = partial pressure of non-condensable gas for bubble at maximum radius

Surface tension and viscosity also may be included in the force term; however, for this investigation the absolute values of  $R$  are large enough, and the values of the bubble wall velocity  $\dot{R}$  are small enough so that the surface tension and viscosity effects are always negligible. Compression of the non condensable gas is assumed to be adiabatic ( $\gamma=4/3$ ). Applying Green's theorem to the potential flow field, the kinetic energy,  $T$ , may be determined by the surface integral

$$T = - \frac{\rho}{2} \iint \phi \frac{\partial \phi}{\partial n} dS \quad 4.11$$

where the velocity potential,  $\phi$ , is given by

$$\begin{aligned} \phi = & \frac{R^2 \dot{R}}{r} + \frac{R^2 \dot{R}}{(r^2 + 2b^2 - 4br \cos \theta)^{1/2}} \\ & + \frac{\dot{b}R \cos \theta}{2r^2} + \frac{\dot{b}R^3 \left(1 - \frac{\sin^2 \theta r^2}{r^2 + 4b^2 - 4br \cos \theta}\right)^{1/2}}{2(r^2 + 4b^2 - 4br \cos \theta)^{1/2}} \end{aligned} \quad 4.10$$

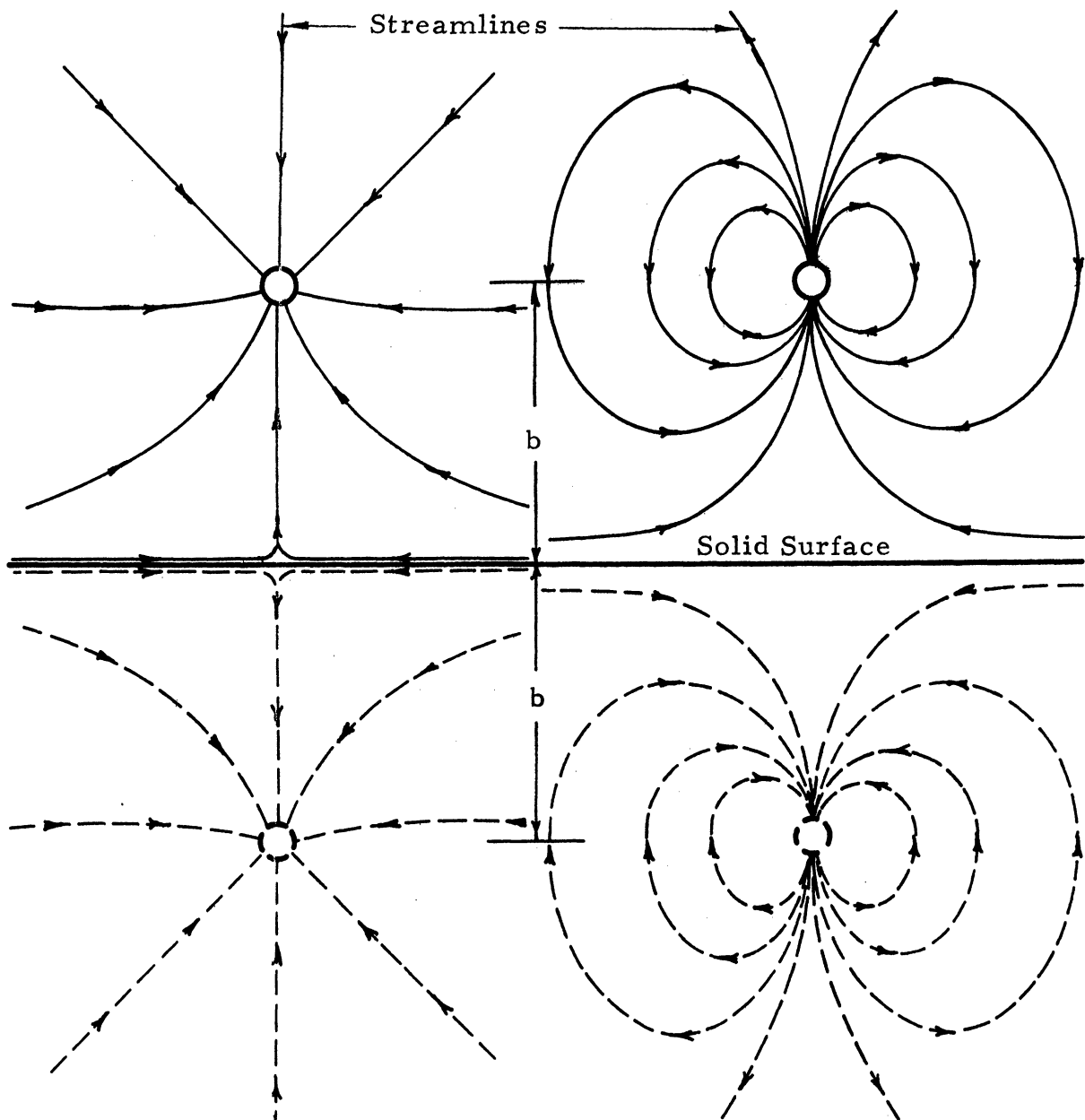
The first two terms of equation 4.10 are the source and corresponding image for the radial collapse of the bubble while the last two terms are the dipole source and corresponding image which account for the translation of a centroid of the bubble. Placing equation 4.10 and its differential into equation 4.9 and then integrating, we obtain for the kinetic energy,  $T$ ,

$$T = 2\pi \rho R^3 \left[1 + \frac{R}{2b}\right] \dot{R}^2 + \frac{\pi}{3} \rho R^3 \left[1 + \frac{3R^3}{8b^3}\right] \dot{b}^2 \quad 4.11$$

Substituting this equation for kinetic energy into the basic equations (eq. 4.7 and 4.8) results in a set of differential equations:

$$\ddot{R} = \frac{1}{Rb(R+2b)} \left\{ \left[ \frac{2Q}{R} \left(\frac{R_m}{R}\right)^4 - \frac{2\Delta P}{\rho} - 3\dot{R}^2 + \frac{1}{2} \dot{b}^2 \right] b^2 - 2bR\dot{R}^2 + R^2 \dot{b}\dot{R} \right\} \quad 4.12$$

$$\ddot{b} = \frac{9}{16} \frac{R^3 \dot{b}^2}{b^4} - \frac{3R\dot{b}}{R} - \frac{3}{2} \frac{R\dot{R}^2}{b^2} \quad 4.13$$



a) Radial sink and reflected image

b) Dipole sink and Reflected image

2982

Figure 4.1 Representative Flow Patterns for Sinks Used in "Method of Images"



for the translation and radial velocity of the bubble. Finally these equations are normalized using the following normalization parameters

$$R' = \frac{R}{R_m} \quad 4.14$$

$$b' = \frac{b}{R_m} \quad 4.15$$

$$t'_n = a R_m \left( \frac{\rho}{\Delta P} \right)^{1/2} \quad 4.16$$

$a$  = time magnification factor

resulting in (omitting the primes)

$$\ddot{R} = \frac{1}{Rb(R+2b)} \left\{ \left[ \frac{2Qa^2}{\Delta P} \left( \frac{1}{R} \right)^4 - 2a^2 - 3\dot{R}^2 + \frac{1}{2} b^2 \right] b^2 - 2bR\dot{R}^2 + R^2 \ddot{b} \right\} \quad 4.17$$

$$\ddot{b} = \frac{9}{16} \frac{R^3 b^2}{b^4} - \frac{3R\dot{b}}{R} - \frac{3}{2} \frac{R\dot{R}^2}{b^2} \quad 4.18$$

A special case of these equations for  $b \rightarrow \infty$  results in a normalized differential equation:

$$\dot{R} = \frac{\frac{Qa^2}{\Delta P} \left( \frac{1}{R} \right)^4 - a^2 - \frac{3}{2} \dot{R}^2}{R} \quad 4.19$$

which may be derived from the classical Rayleigh collapse equation with a provision for internal gas or vapor. These differential equations were programmed on the PACE analog computer of the Nuclear Engineering of the University of Michigan (Appendix B). Results using eq's. 4.17 and 4.18 will be compared with bubbles collapsing in close proximity to a wall, while results using eq. 4.19 will be compared with bubbles collapsing far from a solid wall.

When the hydrostatic pressure,  $\Delta P$ , the maximum radius,  $R_m$ , and the minimum radius,  $R_o$ , are known with accuracy (i. e.,

for the Beckman and Whitley Model 330 sequences) an estimate of the partial gas pressure,  $Q$ , can be made. Equating the maximum potential energy of the bubble (eq. 4.3) to the energy of expanding the bubble from its minimum to its maximum volume

$$E = \frac{4}{3} \pi \Delta P R_m^3 = \int_{R_o}^{R_m} PdV = 4 \pi \int_{R_o}^{R_m} PR^2 dR \quad 4.20$$

and assuming adiabatic expansion

$$P = Q \left( \frac{R_m}{R} \right)^4 \quad 4.21$$

results in

$$Q = \frac{\Delta P}{3 \left( \frac{R_m}{R_o} - 1 \right)} \quad 4.22$$

Using eq. 4.21 again, the maximum pressure,  $P_o$ , in the bubble at minimum volume is:

$$P_o = \frac{\Delta P}{3} \frac{(R_m/R_o)^4}{(R_m/R_o - 1)} \quad 4.23$$

For cases where the minimum volume is not accurately known (i. e., for the Dynafax sequences) a partial gas pressure,  $Q$ , is chosen which best fits the experimental data.

Generalized results are shown in Figs. 4.2, 4.3, and 4.4. Results using eq. 4.16 for various partial pressures of non-condensable gas (Fig. 4.2) show that as the partial pressure is increased the minimum radius and the time to reach minimum radius are increased. Figs. 4.3a and b are plots of normalized radius and wall distance for a fixed wall distance and a variable internal gas content.

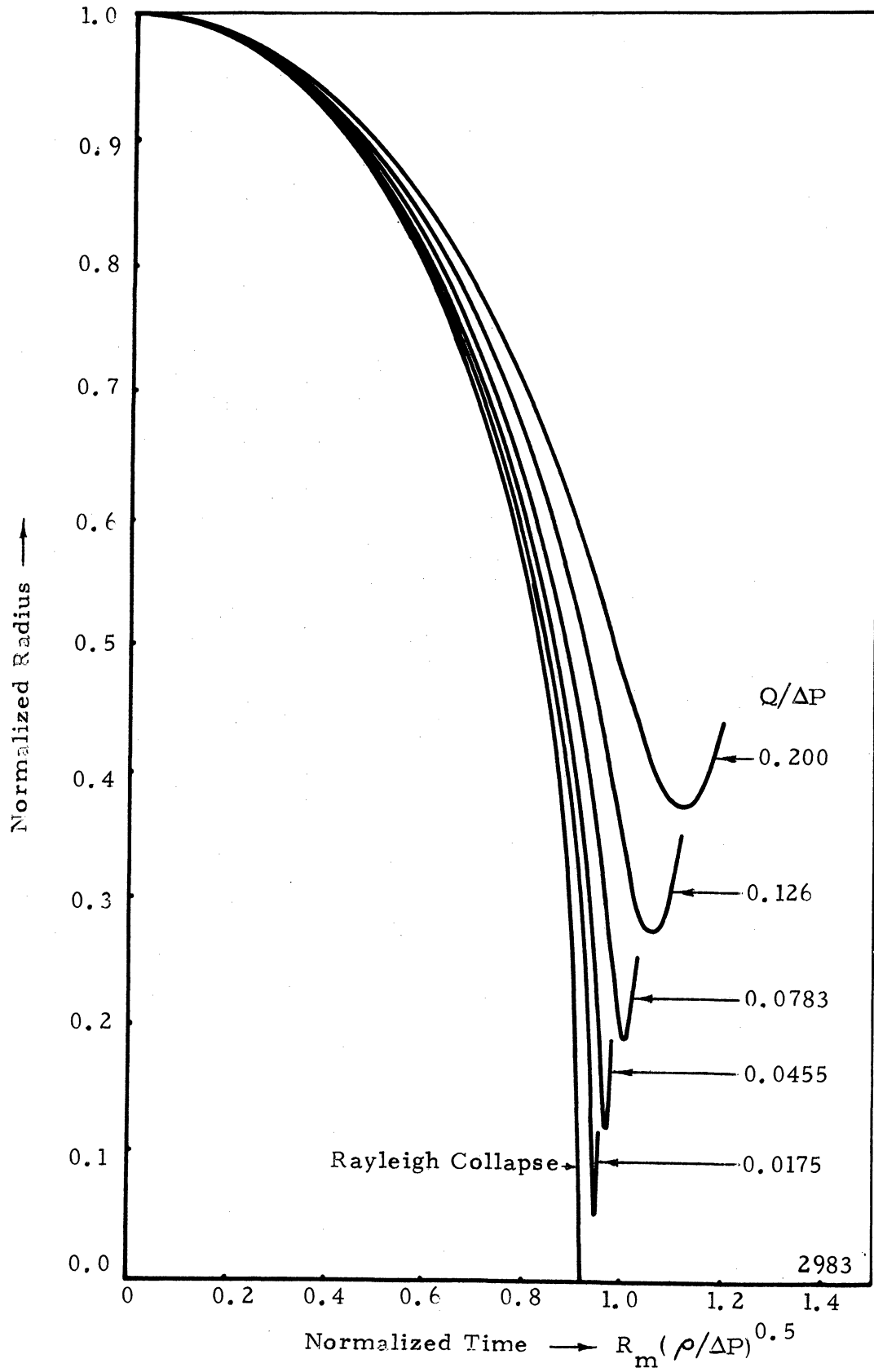


Figure 4.2 Theoretical Solution of Bubble Collapse Far from a Solid Surface with Various Internal Gas Contents

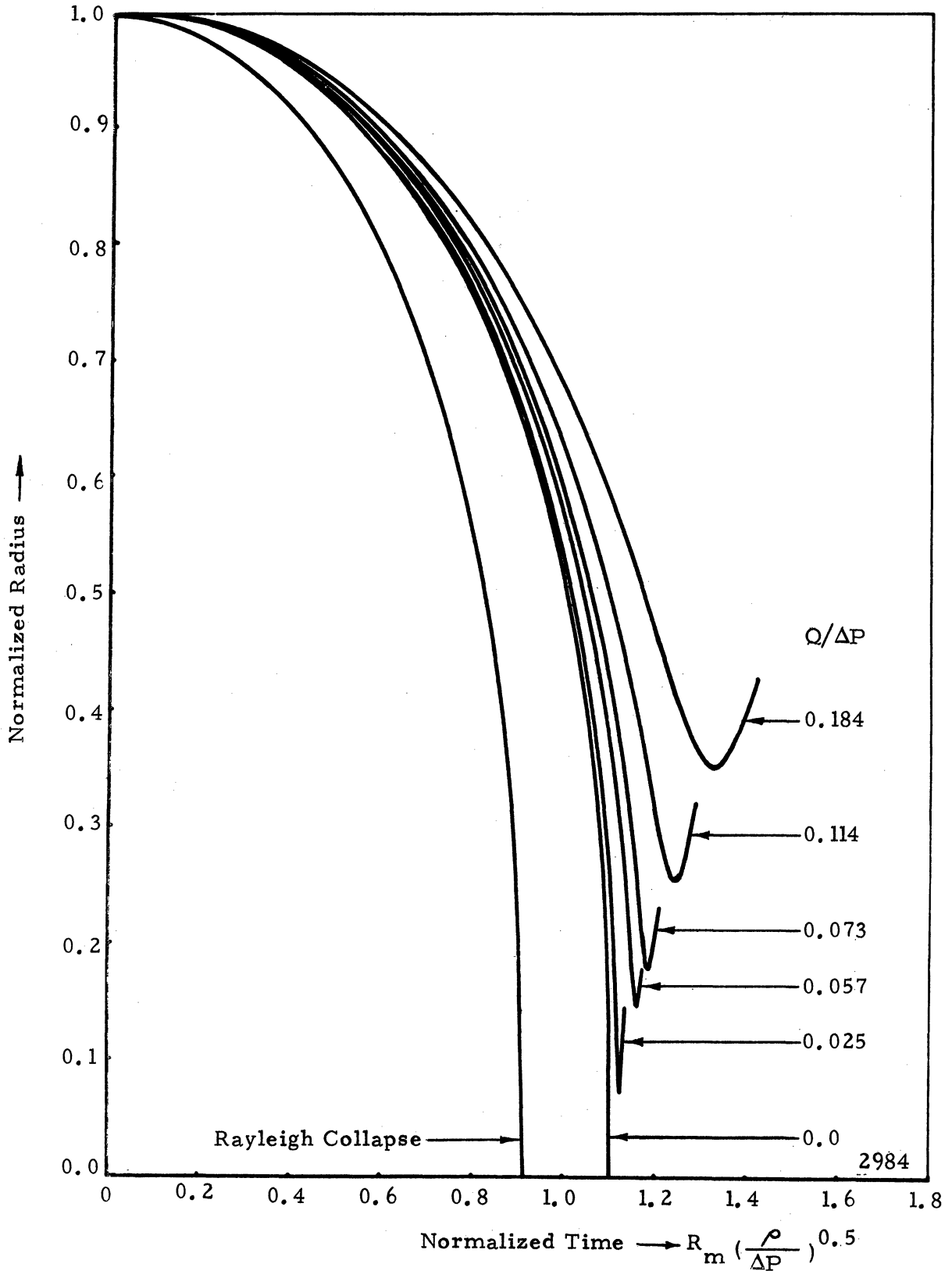


Figure 4.3a Normalized Radius vs. Normalized Time for a Fixed Initial Wall Distance ( $b_0 = 1.3$ ) and a Variable Internal Gas Content<sup>o</sup>

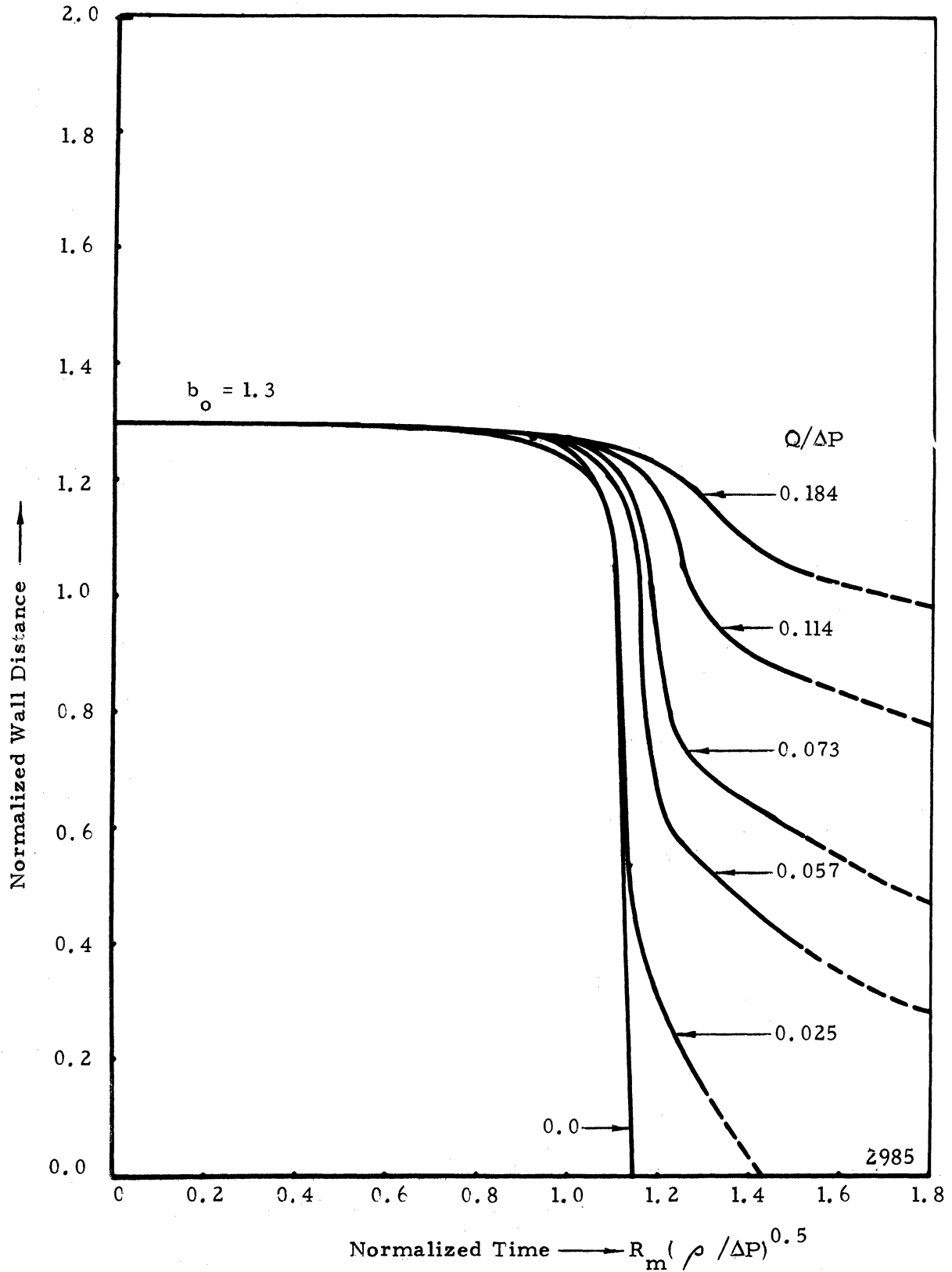


Figure 4.3b Normalized Wall Distance vs. Normalized Time for a Fixed Initial Wall Distance ( $b_o = 1.3$ ) and a Variable Internal Gas Content

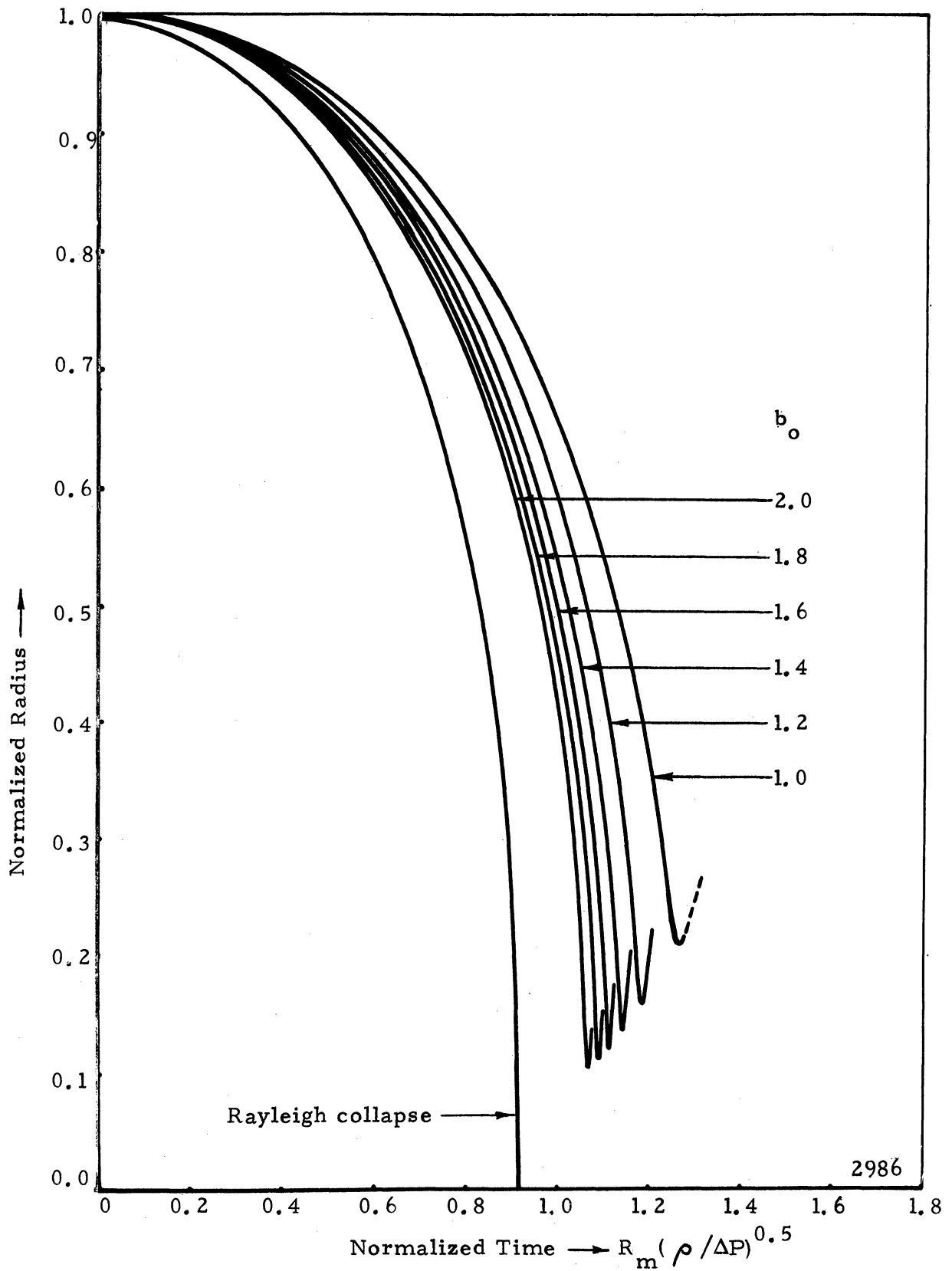


Figure 4.4a Normalized Radius vs. Normalized Time for a Fixed Internal Gas Content ( $Q/\Delta P = 0.040$ ) and a Variable Initial Wall Distance

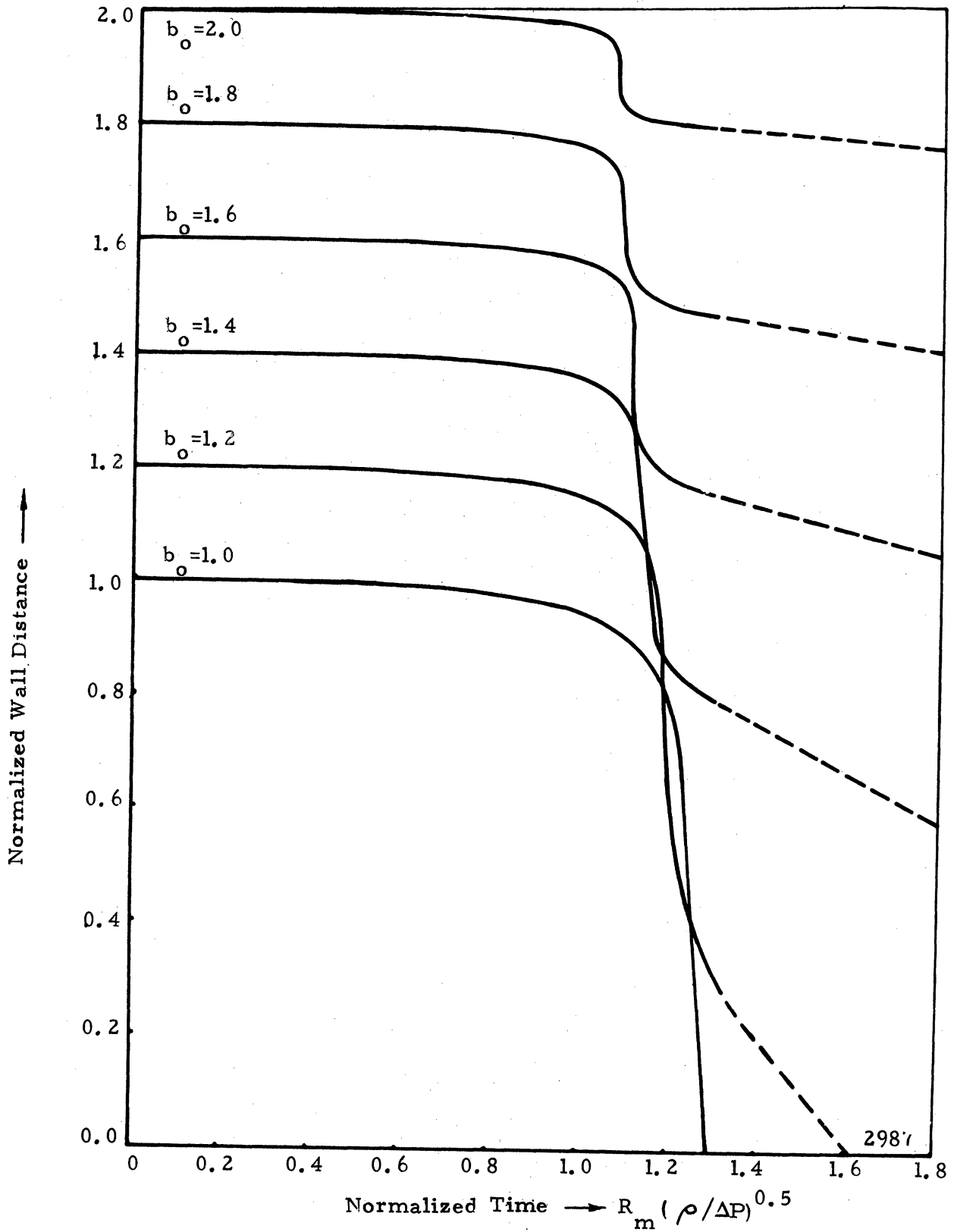


Figure 4.4b Normalized Wall Distance vs. Normalized Time for a Fixed Internal Gas Content ( $Q/\Delta P = 0.040$ ) and a Variable Initial Wall Distance

The results show that as the gas content of the bubble is reduced, the minimum radius decreases, while the migration towards the surface increases. It is interesting to note that most of the migration occurs while the bubble is near its minimum volume. Figs. 4.4a and b are plots of the effect of varying the wall distance for a bubble with constant partial gas pressure,  $Q$ . The plots show that as the initial distance between the bubble and wall are reduced, the migration that occurs upon collapse and rebound is increased and the time to reach minimum volume is increased. For  $b_0 = R_m$  (bubble initially touching wall) there is no rebound of the bubble and the collapse time compared to collapse in an infinite fluid is increased by 42%. Even for this case the migration of the bubble centroid occurs during the final portion of the bubble collapse when the bubble is near minimum volume. If the bubble remains attached to the wall (as is generally the case for the experimentally observed bubbles) the rate of centroid migration would be equal to the rate of bubble collapse (i. e.,  $\dot{b} = \dot{R}$ ). During the initial stages of collapse  $\dot{b} < \dot{R}$  so that the surface of the bubble would detach from the surface. This discrepancy in the theoretical results is due to the neglect of higher order terms in the solution.

### C. Analysis of the Photographic Results

After processing the negatives, the high speed motion pictures were first viewed using a microfilm reader for qualitative analysis. The most interesting films were then projected upon a screen and rephotographed onto 16 mm film. These films were shown using a 16 mm projector for motion analysis.

For those films with a large enough number of frames per bubble lifetime, qualitative data was taken of bubble size, shape, and position. Measurements were made from the original negatives by projecting the images upon a screen. The projected images were

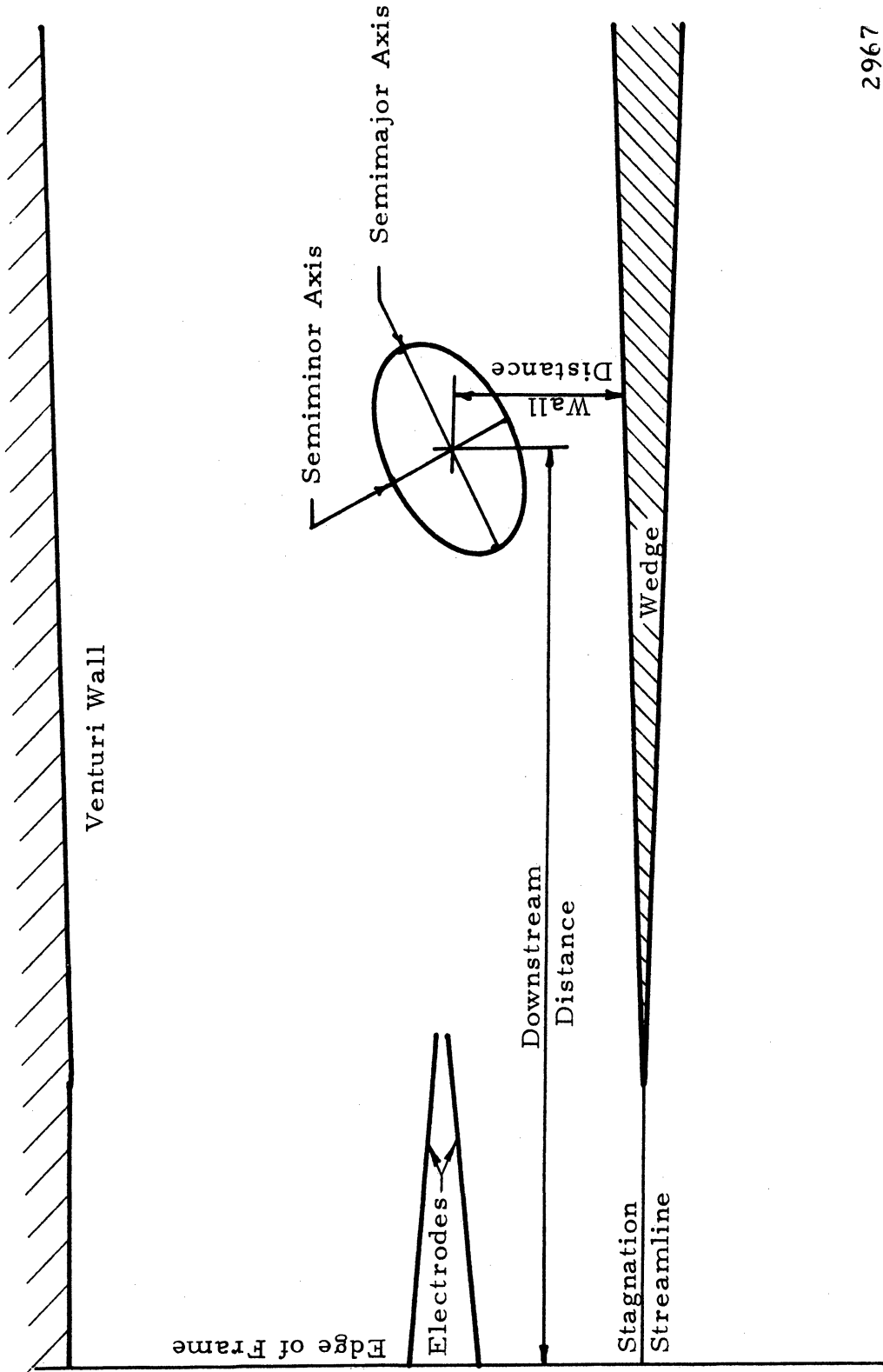


about 12.5 times actual size; however, the limiting factor in the precision of the measurements was the camera-film resolution. For the Beckman and Whitley Model 330 camera this limit was about 0.1 mm or about 2% of the maximum diameter of typical spark-induced cavitation bubbles. For the Dynafax camera a smaller negative resulted in a limit of about 5% of the maximum diameter of typical cavitation bubbles photographed.

The measurements of each frame (Fig. 4.5) were made from a defined datum plane. The bubble is assumed during collapse and rebound to be an ellipsoid. For bubbles collapsing in a pressure gradient the measured two-dimensional ellipse is rotated around the axis parallel to the pressure gradient. For bubble collapse oriented toward a wall the two-dimensional ellipse is rotated around the axis perpendicular to the wall (Fig. 4.6). With this assumption only measurements of the location of the semi-major axis and semi-minor axis of the bubble are required for each frame. The data for each bubble which also includes information on the fluid conditions, camera framing rate, and maximum bubble size, were reduced to more meaningful results using the IBM 360 computer available at the University of Michigan. The computer program (Appendix C) first determined the bubble maximum potential energy,  $E_p$  (using eq. 4.3) a characteristic time,  $T_n$  (using eq. 4.16), and a characteristic velocity,  $\dot{R}_n$ , where

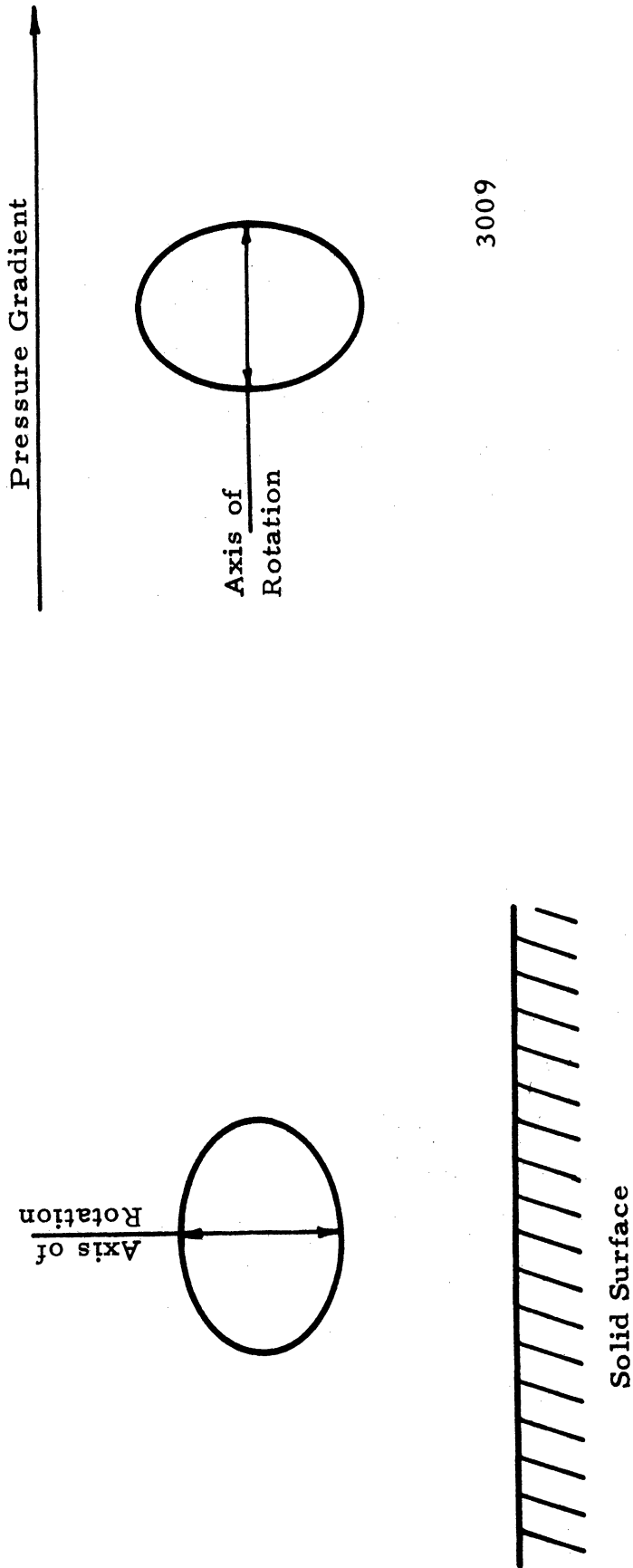
$$\dot{R}_n = R_m / T_n \quad 4.24$$

which, along with the maximum radius,  $R_m$ , were used to normalize the time, mean radius, mean wall velocity, horizontal velocity, vertical wall velocity, and wall distance for each frame. The normalization procedure is used to eliminate variation in maximum bubble size,  $R_m$ , and hydrostatic pressure,  $\Delta P$ , for comparisons



2967

Figure 4.5 Measurements Taken From the Projected Image of a Cavitation Bubble and Typical Datum Lines



3009

Figure 4.6 Diagram of Axis of Rotation for Bubbles with an Assumed Ellipsoid Shape

between bubbles; and to facilitate comparisons with the normalized theoretical results. For analyses of bubbles collapsing in a pressure gradient, the hydrostatic pressure,  $\Delta P$ , used to determine the characteristic time,  $T_n$ , is the measured pressure at the axial position where the bubble just begins to collapse.

In addition, the eccentricity,  $e$

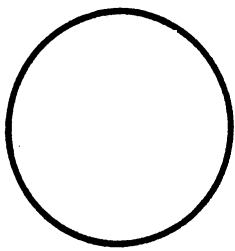
$$e = \frac{(X^2 - Y^2)^{\frac{1}{2}}}{X} \quad 4.25$$

where  $X$  = semi-major axis

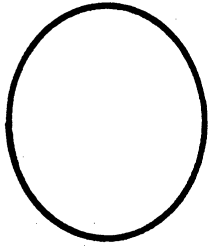
$Y$  = semi-minor axis

(a measure of the bubble deformation as shown in Fig. 4.7), the vertical and horizontal centroid velocity, and the instantaneous and average slip velocity were also computed. Finally, the normalized mean radius, normalized wall distance, maximum wall velocity, and instantaneous slip velocity were plotted on graphs using the CALCOMP plotting facilities of the University of Michigan. About 70 data sets were analyzed and typical printed results are shown in Table 4.2. The results produced on the CALCOMP are compared with the results produced by the analog solution previously discussed.

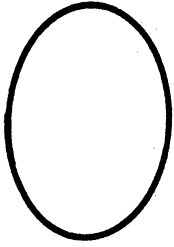
For applicable bubbles additional analyses included the calculation of the size and impingement velocity of jets and bubble walls on the adjacent surface. Detailed plots of bubble deformation and subsequent jet formation for one of the bubbles were produced from high contrast enlargements of the photographic negatives.



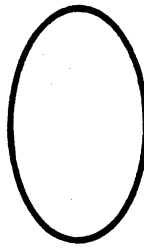
$e = 0.0$   
Spherical



$e = 0.5$



$e = 0.7$



$e = 0.8$



$e = 0.9$



$e = 0.95$

Figure 4.7 Typical Values of Eccentricity,  $e$ , and a Visual Representation of the Associated Bubble Deformation

TABLE 4.2 Typical Results from the Digital Computer Program

BUBBLE	04003		NORMALIZED PROPERTIES												
	MEAN RADIUS	MAX RADIUS	MEAN	PADIAL	VEL	WALL	ECCEN	BURRLE	VEL	INST	SLIP	AVE			
				HOR	VERT	DIST		HOR	(M/S)	(M/S)	(M/S)	(M/S)			
PRESS DIFF	0.439	1.46 MM	-4.720	-5.459	-4.425	1.884	0.466	7.40	0.0	-7.73	-7.73	-7.73			
RURR ENER	0.552	0.1152E 07 DYNES/CM2	-1.905	-2.011	-1.667	1.911	0.340	8.64	-4.93	-6.49	-6.49	-7.11			
FLUID VEL	0.654	0.1502E-02 JOULES	-1.708	-1.839	-1.437	1.952	0.176	19.74	-7.40	4.61	4.61	-3.21			
NORM VEL	0.733	15.13 M/S	-1.318	-1.149	-1.667	1.959	0.324	12.34	-1.23	-2.79	-2.79	-3.10			
NORM TIME	0.785	10.73 M/S	-0.885	-1.092	-0.460	1.979	0.093	25.91	-3.70	10.78	10.78	-0.33			
	0.826	136.03 MICROSEC	-0.689	-0.805	-0.460	1.979	0.202	16.04	0.0	0.91	0.91	-0.12			
	0.897		-0.592	-0.561	-0.460	1.979	0.297	14.19	0.0	-0.94	-0.94	-0.33			
	0.960		-0.527	-0.517	-0.546	1.979	0.276	16.04	0.0	0.91	0.91	-0.08			
	1.002		-0.141	-0.161	-0.103	1.959	0.323	15.54	0.74	0.41	0.41	0.08			
	0.983		0.065	0.069	0.057	1.966	0.316	15.54	-0.25	0.41	0.41	0.17			
	0.912		0.238	0.230	0.253	1.986	0.348	14.80	-0.74	-0.33	-0.33	0.07			
	0.765		0.491	0.483	0.506	1.938	0.308	13.08	1.73	-2.05	-2.05	-0.29			
	0.601		0.919	0.939	0.881	1.870	0.411	17.68	4.11	2.55	2.55	-0.03			
	0.518		1.389	1.667	0.862	1.836	0.162	19.74	6.17	4.61	4.61	0.11			
	0.341		2.982	1.379	5.172	1.671	0.883	18.50	29.61	3.37	3.37	0.20			
	0.203		2.305	3.908	0.115	1.644	0.256	-3.70	4.93	-18.83	-18.83	-0.33			
	0.301		-1.637	-1.839	-1.264	1.596	0.494	-4.93	8.64	-20.06	-20.06	-0.86			
	0.411		-1.847	-2.011	-1.552	1.534	0.539	9.87	11.10	-5.26	-5.26	-0.98			
	0.462		-0.864	-0.517	-1.494	1.466	0.209	22.20	12.34	7.07	7.07	-0.77			
	0.485		-0.382	-0.230	-0.690	1.459	0.260	12.34	1.23	-2.79	-2.79	-0.82			
	0.576		-0.766	-0.776	-0.747	1.356	0.215	14.80	9.25	-0.33	-0.33	-0.80			
	0.584		-0.060	0.086	-0.374	1.301	0.453	16.04	4.93	0.91	0.91	-0.72			
	0.578		0.043	-0.029	0.201	1.295	0.362	14.19	0.62	-0.94	-0.94	-0.73			
	0.516		0.525	0.345	0.891	1.233	0.299	14.80	5.55	-0.33	-0.33	-0.71			
	0.474		0.348	0.172	0.661	1.192	0.548	15.42	3.70	0.29	0.29	-0.67			
	0.417		0.967	1.092	0.747	1.164	0.511	17.27	4.93	2.14	2.14	-0.62			
	0.345		1.205	1.092	1.379	1.096	0.614	22.20	12.34	7.07	7.07	-0.47			
	0.261		1.417	0.977	1.954	1.089	0.825	14.80	1.23	-0.33	-0.33	-0.47			
	0.135		2.112	2.701	1.264	1.027	0.745	8.64	11.10	-6.49	-6.49	-0.58			
	0.241		-1.778	-1.896	-1.552	0.993	0.683	19.74	6.17	4.61	4.61	-0.48			
	0.283		-0.714	-0.575	-0.919	0.959	0.558	8.64	6.17	-6.49	-6.49	-0.59			
	0.283		0.0	0.0	0.0	0.904	0.558	11.10	4.93	-4.03	-4.03	-0.71			
	0.279		0.033	0.0	0.086	0.829	0.606	18.50	6.78	3.37	3.37	-0.57			

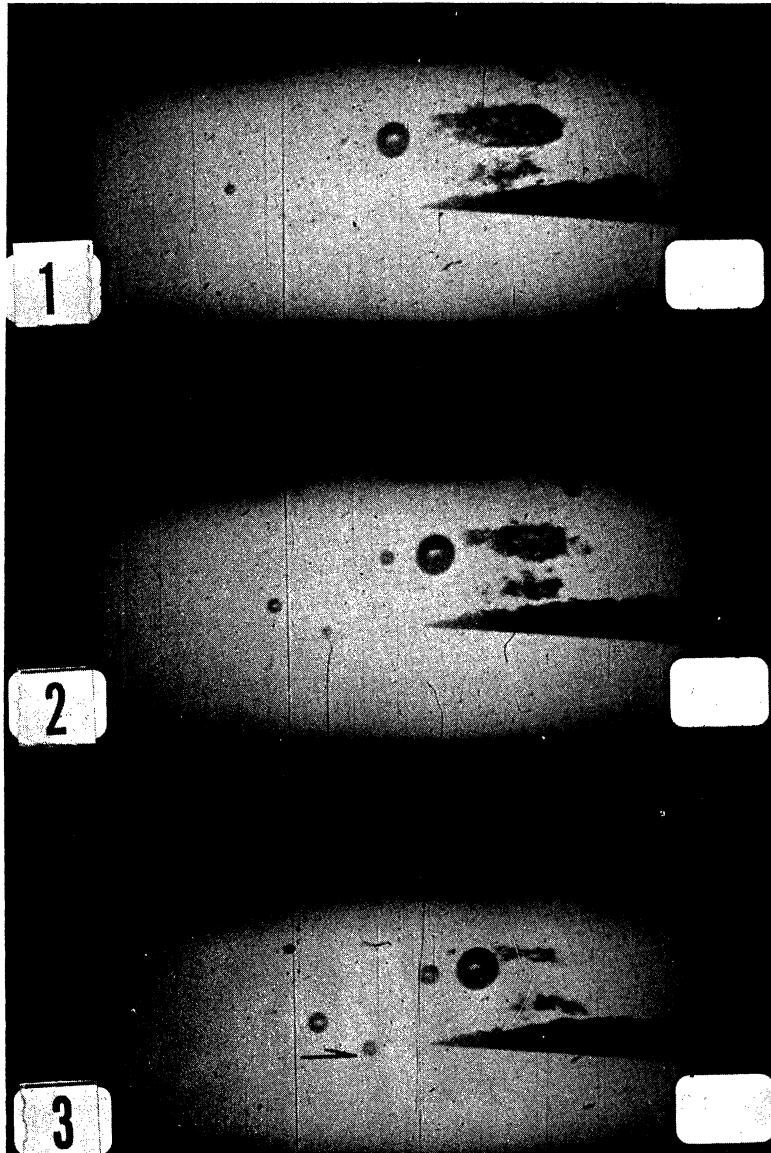
## CHAPTER V

### DISCUSSION OF RESULTS

#### A. Plexiglas Two-Dimensional Venturi

High speed photographs of the growth and collapse of natural cavitation bubbles in the diffuser section of the plexiglas two-dimensional venturi were made with the Fastax and Dynafax cameras. Although the framing rates were low, (7,000 to 25,000 frames/second), the writing times of the cameras were large (9ms to 500 ms) compared to the typical bubble lifetime of 1 ms. Therefore, if the cavitation cloud in the throat and diffuser section of the venturi is properly adjusted, the probability of photographing several of the randomly occurring cavitation bubbles during each photographic sequence is high. The low framing rate results in a low number of frames/individual bubble (10 to 30 frames) with only a fair probability of 1 frame during the critical collapse phase.

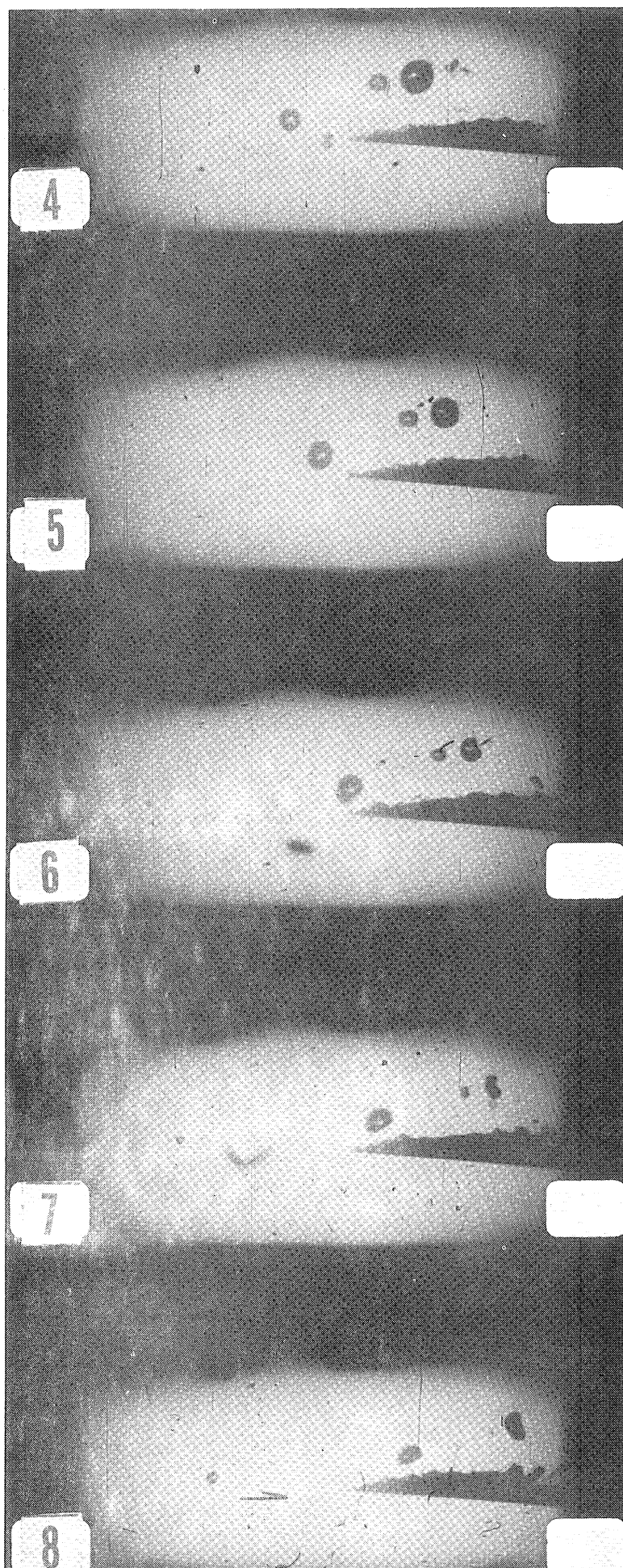
Figure 5.1 is a sequence of frames taken with the Fastax camera. It is immediately noted that an analysis is complicated by a wake formed at the tip of the wedge. Modifications to reduce this wake were not made until the Fastax photographs were completed. The photographs show that the growth of the bubble in the throat section of the venturi, where the pressure is relatively constant, is nearly spherically symmetric for bubbles that do not touch the walls of the venturi. During the collapse phase in the diffuser section of the venturi, the shape of the bubble is influenced by both the pressure gradient and the wall. The initial flattening of one side of a bubble (Frame 4 of Fig. 5.1) is at an angle between the direction of the pressure gradient and the plane formed by the wall or wake surface. This angle depends partially upon the relative distance between the bubble and the venturi wall or wake as shown in Fig. 5.2. The short dashes in this figure represent the position and angle of the flattened surfaces



2230a

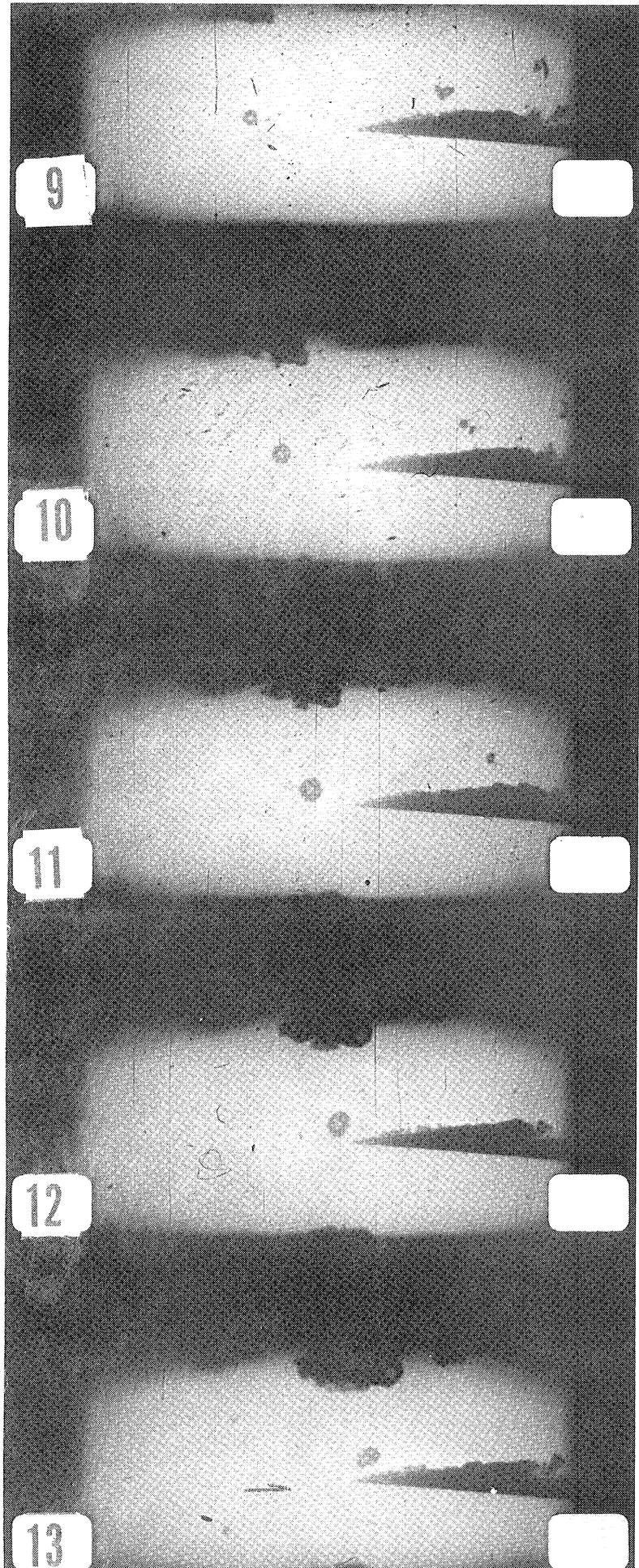
Figure 5.1 Fastax High Speed Photographs Using Diffuse Back Lighting, 7200 Frames/Second,  $1.0 \mu\text{s}$  Exposure/Frame, Flow Left to Right, Fluid Velocity 27.7 m/s, Air Content 1.3%, Scale Length (Arrow) 0.52 cm.





2230b

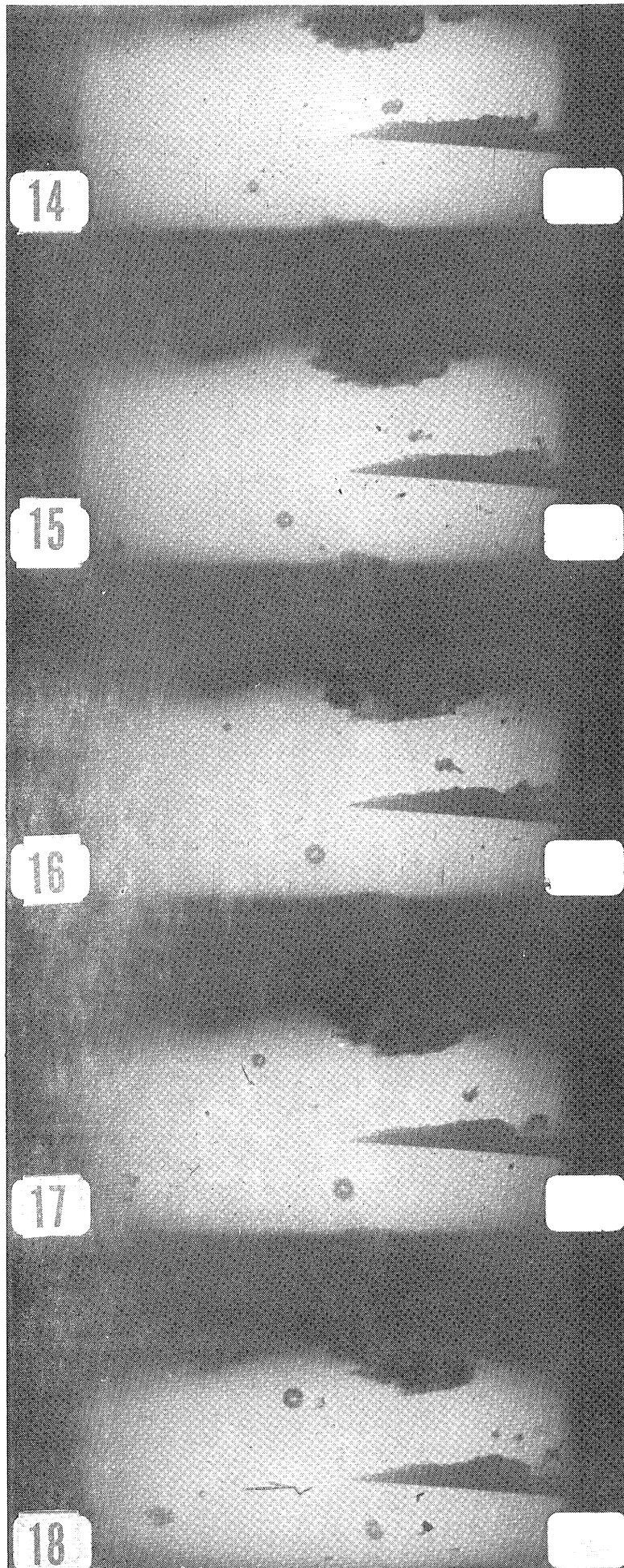
Figure 5.1 Continued



2230c

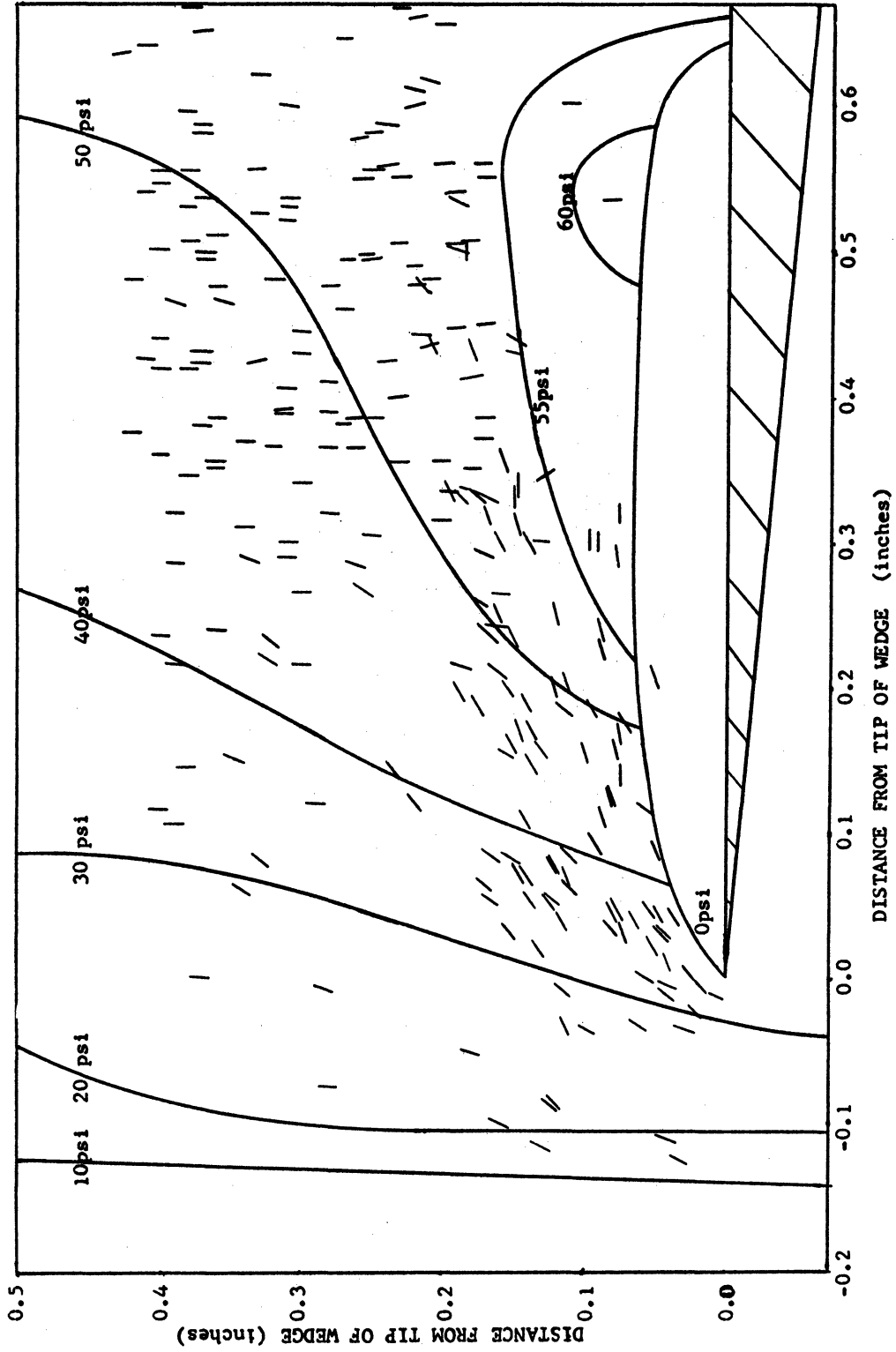
Figure 5.1 Continued





2230d

Figure 5.1 Continued



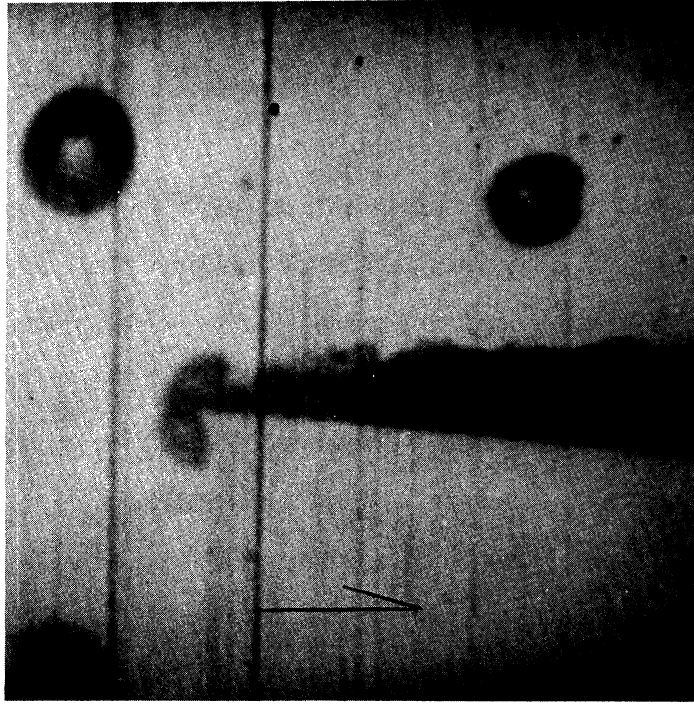
2232

Figure 5.2 Orientation of Flattened Side of Bubble vs. Distance from Tip of Wedge and Relation to Constant Pressure Lines

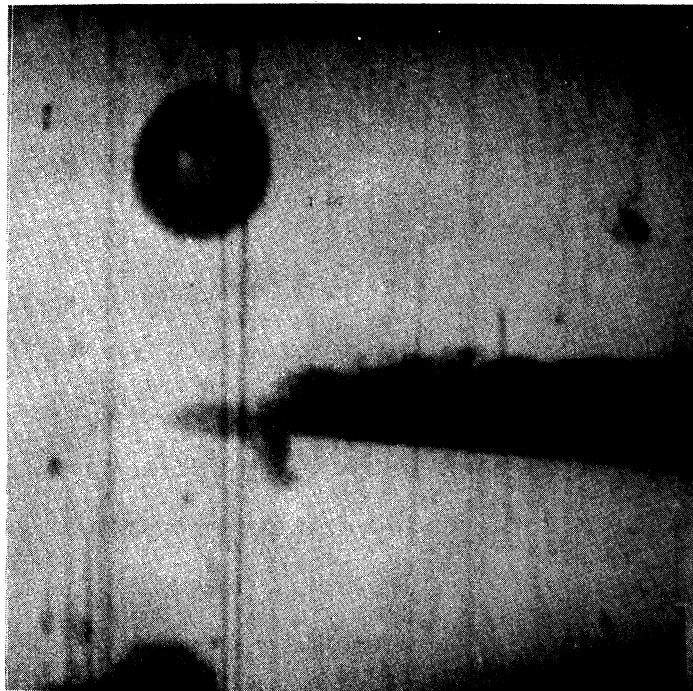
for about 30 bubbles. Also note the formation of a jet toward the surface in the collapse of the bubble shown in Frame 9, and the rebound of a bubble from a minimum volume in Frame 7 to a larger volume in Frame 8. Any migration of the centroid of the bubble toward the wall or away from the wake during collapse and rebound is not noticeable, probably because the collapse could not be followed through a large enough volume ratio and because of the large effect of the pressure gradient. The possibility of analysis of individual bubbles near their minimum collapse point is reduced by the low photographic resolution, as shown in Fig. 5.3, for these pictures obtained with the Fastax camera. Therefore, bubble shape information could only be inferred from the initial collapse and final rebound shapes. Several sequences such as Fig. 5.4 were observed in which the first frame showed the partially collapsed cavitation bubble with the flattened side angled toward the wall. The next frame shows the rebound phase of the bubble with a vapor trail probably left by a microjet impinging upon the surface of the wedge.

High speed photographs taken with the Dynafax camera were made after the spoiler (Fig. 2.4) had been added to the plexiglas two-dimensional venturi in order to control flow separation at the tip of the wedge. A sequence of photographs (Fig. 5.5) contains several more frames of each individual bubble. However the critical portion of collapse, during which damaging potential is produced, still occurs between frames. The collapse of bubbles even quite close to the wedge is apparently dominated by the pressure gradient since the collapse and rebound appear similar to those for bubble subjected to only a pressure gradient (Fig. 5.22) with little or no effect produced by the adjacent wedge.

The wedge influences only those bubble which impinge upon or are attached to it. This conclusion is shown in plots of radius vs. time for two of the bubbles seen in Fig. 5.5. The bubble (Figs. 5.6a and b)



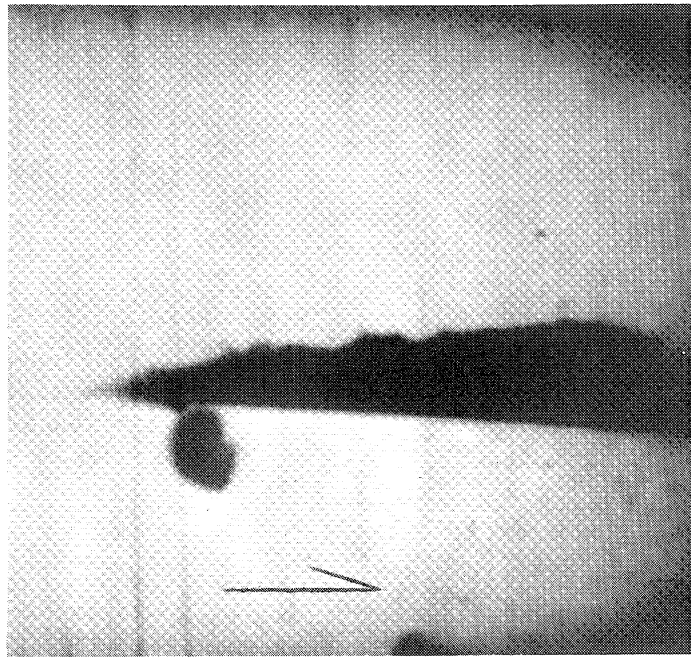
FRAME 1



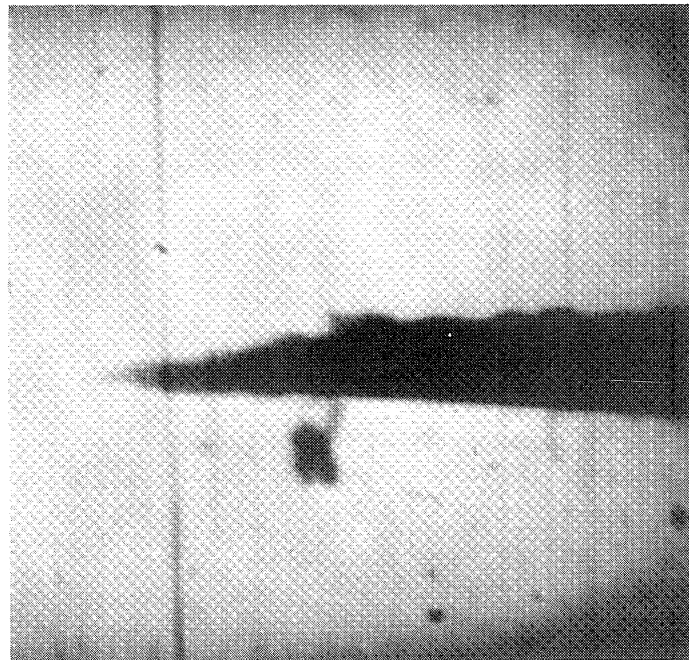
FRAME 2

2233

Figure 5.3 Fastax High Speed Photographs Using Diffuse Back Lighting and Showing the Poor Resolution of the Fastax System. Scale Length (Arrow) 0.52 cm.



FRAME 1



FRAME 2

2235

Figure 5.4 Fastax High Speed Photographs Using Diffuse Back Lighting and Showing the Remains of a High Speed Jet Striking the Wedge During Cavitation Bubble Rebound



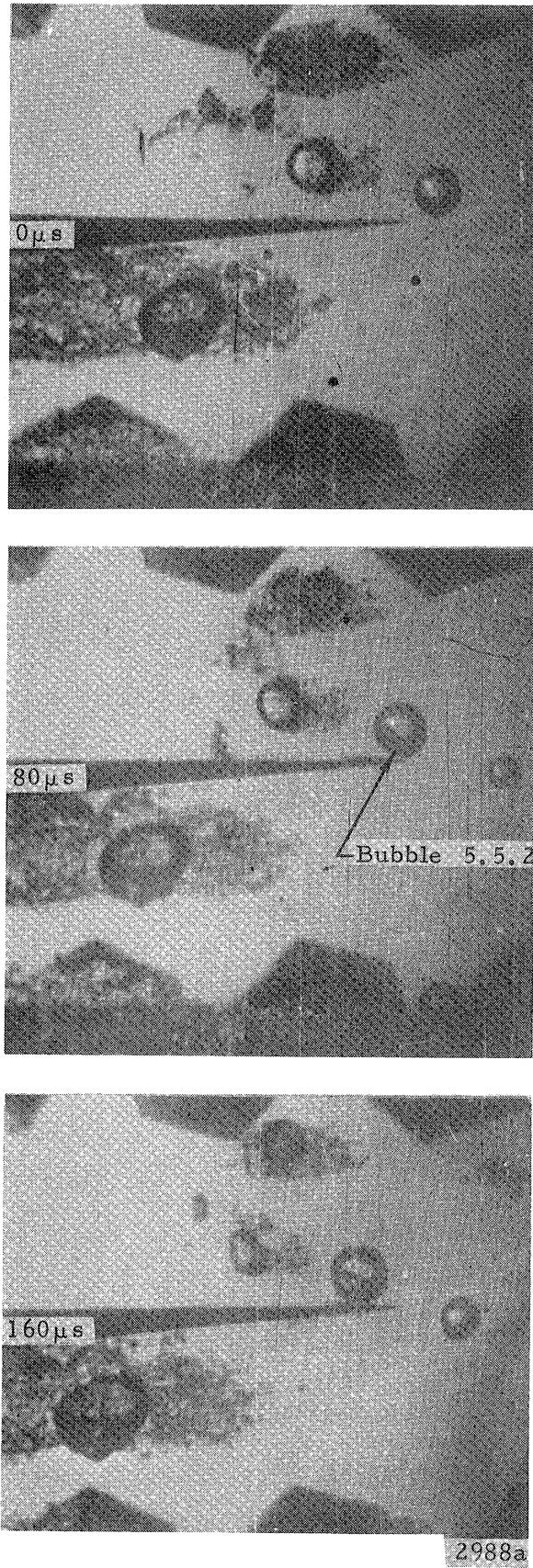


Figure 5.5 Dynafax High Speed Photographs Using Diffuse Back Lighting. 12,500 Frames/Second,  $1.0 \mu\text{s}$  Exposure/Frame, Fluid Velocity  $34.2 \text{ m/s}$  Right to Left, Air Content  $1.2\%$ , Magnification  $2.0$



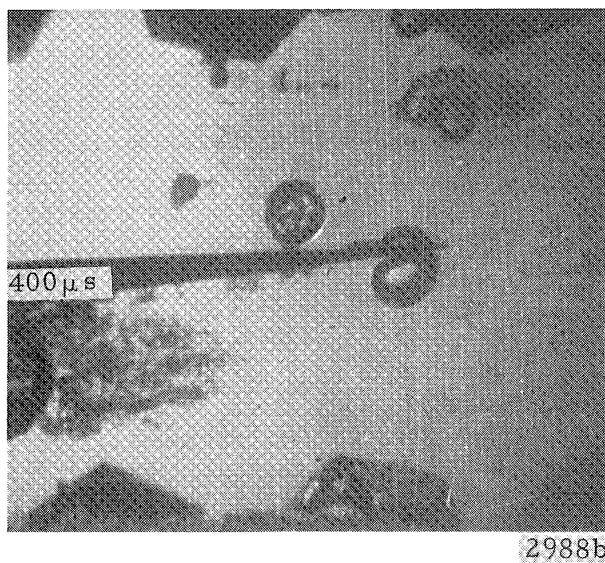
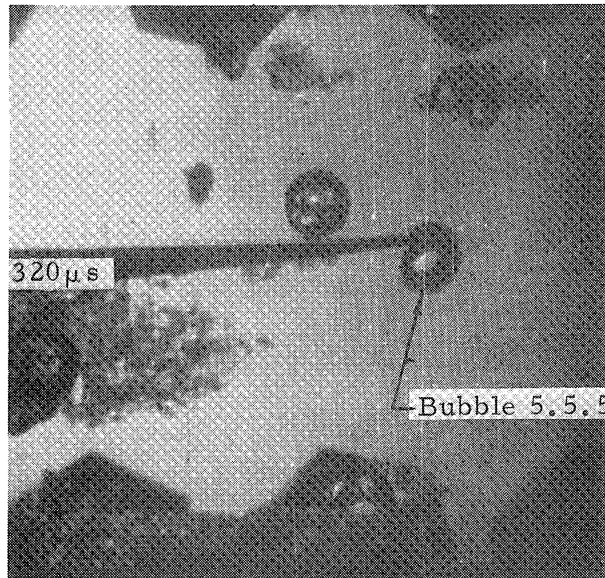
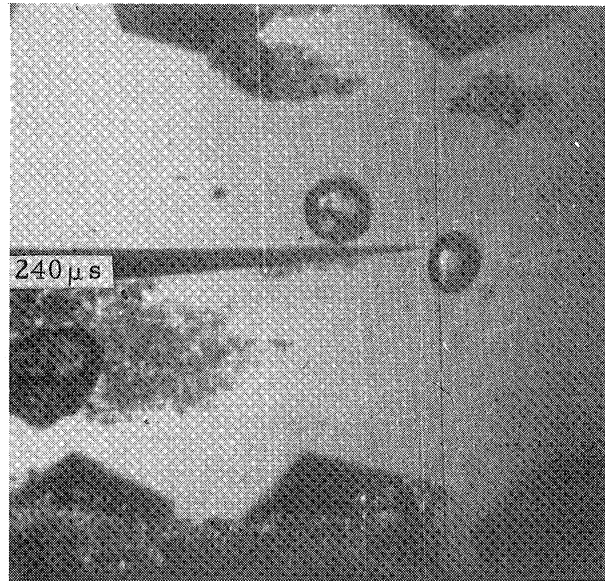


Figure 5.5 Continued

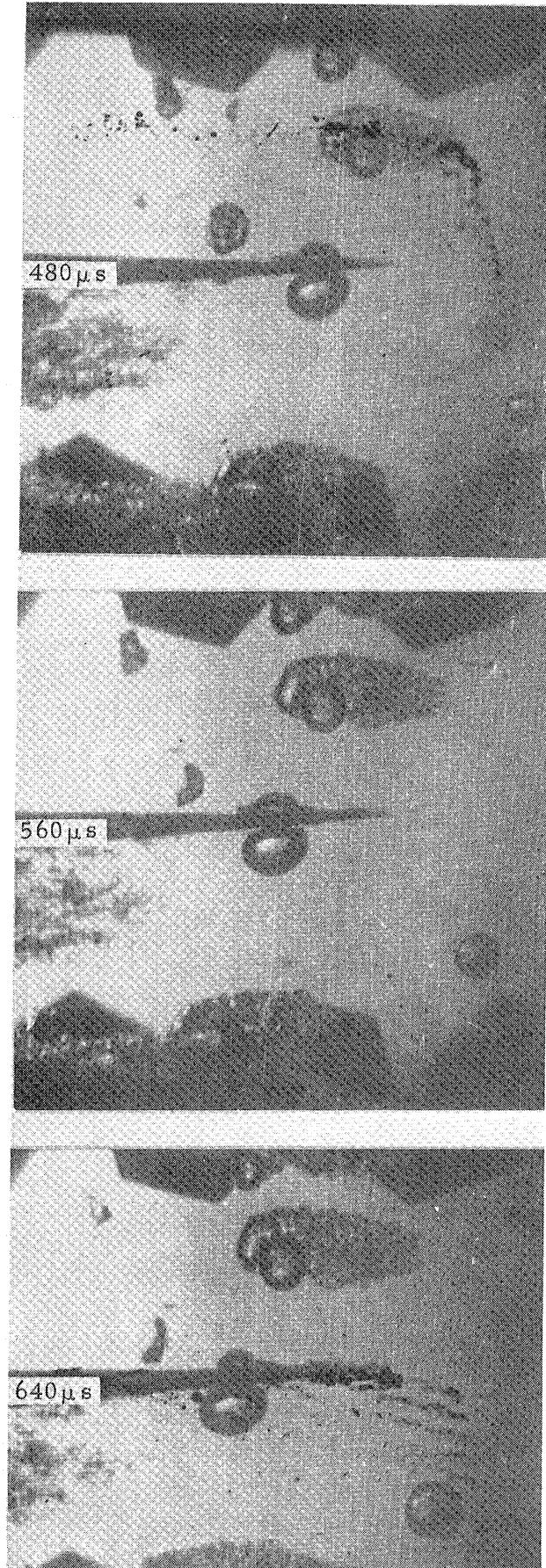
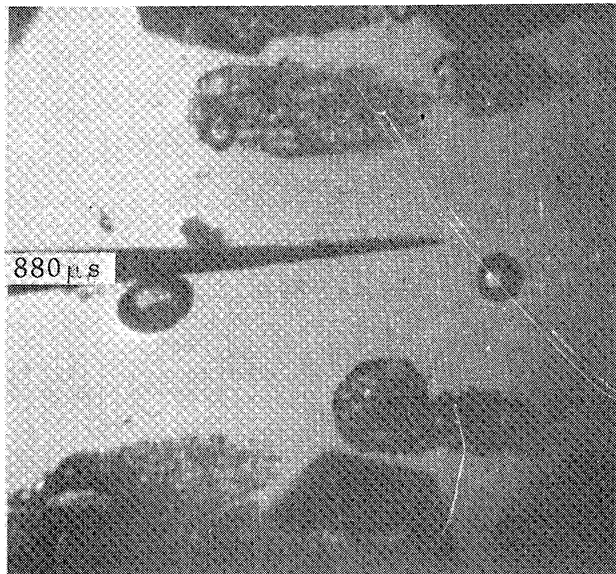
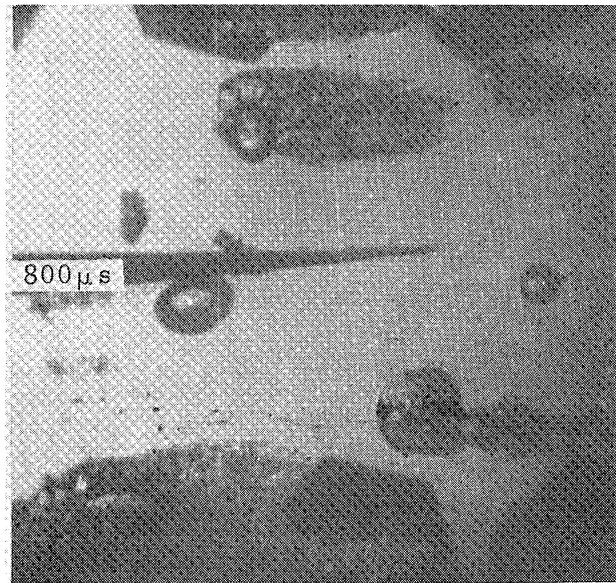
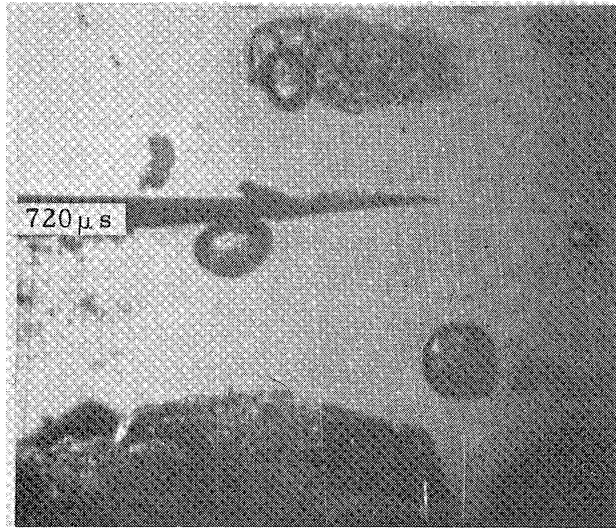


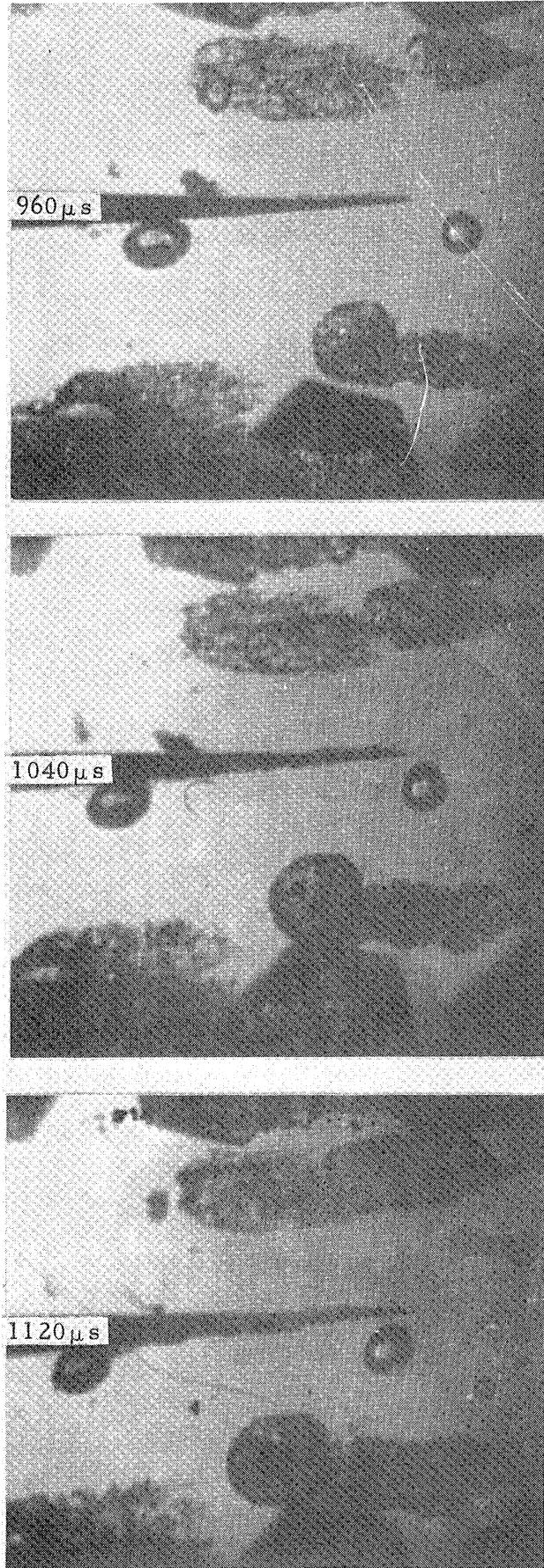
Figure 5.5 Continued 2988c



2988d

Figure 5.5 Continued





2988e

Figure 5.5 Continued

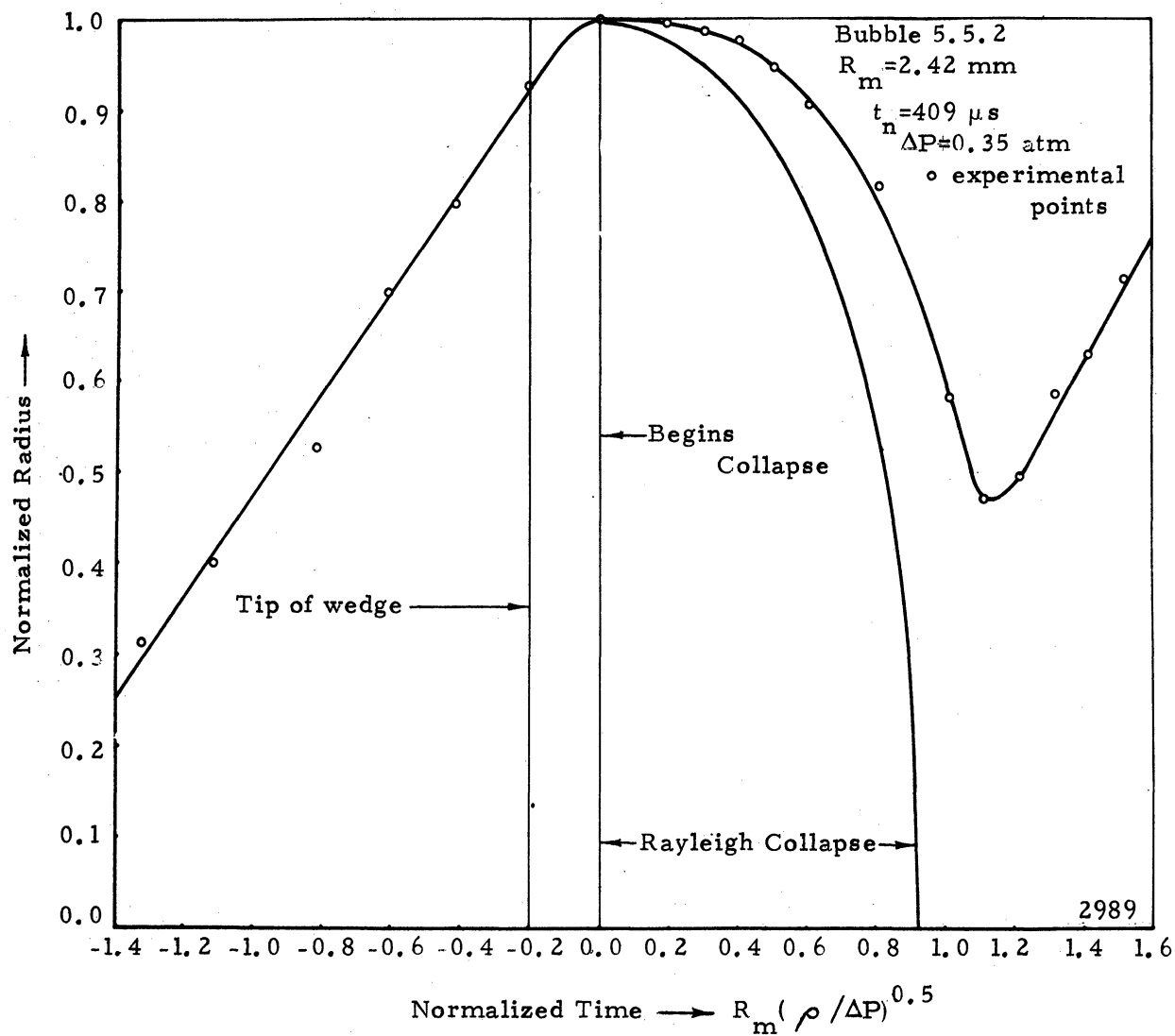


Figure 5.6a Normalized Radius vs. Normalized Time for the Natural Cavitation Bubble Reaching the Tip of the Wedge in Frame 2 of Figure 5.5

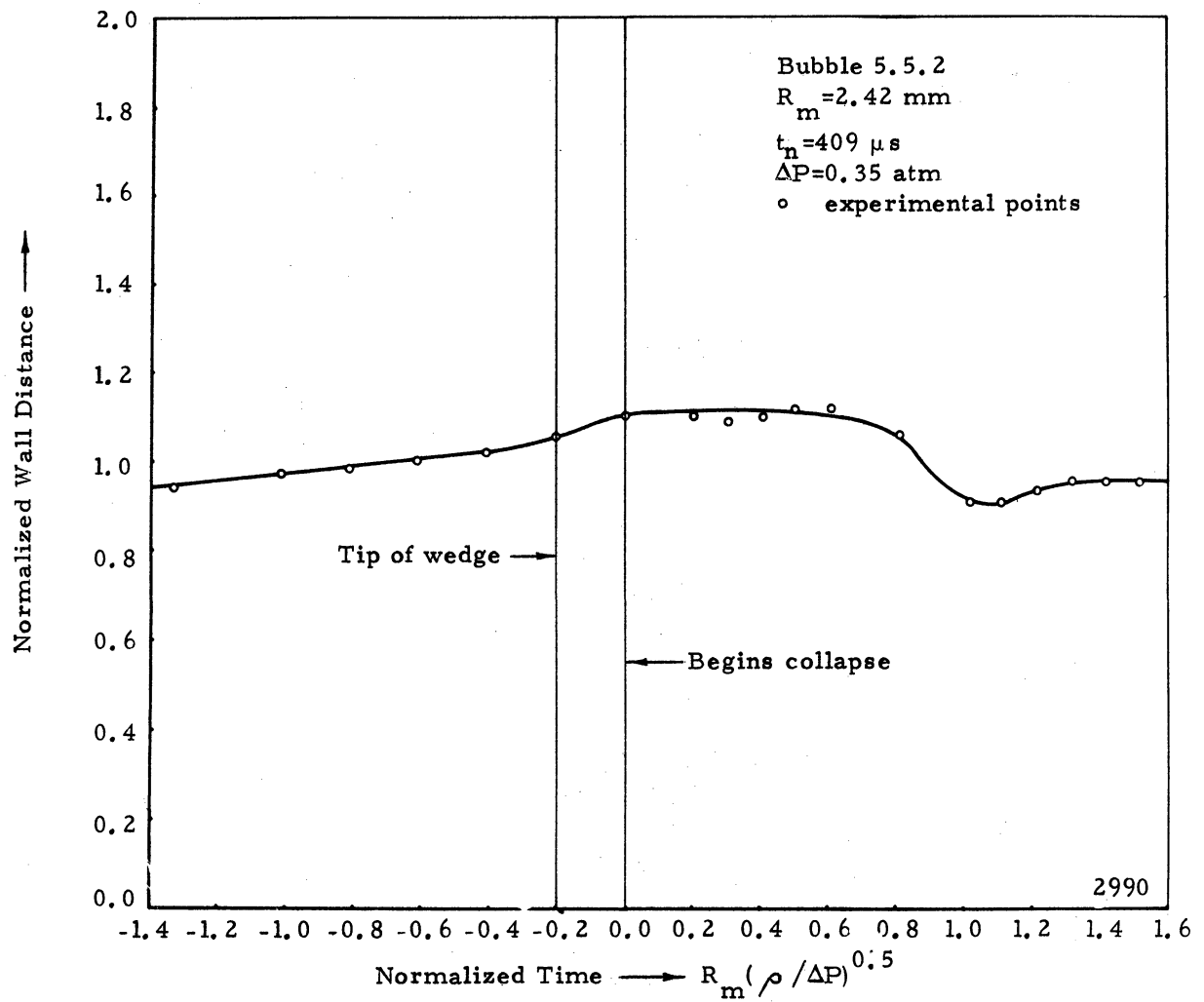


Figure 5.6b Normalized Wall Distance vs. Normalized Time for the Natural Cavitation Bubble Reaching the Tip of the Wedge in Frame 2 of Figure 5.5

which reaches the wedge in Frame 2 of Fig. 5.5 has an initial normalized wall distance,  $b_o$ , of 1.12; however, it migrates to a minimum wall distance of only 0.91 during collapse and rebound. Although the collapse is asymmetric, with the bubble eccentricity (eq. 4.21) increasing from 0.20 to 0.95, the collapse mode appears more like a bubble collapsing in a pressure gradient (Fig. 5.22) than a bubble collapsing near a solid boundary (Fig. 5.28). The next bubble (Figs. 5.7a + b), in Frame 2 of Fig. 5.5 impinges upon the wedge in Frame 5 of Fig. 5.5. Since the wedge intersects the bubble, its initial normalized wall distance is  $< 1.0$  ( $b_o = 0.78$ ), and during collapse significant migration occurs ( $b = 0.23$  at minimum volume). The combination of the wall and pressure gradient actually decreases the asymmetry of the bubble (eccentricity, eq. 4.25, decreases from 0.71 to 0.27 during the initial stages of collapse). However, for this bubble the semi-major axis is parallel to the wall instead of to the pressure gradient. The wall also apparently affects this bubble by increasing the normalized collapse time (i. e., normalized time between observation of bubble at its maximum radius and at its first minimum radius) by  $\sim 25\%$  as shown in Figs. 5.6 and 5.7. For both bubbles the plots show that the growth of the bubbles takes place over a longer period than the collapse because the growth nearly always takes place under a smaller driving pressure than the collapse.

### B. High Speed Liquid Jet Impact

Using the gas gun momentum exchange facility of this laboratory (previously described), high speed motion pictures of water jets impacting upon solid targets were made. Because the duration of the event (from the time the jet leaves the orifice until it impacts upon the surface) is only  $\sim 20\mu s$ , and because the event can be defined precisely in time, only a few frames are required per photographic sequence. Therefore, the Cranz-Schardin photographic

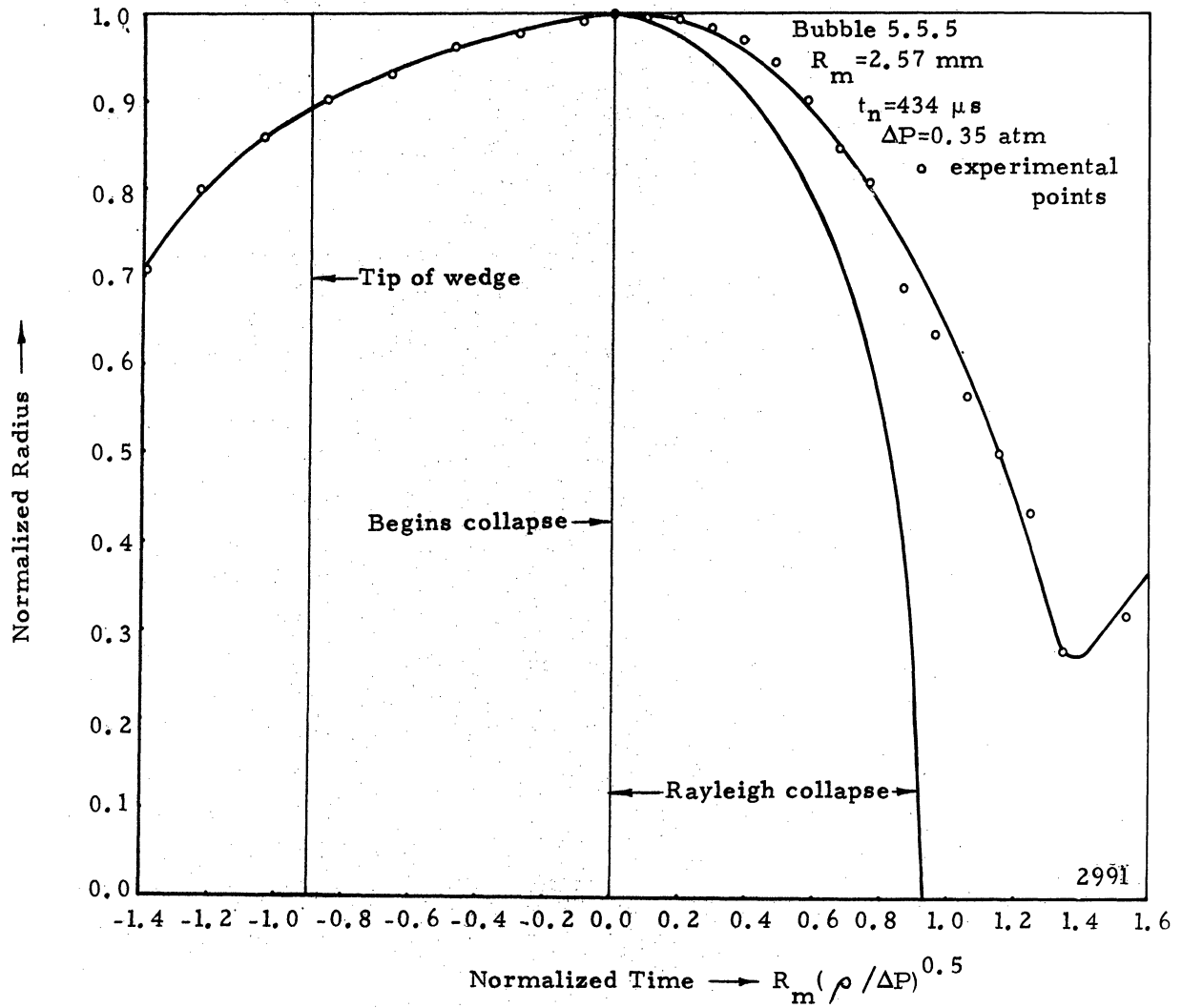


Figure 5.7a Normalized Radius vs. Normalized Time for the Natural Cavitation Bubble Impinging upon the Tip of the Wedge in Frame 5 of Figure 5.5



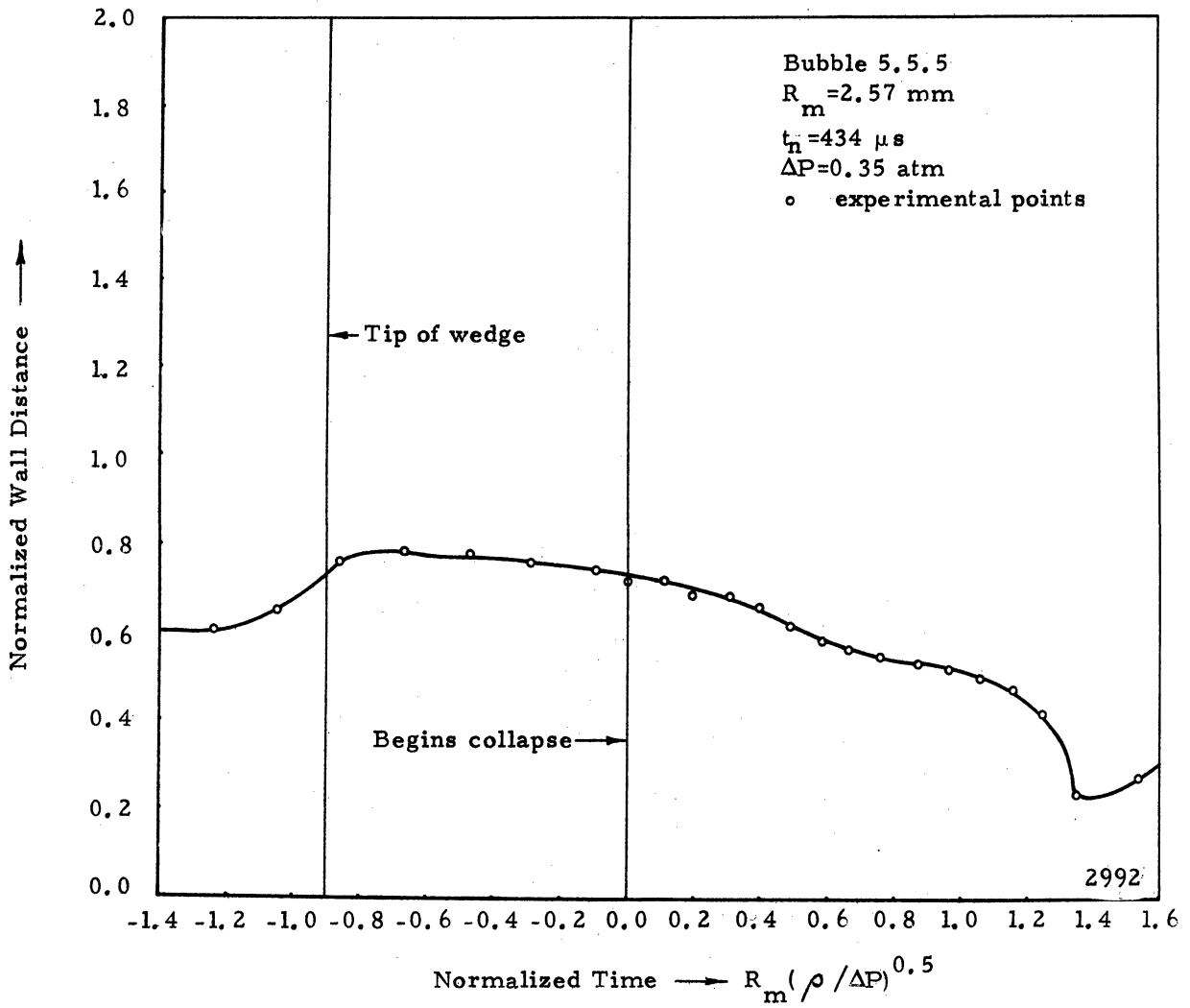


Figure 5.7b Normalized Wall Distance vs. Normalized Time for the Natural Cavitation Bubble Impinging Upon the Tip of the Wedge in Frame 5 of Figure 5.5

system is ideally suited for this study. Fig. 5.8 is a sequence of a high speed jet impacting upon a plexiglas specimen. This jet as well as the jets which produced the pits of Fig. 5.10, 5.11, and 5.12 all have impact velocities within  $\pm 10\%$  of 670m/s. The small precursor or "Monroe" jet noted in the first frame is caused by the "shaped charge" effect of the miniscus.<sup>(26)</sup> Although the velocity of this small jet is about twice the velocity of the main jet, its mass is so small that it is believed the majority of damage is caused by the main jet. This is confirmed by recent work by Brunton.<sup>(37)</sup> Upon impact, the main jet produces a pressure upon the surface of the order of the water hammer pressure,  $P_{wh}$

$$P_{wh} = \rho_{cv}$$

where:  $\rho$  = water density

$c$  = speed of sound in water

$v$  = jet velocity

This pressure, which may substantially depress the surface, is relieved by the propagation and reflection of shock or pressure waves, and by the outward radial flow (at measured velocities 2 to 3 times the impact velocity) of the jet. Damage may be produced by material failure caused by compressive stresses under the jet, tensile stresses around the edge of the jet, and shear stresses produced by the outward radial flow (Fig. 5.9). This damage may take the form of a crater with a raised rim, or of a damage ring with little or no damage in the center depending upon the type of material.

For plexiglas (Fig. 5.10) which is much stronger in compression than in tension, the damage appears as a ring with no damage in the center. The accompanying proficorder trace of the

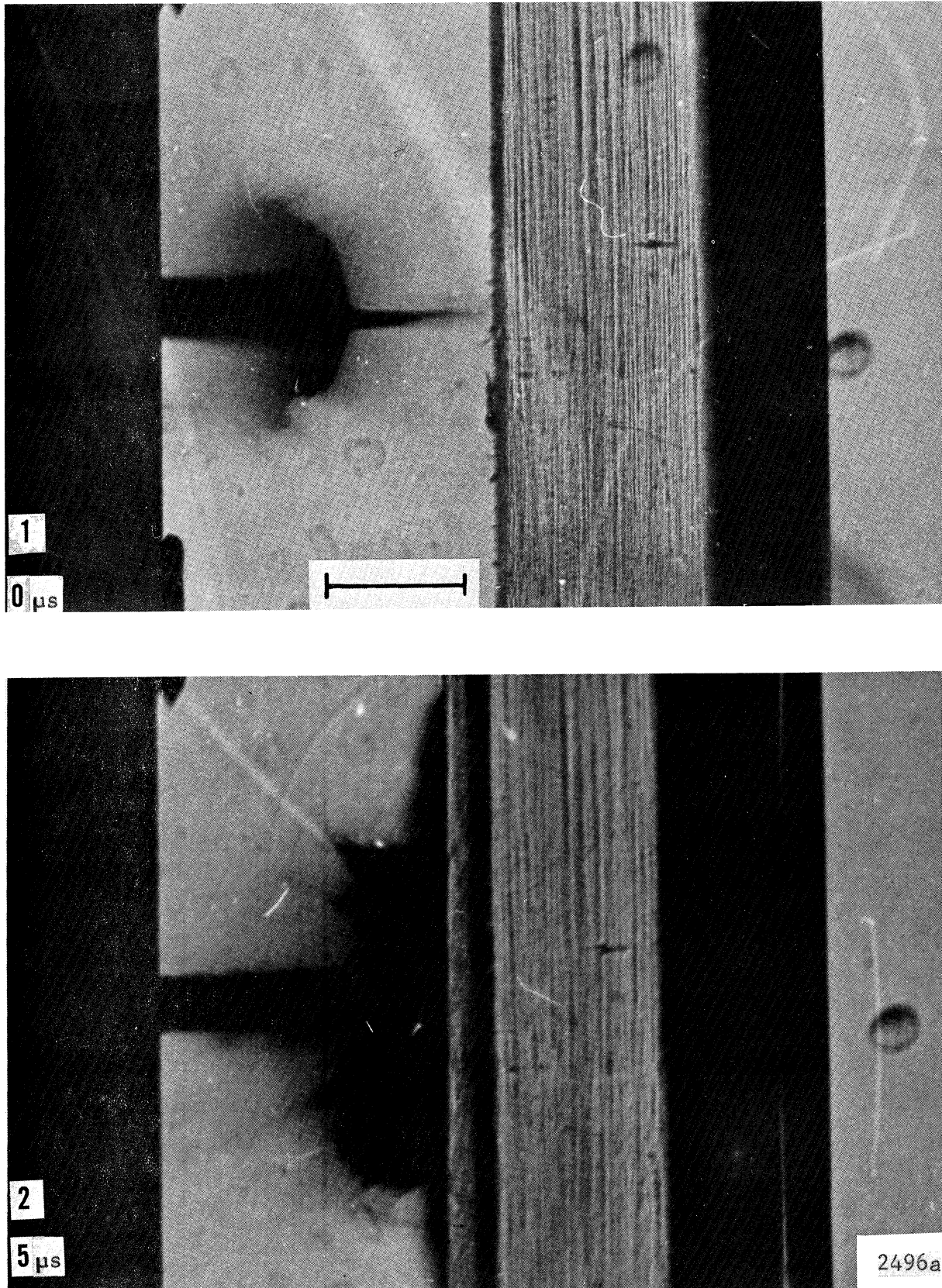


Figure 5.8 Spark Camera Photographs Using Focused Back Lighting and Showing a Water Jet Impacting on a Plexiglas Specimen. Time Measured from First Frame,  $0.22 \mu\text{s}$  Exposure/Frame, Scale Length 0.5 cm.

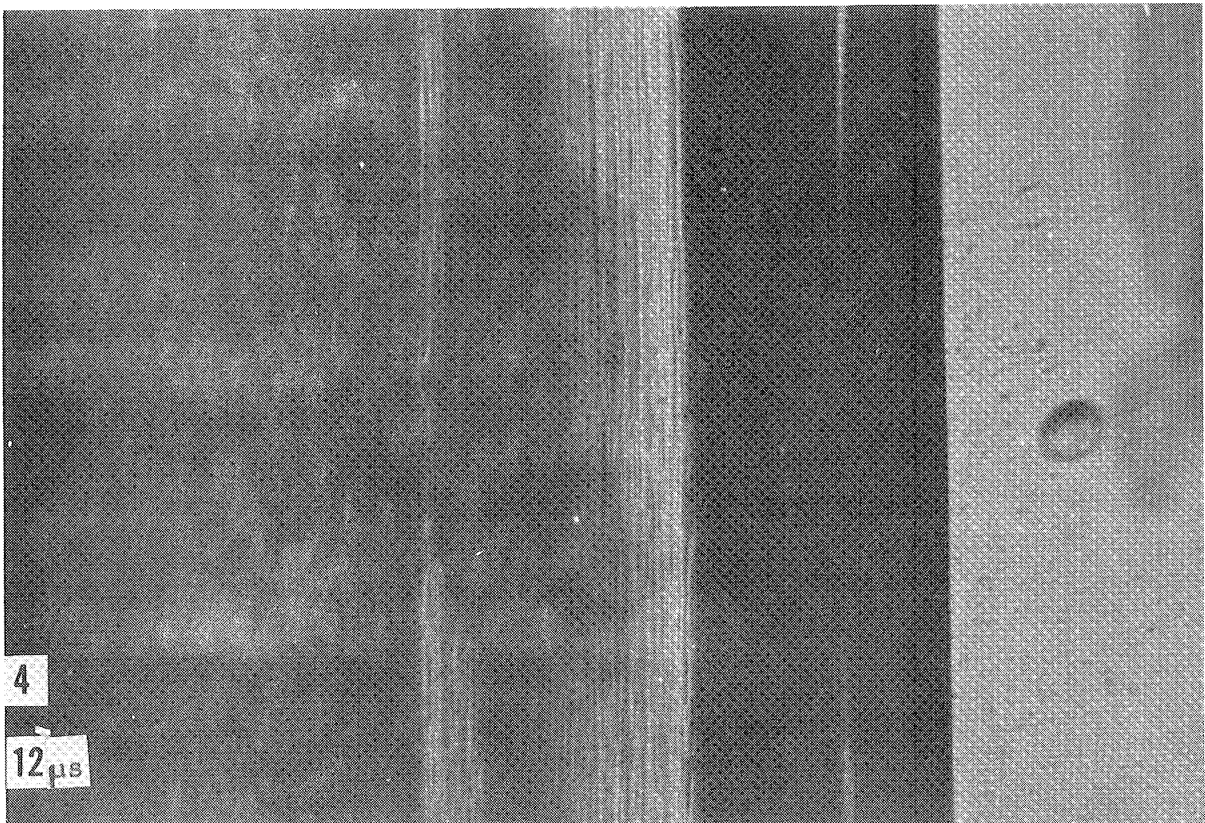
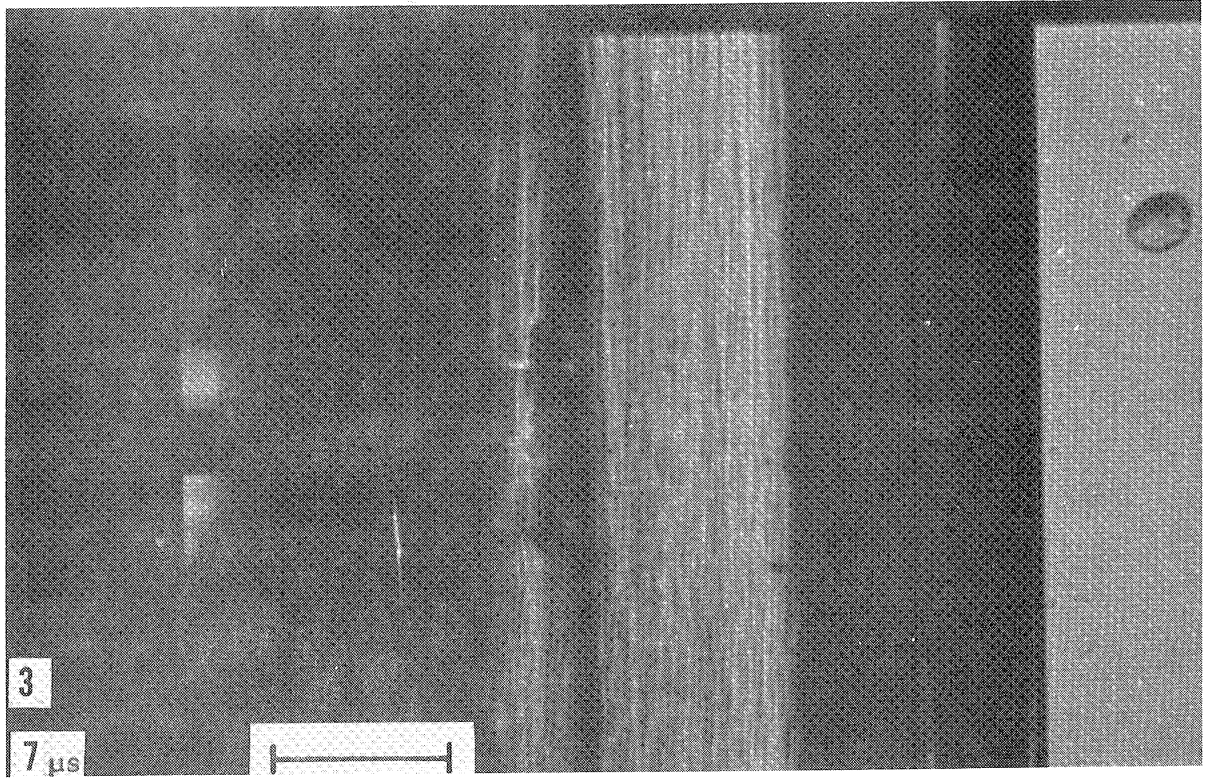


Figure 5.8 Continued

2496b

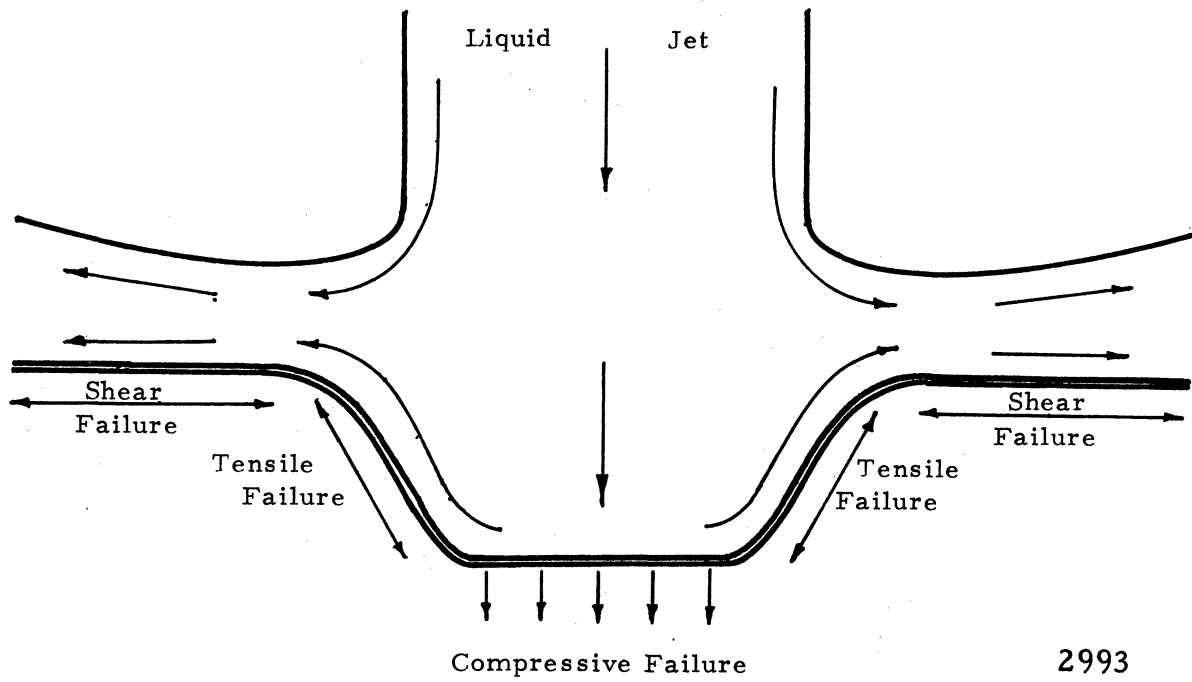


Figure 5.9 Model of Material Failure During High Speed Liquid Jet Impact. Axial Deformations are Greatly Exaggerated



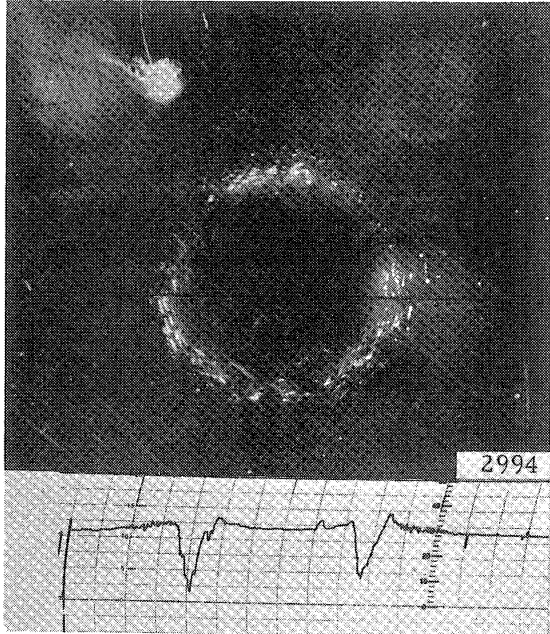


Figure 5.10 Pits Produced in Plexiglas by Impact of High Speed Liquid Jet. Proficorder Graduations:  $660 \mu$  Horizontal,  $0.635 \mu$  Vertical

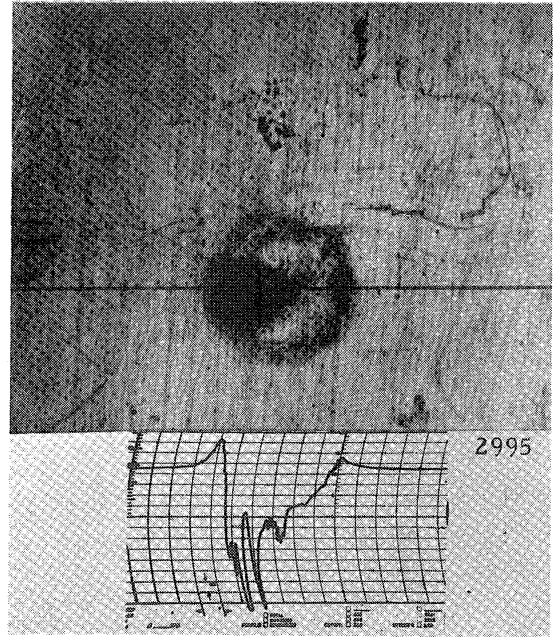


Figure 5.11 Pit Produced in 1100-0 Aluminum by Impact of High Speed Liquid Jet. Proficorder Graduations:  $660 \mu$  Horizontal,  $6.35 \mu$  Vertical

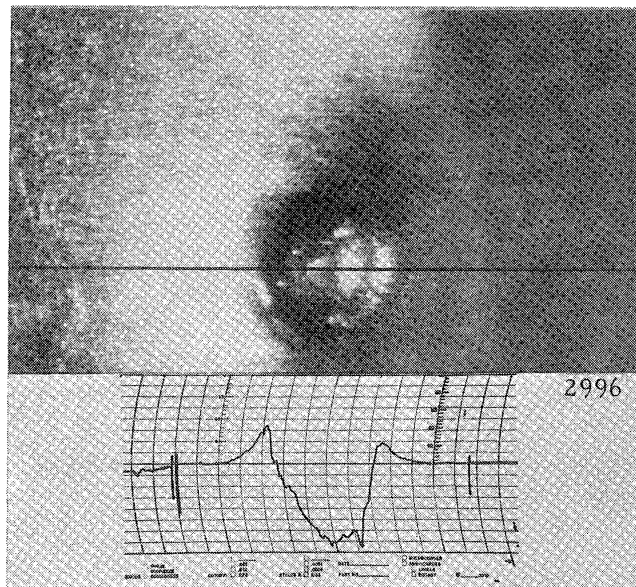


Figure 5.12 Pit Produced in Aluminum Lighting Sheet by Impact of High Speed Water Jet. Proficorder Graduations:  $660 \mu$  Horizontal,  $2.54 \mu$  Vertical

surface shows that the central undamaged portion recovers after the pressure from the jet is released. Therefore, material removed in this case is predominantly due to the failure in tension around the edge of the jet, and to the shear failure from the radial outward flow. Remarkably similar damage patterns are produced in soft (1100-0) aluminum (Fig. 5.11) used for the 50  $\mu$  thick coating. The major differences are the additional damage in the central region (possibly produced by the "Monroe jet") and the permanent set of the central region forming a crater with a raised rim. This permanent set (shown by the accompanying proficorder trace) is caused by the failure of the aluminum during compression. The stronger aluminum "lighting sheet", used in the 0.5 mm coating, fails mainly in compression (Fig. 5.12). This failure, coupled with material movement by radial flow, results in a relatively uniform crater with a raised rim. Probably very little material is actually removed from the surface during a single impact. However, a second impact adjacent to the first crater for example, could easily cause the removal of part of the raised rim. The delay in material removal until individual craters begin to overlap probably accounts to a large extent for the "incubation period" often found in droplet impact and cavitation damage studies.

### C. Spark Bubble Chamber

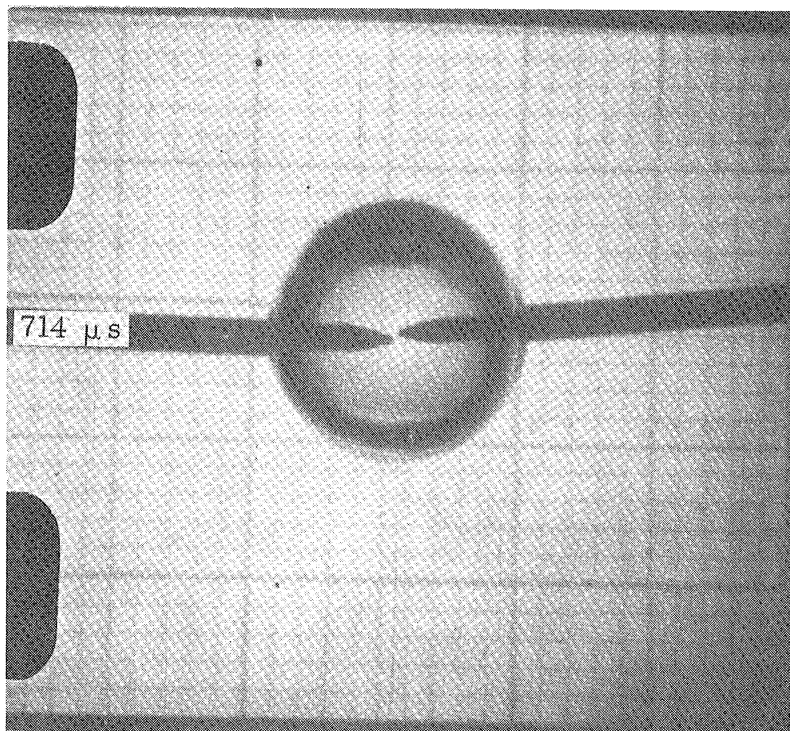
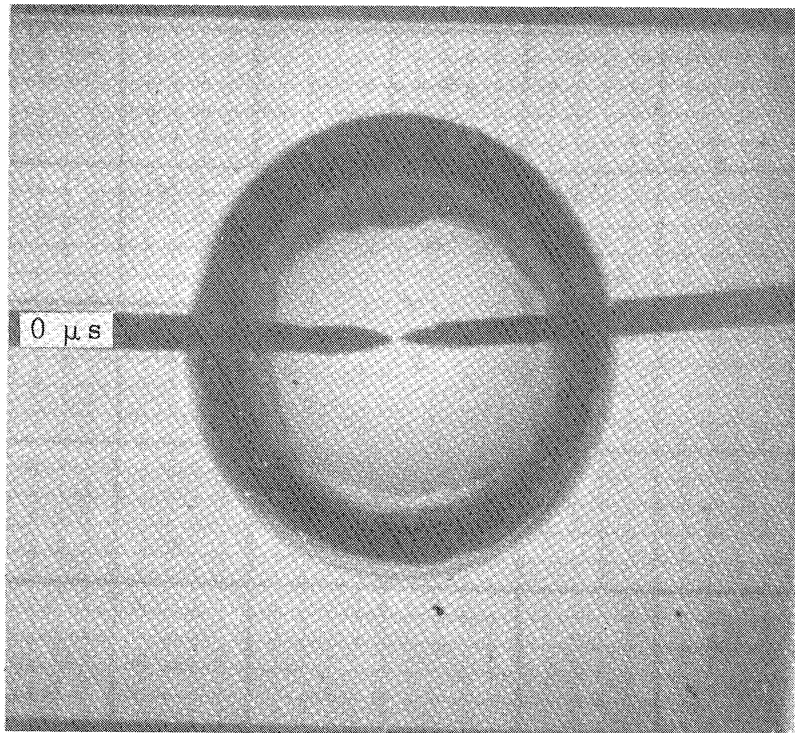
The spark bubble chamber was used to determine parameters of the spark generation network and to obtain visual information on the growth, collapse, shape and internal content of spark induced cavitation bubbles. Idealized visual information was obtained by studying bubbles away from solid surfaces in a static fluid, and with gravity as the only external non-symmetrical force acting on the bubble. Since information is required over the entire bubble lifetime (up to 3 ms) the Dynafax camera was used for this study. The spark

bubbles produced (Fig. 5.13 shows life history of a typical bubble) have a very smooth surface during the initial growth and collapse stages. The electrodes within the bubble and dividing lines on the light diffuser are clearly visible through the bubble which acts as a simple lens. Although the final collapse stage of the spark bubbles generally occurs between frames, a study of the several sequences taken show that the minimum normalized radius for spark bubbles collapsing under a hydrostatic pressure of 1 atmosphere is about 0.1 times the maximum radius of the bubble as shown by the theoretical curve of Fig. 5.14. The centroid of the bubble as it reaches this minimum volume has migrated due to the pressure gradient produced by gravity a distance approximately equal to the minimum radius away from the electrodes. The first rebound produces a bubble with a very roughened surface which obliterates any internal structure. The maximum potential energy of this rebound bubble is only  $\sim 20\%$  of the energy of the original bubble, so that  $\sim 80\%$  of the initial energy is lost due to viscous dissipation, breakup of the surface, thermal radiation and conduction, acoustic radiation, and emission of a pressure wave during the final collapse and initial rebound phase. The low pressure region left by the passage of the pressure wave is noted by the growth of many small bubbles (Frame 6 of Fig. 5.13) in the region of the spark induced bubble.\* In some cases these small bubbles may be the nuclei of other cavitation bubbles. Rapid migration occurs during the collapse and rebound so that eventually the rebound bubble detaches itself from the electrodes. The bubble may collapse and rebound several more times as it migrates away from the electrodes, finally breaking up into a mass of small bubbles. A plot (Fig. 5.14) of the mean radius vs. time follows

---

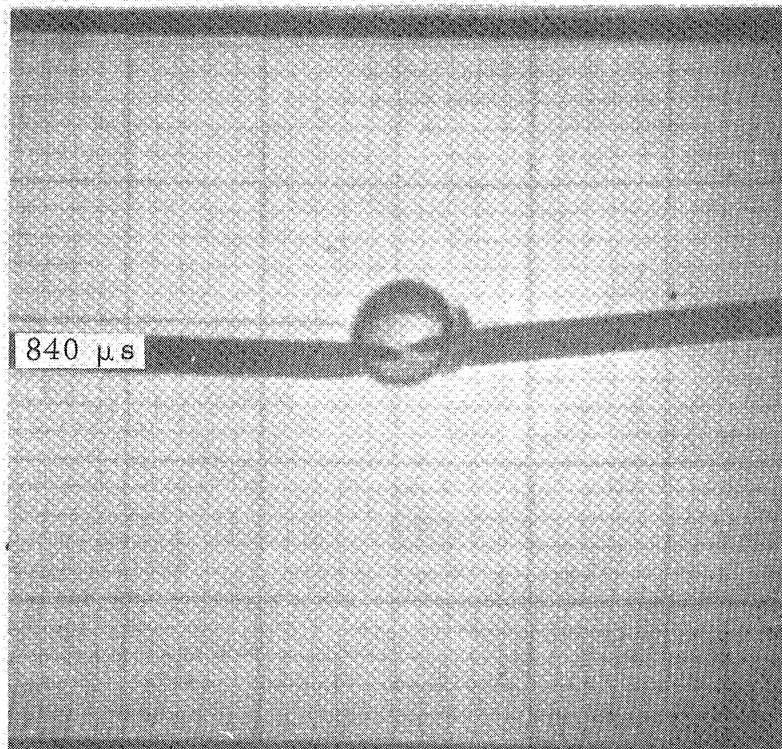
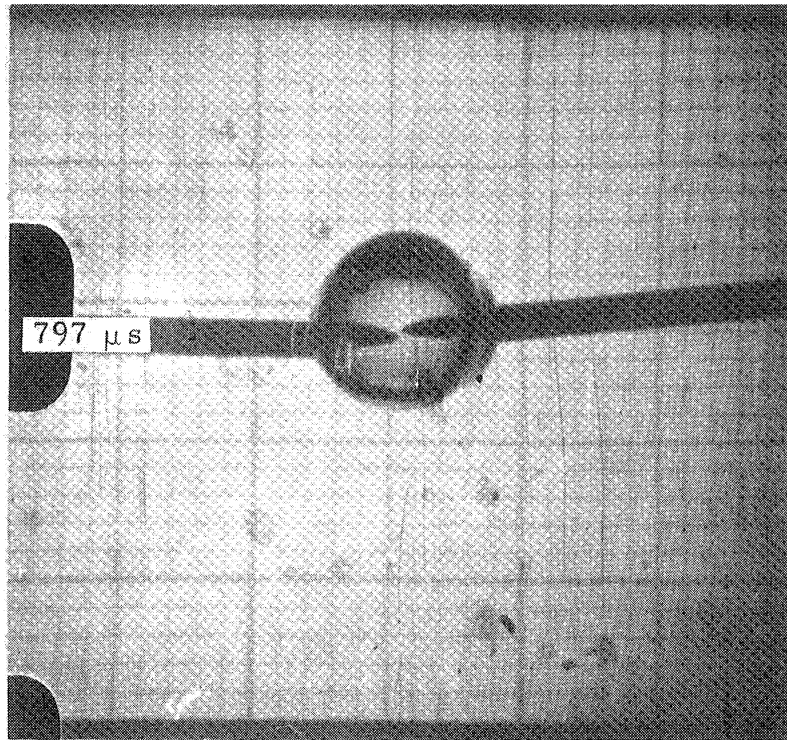
\* This same observation has been made independently in the as yet unpublished work of Green and Mesler<sup>(44)</sup> and similar evidence was shown in an earlier paper by Harrison<sup>(45)</sup>.





2997a

Figure 5.13 Dynafax High Speed Photographs of Spark Bubble Collapse in the Static Underwater Spark Bubble Chamber. Diffuse Backlighting Time Measured from First Frame,  $1.05 \mu\text{s}$  Exposure/Frame, Magnification 2.5. Air Content 2.2%



2997b

Figure 5.13 Continued

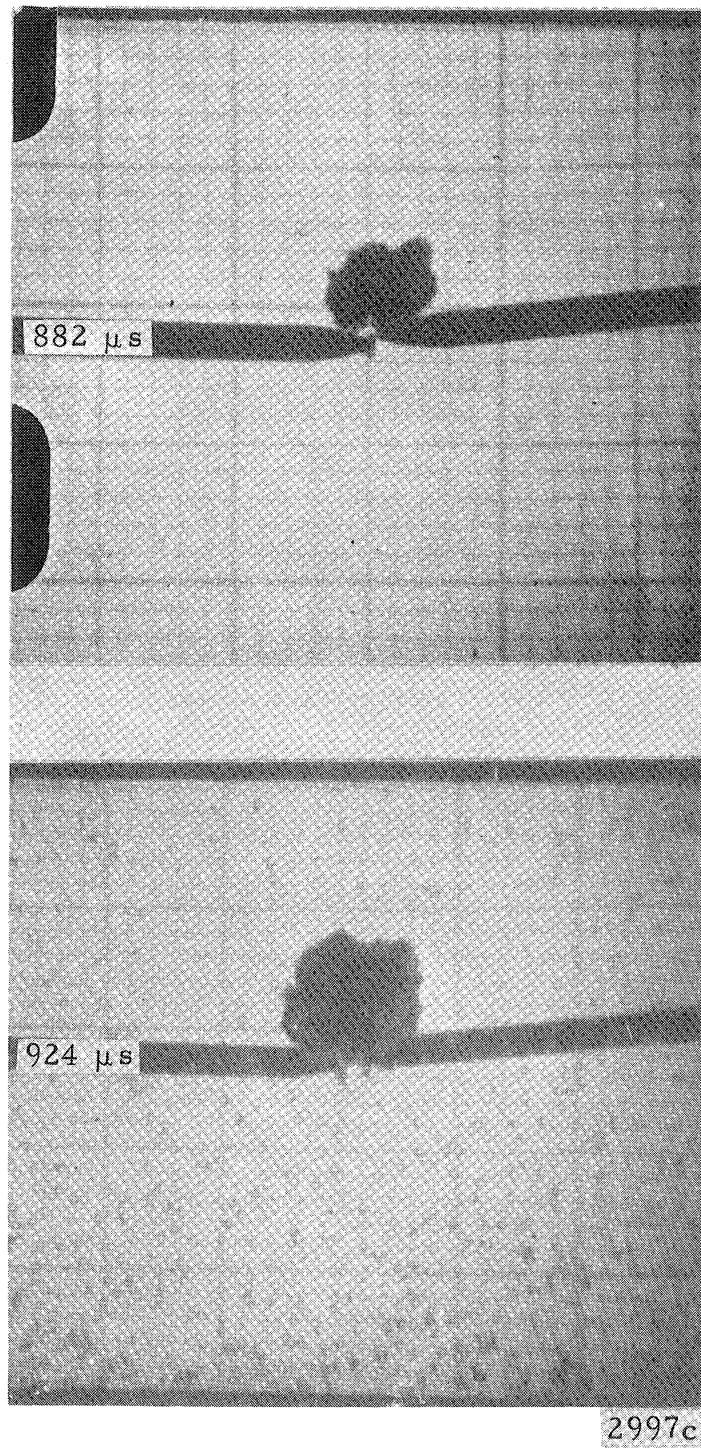
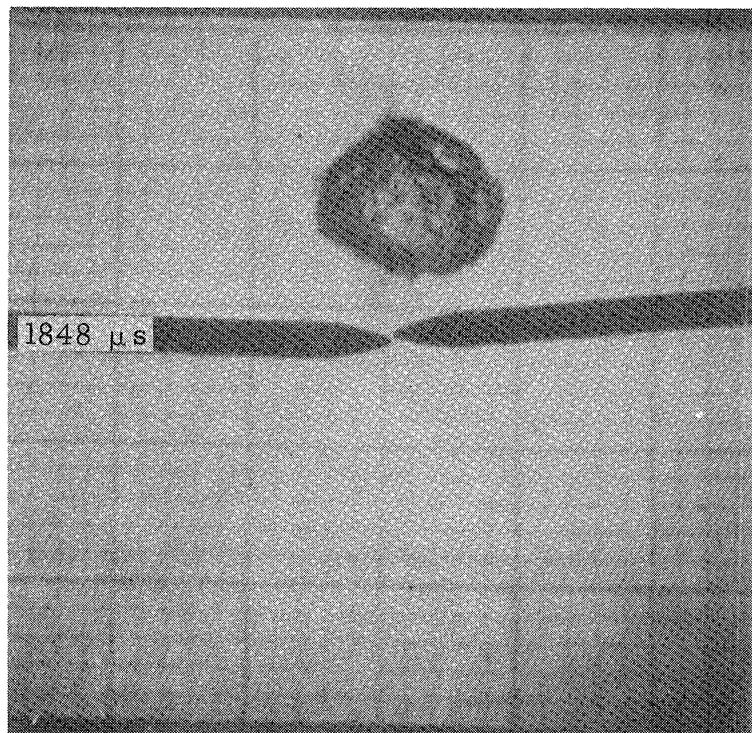
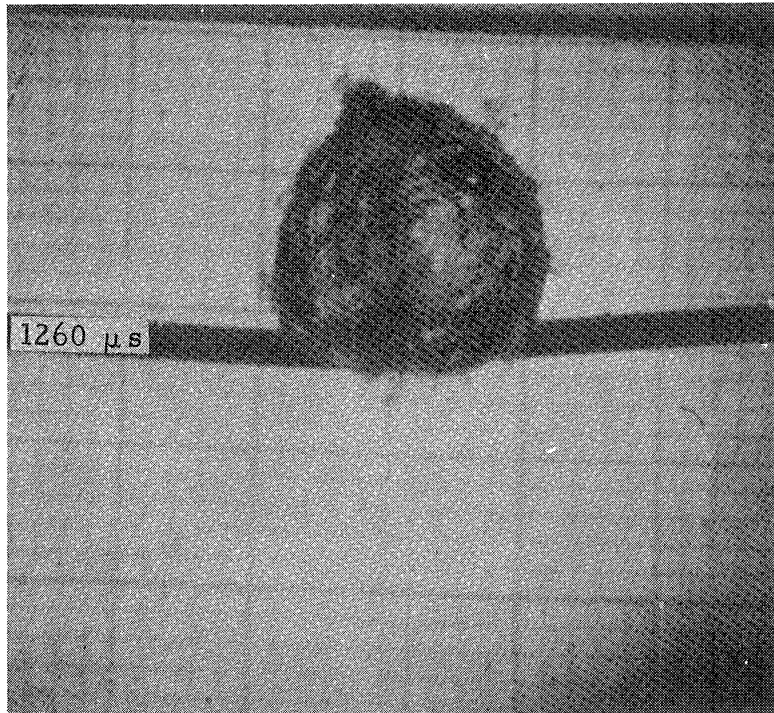


Figure 5.13 Continued





2997d

Figure 5.13 Continued

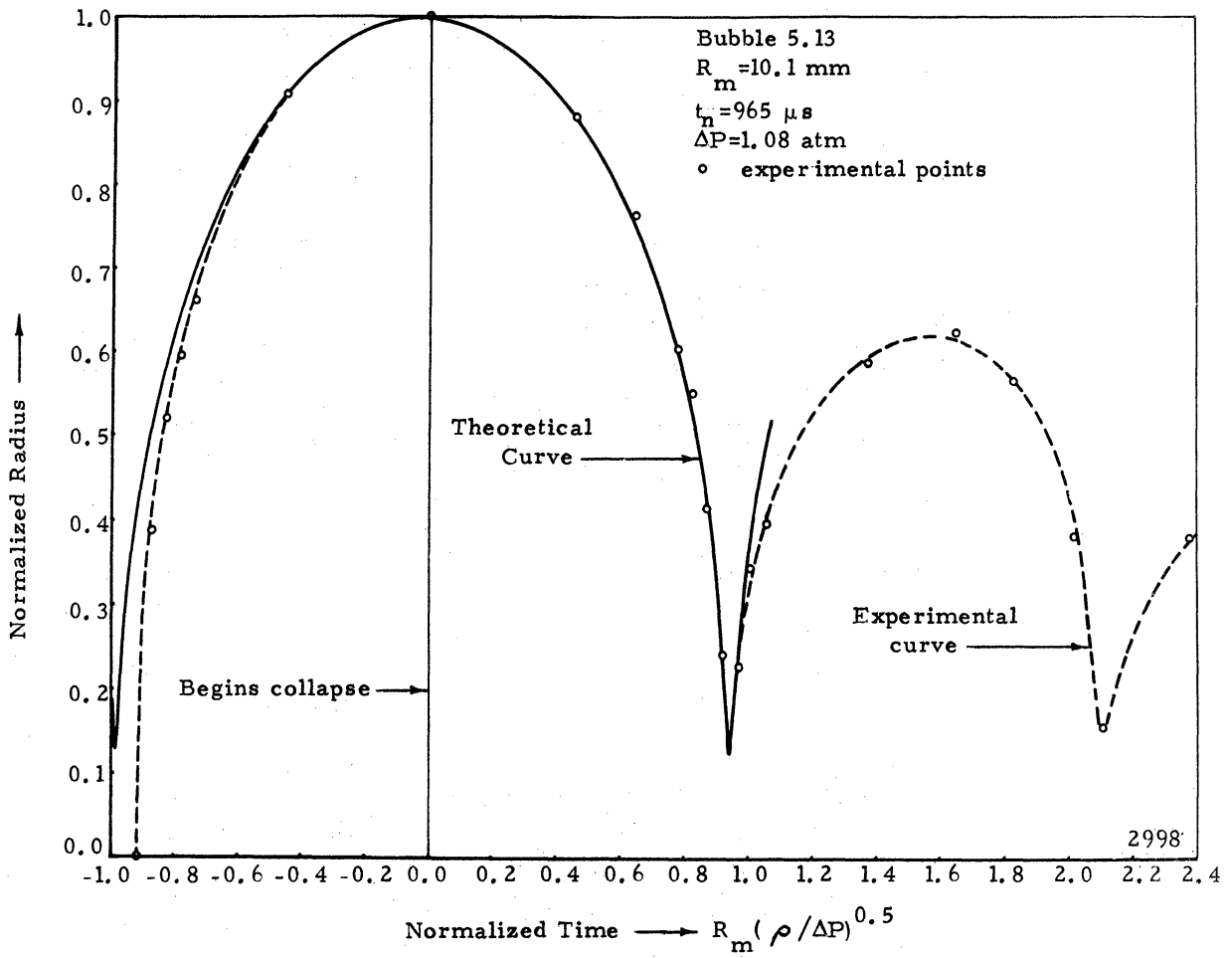


Figure 5.14 Normalized Radius vs. Normalized Time for the Spark Generated Cavitation Bubble Shown in Figure 5.13

the theoretical ideal fluid eq. 4.7 very closely from the maximum radius through the first minimum volume. Since there is no provision in the equation for any energy loss during the collapse and rebound of the bubble, the plot quickly becomes invalid as the bubble grows from its first minimum volume. Also, the initial growth of the bubble is noticeably more rapid than the corresponding collapse, due to the initial outward momentum imparted to the water by the passage of the shock wave produced upon the initiation of the spark bubble and to the initial high internal gas and vapor pressure. Until these bubbles reach their first minimum volume, the maximum value of the eccentricity (eq. 4.25) is less than 0.4, so that the effect of gravity and other factors does not produce large asymmetries until after the first minimum volume is reached.

The relationship of the electrical input energy to both total energy deposited in the water and the fraction of this energy which goes into the formation of the spark bubble is given in Table 4.1. The 10% variation in the bubble lifetimes for bubbles produced under apparently identical conditions is due to variations in the measured hydrostatic pressures,  $\Delta P$ , and in the fraction of energy forming the bubble.

#### D. The Two-Dimensional Aluminum Venturi

High speed photographs of both natural and spark induced cavitation bubbles in the two dimensional aluminum venturi were made using the Beckman and Whitley Dynafax and Model 330 cameras. For the studies of the natural cavitation bubbles, glass plates were used in the sides of the venturi while for the spark induced bubbles, plexiglas plates incorporating the stream-lined electrodes were used. Results using the Dynafax camera were obtained both before and after modifications were made to the venturi to produce flow parallel to the wedge. With the unmodified venturi, the flow streamlines (Fig. 2.6)

were not parallel to the wedge. In addition, flow separation occurred either at the exit of the venturi throat, or at the tip of the wedge depending upon the wedge position. In order to obtain negatives of optimum density, focused back lighting was generally used because of the poor light economy of the Dynafax system at high framing rates and short exposure times. With this type of lighting, only the outline of the bubble could be determined, with no information available on the internal contents of the bubble. Fig. 5.15 is a sequence of photographs showing the overall effects of separation at the throat exit, of non-parallel streamlines, and of focused backlighting. Even those bubbles which initially attached themselves to the wedge are seen to move away during the collapse and rebound due to the non-parallel streamlines and separation at the throat exit. The collapse mode of the bubbles attached to the wedge is greatly affected by the large pressure gradient (Fig. 5.17, Curve C) to which the bubbles are subjected as they travel down the venturi diffuser. In all cases, the initial flattening and collapse of the bubbles occurs perpendicular to the pressure gradient. As shown in the typical graphical representations (Fig. 5.16), the initial movement (i. e., bubble path-line) is approximately along the stream-lines of the diffuser. The streamlines are constructed assuming potential flow in a simple diffuser with the streamlines at the walls assumed parallel to the walls (i. e., no flow across the solid boundaries). When the tip of the wedge is encountered, the vertical migration away from the wedge becomes more rapid than the liquid flow along a streamline. Another small increase in the rate of vertical migration away from the wedge is noticed as the bubble collapses and rebounds. This change in migration rate is probably due to both the collapse of the bubble and to the interaction with the separation wake which ends at a position slightly upstream of the position where the bubble reaches minimum volume.

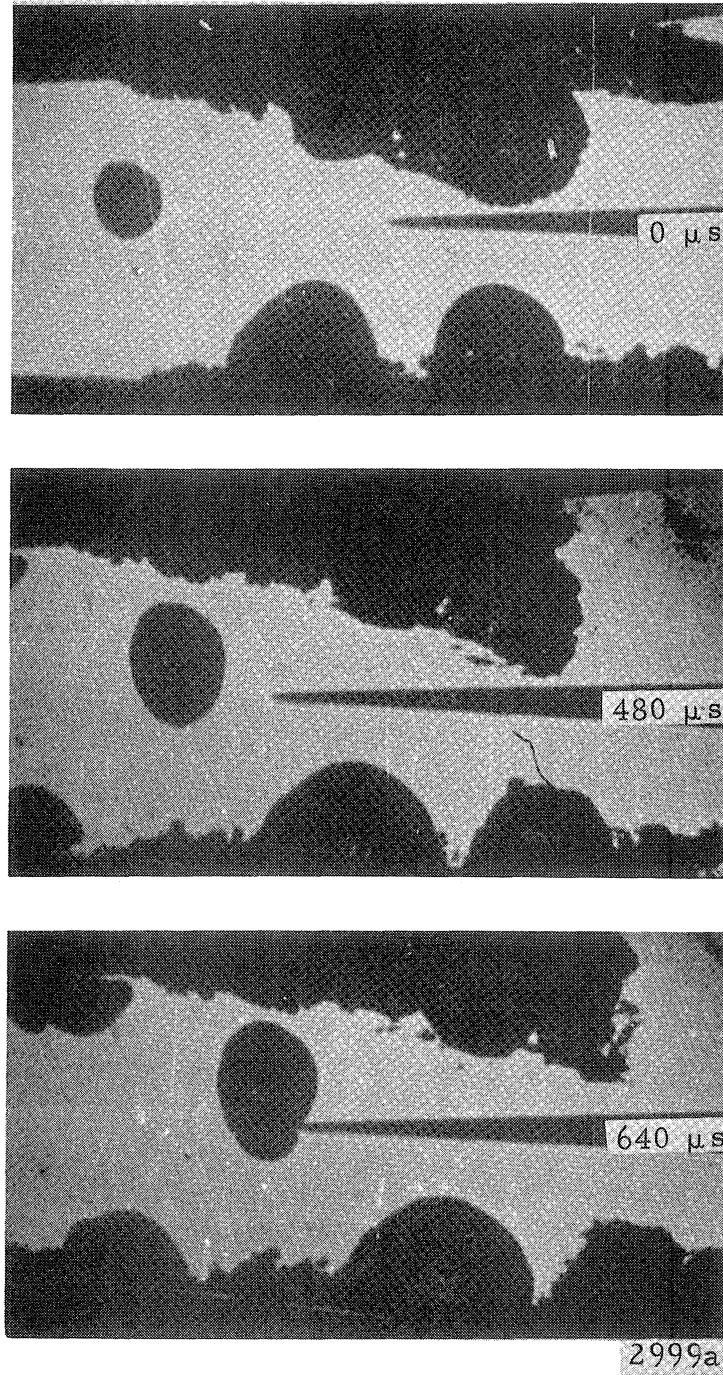
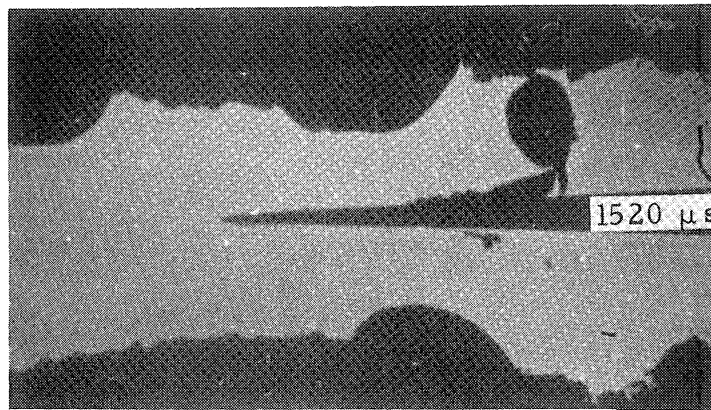
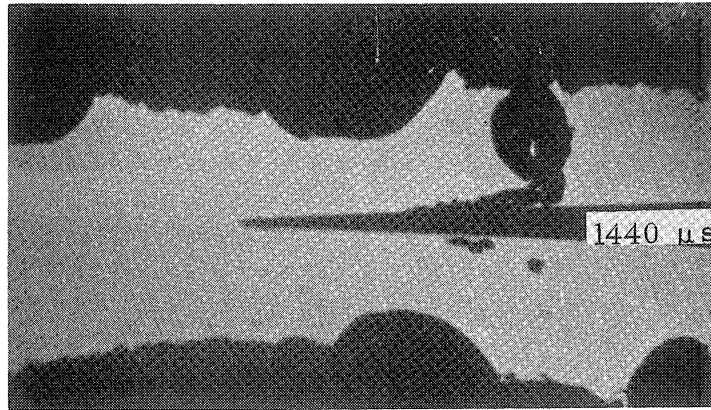
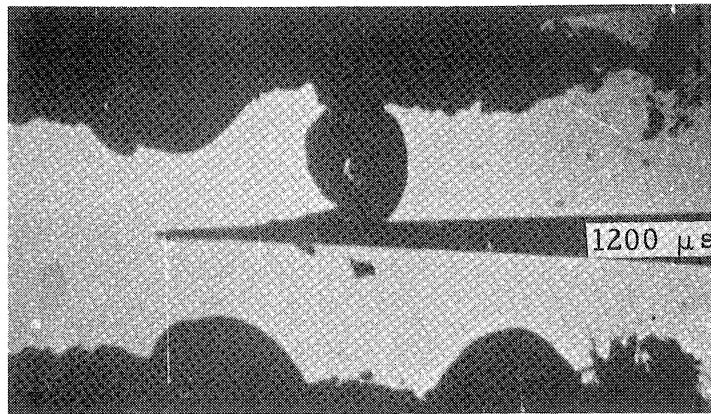
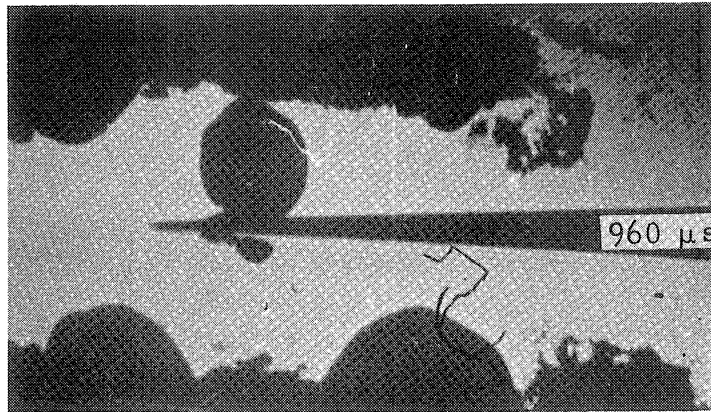


Figure 5.15 Dynafax High Speed Photographs of Natural Cavitation Bubble Collapse in the Unmodified Aluminum Two-Dimensional Venturi. Focused Back Lighting, Time Measured From First Frame,  $1.0 \mu\text{s}$  Exposure/Frame, Fluid Flow  $20.0 \text{ m/s}$  Left to Right, Magnification 2.2. Air Content 0.9%





2999b

Figure 5.15 Continued

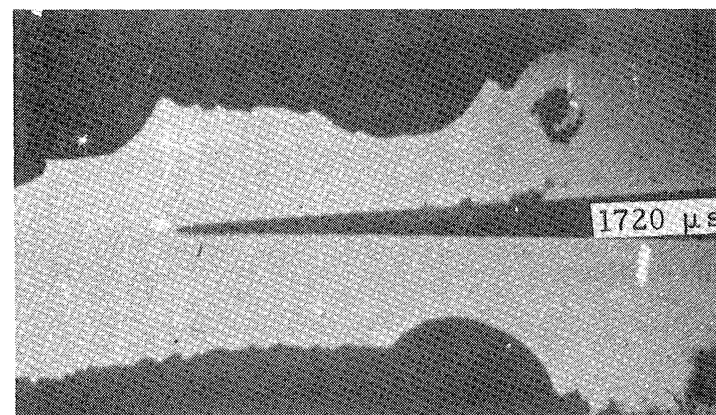
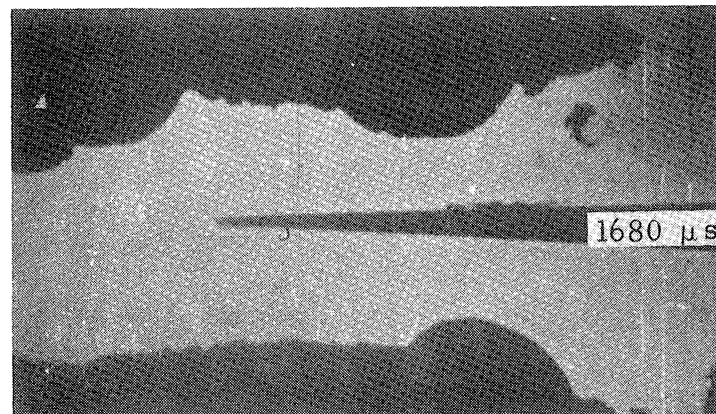
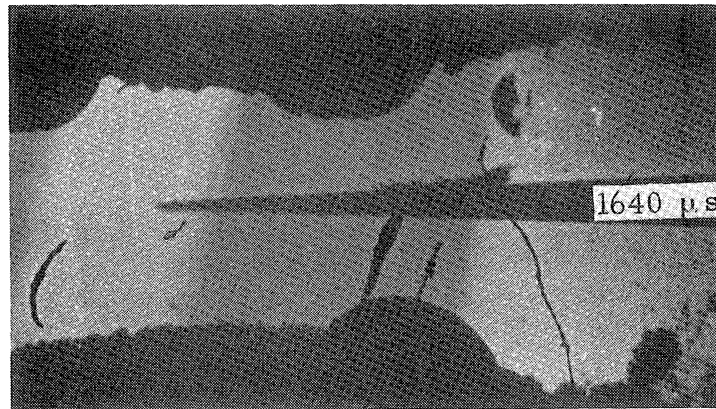
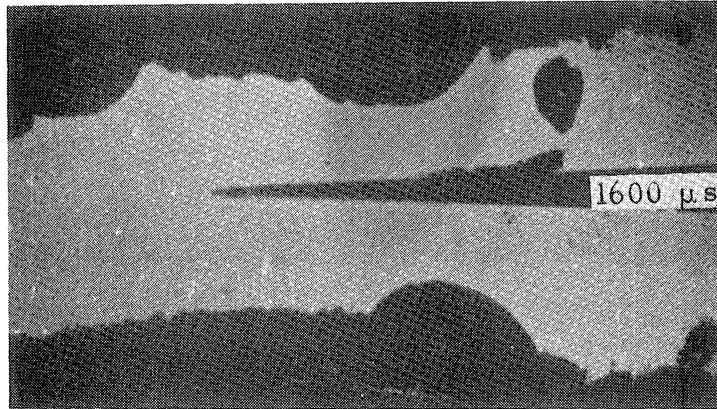


Figure 5.15 Continued

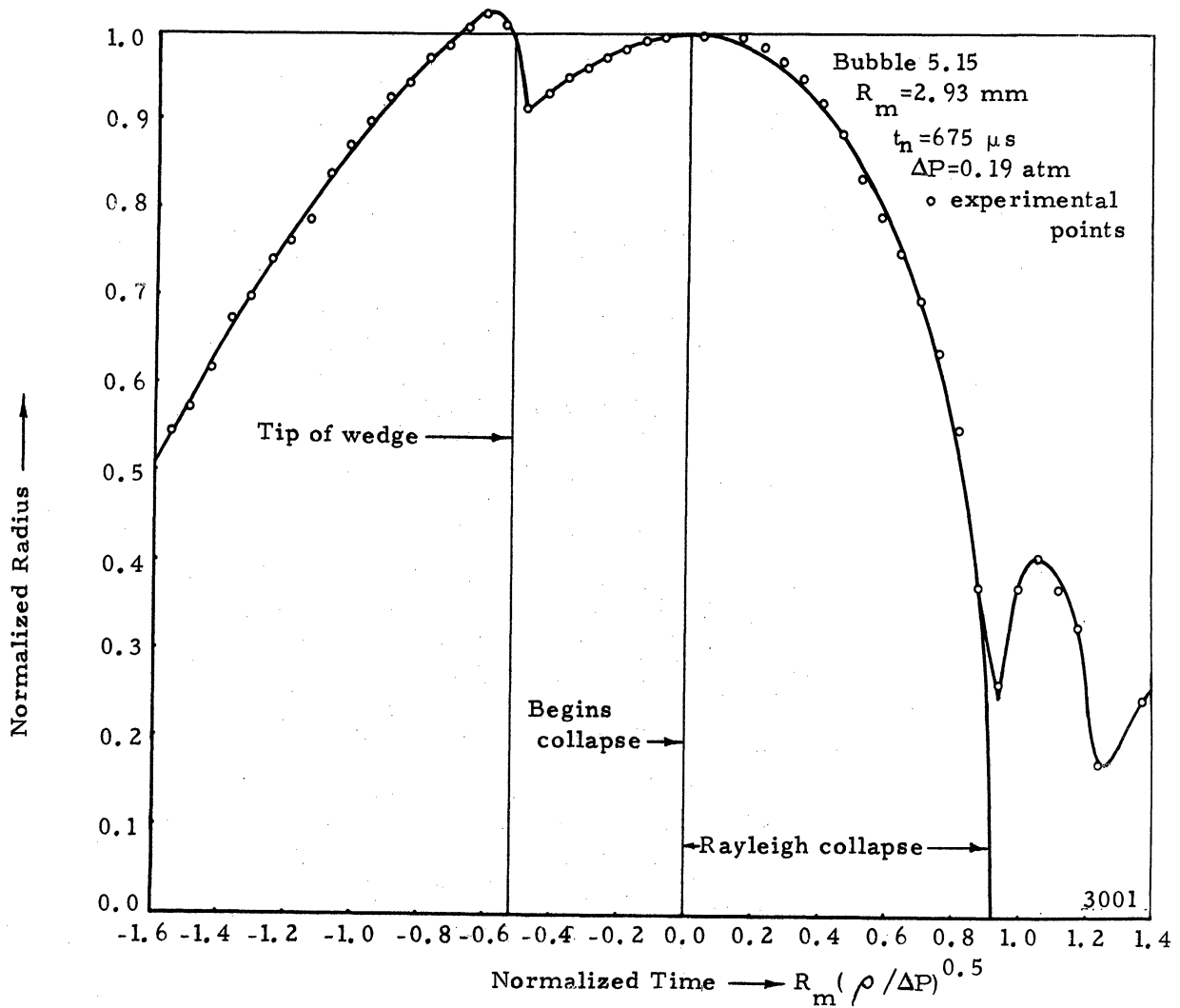


Figure 5.16a Normalized Radius vs. Normalized Time for the Natural Cavitation Bubble Shown in Figure 5.15

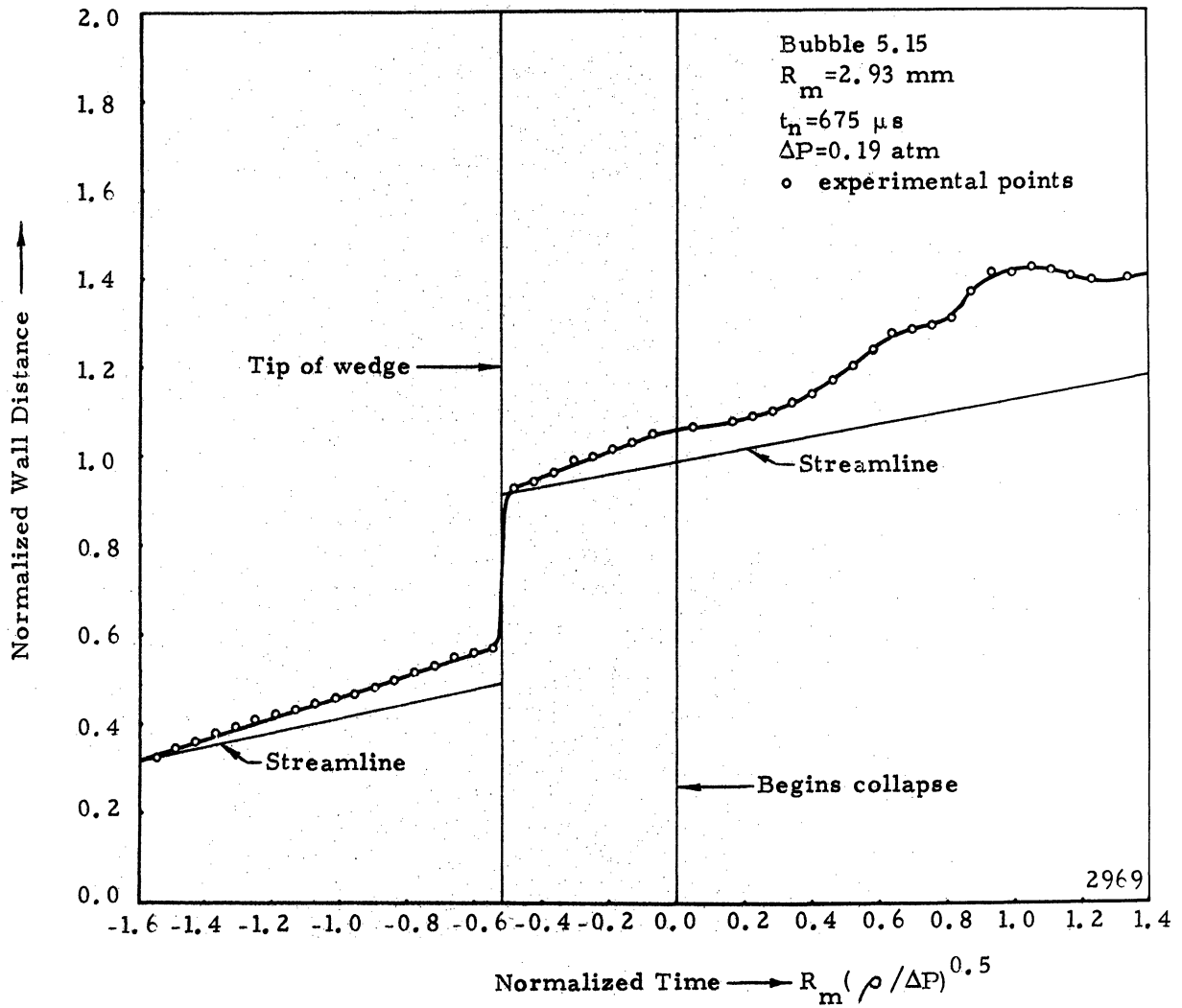


Figure 5.16b Normalized Wall Distance vs. Normalized Time for the Natural Cavitation Bubble Shown in Figure 5.15

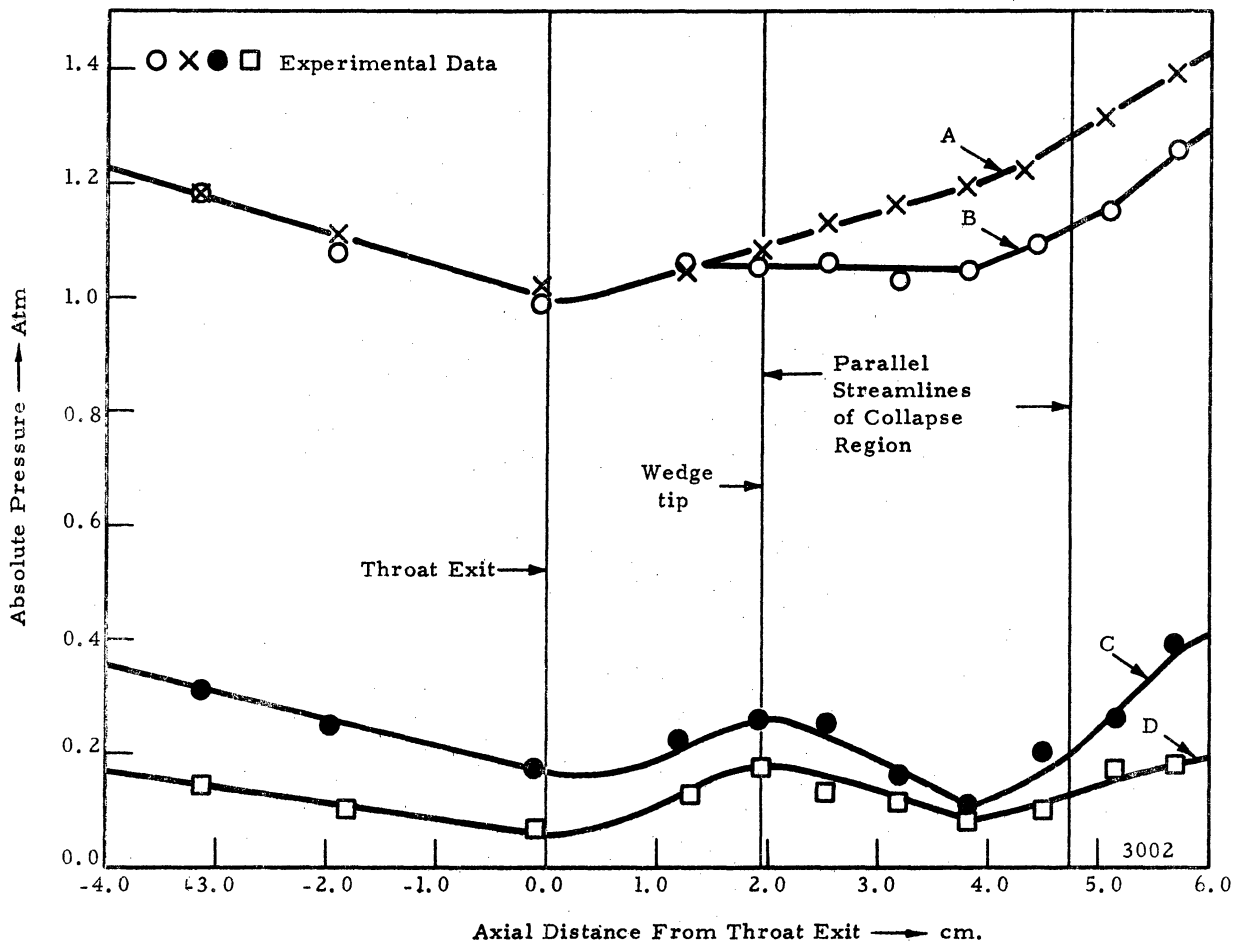


Figure 5.17 Typical Axial Pressure Profiles for the Modified Aluminum Two-Dimensional Venturi with and without the Wedge in Place

Problems of throat separation and non-parallel streamlines were greatly reduced by modifying the venturi so that flow in the diffuser section was initially parallel to the wedge. This modification reduced the initial angle of the diffuser enough so that separation at the throat exit occurred only periodically even when the wedge was withdrawn from the throat exit. Also with the flow parallel to the wedge, there is little pressure gradient to affect the collapse of the bubble. Fig. 5.17 (curves A-D) shows a typical set of axial pressure profiles for the aluminum two-dimensional venturi. Curve A shows the pressure profile used for spark induced cavitation bubble studies without the wedge in the venturi. Curve B shows the relatively flat pressure profile in the collapse region for spark induced cavitation bubble studies with the wedge inserted in the venturi. Curve C shows the pressure profile for natural cavitation bubble studies in the unmodified venturi with the wedge inserted. Curve D shows the pressure profile for natural cavitation bubble studies in the modified venturi with the wedge inserted. For the last two cases the negative slope of the pressure profile in part of the collapse region accounts for some of the problems encountered with stabilizing the cavitation cloud. The lowest pressure in the venturi, where the initial bubble growth occurs, is in the throat section. In order to increase the pressure in the diffuser section so that the bubbles will collapse, the wedge must be withdrawn from the throat exit. From the measured axial pressure profile (Fig. 5.17-Curve D) with the wedge withdrawn its maximum distance of 15mm, the pressure in the collapse region is  $\sim 0.15$  atm. Therefore, the driving pressure collapsing the cavitation bubble is relatively low. Due to the overall dynamics of the water loop, this hydrostatic pressure fluctuates somewhat, causing flow conditions that produce low density clouds which are hard to stabilize. Bubbles would sometimes collapse before reaching the wedge or after leaving the section of the diffuser where the flow streamlines are parallel to the wedge and the pressure

is fairly constant. This flow instability also produced a periodic separation at both the exit of the throat and the tip of the wedge.

Even though the divergent streamlines and separation wake were greatly reduced by the venturi modifications, the flow field set up by the tip of the wedge still greatly affects the bubble collapse. Bubbles leaving the exit of the throat and not directly impinging upon the wedge (Fig. 5.18) are initially repelled by the wedge. Any subsequent attraction produced by the collapse of the bubble is not enough to overcome this repulsion. From another point of view, this repulsion by the tip of the wedge results in migration toward the bounding wall of the venturi. A plot (Fig. 5.19) of the bubble collapsing and rebounding in Fig. 5.18 from this point of view shows an initial migration toward the venturi wall away from the wedge, when the tip is encountered. This initial migration results in a greater migration during collapse and rebound than would be expected without the presence of the wedge. Only those bubbles which directly impinge upon the wedge (Fig. 5.20) remain attached to it during collapse and rebound.

Coating the wedge with the 50  $\mu$  thick aluminum foil and subjecting it to the cavitation environment of the modified venturi for a period of ten minutes produced eight pits of the type shown in Fig. 5.21. High speed photographs taken during this period with the Dynafax camera were used to determine an average density of bubbles collapsing near the surface of the wedge. The average bubble density was used to determine the ratio of number of bubbles collapsing near the surface of the wedge to the number of pits produced. This ratio was about  $10^4$  \* so that the random probability of photographing one of the destructive bubbles is very small.

---

\* Confirming other previous observations of this type. (20, 21)



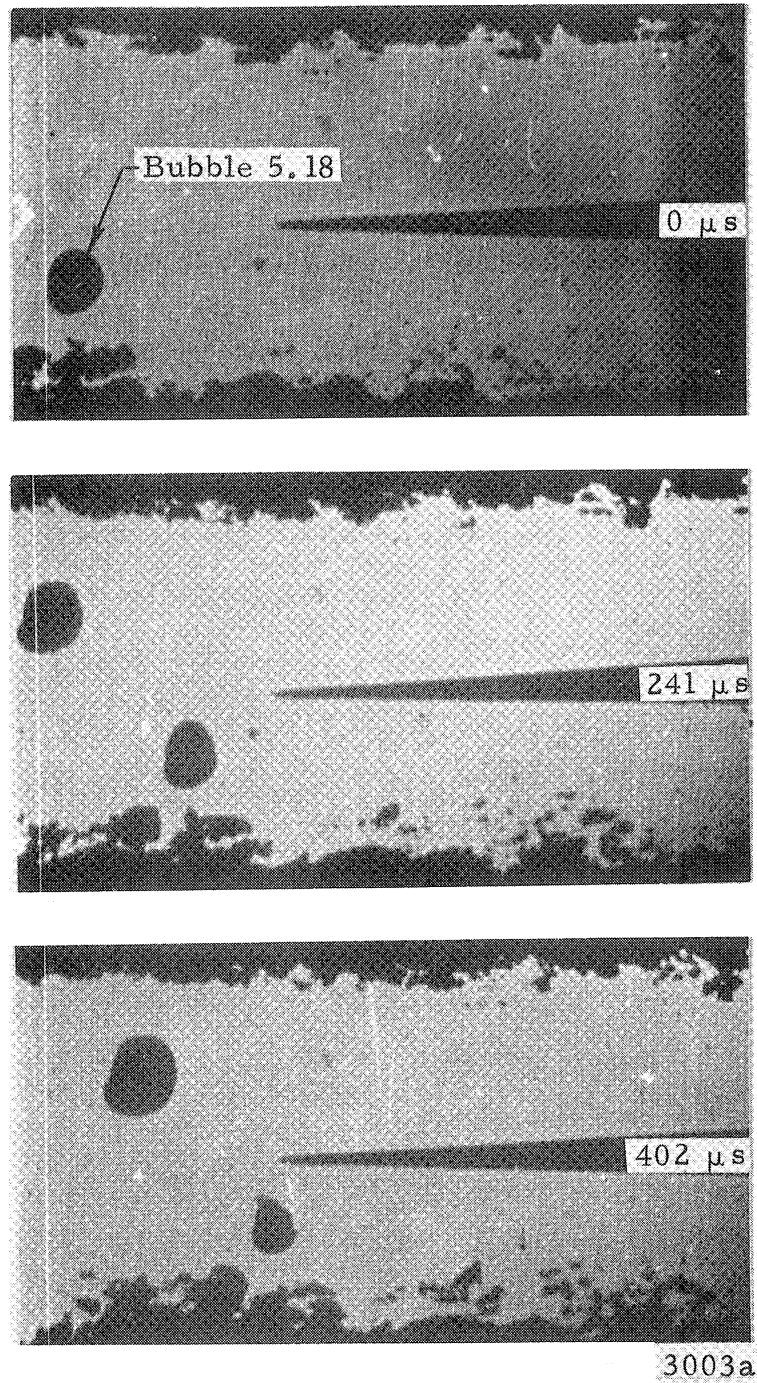


Figure 5.18 Dynafax High Speed Photographs of a Natural Cavitation Bubble Collapse in the Modified Aluminum Two-Dimensional Venturi. Focused Back Lighting; Time Measured from First Frame,  $10 \mu\text{s}$  Exposure/Frame, Fluid Flow  $24.2 \text{ m/s}$  Left to Right, Magnification 2.3. Air Content 1.09%



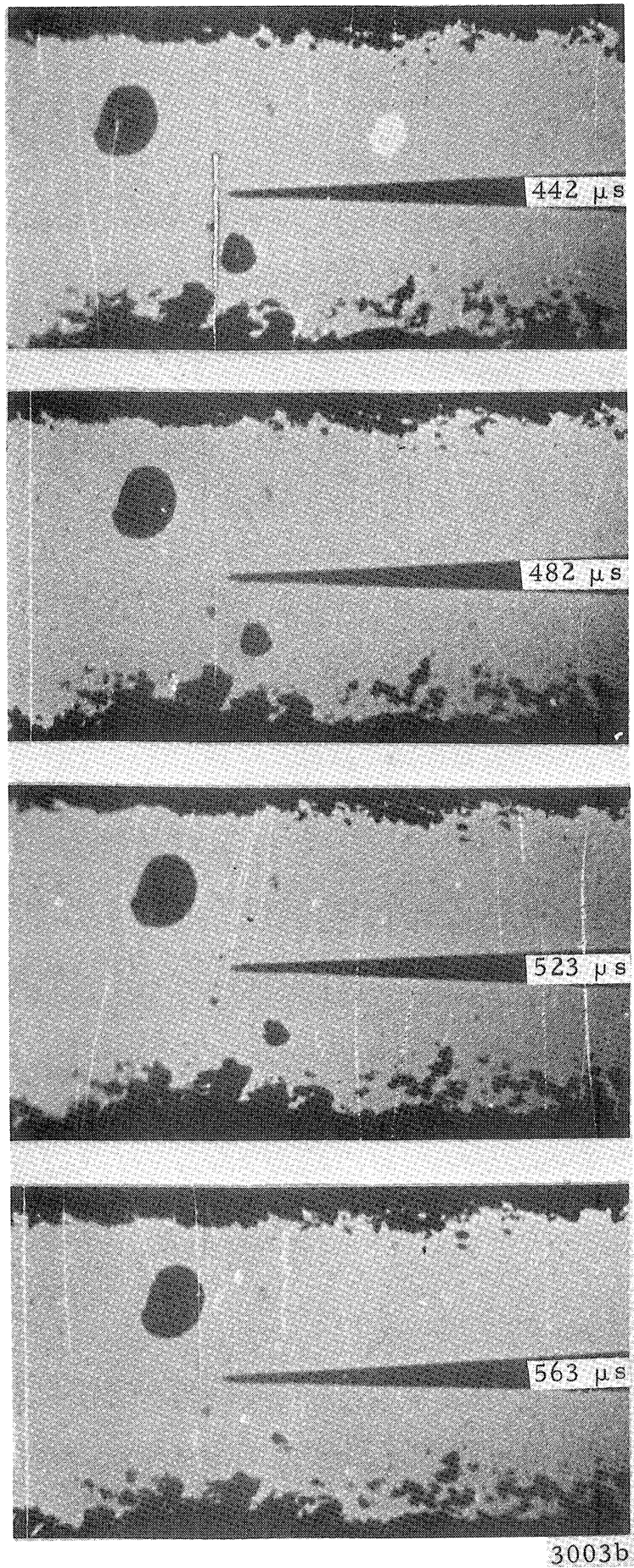
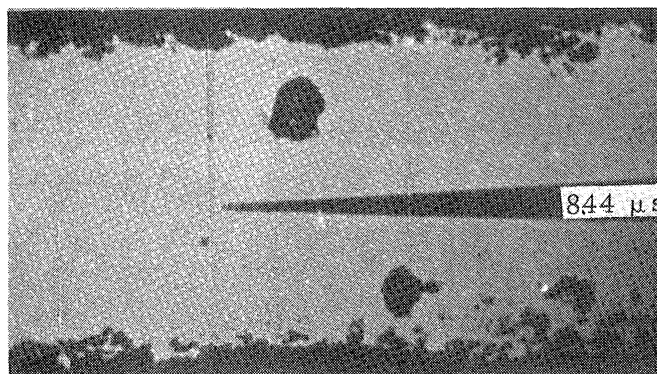
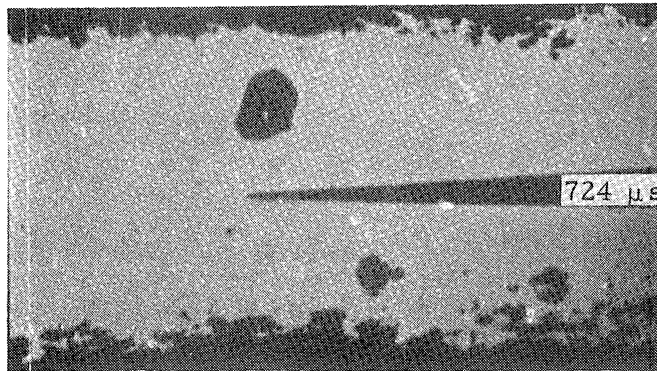
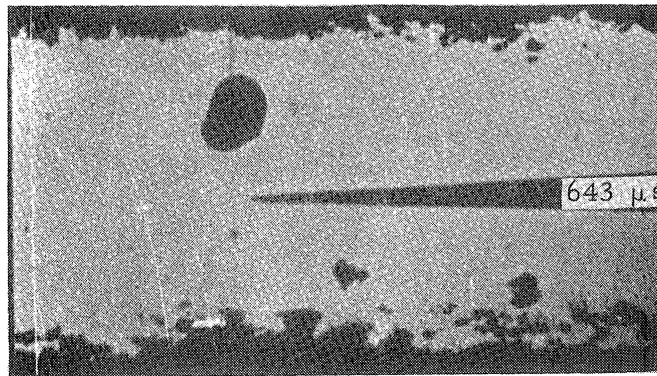
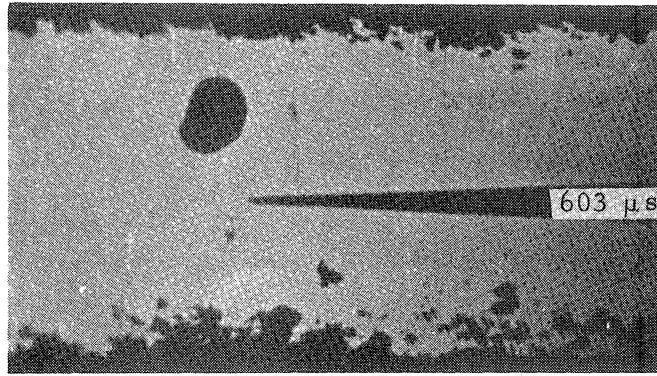


Figure 5.18 Continued



3003c

Figure 5.18 Continued

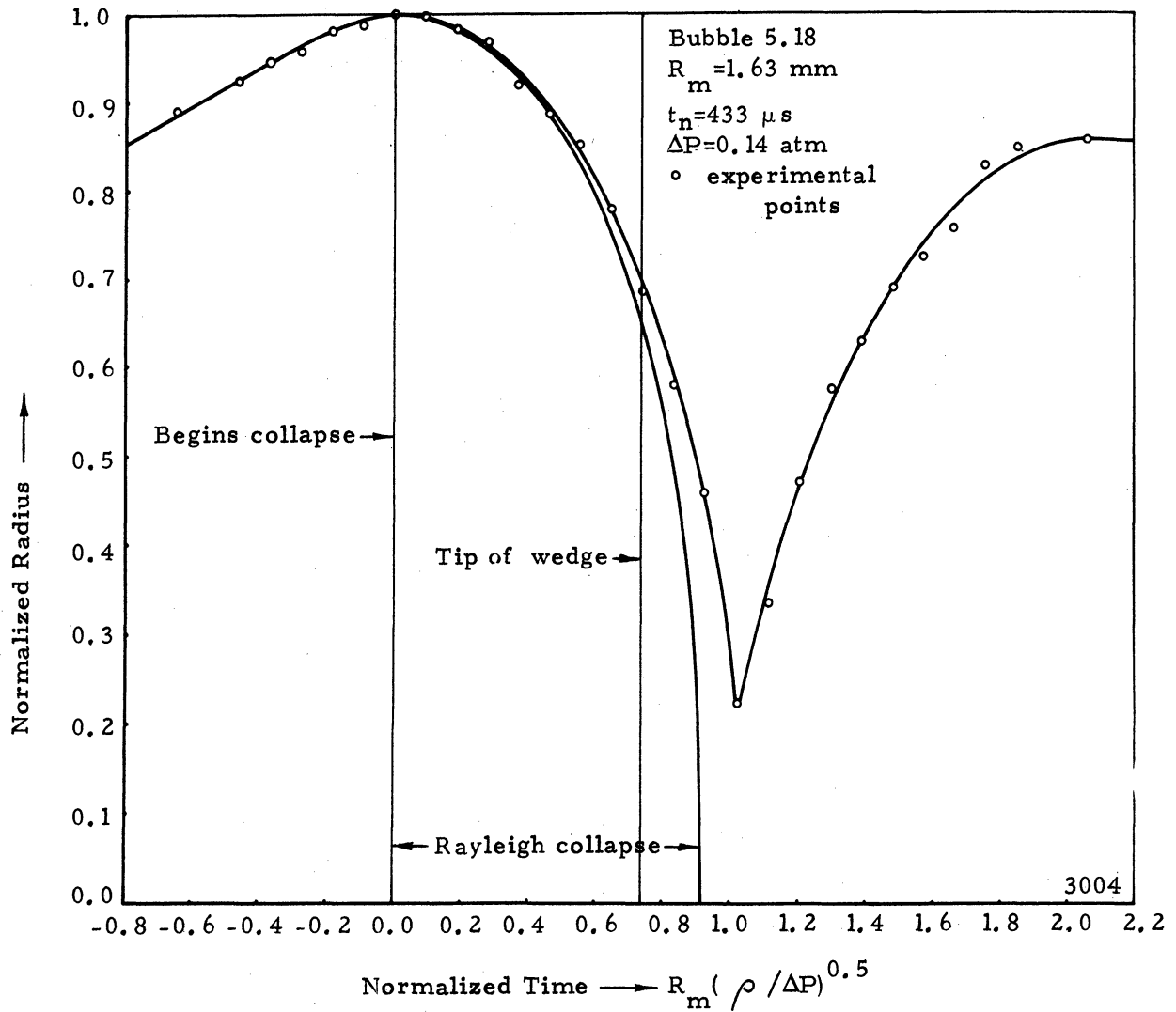


Figure 5.19a Normalized Radius vs. Normalized Time for the Natural Cavitation Bubble Shown in Figure 5.18

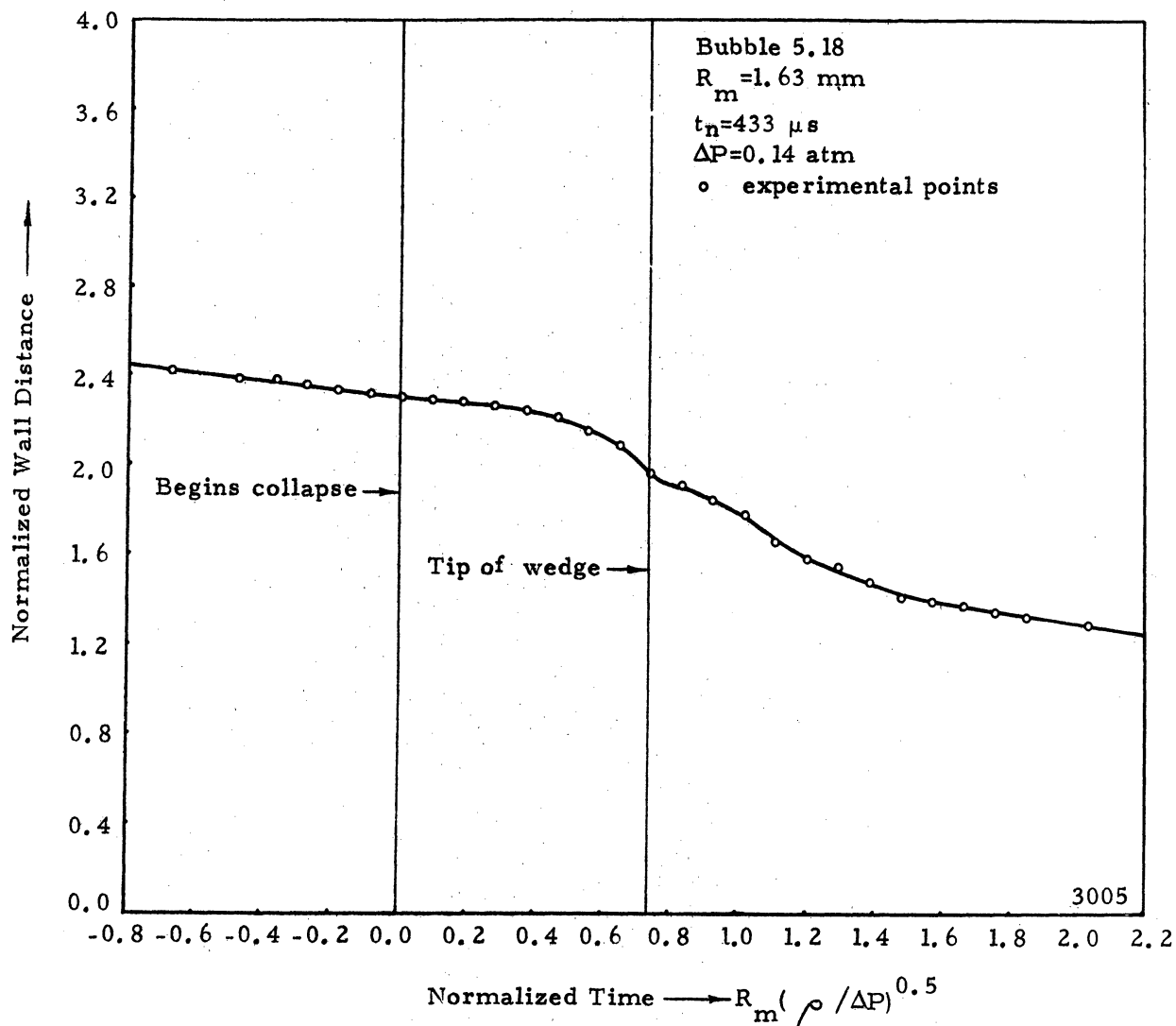


Figure 5.19b Normalized Wall Distance vs. Normalized Time for the Natural Cavitation Bubble Shown in Figure 5.18

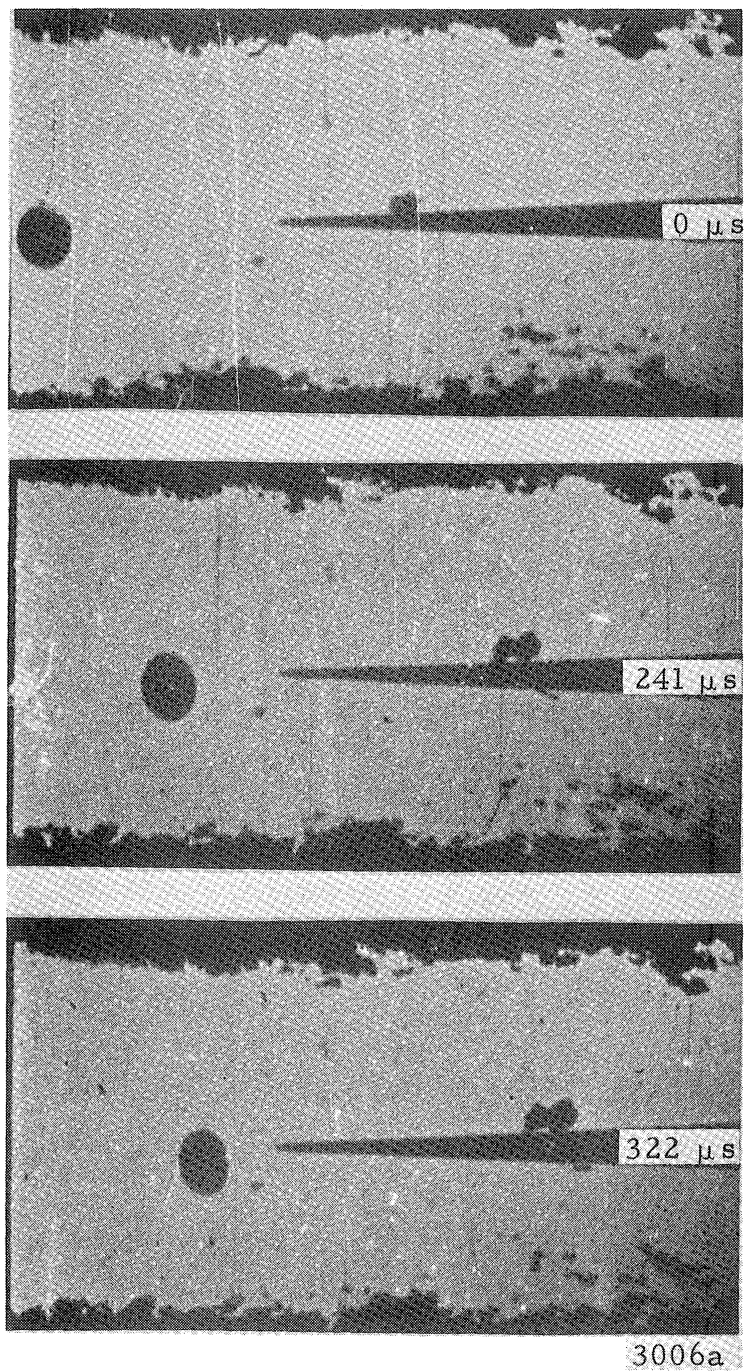


Figure 5.20. Dynafax High Speed Photographs of a Natural Cavitation Bubble Impinging on the Wedge in the Modified Aluminum Two-Dimensional Venturi. Focused Back Lighting, Time Measured from First Frame,  $10 \mu\text{s}$  Exposure/Frame, Fluid Flow  $24.2 \text{ m/s}$  Left to Right, Magnification 2.3. Air Content 1.0%



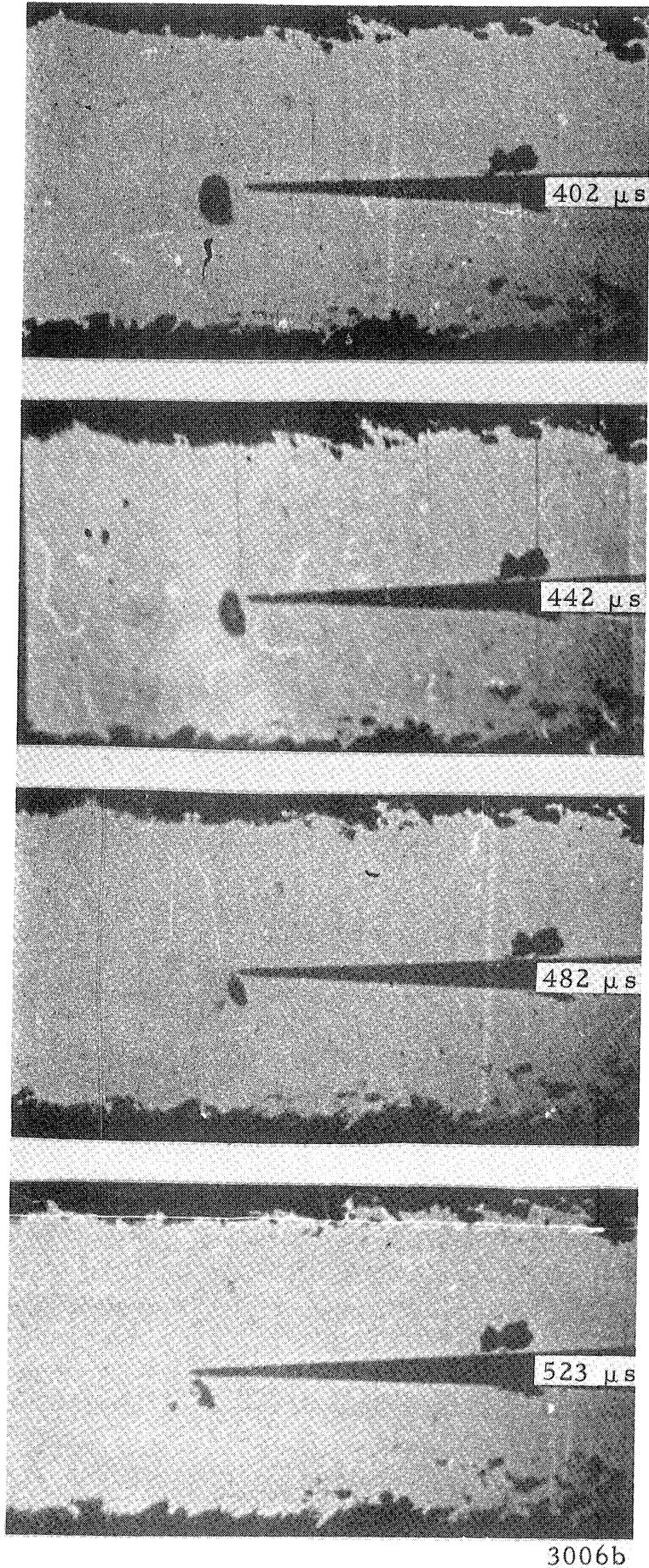


Figure 5.20 Continued

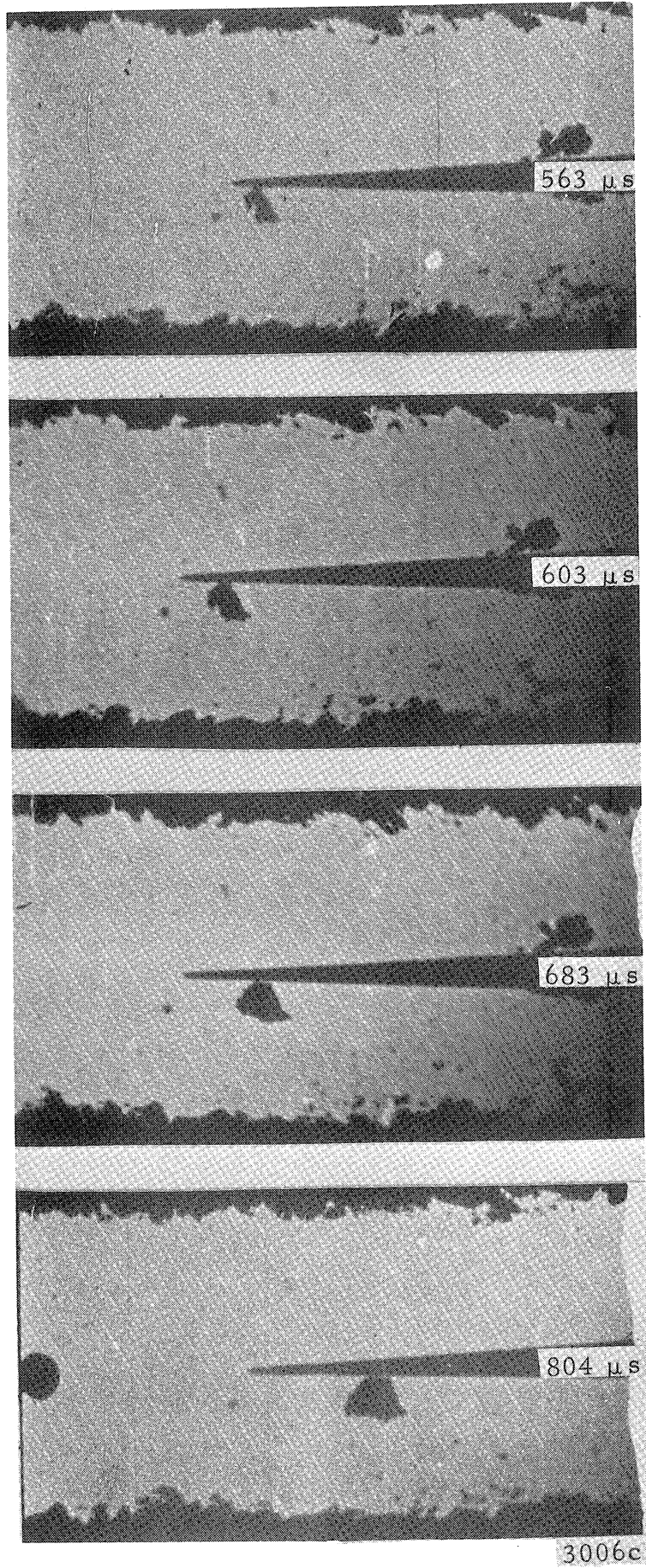


Figure 5.20 Continued

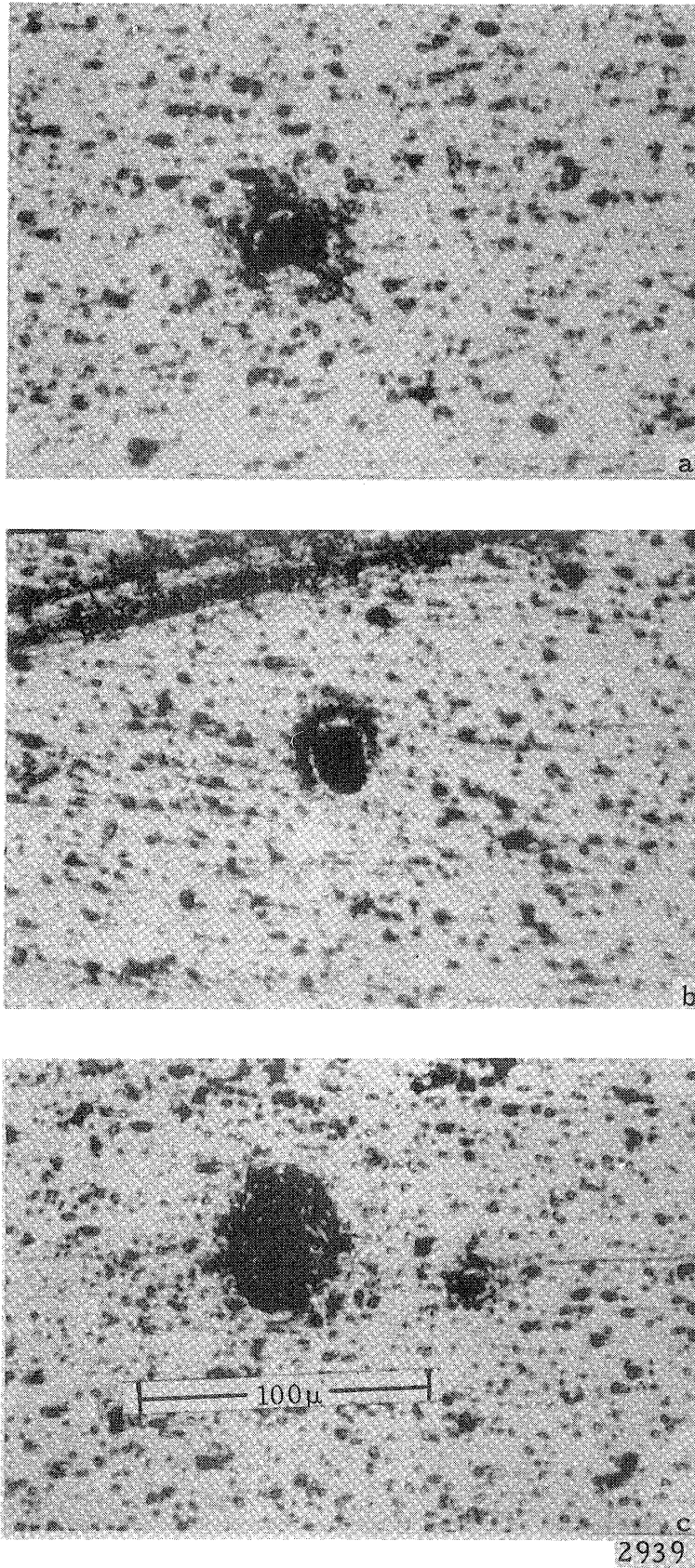


Figure 5.21 Photomicrographs of Natural Cavitation Pits Produced on the 500  $\mu$ , 1100-0 Aluminum Sheet. All Pits are Shown on the Same Scale



The Beckman Whitley Model 330 camera was used to study spark-generated cavitation bubbles in the aluminum two-dimensional venturi. Although attempts were made to use a bubble detector for studies of natural cavitation bubbles with this camera, no usable results were obtained. Spark-generated cavitation bubbles were photographed at a framing rate low enough ( $\sim 10^5$  frames/second) so that the entire bubble lifetime was obtained in one photographic sequence. These photographic sequences were used to obtain information on the bubble lifetime and shape. Then, specific phases of the bubble collapse were studied at much higher framing rates ( $2 \times 10^6$  frames/second maximum) in order to obtain much more detailed information on the bubble size and shape with respect to time. This type of study is possible because the spark bubble generator can produce bubbles nearly identical in space and time in a repeatable fashion. The resulting figures and graphs are made more concise by combining the information for each type of nearly identical bubble into one data set. In this way, one figure or graph shows the bubble through its entire lifetime with increased temporal resolution in the critical collapse stages.

Without the wedge in the venturi, an axial pressure gradient (Fig. 5.17-Curve A) is present which affects the collapse of the spark-induced cavitation bubbles (Fig. 5.22).<sup>\*</sup> The graphs of bubble size vs. time (Fig. 5.23) show the same characteristics as the spark chamber bubbles (Fig. 5.13), i. e., the initial more rapid growth of the bubble due to the spark afterflow and initial high bubble internal pressure and the departure from theory after the minimum volume is reached due to the absence of energy loss mechanisms in the mathematical model. Spark bubble collapses from this type produced the smallest minimum

---

<sup>\*</sup>The heavy black line present in this and other Beckman and Whitney Model 330 sequences is the part of the frame removed for the streak portion of the camera (generally not used during this study).

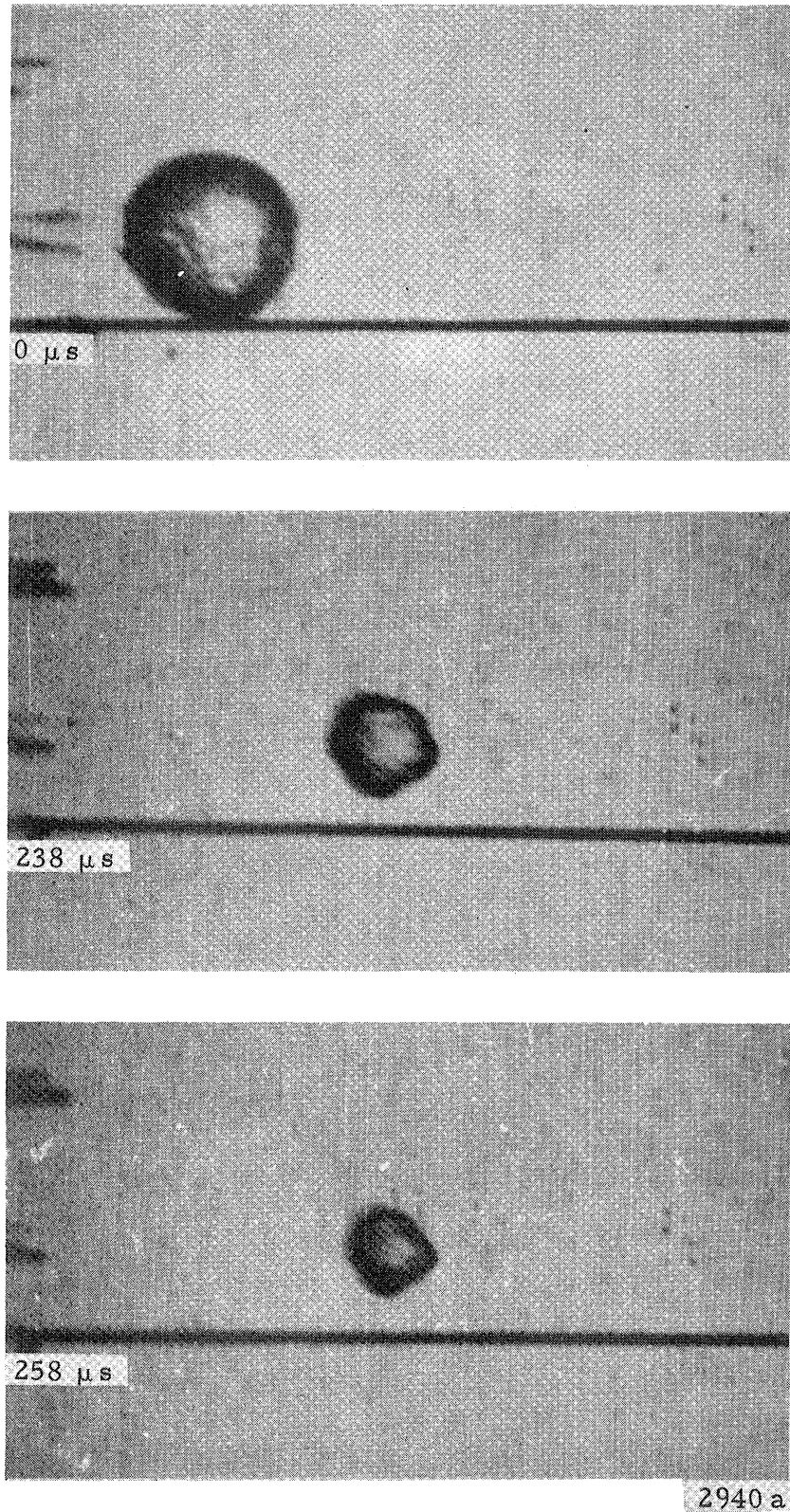
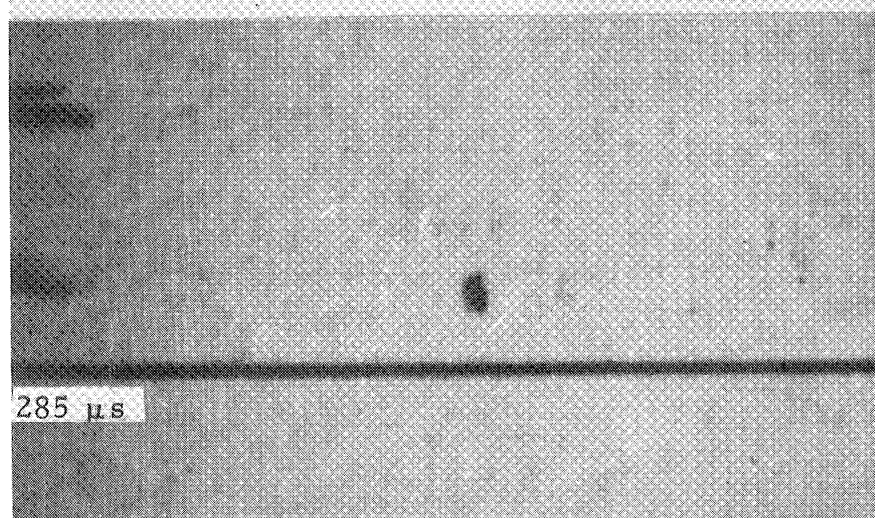
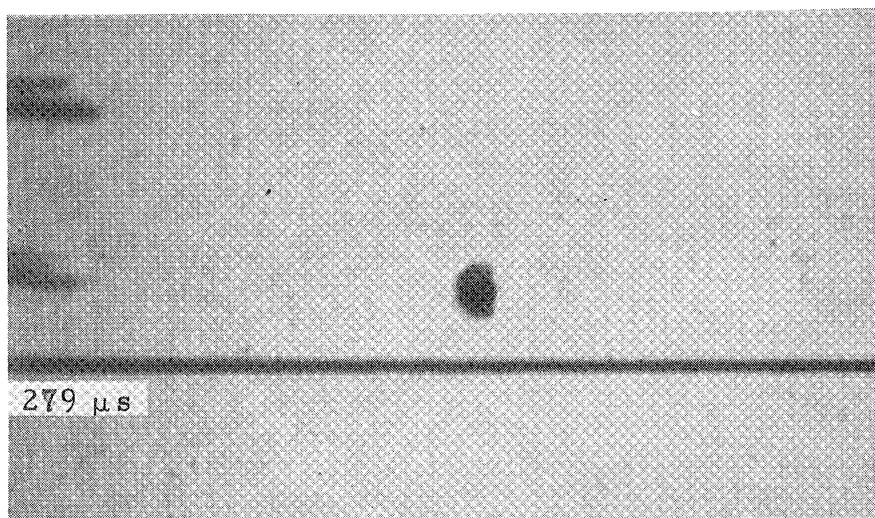
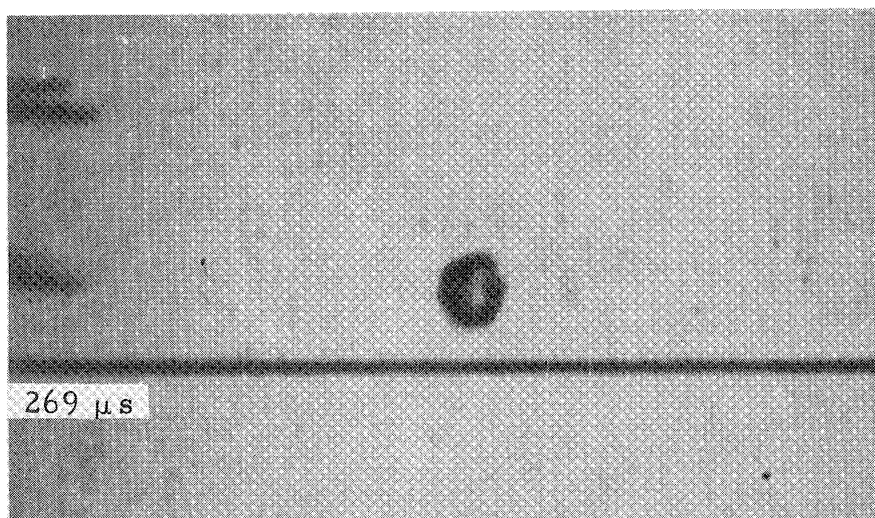


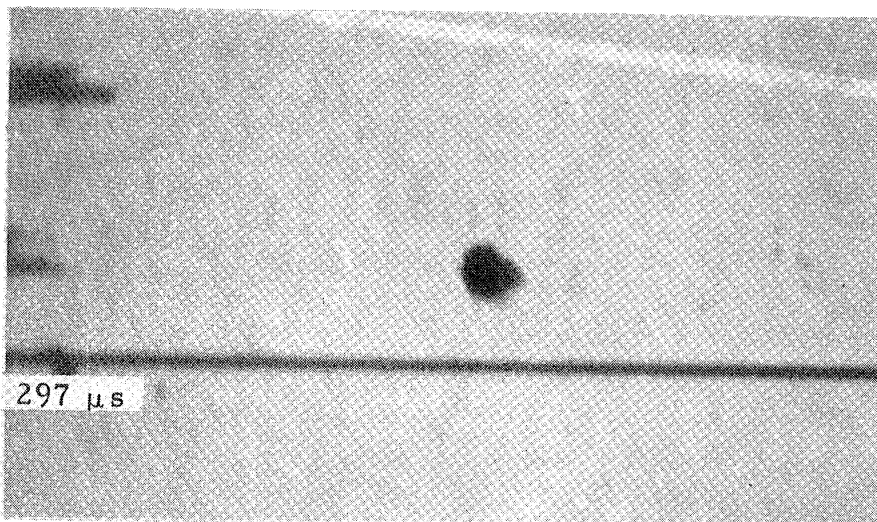
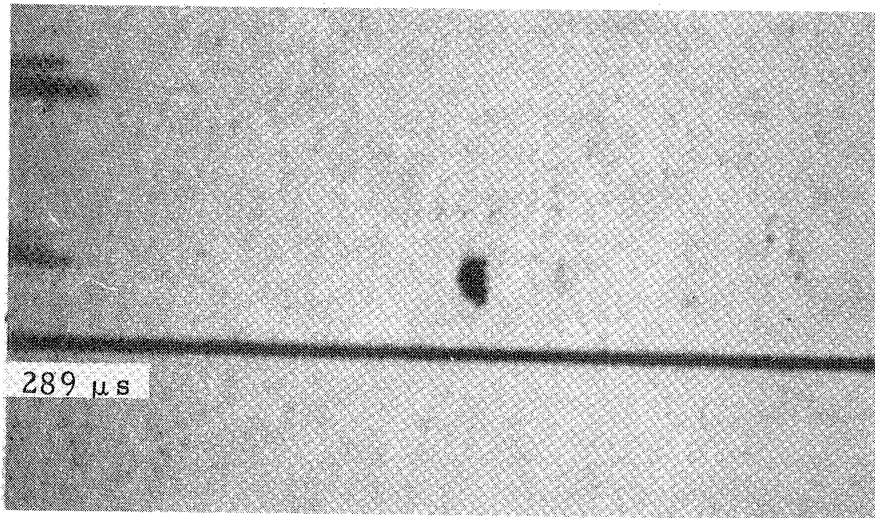
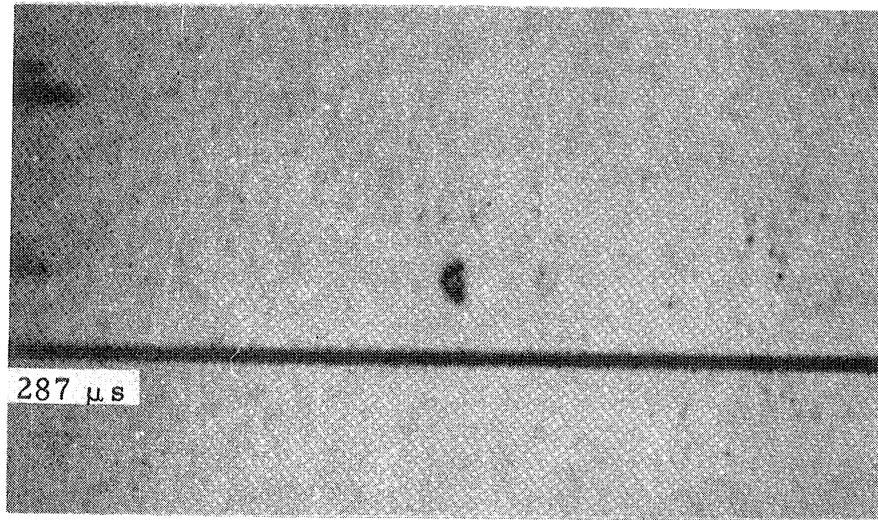
Figure 5.22 Model 330 High Speed Photographs of a Spark Induced Cavitation Bubble Collapsing in the Modified Aluminum Two-Dimensional Venturi without the Wedge Present. Diffuse Back Lighting, Time Measured from First Frame,  $2.0 \mu\text{s}$  Exposure/Frame, Fluid Flow  $24.7 \text{ m/s}$  Left to Right, Magnification  $6.1$ . Air Content  $0.7\%$



2940 b

Figure 5.22 Continued





2940 c

Figure 5.22 Continued

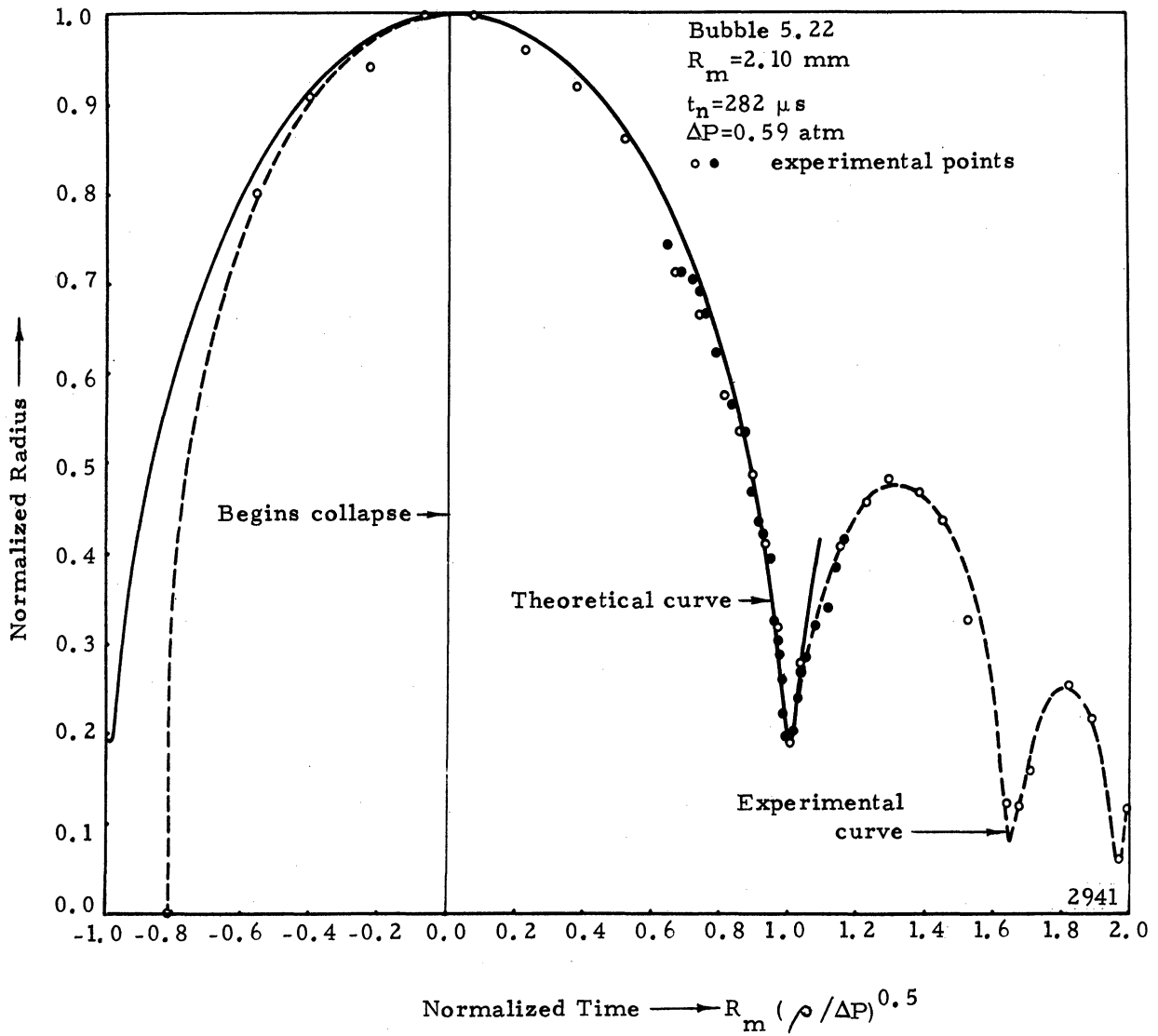


Figure 5.23 Normalized Radius vs. Normalized Time for the Spark Induced Cavitation Bubble Shown in Figure 5.22

radii ( $R_o = 0.081 R_m$ ) and therefore the highest internal gas pressures. With an external liquid pressure differential to infinity,  $\Delta P$ , of 1.10 atm, and using eq. 4.23, the maximum pressure achieved in the bubble is 750 atm. Although this pressure is marginally high enough to produce damage on the weaker of the aluminum foils used, it is only produced at a large distance from the solid surface, and would be greatly attenuated before reaching this surface. It will be shown that one of the effects of a nearby solid surface is to increase the minimum volume thereby decreasing maximum pressures below even this marginally damaging value. The collapse mode, which produces large asymmetries (eccentricities, eq. 4.2, as high as 0.94), appears similar to predictions of a previous investigation<sup>(9)</sup> of natural cavitation bubble collapse in a pressure gradient. This form of collapse should be compared to previous natural cavitation bubbles (Figs. 5.1 and 5.5) which also appear to be effected more by the pressure gradient than by the nearby wedge.

With the wedge introduced into the diffuser section of the venturi, the effect of the pressure gradient (Fig. 5.1.7-Curve B) on the spark induced cavitation bubbles is greatly reduced. By moving the electrodes relative to the wedge, various forms of spark-induced cavitation bubbles could be produced. Those studied ranged from attached hemispheres ( $b_o = 0$ ) to bubbles that were up to two maximum radii ( $b_o = 2.0$ ) away from the wedge. Fig. 5.24 through 5.35 show several spark induced cavitation bubbles ( $b_o = 0.0$  to 1.62) with their corresponding graphical and theoretical results for comparison. These results show that for a bubble at an initial normalized wall distance,  $b_o > 1.5$  (Fig. 5.24) very little migration occurs toward the wedge during the collapse and rebound of the bubble. As the relative distance between the wedge and bubble is decreased, the

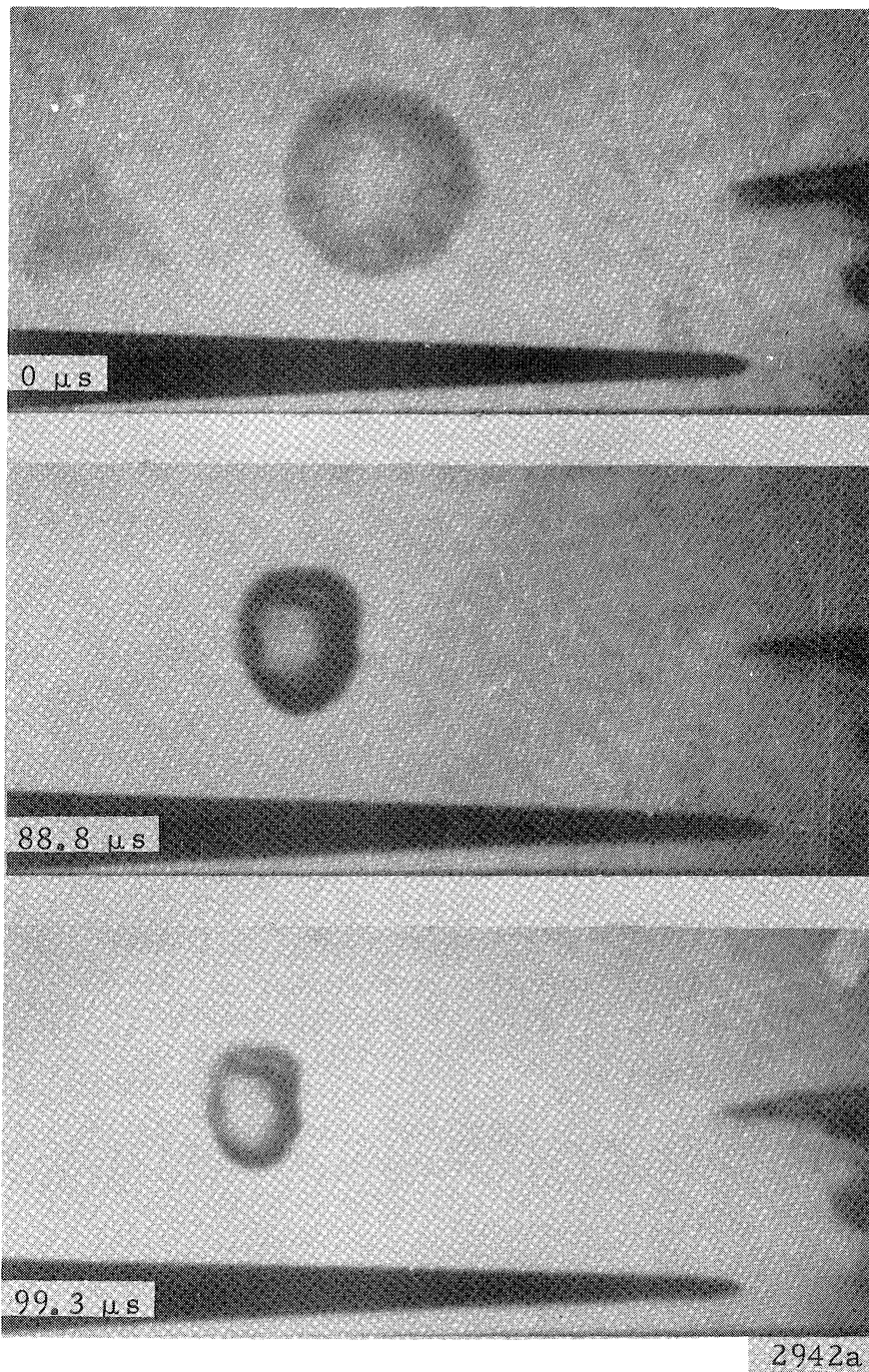
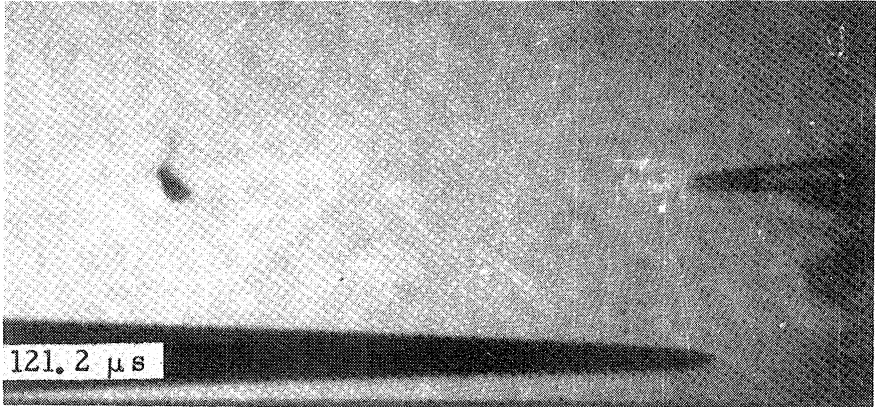
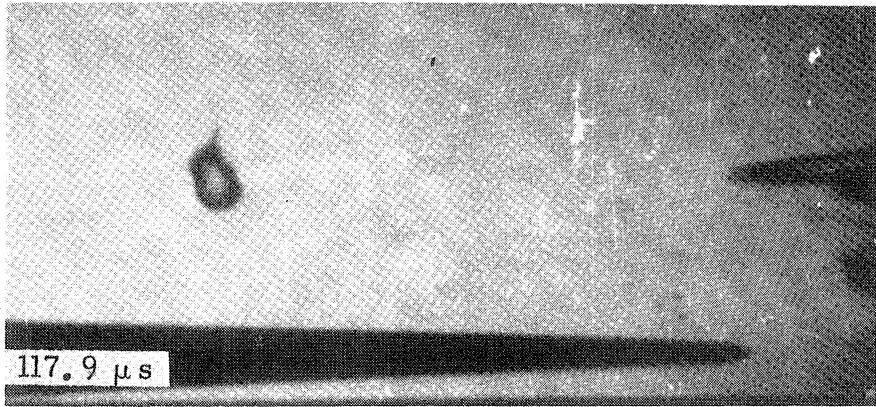
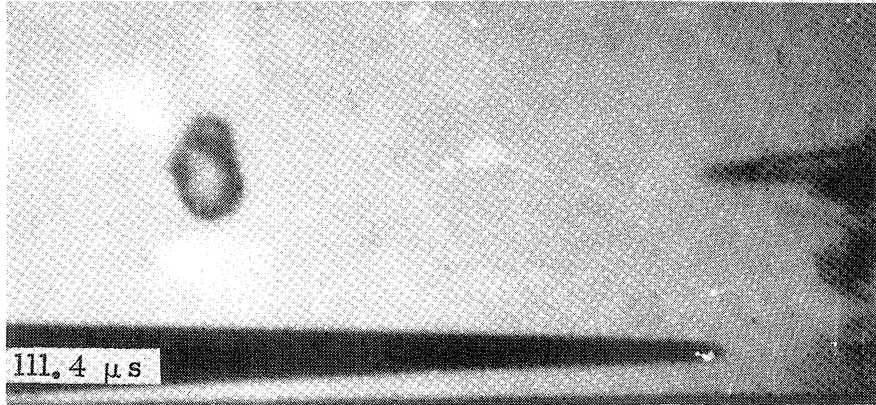


Figure 5.24 Model 330 High Speed Photographs of a Spark Induced Cavitation Bubble Collapsing in a Modified Aluminum Two-Dimensional Venturi. Diffuse Back Lighting, Time Measured from First Frame,  $0.8 \mu\text{s}$  Exposure/Frame, Fluid Velocity  $26.7 \text{ m/s}$  Right to Left, Initial Wall Distance,  $b_0 = 1.62$ , Magnification  $5.0$ . Air Content  $0.8\%$



2942b

Figure 5.24 Continued



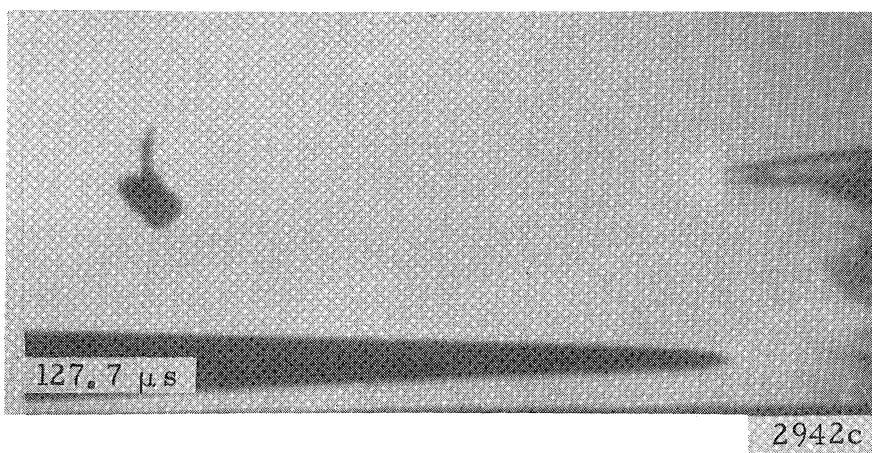
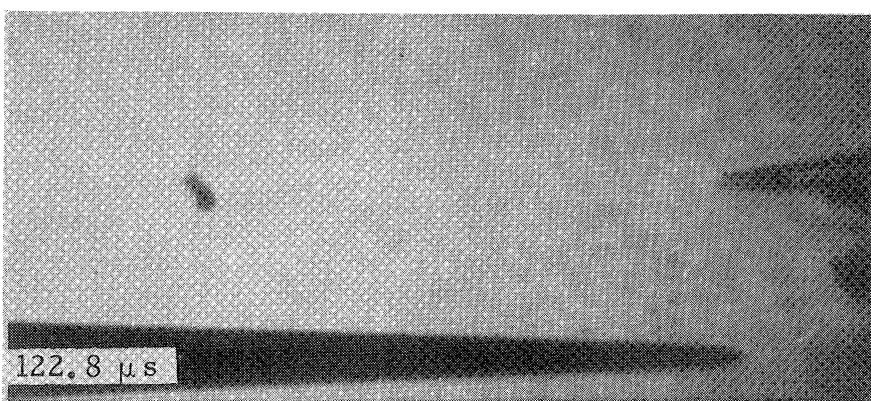
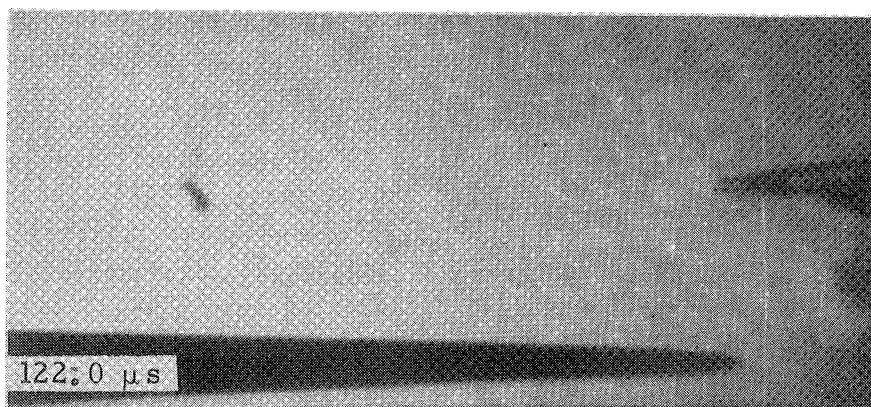


Figure 5.24 Continued

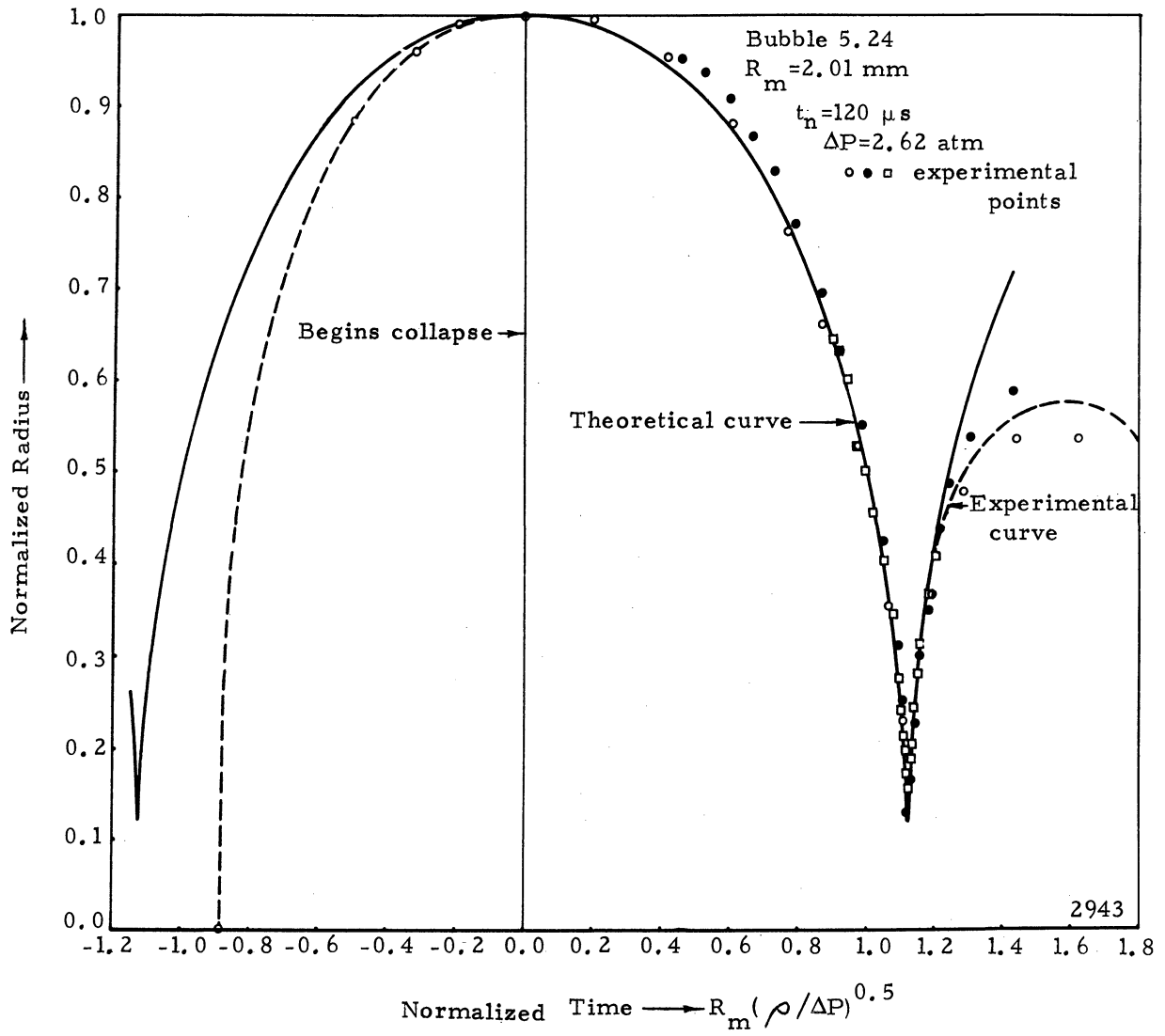


Figure 5.25a Normalized Radius vs. Normalized Time for the Spark Induced Cavitation Bubble Shown in Figure 5.24

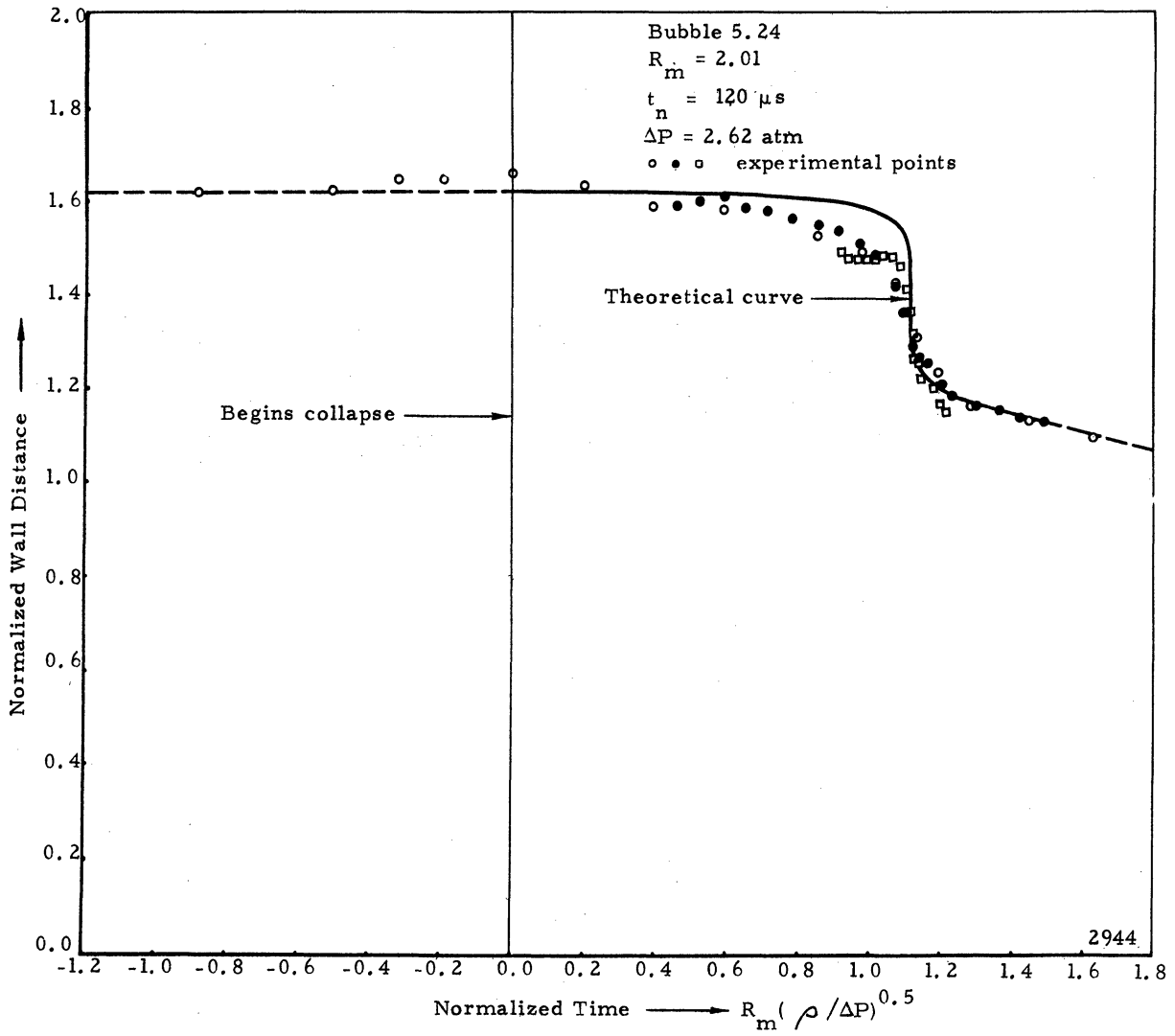
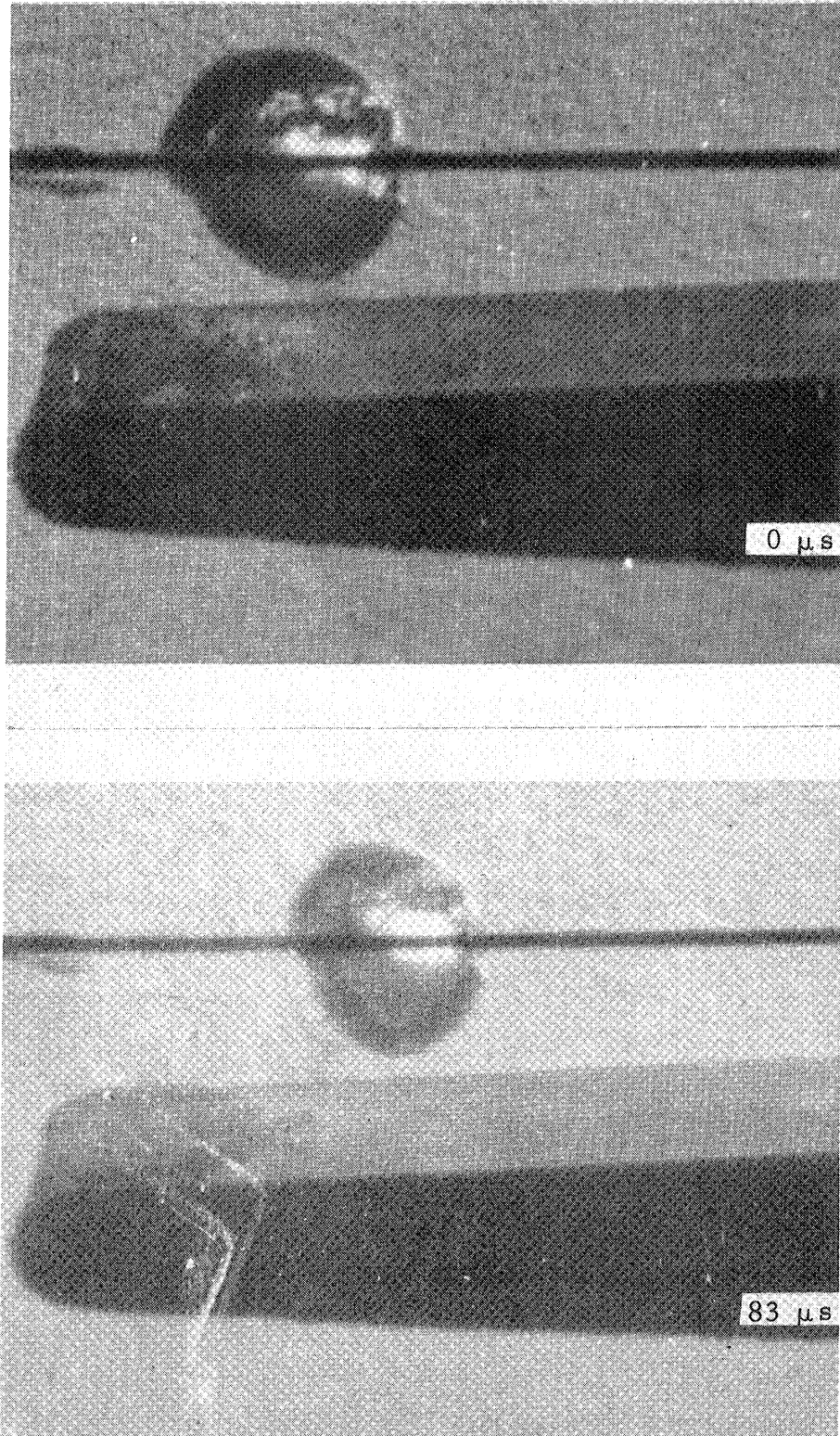
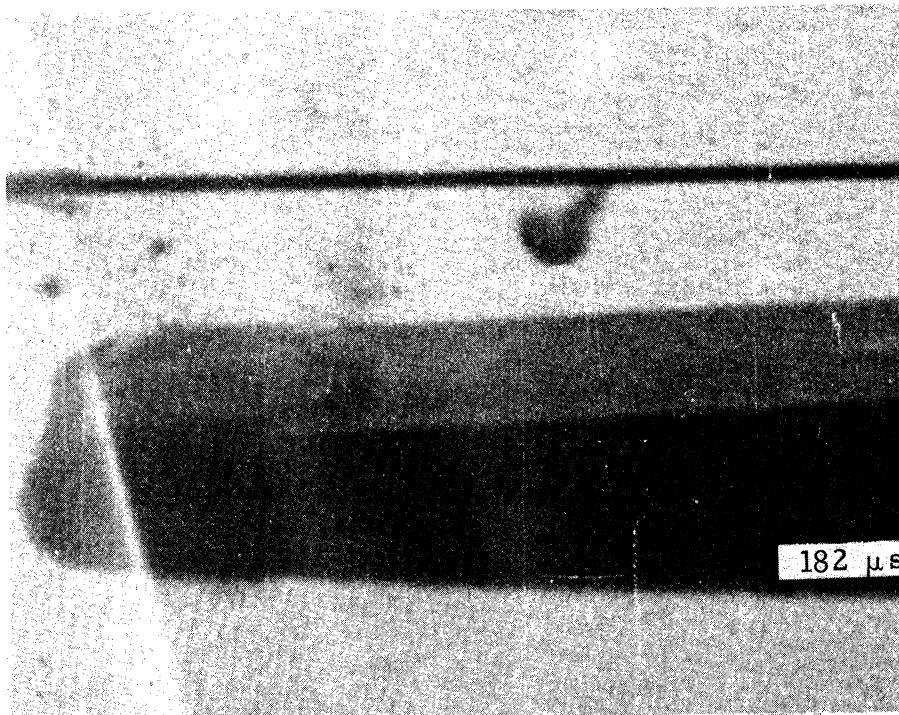
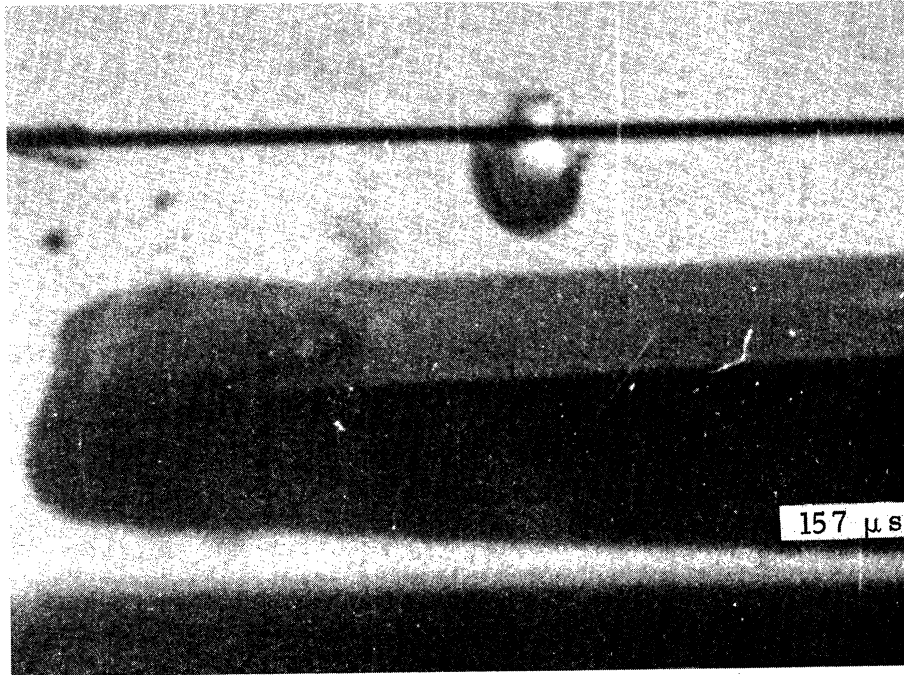


Figure 5.25b Normalized Wall Distance vs. Normalized Time for the Spark Induced Cavitation Bubble Shown in Figure 5.24



2945a

Figure 5.26 Model 330 High Speed Photographs of a Spark Induced Cavitation Bubble Collapsing in the Modified Aluminum Two-Dimensional Venturi, Diffuse Back Lighting, Time Measured from First Frame,  $4.0 \mu\text{s}$  Exposure/Frame, Fluid Velocity  $27.1 \text{ m/s}$  Left to Right, Initial Wall Distance,  $b = 1.40$ , Magnification  $7.0$ . Air Content  $0.7\%$



2945b

Figure 5.26 Continued



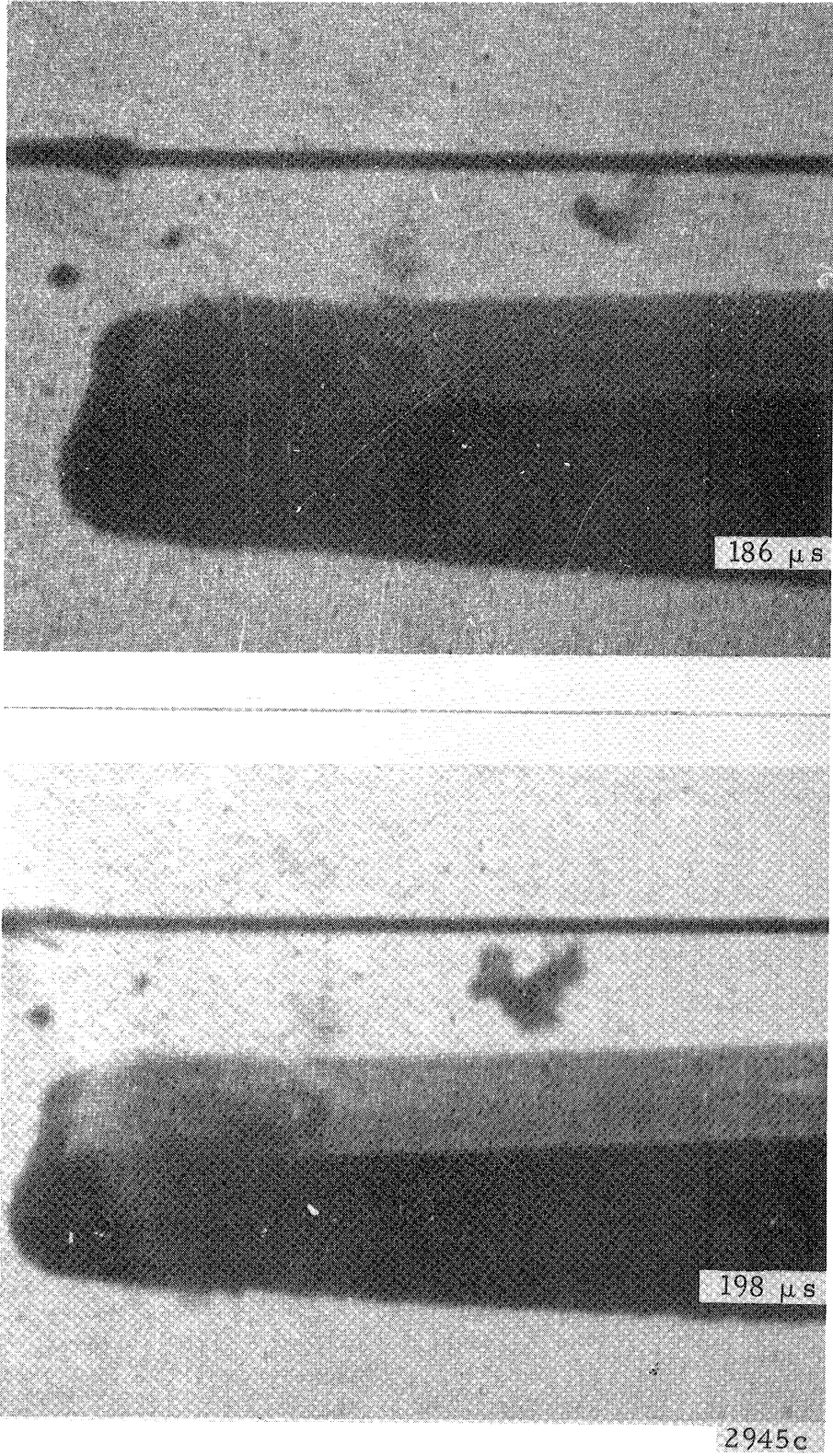
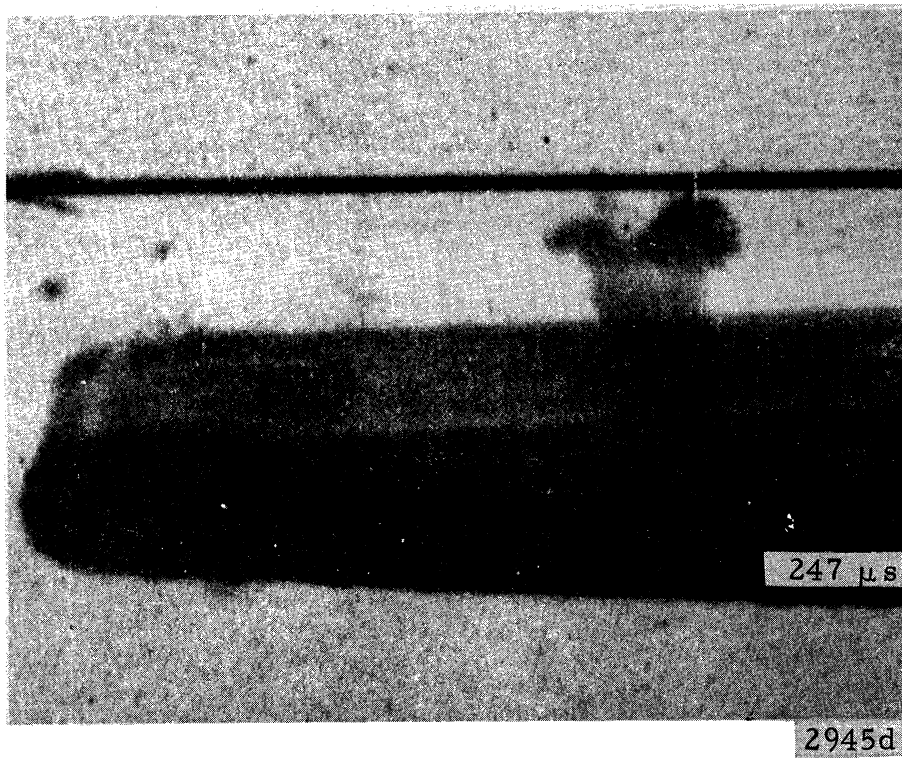
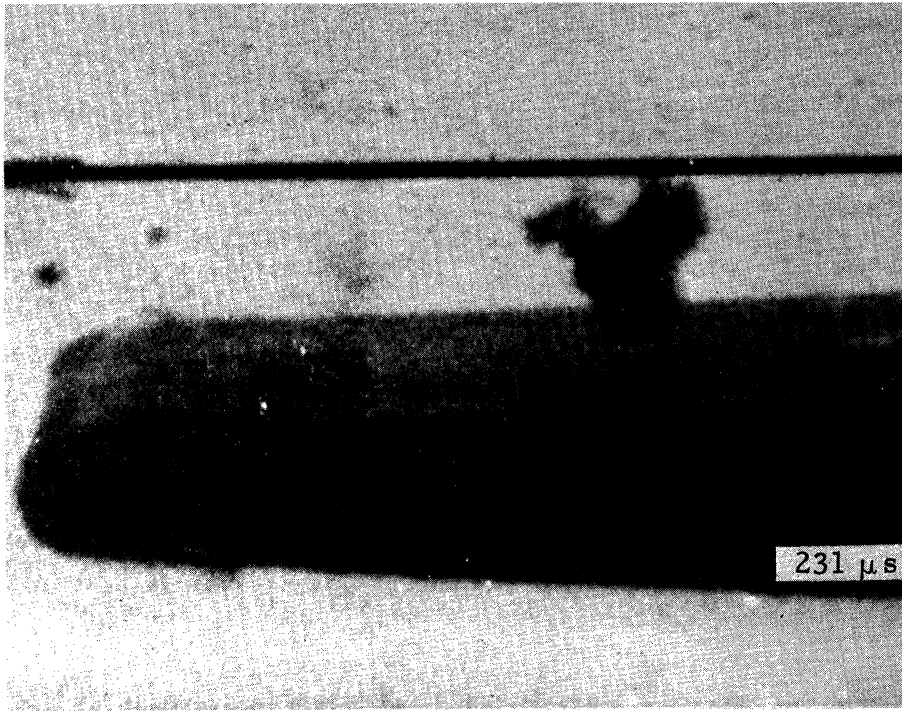


Figure 5.26 Continued



2945d

Figure 5.26 Continued

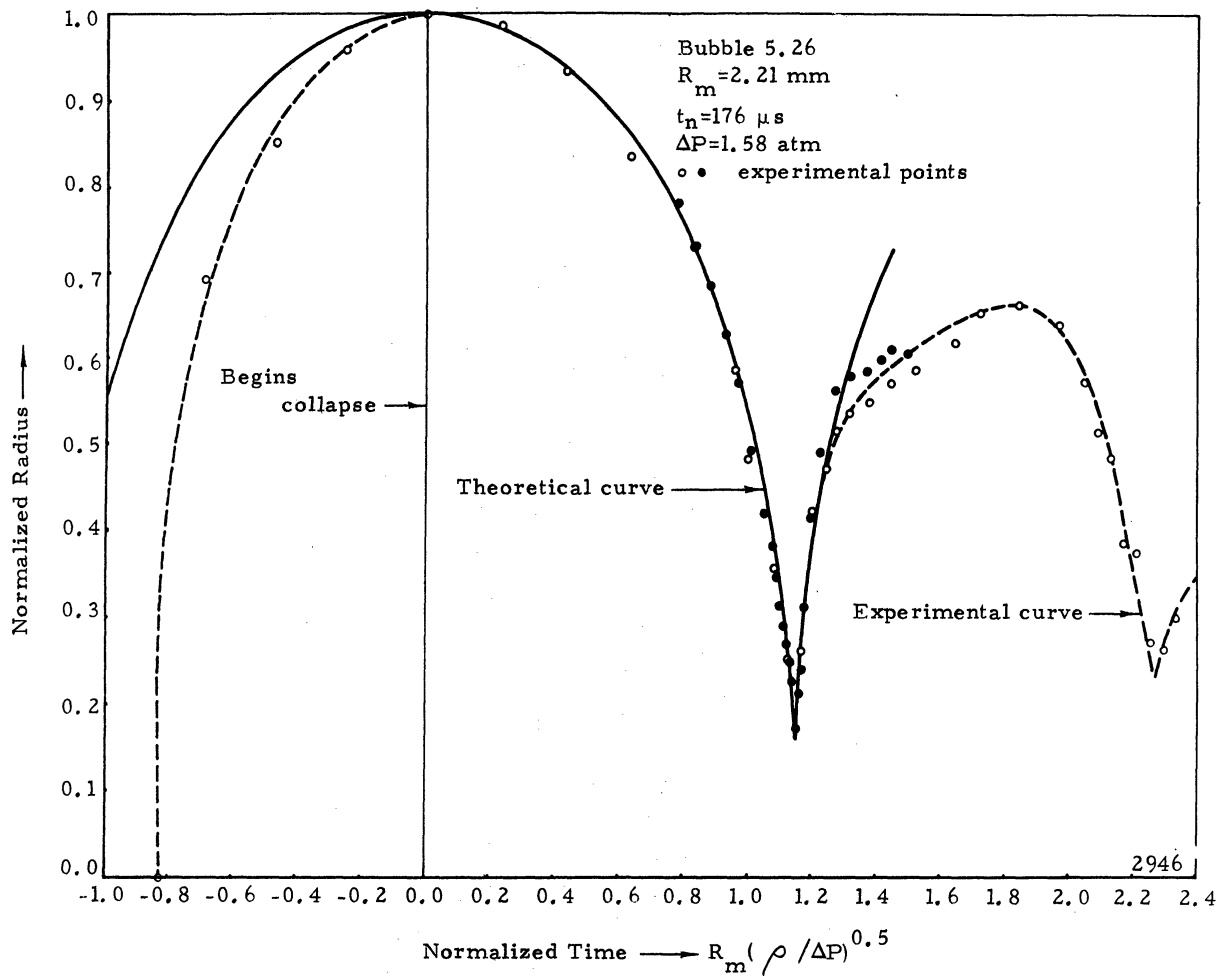


Figure 5.27a Normalized Radius vs. Normalized Time for the Spark Induced Cavitation Bubble Shown in Figure 5.26



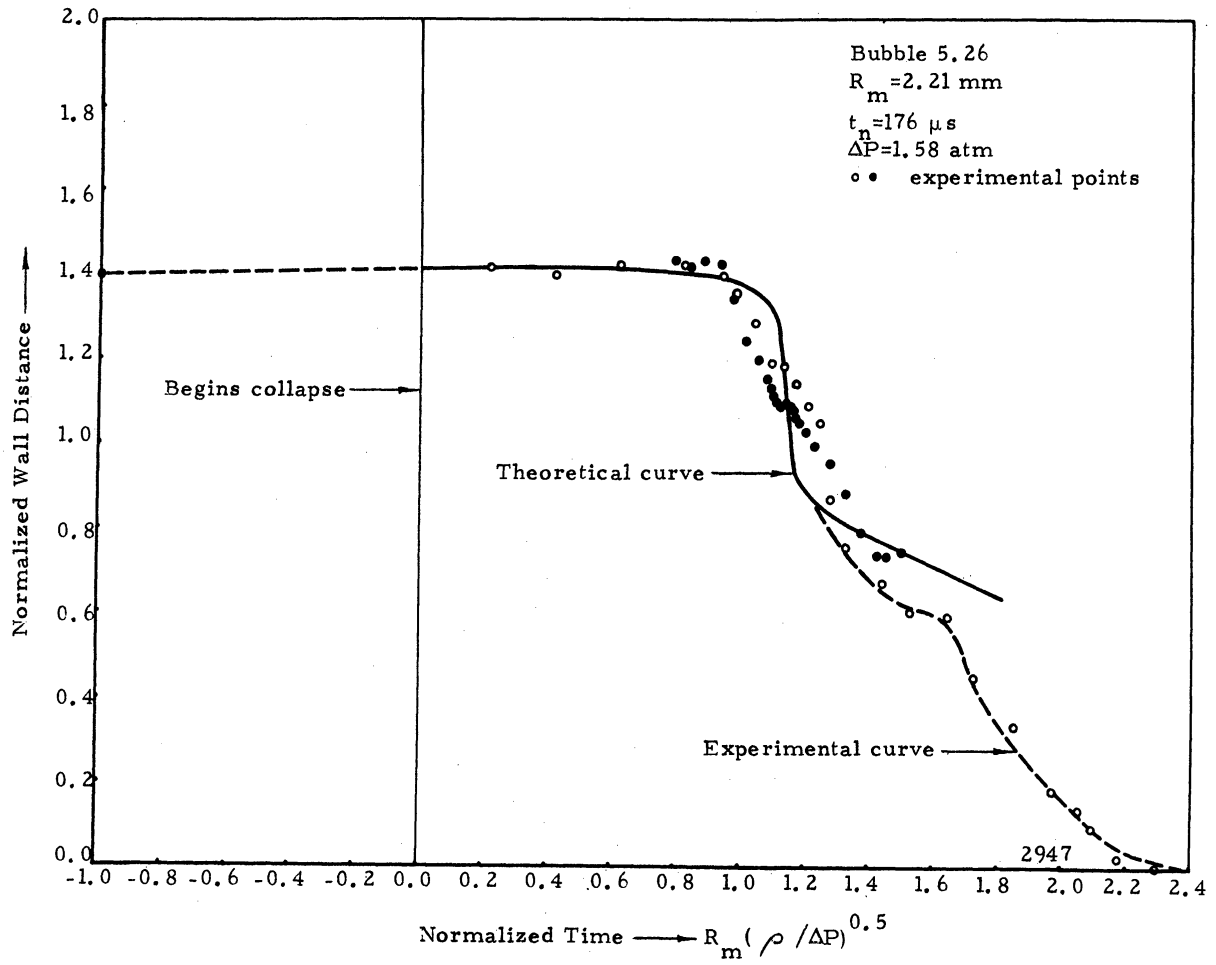


Figure 5.27b Normalized Wall Distance vs. Normalized Time for the Spark Induced Cavitation Bubble Shown in Figure 5.26

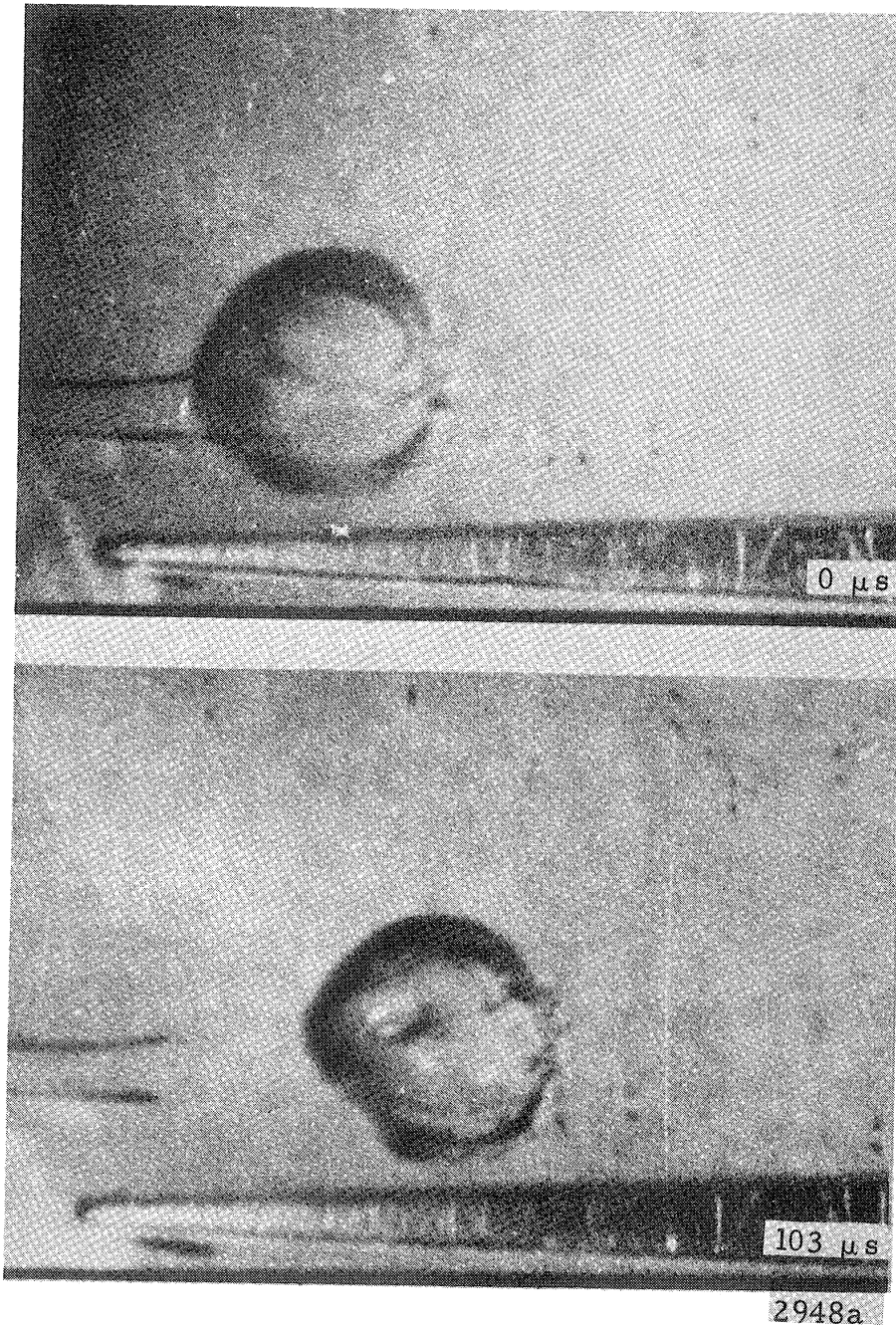


Figure 5.28 Model 330 High Speed Photographs of a Spark Induced Cavitation Bubble Collapsing in the Modified Aluminum Two-Dimensional Venturi. Focused Front Lighting, Time Measured from First Frame,  $2.6 \mu$ s Exposure/Frame, Fluid Velocity 20.1 m/s Left to Right, Initial Wall Distance,  $b = 1.21$ , Magnification 8.0. Air Content 0.7%

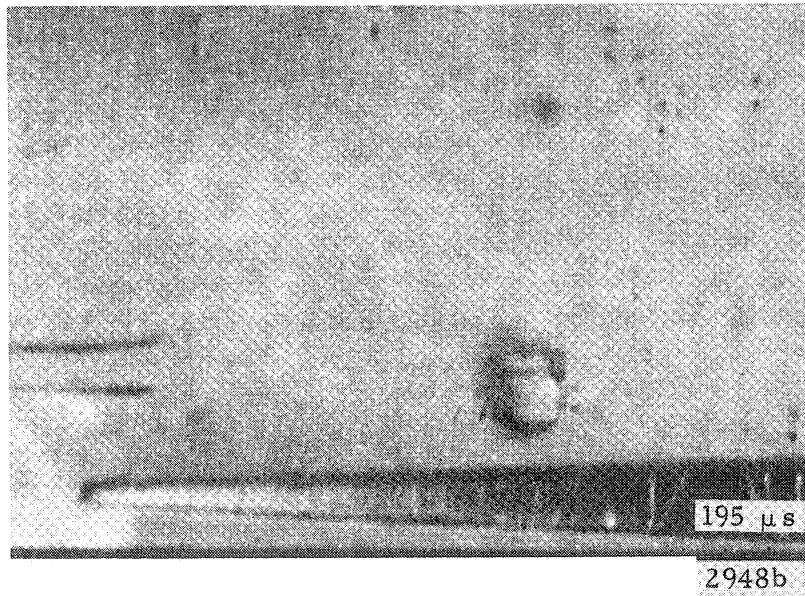
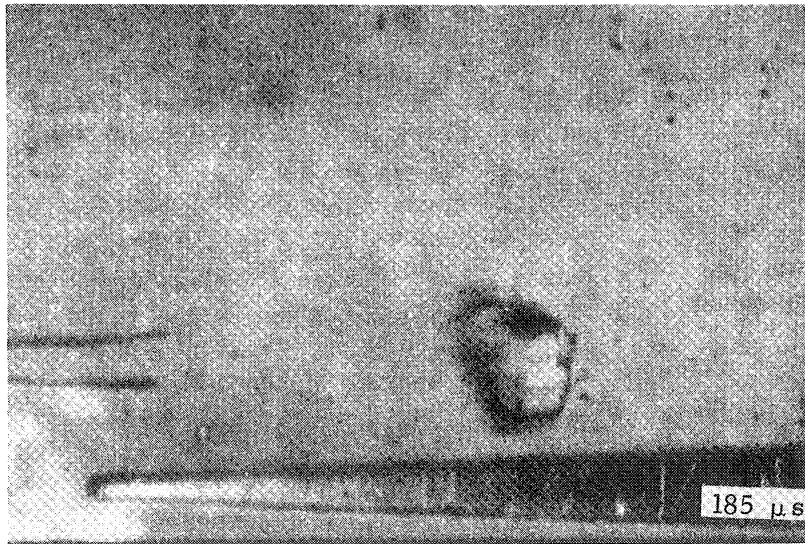
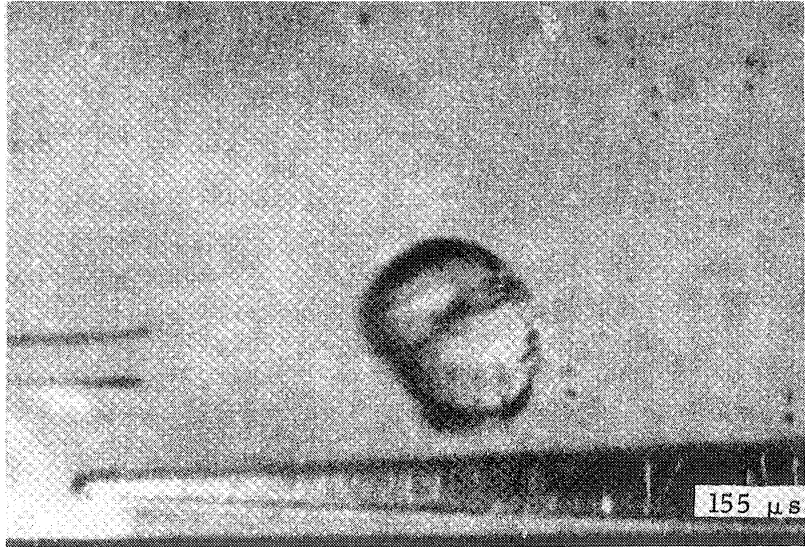


Figure 5.28 Continued

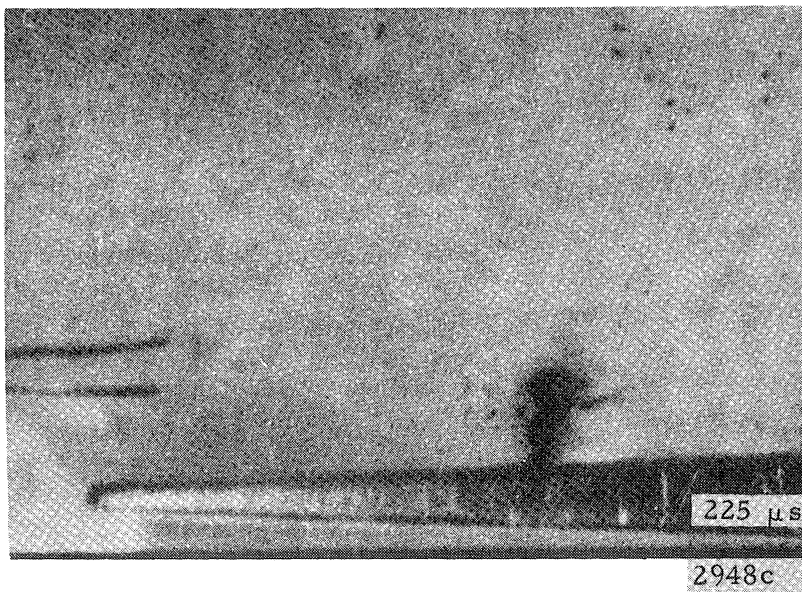
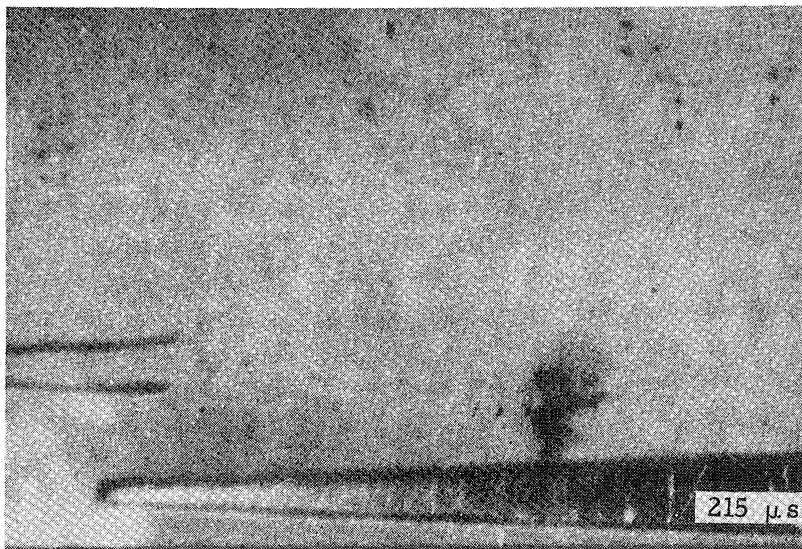
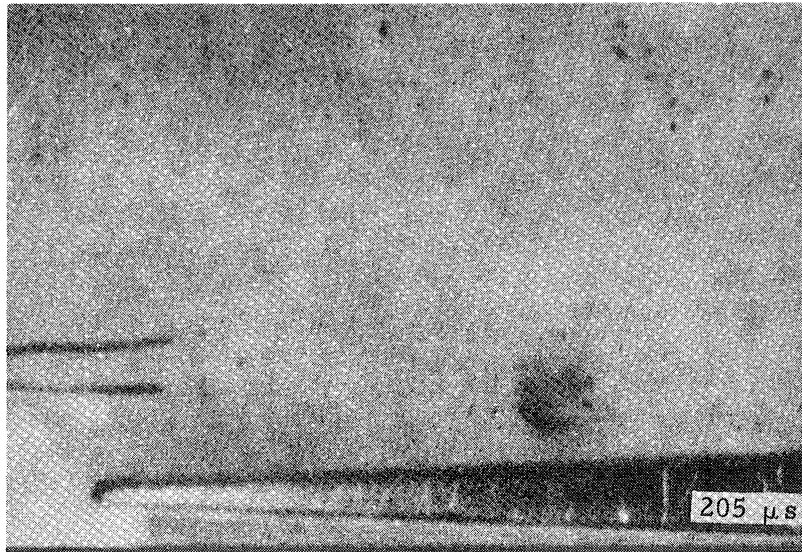


Figure 5.28 Continued

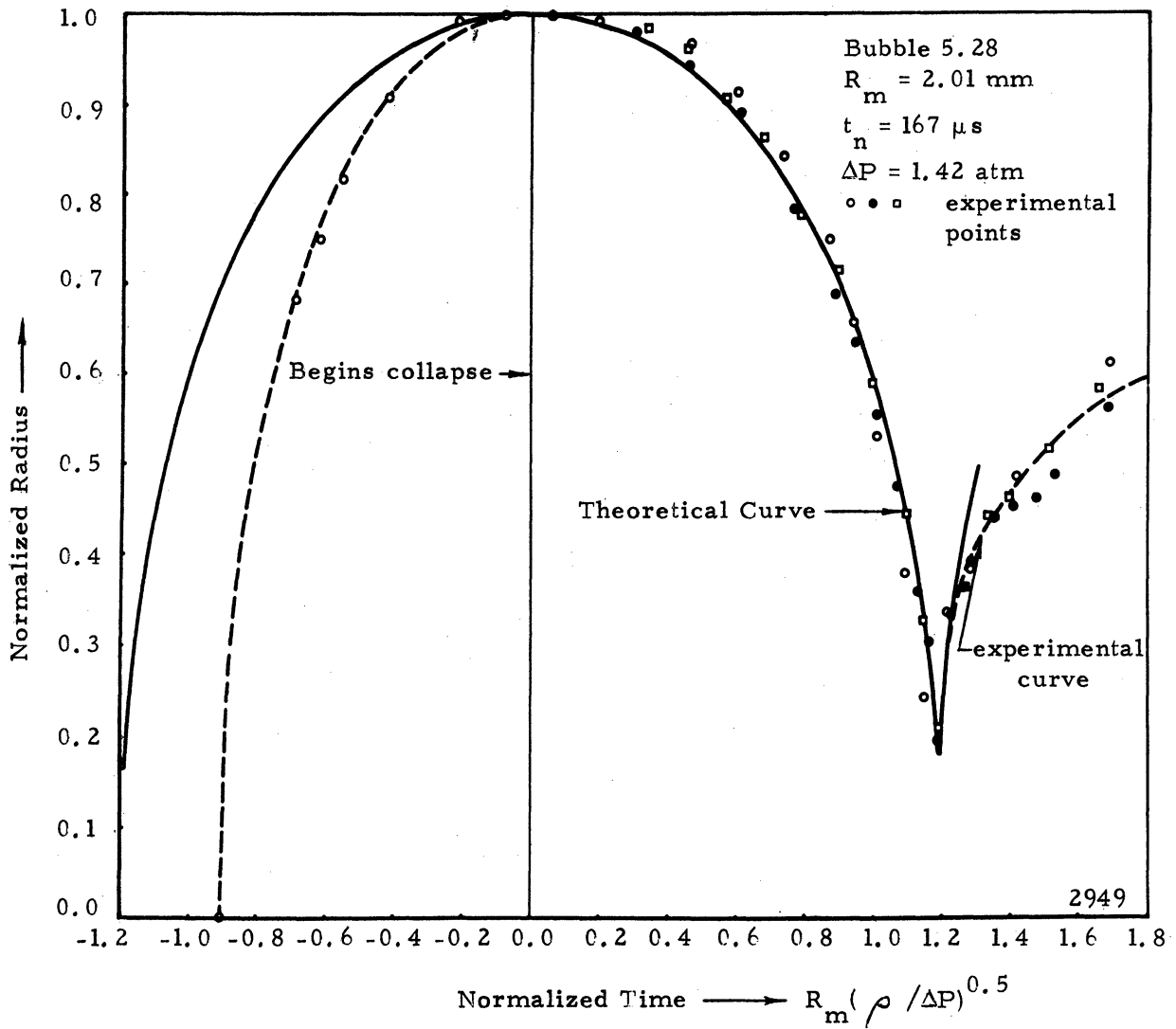


Figure 5.29a Normalized Radius vs. Normalized Time for the Spark Induced Cavitation Bubble Shown in Figure 5.28

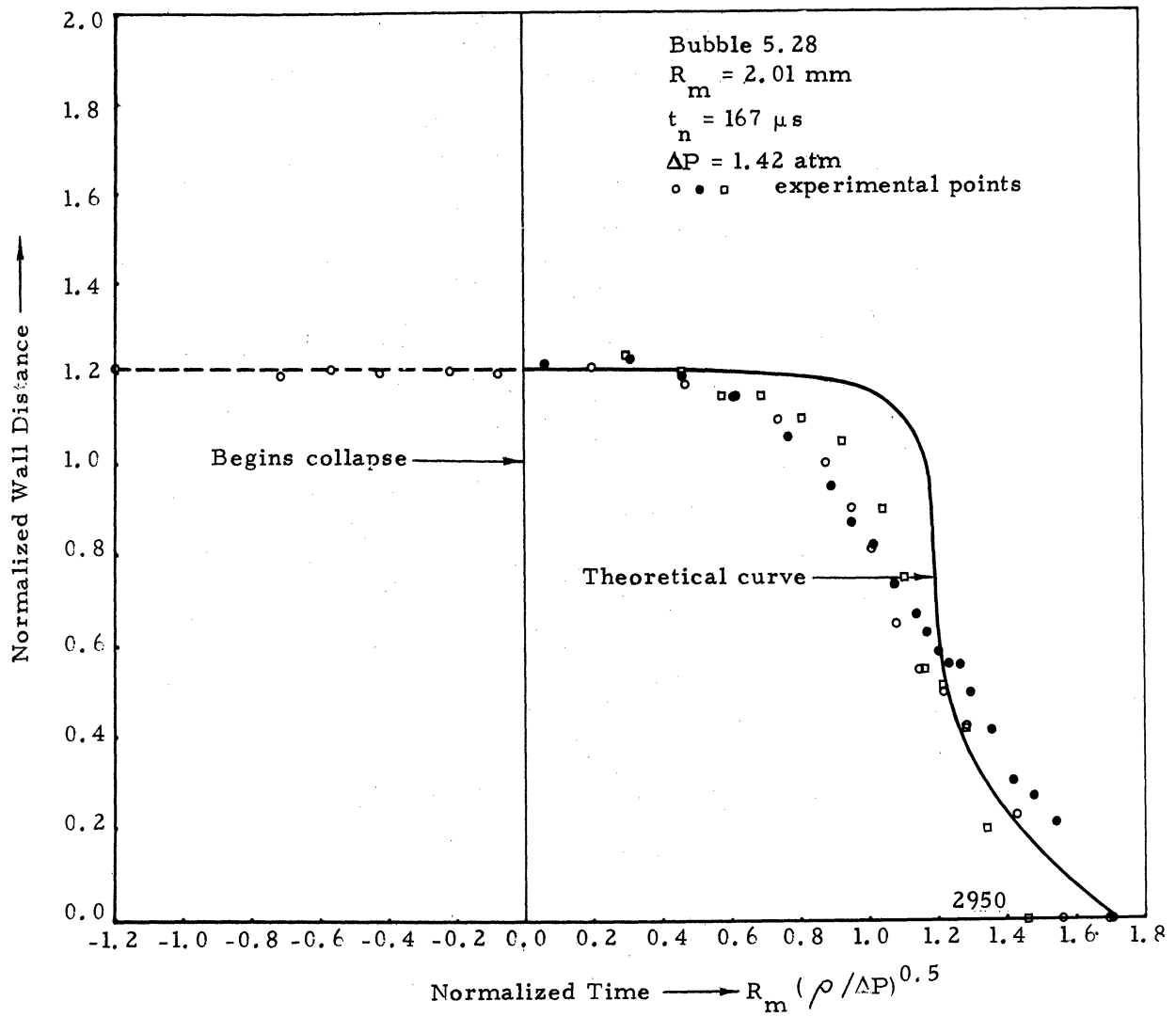


Figure 5.29b Normalized Wall Distance vs. Normalized Time for the Spark Induced Cavitation Bubble Shown in Figure 5.28



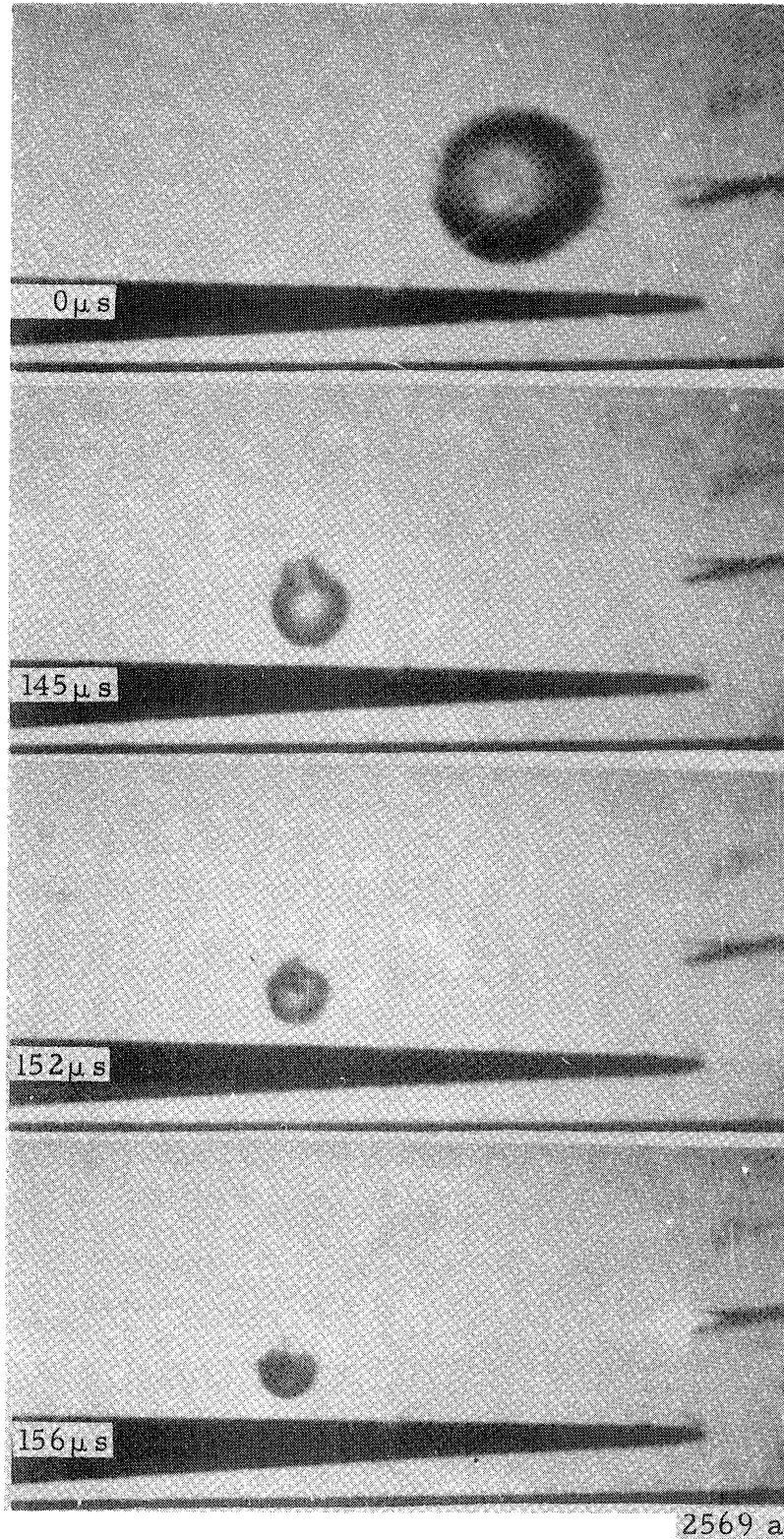


Figure 5.30 Model 330 High Speed Photographs of a Spark Induced Cavitation Bubble Collapsing in the Modified Aluminum Two-Dimensional Venturi. Diffuse Back Lighting, Time Measured from the First Frame,  $1.8 \mu$ s Exposure/Frame, Fluid Velocity 26.7 m/s Right to Left, Initial Wall Distance,  $b_1 = 1.14$ , Magnification 6.0. Air Content 0.6%.

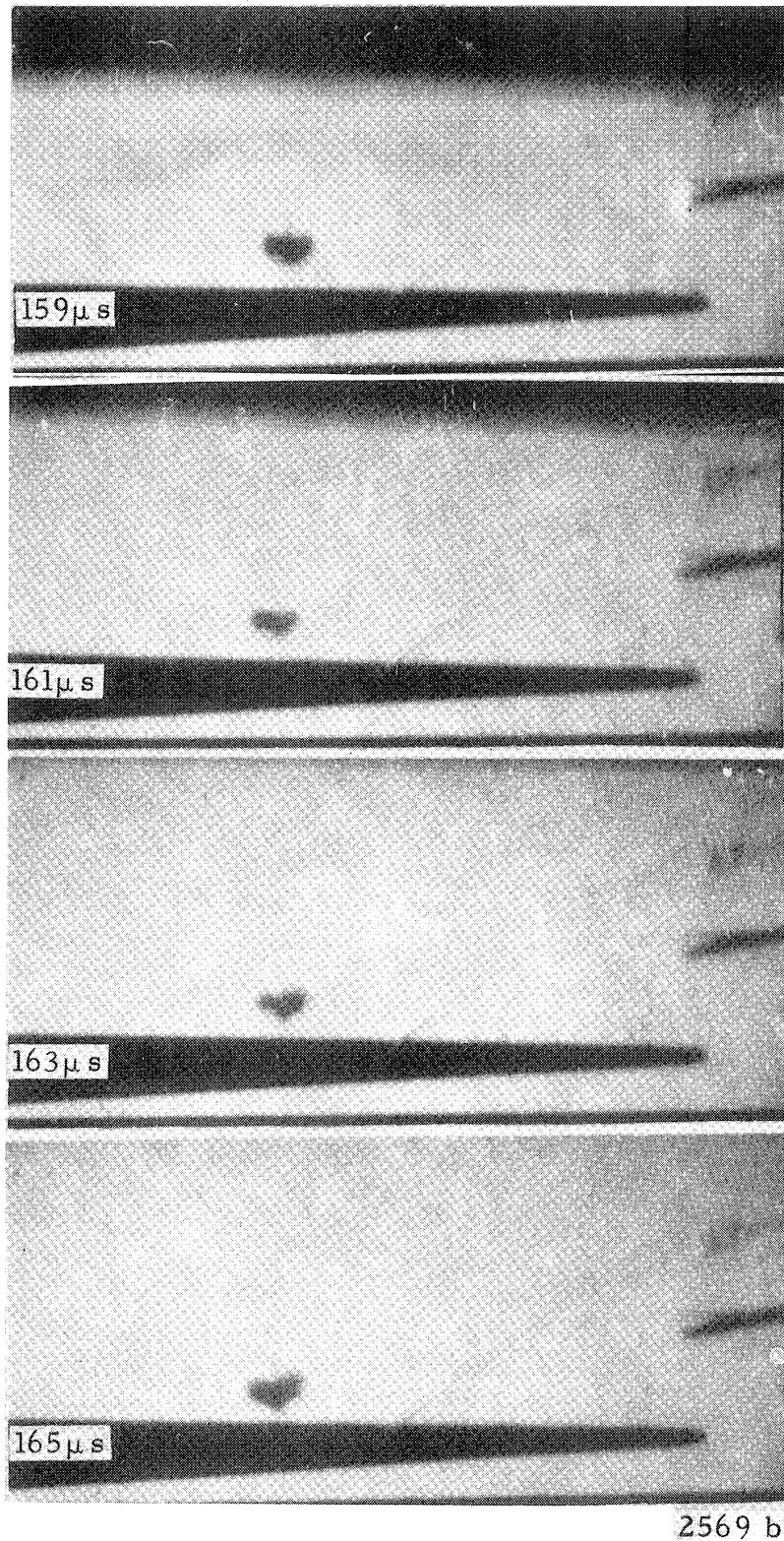


Figure 5.30 Continued



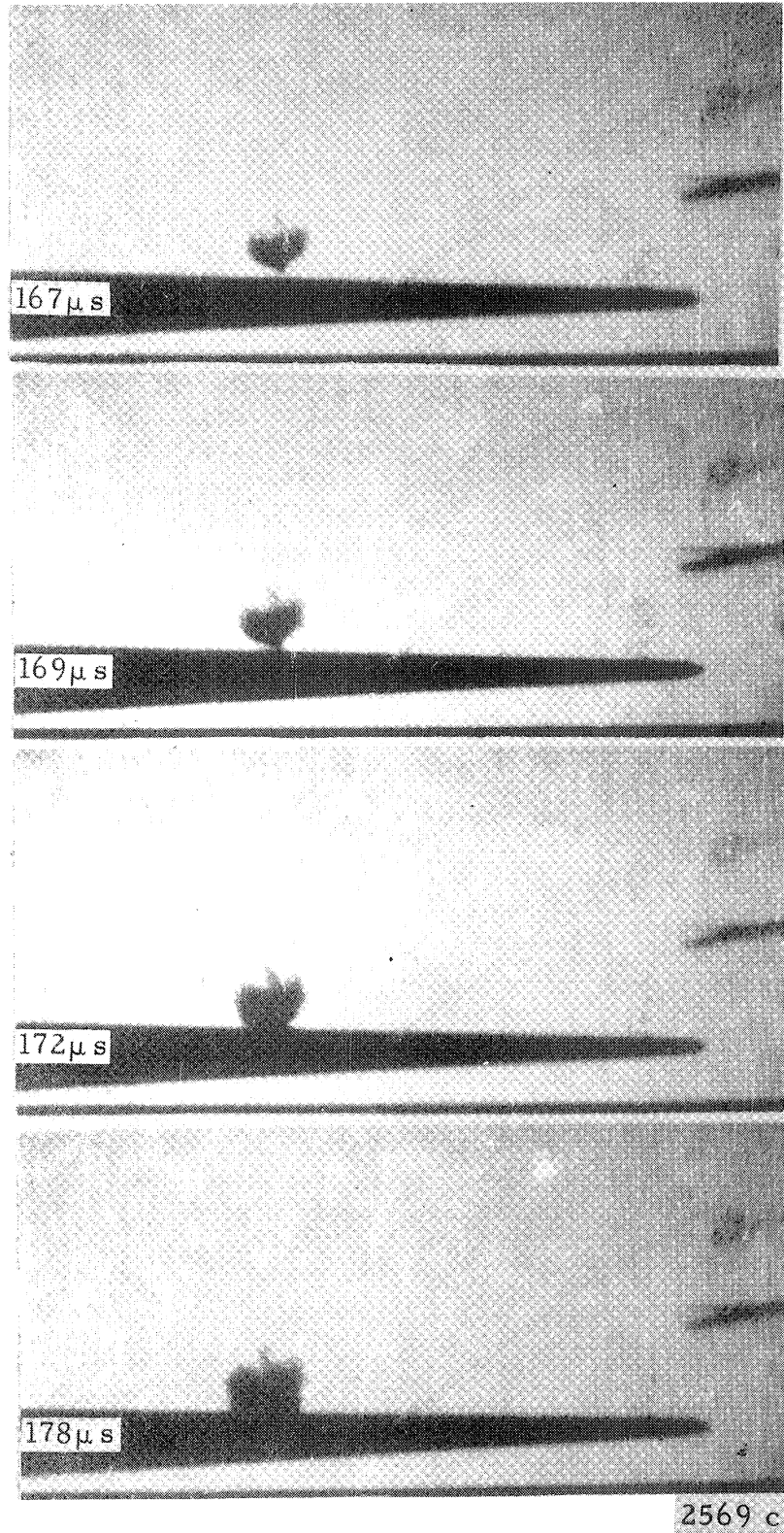


Figure 5.30 Continued

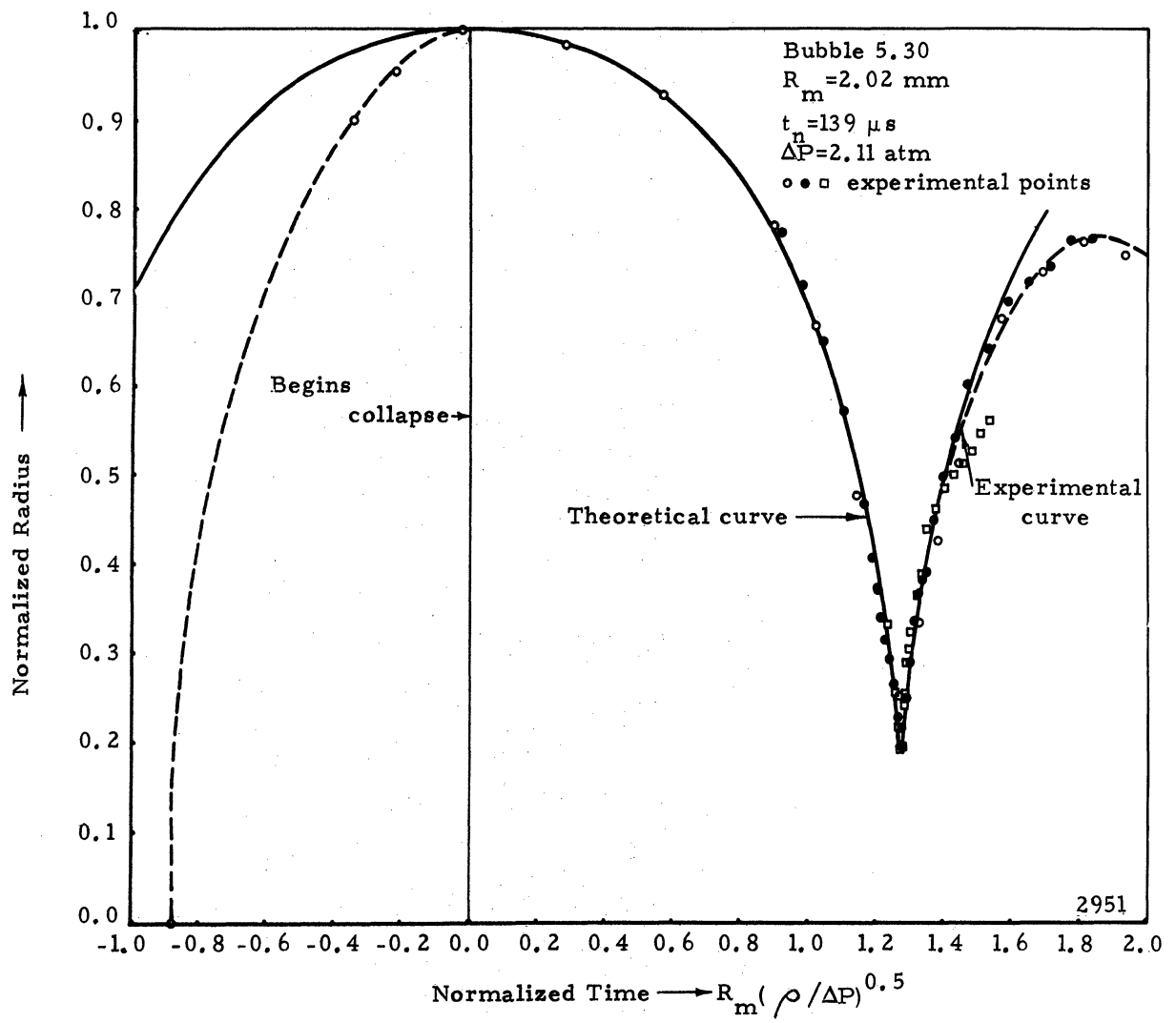


Figure 5.31a Normalized Radius vs. Normalized Time for the Spark Induced Cavitation Bubble Shown in Figure 5.30

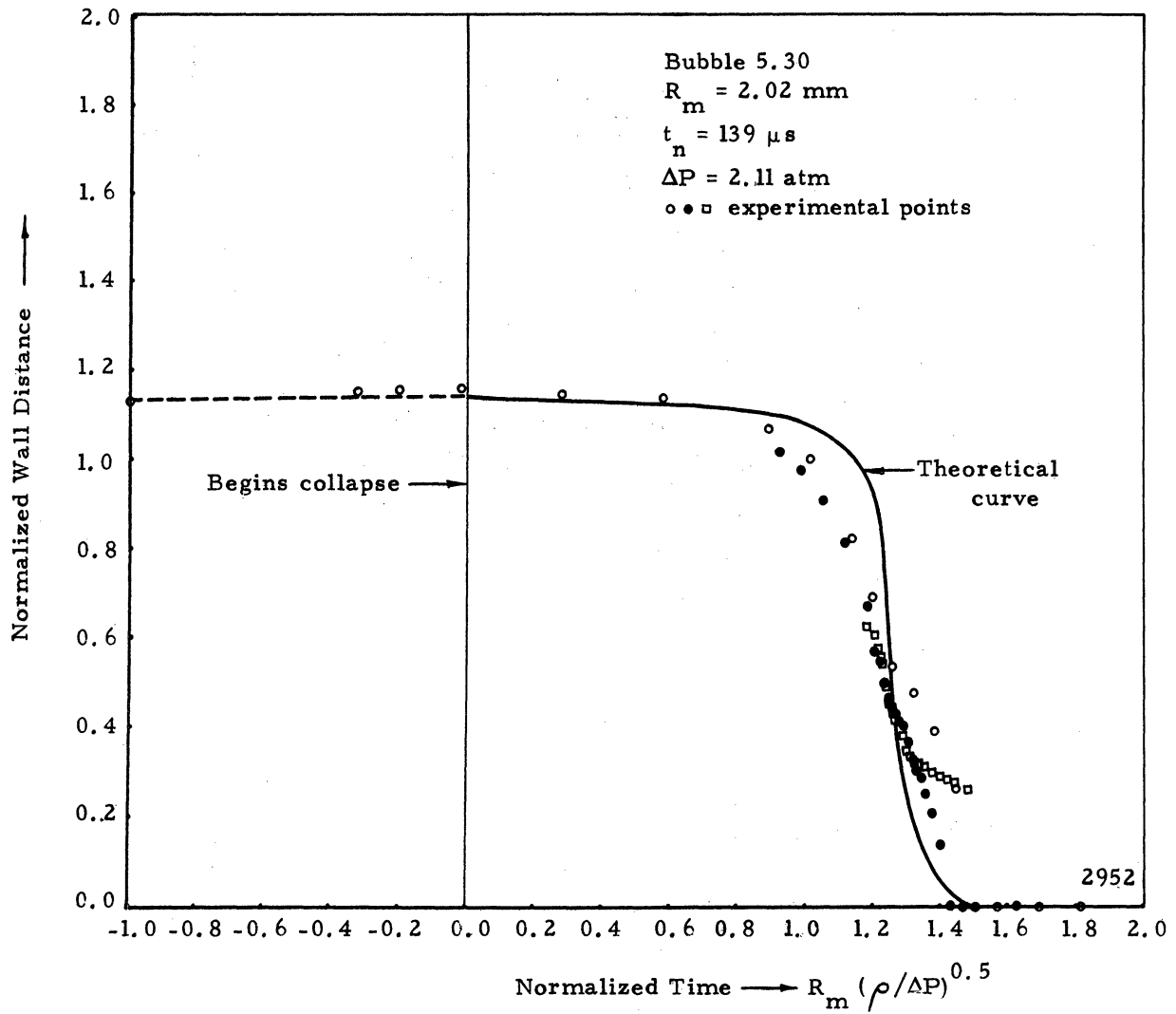


Figure 5.31b Normalized Wall Distance vs. Normalized Time for the Spark Induced Cavitation Bubble Shown in Figure 5.30

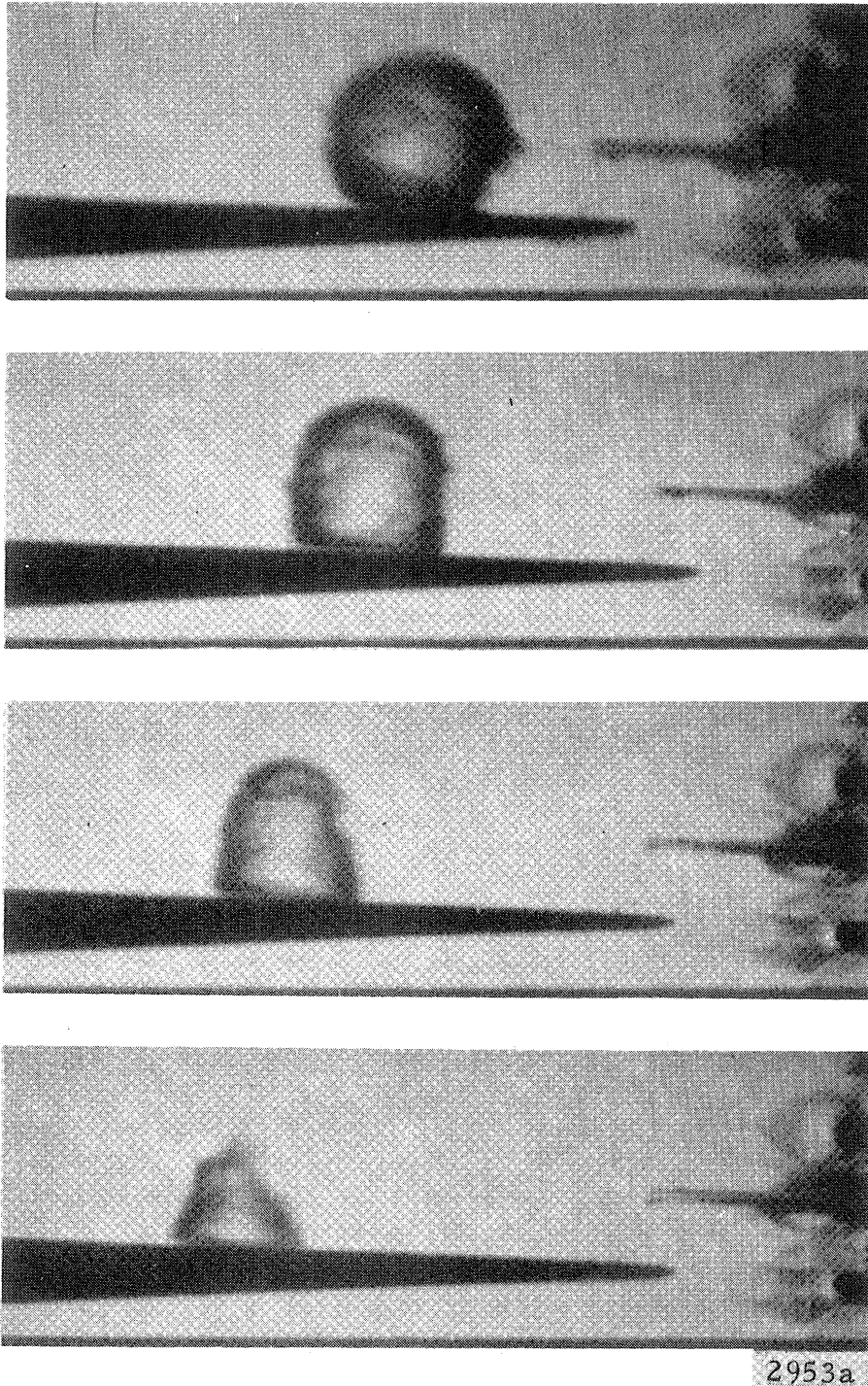
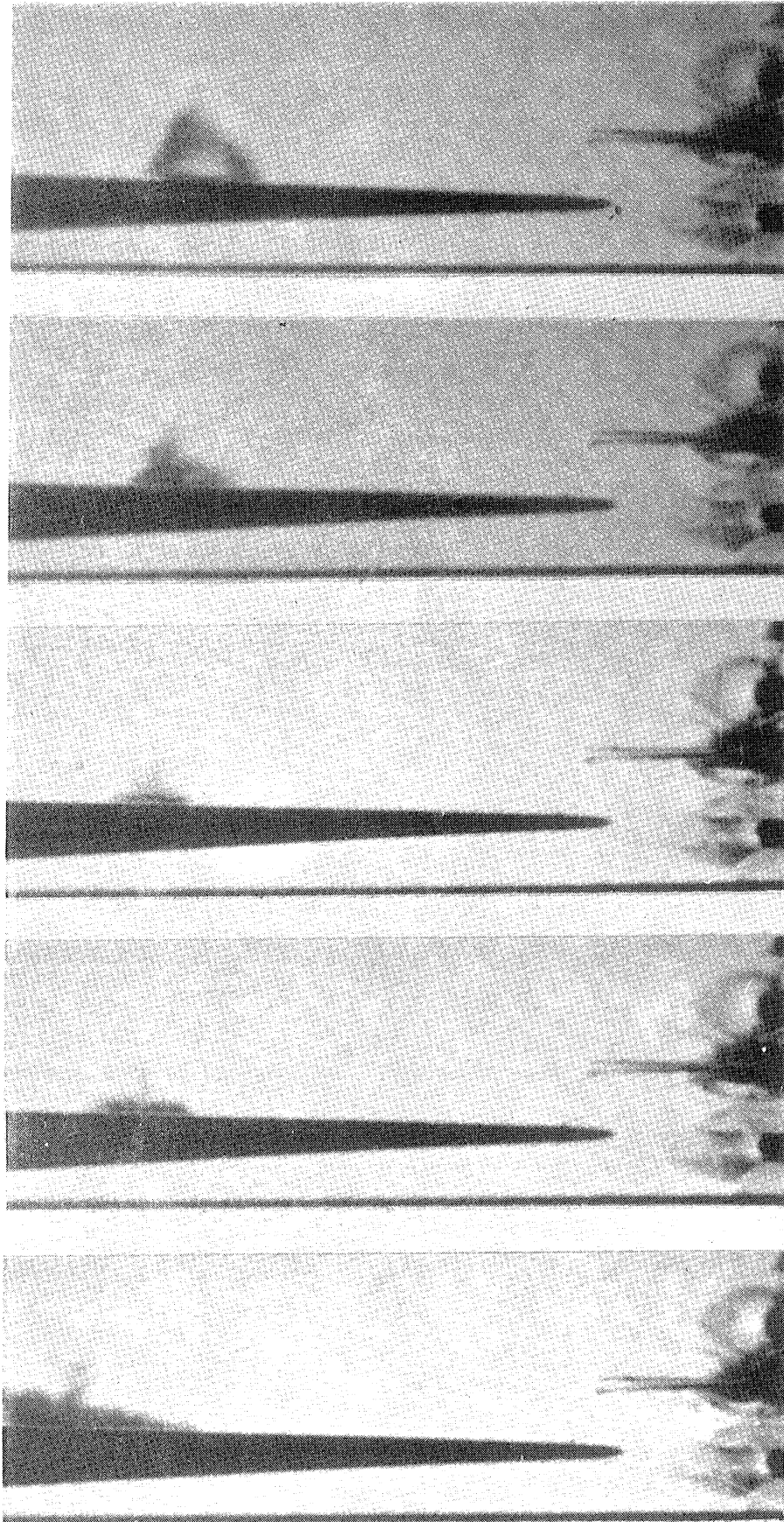


Figure 5.32 Model 330 High Speed Photographs of a Spark Induced Cavitation Bubble Collapsing in the Modified Aluminum Two-Dimensional Venturi. Diffuse Back Lighting, Time Measured from the First Frame,  $6.2 \mu\text{s}$  Exposure/Frame, Fluid Velocity  $26.7 \text{ m/s}$  Right to Left, Initial Wall Distance,  $b_0 = 0.94$ , Magnification 5.5. Air Content  $0.6\%$



2953b

Figure 5.32 Continued

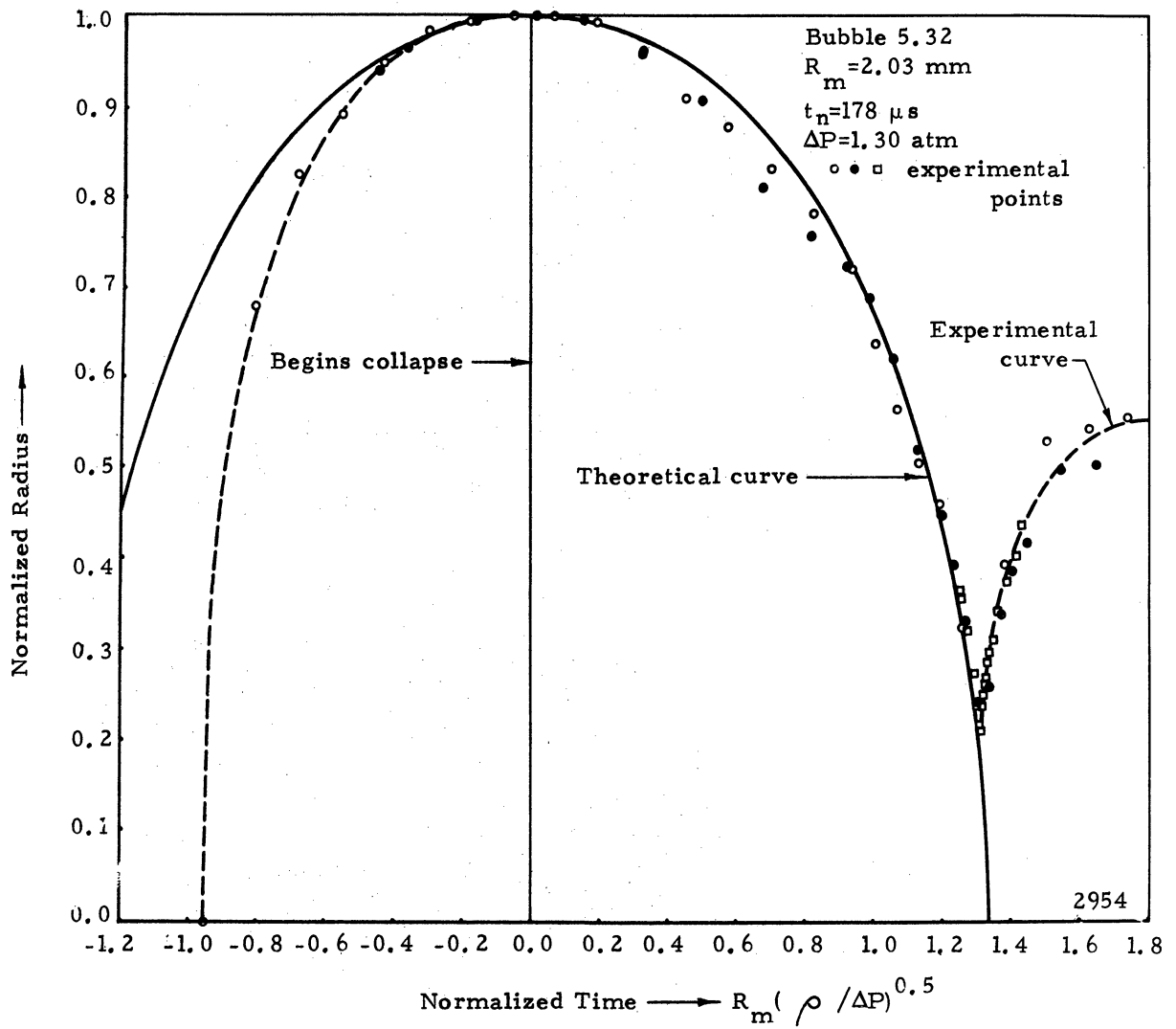


Figure 5.33a Normalized Radius vs. Normalized Time for the Spark Induced Cavitation Bubble Shown in Figure 5.32

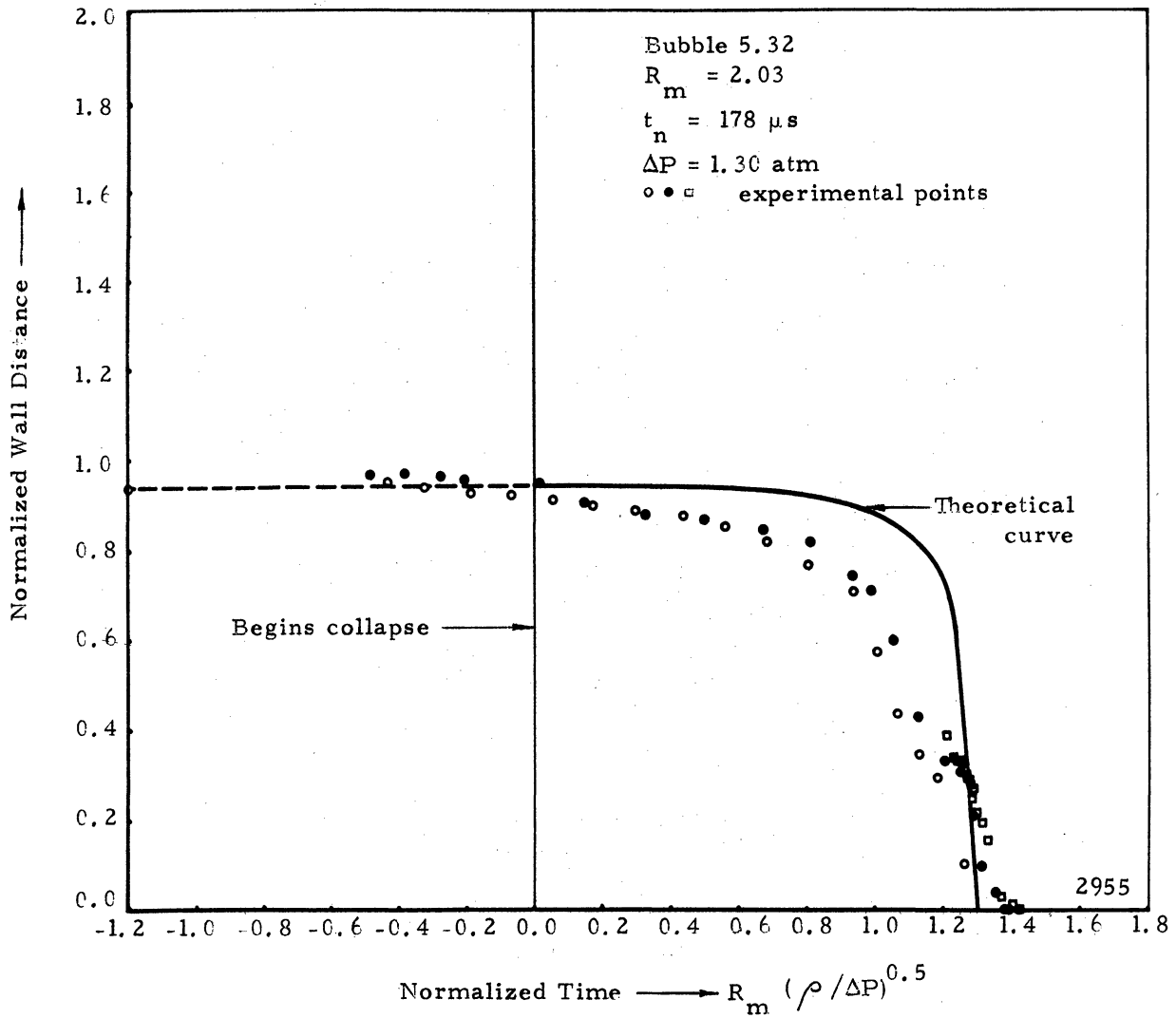


Figure 5.33b Normalized Wall Distance vs. Normalized Time for the Spark Induced Cavitation Bubble Shown in Figure 5.32



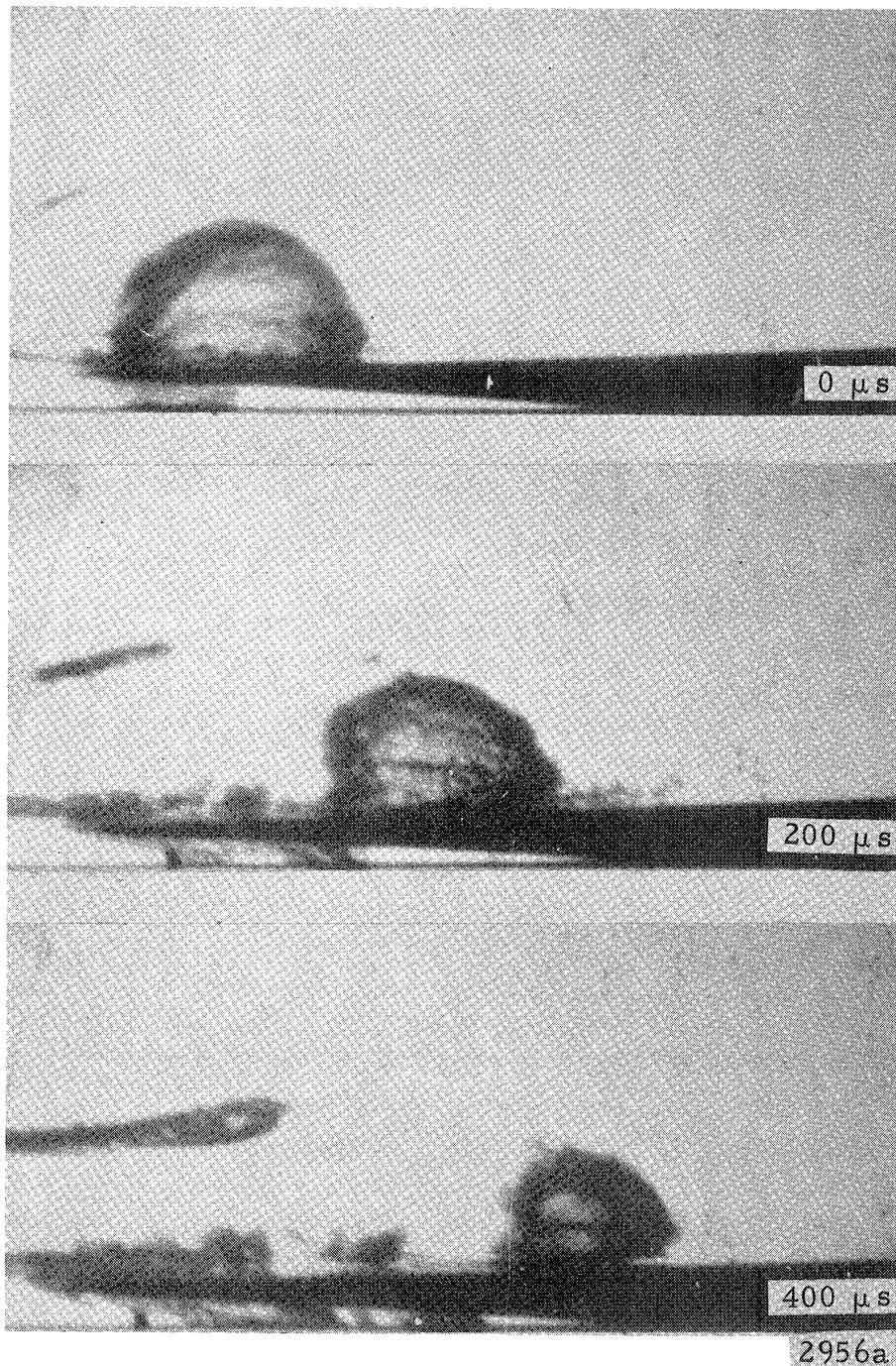


Figure 5.34 Model 330 High Speed Photographs of a Spark Induced Cavitation Bubble Collapsing in the Modified Aluminum Two-Dimensional Venturi. Diffuse Back Lighting, Time Measured from the First Frame,  $5.0 \mu\text{s}$  Exposure/Frame, Fluid Velocity  $24.7 \text{ m/s}$  Left to Right, Initial Wall Distance,  $b_0 = 0.0$ , Magnification 6.2. Air Content  $0.7\%$

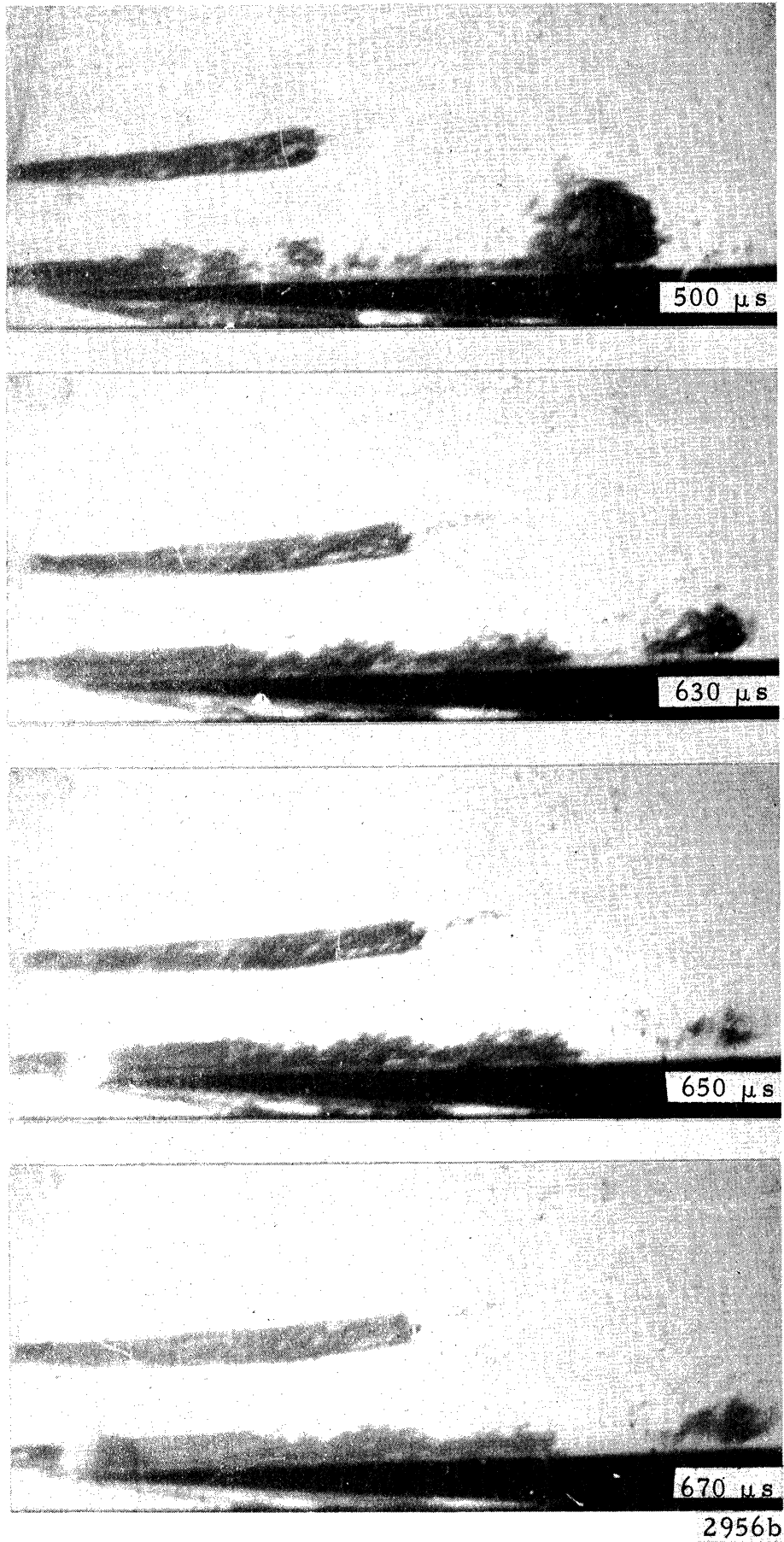


Figure 5.34 Continued

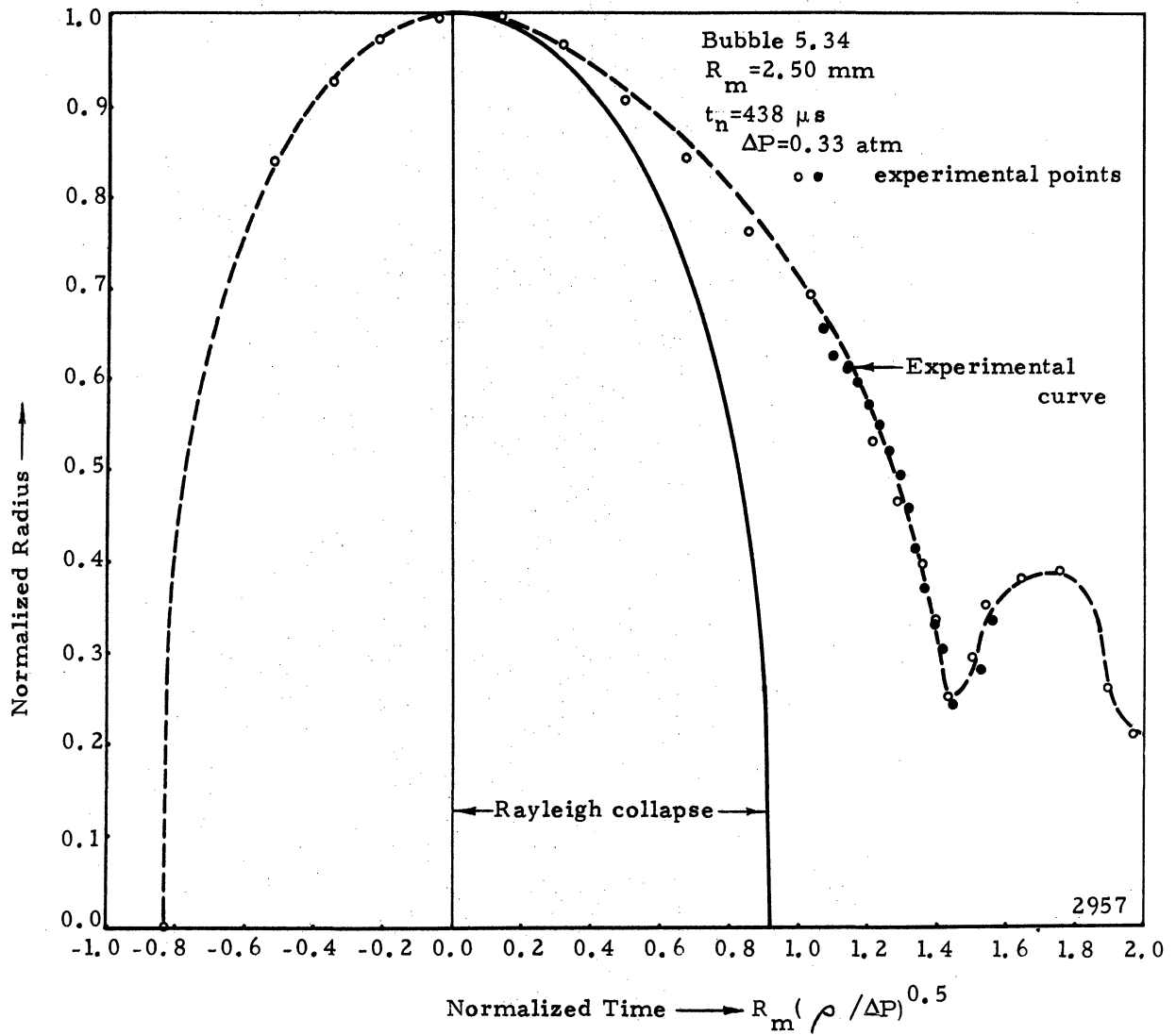


Figure 5.35a Normalized Radius vs. Normalized Time for the Spark Induced Cavitation Bubble Shown in Figure 5.34

attraction towards the wedge increases in both the experimental and theoretical results. When the bubble starts with an initial distance,  $b_0$ , of about 1.2 from the wedge (Fig. 5.28), the attraction becomes so great that during the first rebound of the bubble, it actually strikes the surface of the wedge. Although the experimental and theoretical results agree quite well in the degree of migration that occurs, for the theoretical results the migration occurs over the much shorter time span during which the bubble is near its minimum volume, as compared with the experimental measurements for which the migration is more gradual.

This migration of the bubble has been previously explained as apparent "attraction" between the real bubble and its image reflected in the surface of the wedge. Another description of this process accounts for the interference in the fluid flow between the wedge and the bubble. Fig. 5.28 and 5.30 show that the surface of the bubble closest to the wedge remains a nearly constant distance from the wedge during the collapse phase, and does not move toward the wedge until the bubble begins to rebound. Although this surface does not move toward the wedge during collapse, the surface furthest from the wedge, and thus the bubble centroid, do move toward the wedge during collapse. This movement of the centroid of the bubble produces a momentum directed toward the wall which must be conserved after minimum volume is reached; therefore, the bubble moves on to strike the surface of the wedge.

Similar arguments have been used <sup>(24, 27)</sup> to describe the motion of bubbles having an initial slip velocity,  $V_{s0}$ , relative to the surrounding fluid. A bubble moving in a fluid has a virtual mass associated with it equal to 0.50 of the mass of the displaced fluid

$(M_v = \frac{2}{3} \pi R^3)$  (38). Coupled with the initial slip, the bubble has an initial momentum ( $P = M_{vo} V_{so} = \text{const.}$ ). As the bubble decreases in size, its virtual mass decreases and, in order to conserve momentum, the slip velocity must be increased.

$$V_s = \frac{M_{vo}}{M_v} V_{so} = \frac{R_o^3}{R_s^3} V_{so} \quad 5.1$$

where:

- $V_s$  = slip velocity
- $M_v$  = virtual mass
- $R$  = bubble radius
- $V_{so}, M_{vo}, R_o$  - initial values

As the radius,  $R$ , of the bubble approaches zero, the slip velocity,  $V_s$ , approaches infinity. With the asymmetries noted in this study, the bubble deforms into a jet which contains some of the initial momentum of the bubble. For the case of a bubble adjacent to a wall, the initial momentum that must be conserved is produced by the apparent "attraction" of the wall produced by the interference of the flow around the bubble.

The variation in slip velocity is shown in both the increased migration toward the wedge and the variation in axial slip velocity as the bubble nears minimum volume. Because the duration of the stationary spark which forms the spark bubble is only a few microseconds, the instantaneous slip velocity of the spark bubble is initially nearly equal to the free stream velocity. As the bubble grows, this slip velocity should quickly decrease to a small value (eq. 5.1), as it does. Then as the bubble collapses again, the slip velocity should again increase, as is observed. Results to this effect are shown in Table 5.1. The average slip velocity is the slip velocity measured over the entire bubble lifetime. The freestream velocity is calculated

TABLE 5.1

Comparison of the Average Horizontal Slip Velocity and the Instantaneous Horizontal Slip Velocity at Minimum Volume for Spark Induced Cavitation Bubbles.

Bubble Number	Average Horizontal Slip Velocity m/s	Instantaneous Horizontal Slip Velocity at Minimum Volume m/s
5.22	-3.02	-24.6
5.24	-1.31	-10.3
5.26	-2.02	-23.1
5.28	-1.20	-12.9
5.30	-1.18	-22.1

Bubble Number refers to corresponding figure number.

Average slip velocity is determined over the entire bubble lifetime.

using orifice plates placed in the high velocity water loop (Fig. 2.1). With the measured pressure drop across the plate calibration curves were used to obtain the volumetric flow rate. Using the cross-sectional area of the two-dimensional venturi at any axial position, a free-stream velocity was calculated. No correction was made for boundary layer effects since boundary layer thickness should be extremely small in these experiments. The major error in these values is the possible difference between the actual and calculated free stream velocities. The instantaneous slip velocity is measured when the bubble is near minimum volume. The slip velocity values may be in error as much as 50% because of the low resolution of the film-camera system and dimensional changes in the film during processing; however, they show the same substantial trend of increased slip velocity with decreased bubble size without exception.

The motion picture analyses were made by rephotographing the original negatives on to 16 mm film, and then projecting this film strip using a 16 mm projector. Using a minimum replay rate of 8 frames/second (achieved by rephotographing each frame twice to accommodate the projector framing rate of 16 frames/second), the maximum time magnification of an event was  $2.5 \times 10^5$ . Therefore, an event taking place in about  $10 \mu\text{s}$  would take 2.5 s during the play-back. Viewing these films, it was easy to see that the wedge had little effect upon the bubbles at a wall distance,  $b_0$ , of more than 1.5 initial radii away from the wedge. As the bubbles reached a wall distance,  $b_0$ , of about 1.2 radii from the wedge, the attraction to the wedge became quite strong, and the bubble would migrate very rapidly, striking the wedge soon after minimum volume was reached. For bubbles (Fig. 5.32) attached to the wedge ( $b_0 \leq 1.0$ ) a jet was formed from the surface of the bubble furthest from the wedge early in the collapse stage, and this jet struck the surface



of the wedge before the minimum value of the bubble had been reached.

The low resolution of the film-camera system coupled with the small size of the bubbles photographed greatly reduced the details of bubble deformation and jet formation. Results of making highly enlarged prints of the photographic sequence (Figs. 5.36a + b from Fig. 5.30) shows this loss of detail. The second frame shows the partially deformed bubble with an irregularly shaped mass moving through the interior of the bubble that is not present in the first frame taken  $3.6 \mu\text{s}$  earlier. A detailed study of Fig. 5.30 shows that this mass travels through the bubble eventually protruding through the other side (Frame 8 of Fig. 5.30), and finally striking the wedge (Frame 9 of Fig. 5.30) as a jet. Although the resolution is low, the prints may be used to produce outlines of the bubble during various phases of collapse and rebound (Figs. 5.37 and 5.38 respectively). The outlines show that during the first phase of collapse, the restriction of fluid flow between the wedge and the bubble causes the bubble to elongate slightly along the axis perpendicular to the wedge. Later in the collapse, surface instabilities develop in the upper portion of the bubble. These instabilities results in a more rapid collapse of the upper portion of the bubble with the upper surface eventually moving through the bubble to form an irregular jet. In other cases (Fig. 5.39) the surface instabilities become so large that the bubble actually divides in half before reaching minimum volume with each half collapsing separately. This splitting of the bubble may account for the "tail" which appears on the side of the bubble furthest from the solid surface in several sequences (i. e., Frame 11 of Fig. 5.30).

During the collapse phase, the centroid of the bubble migrates well over half the distance toward the wedge while the bubble surface closest to the wedge remains essentially stationary. The minimum volume reached is much greater than the minimum volume achieved

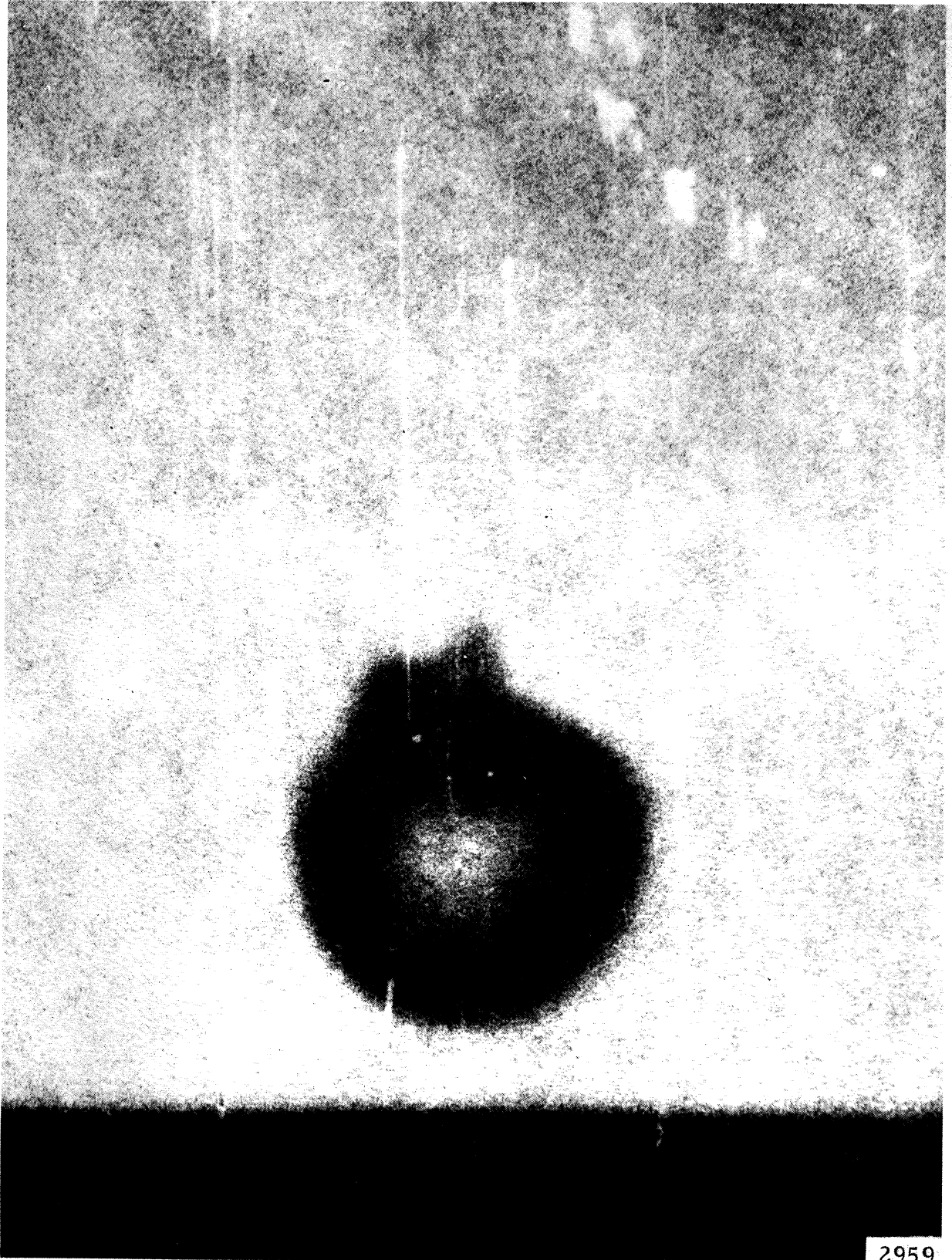


Figure 5.36a Enlargement of Frame 4 of Bubble 5.30.  
Magnification 30

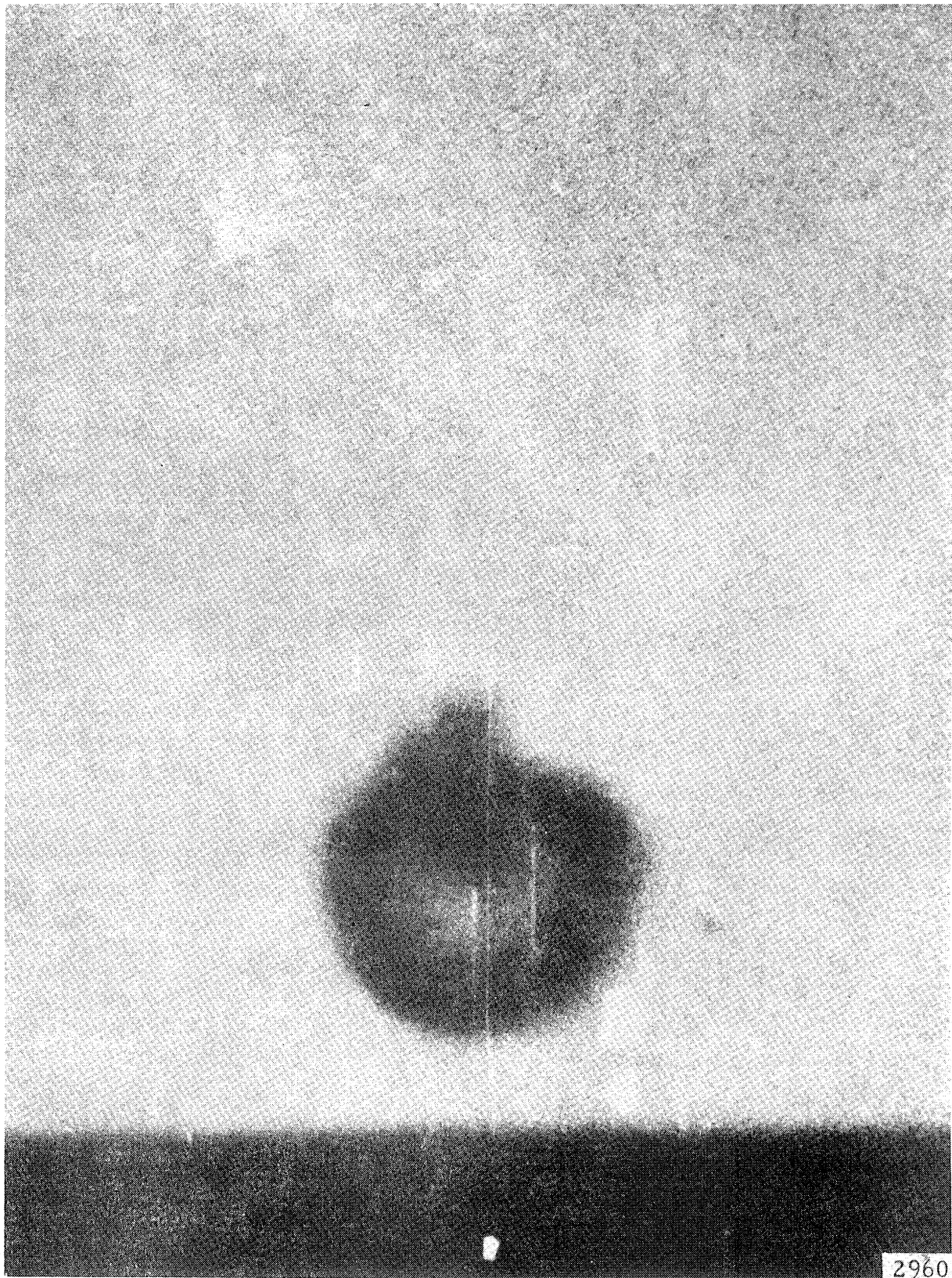


Figure 5.36b Enlargement of Frame 5 of Bubble 5.30 Taken  $3.6 \mu\text{s}$  after Frame 4 and Showing a Jet Moving through the Interior of the Bubble. Magnification 30

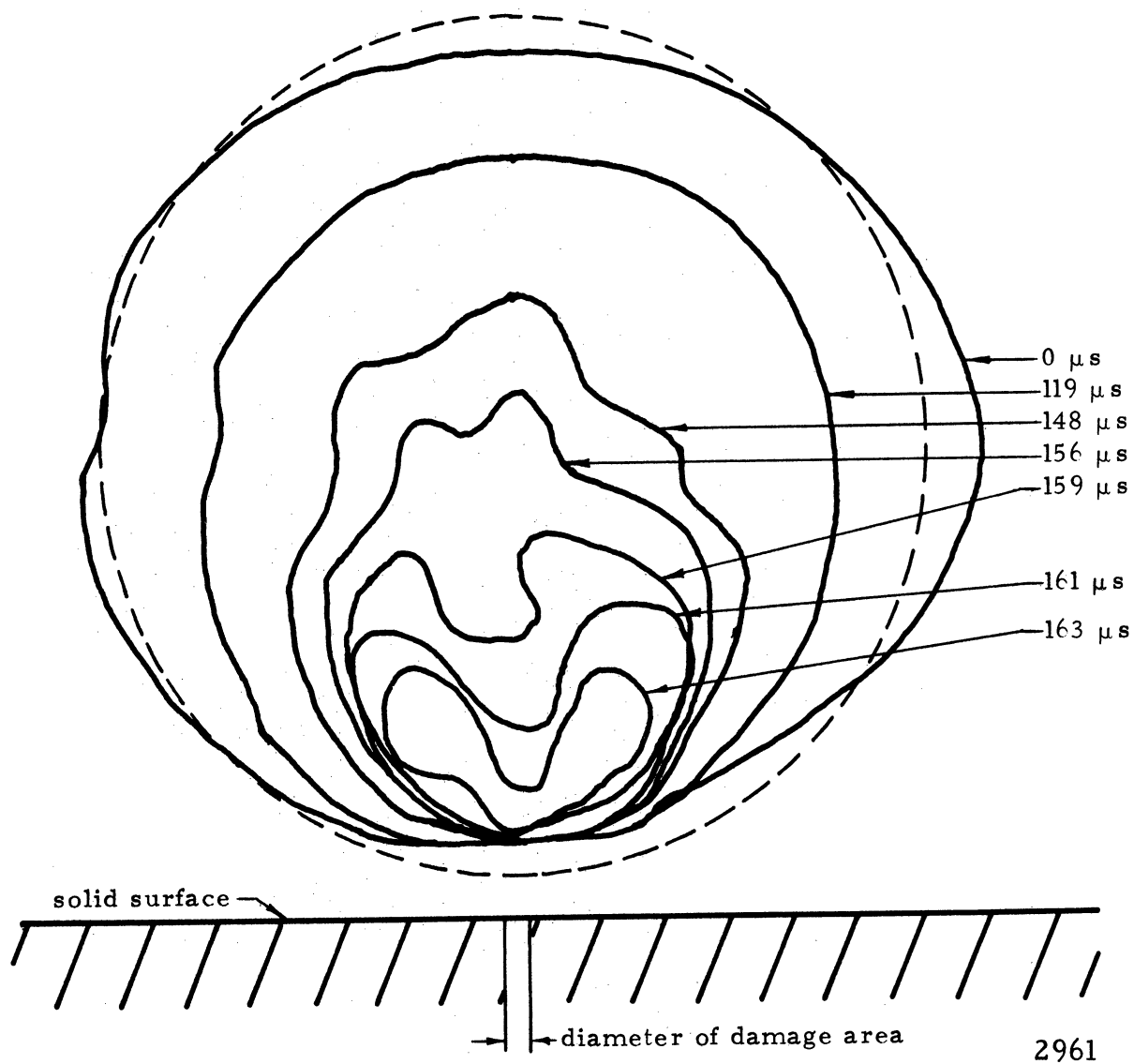


Figure 5.37 Outlines of the Spark Induced Cavitation Bubble 5.30 at Various Stages of Collapse Showing the Mode of Deformation

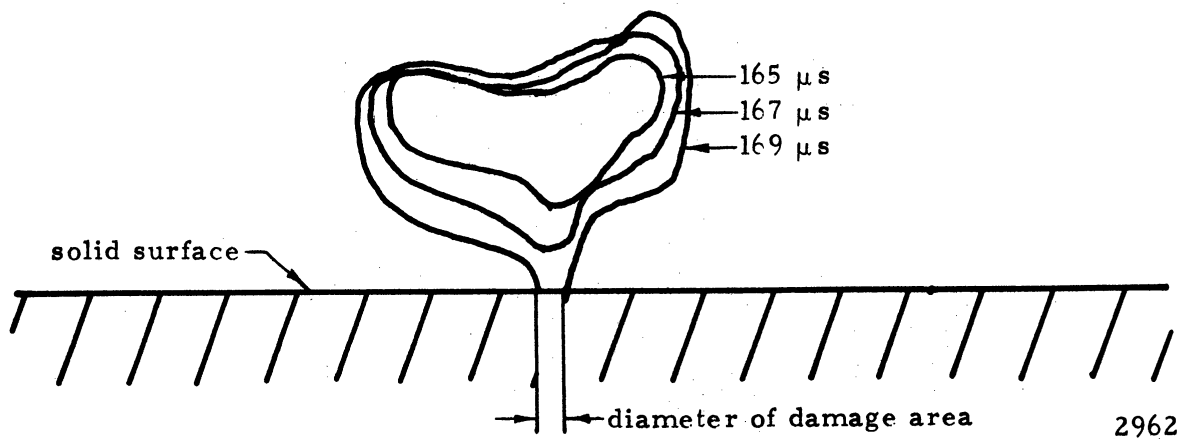


Figure 5.38 Outlines of the Spark Induced Cavitation Bubble 5.30 at Various Stages of Rebound Showing the Bubble Impinging on the Nearby Solid Surface

2962



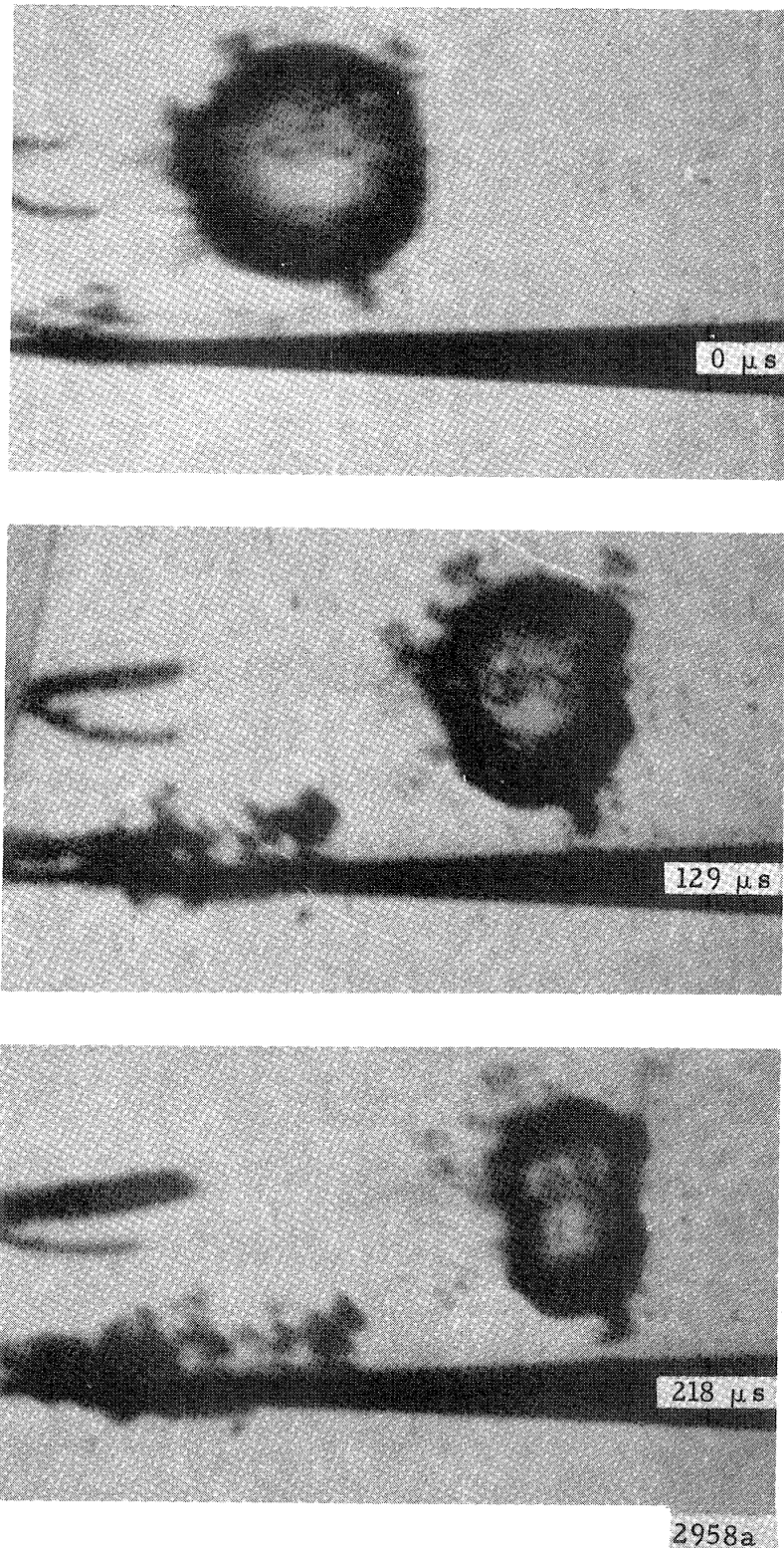


Figure 5.39 Model 330 High Speed Photographs of Spark Induced Cavitation Bubble Breaking up in the Modified Aluminum Two-Dimensional Venturi. Diffuse Back Lighting, Time Measured from First Frame,  $5.1 \mu\text{s}$  Exposure/Frame, Fluid Velocity  $24.7 \text{ m/s}$  Left to Right, Initial Wall Distance,  $b = 1.35$ , Magnification  $7.5$ . Air Content  $0.6\%$

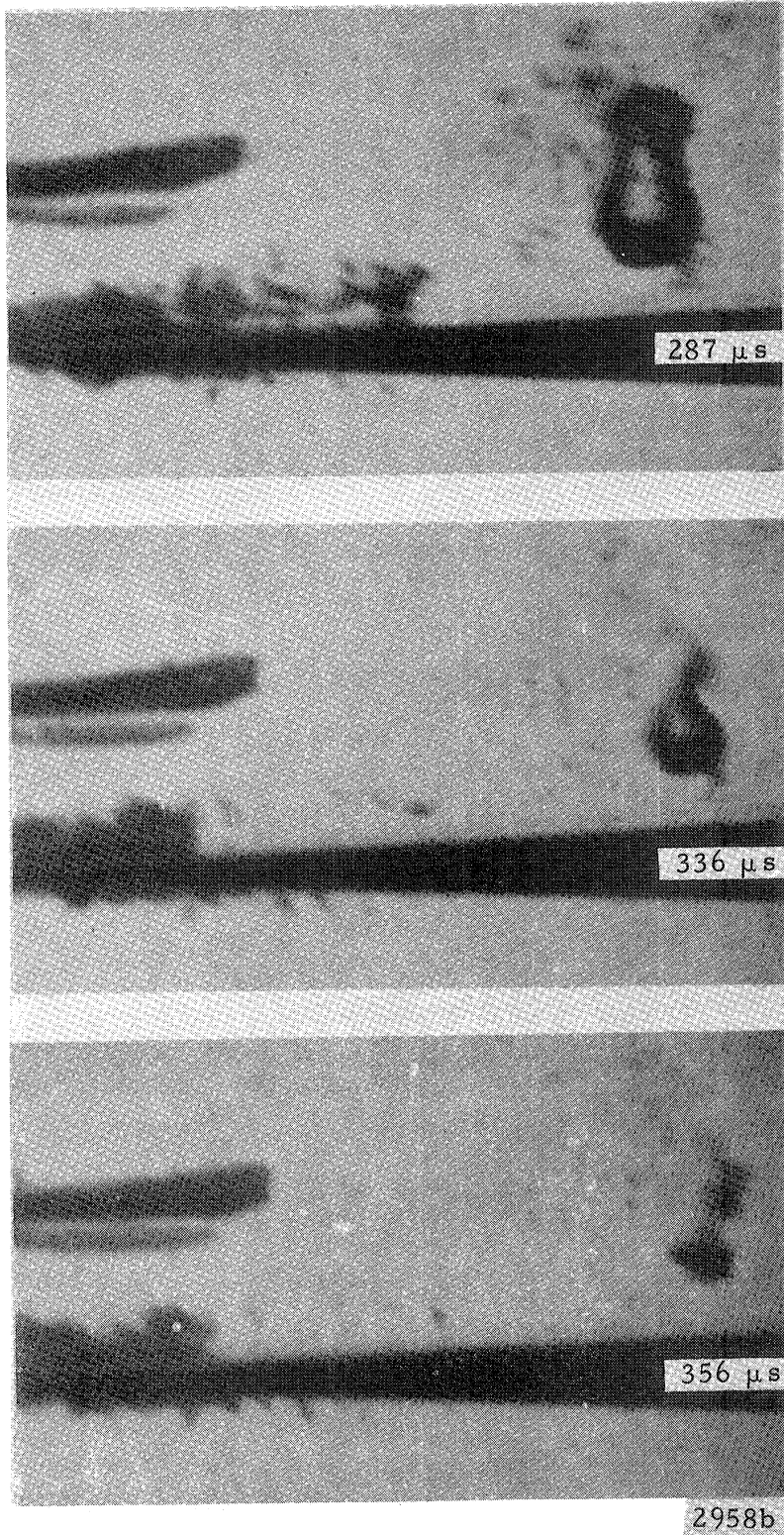


Figure 5.39 Continued



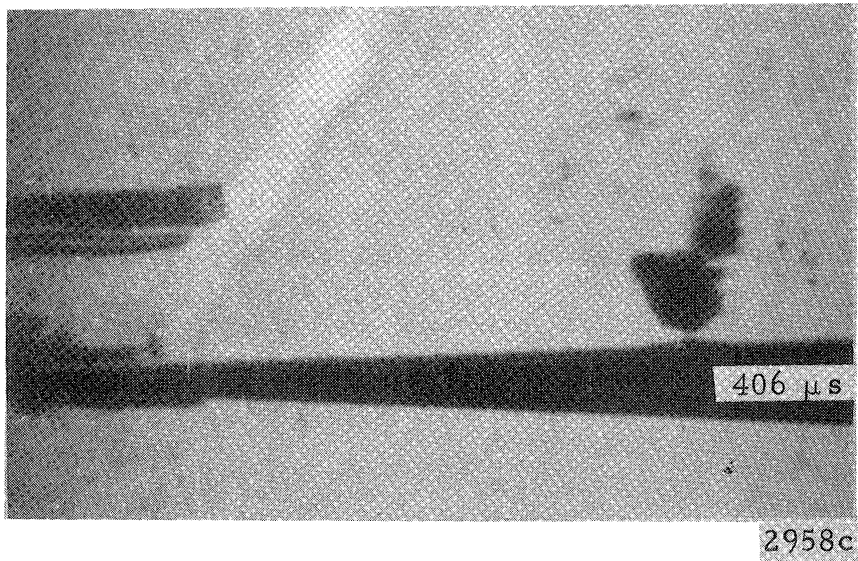
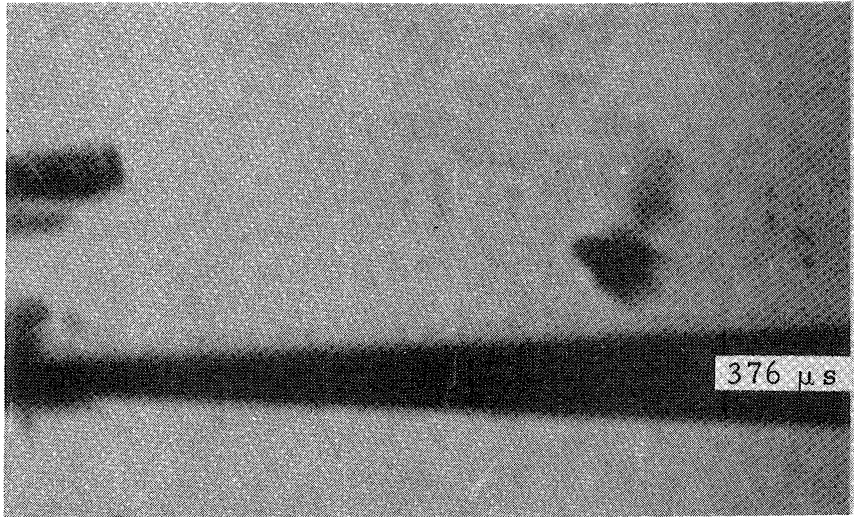
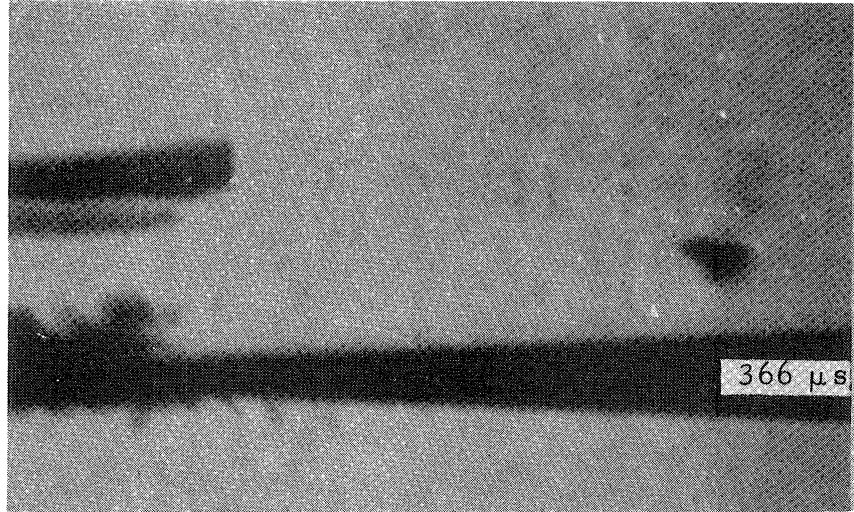


Figure 5.39 Continued

for similar bubbles collapsing in a pressure gradient alone; therefore, the maximum internal pressure and emitted shock wave is also reduced below any damaging potential. However, the water hammer pressure produced by the impinging high speed jet as estimated from the photos is greater than the pressure required to produce damage upon the aluminum specimens used.

The relative minimum volume of a bubble increases as its initial position is moved toward the solid boundary because of several energy loss mechanisms which affect the bubble collapse more severely in this position. Initially, energy is supplied to the bubble virtual mass in order to move the centroid toward the boundary. The larger asymmetries encountered as the initial boundary distance is decreased require more deformation energy and provide a larger surface for a given volume upon which the retarding internal pressure can act. Finally a significant fraction of the bubble energy is transmitted to the high speed jet which is formed during collapse. All of these processes remove energy from the bubble collapse, and result in larger minimum volumes as the initial boundary distance is reduced.

The bubbles shown in Figs. 5.24 through 5.34 are also of particular interest because the wedge near which the bubble collapsed was coated with the  $50\mu$  thick aluminum foil. The pits shown in Fig. 5.40-a and b were produced by the bubbles shown in Fig. 5.28 and 5.30, respectively, which started their collapse at 1.21 and  $\approx 1.14$  initial radii from the wall. The outlines of Figs. 5.38 and 5.39 (from enlargements of Fig. 5.30) show that the diameter of the tip of the jet produced upon bubble collapse and rebound is approximately the same order of magnitude as the damage area produced on the  $50\mu$  thick aluminum foil. For the bubbles of Fig. 5.24, 5.26, 5.32, and 5.34 where the bubbles were either attached to the

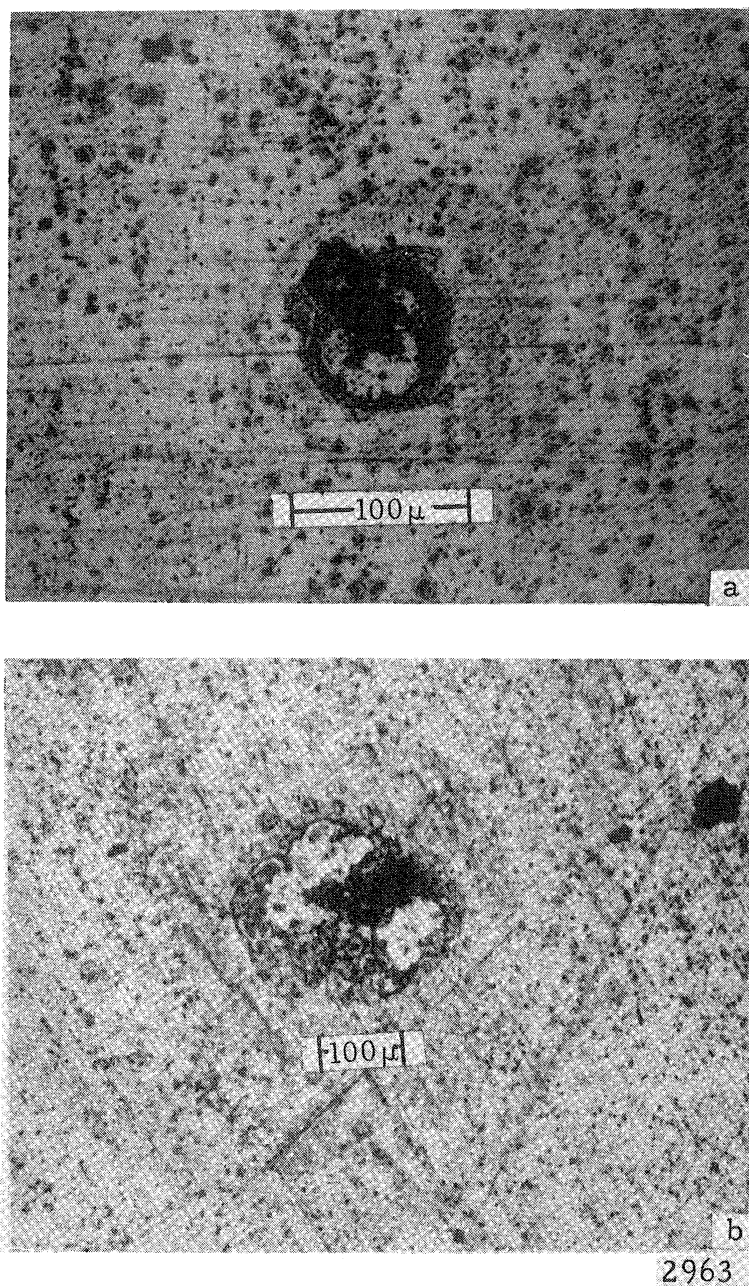


Figure 5.40 Photomicrographs of the Damage Produced on the 50  $\mu$  Thick Aluminum Foil During the Collapse and Rebound of (a) Bubble 5.28 and (b) Bubble 5.30. Scale as Shown

surface of more than 1.4 maximum radii away from the surface, no pits could be detected under the point of bubble collapse. Thus damage is incurred in these tests for bubble collapses which are in a fairly narrow band of initial bubble radii from the wall (between 1.0 and 1.4).

Additional pits (Fig. 5.41) were found directly under the electrodes. Therefore, the shock wave produced upon the initiation of the bubble is strong enough to create a pit quite similar to the pit produced by the collapsing bubble. The high degree of similarity between the pits produced is surprising. No good explanation of how spherical shock waves with radii near 2.0 mm can produce pits with an 0.05 mm radius has been found.<sup>(39)</sup>

This similarity shows that care must be used in differentiating between damage produced by a pure shock wave and damage produced by a collapsing bubble. This differentiation would be very difficult in the spark generated bubble static fluid systems previously studied,<sup>(22, 23)</sup> since the initial shock wave and bubble collapse impinge upon the same point of the solid surface.

Certain measured and calculated parameters for bubbles 5.24 through 5.30 are presented in Table 5.2. All of the bubbles have about the same initial size, partial pressure, and driving collapse pressure. The major difference between the bubbles is in their initial wall distance. The table shows that as the initial wall distance decreases, the minimum radius increases, while the maximum internal pressure decreases. Only for the bubble furthest from the wall, which did not form a jet, was the maximum internal gas pressure (if somehow transmitted undiminished through the liquid to the surface) great enough to damage even the softer aluminum. On the other hand, as the initial wall distance decreases the water jet velocity and resulting water hammer pressures increase to values large enough to damage the harder aluminum.

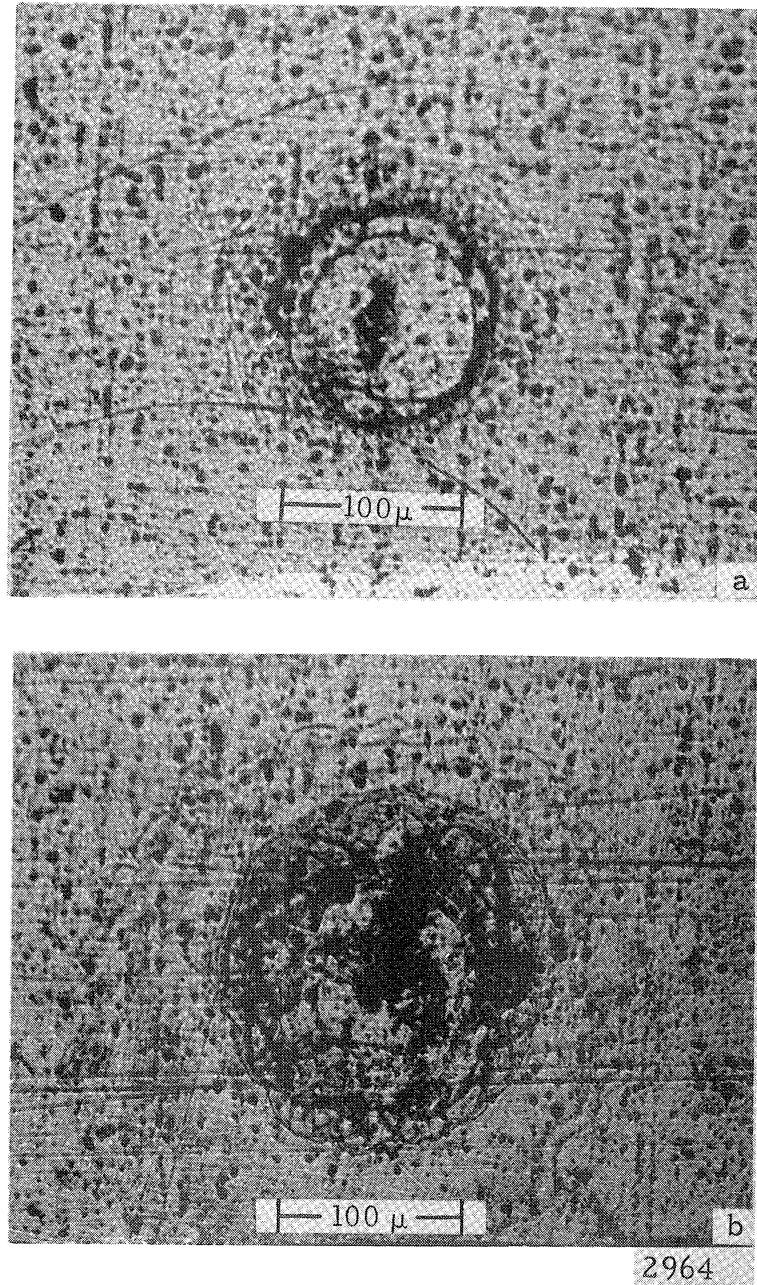


Figure 5.41 Photomicrographs of the Damage Produced on the 50  $\mu$  Thick Aluminum Foil by the Initiating Spark of (a) Bubble 5.28 and (b) Bubble 5.30

TABLE 5.2

## Spark Generated Cavitation Bubble Parameters

Bubble Number	5.24	5.26	5.28	5.30
Maximum radius, $R_m$ (mm)	2.01	2.21	2.01	2.02
(normalized)	(1.0)	(1.0)	(1.0)	(1.0)
Initial wall distance, $b_o$ (mm)	3.26	3.10	2.42	2.29
(normalized)	(1.62)	(1.40)	(1.21)	(1.14)
Partial pressure at $R = R_m$ (atm)	0.129	0.108	0.114	0.136
Minimum radius, $R_o$ (mm)	0.261	0.376	0.393	0.472
(normalized)	(0.129)	(0.171)	(0.195)	(0.233)
Wall distance at $R = R_o$ (mm)	2.67	2.29	1.08	0.88
(normalized)	(1.33)	(1.03)	(0.54)	(0.44)
Pressure inside bubble (atm) at $R = R_o$	455.0	130.0	76.0	44.3
Jet impingement velocity (m/s)	none	35.4	73.2	120.0
Water hammer pressure (atm)	-	514.0	1063.0	1745.0

Bubble Number refers to corresponding figure number.



The only major difference between the pits produced by shock wave vs. bubble collapse in experiments relates to their symmetry. Pits produced by shock waves (i. e., Fig. 5.41) are always very symmetrical with the central damage always in the center of the damage ring. The pit produced by the collapsing bubble, however, is not nearly so symmetrical (see Fig. 5.40 and 5.42). The central damage area of this pit is off-center in the circular damage ring, as would be expected by a high speed jet impinging at an angle or with an asymmetric head.

For the stronger 0.5 mm thick aluminum "lighting" sheet, pits were harder to obtain. Pits like the one shown in Fig. 5.42 were produced by the collapse of 50 spark generated cavitation bubbles with  $b_0 = 1.1$ . Since only 5 pits were formed, the method of causing damage must be highly selective even for bubbles quite close to optimum. Still, this ratio of 10 to 1 is much lower than the ratio of bubbles vs. pits in natural cavitation environment ( $10^4$  to  $10^5$  bubbles per pit)<sup>(20)</sup>. The accompanying proficorder trace of this pit shows a raised rim which is not symmetric around the pit. This non-symmetry would be expected from a high speed jet impinging at an angle. The pit in this harder, thicker aluminum is smaller than the pit produced in the 50  $\mu$  aluminum foil, and is more characteristic of the central damage shown in Fig. 5.40 without the damage ring. A photomicrograph of an isolated damage pit (Fig. 5.43) produced by the initial shockwave impinging upon the stronger aluminum shows a highly symmetric type of damage. The pit appears to be a fairly smooth depression with a symmetric rim in contrast to the ragged asymmetric pits of approximately the same size produced upon bubble collapse and rebound (Fig. 5.40 and 5.42).

The pits produced in the 50  $\mu$  aluminum foil by the natural cavitation bubbles (Fig. 5.20) are somewhat smaller than the pits produced by the spark generated bubbles (Fig. 5.40), even though



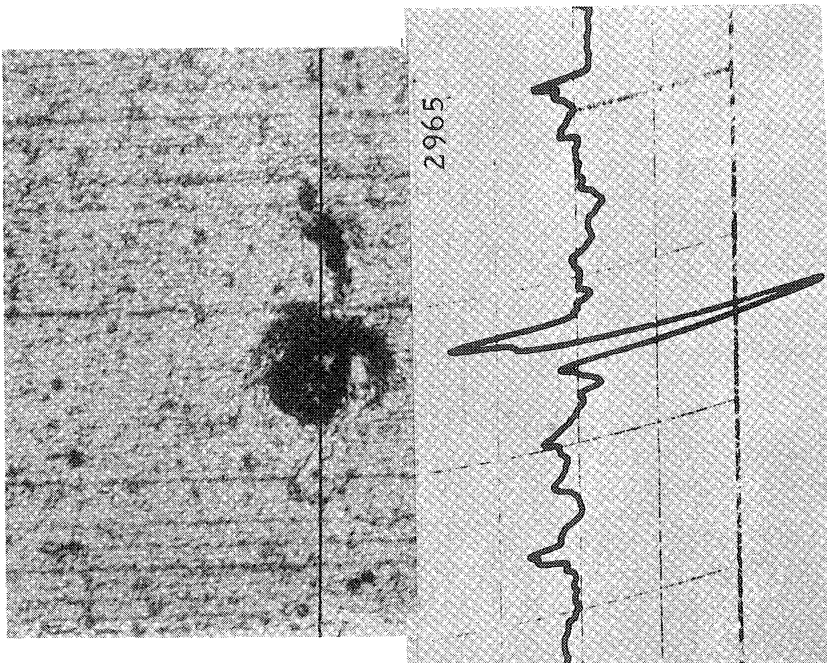


Figure 5.42 Photomicrograph and Accompanying Proficorder Trace of Damage Produced on the 0.5 mm Thick Aluminum Sheet by the Collapse with an Initial Normalized Wall Distance  $b_o$ , of 1.15. Scale Divisions 66.0  $\mu$  Horizontal, 0.635  $\mu$  Verticle

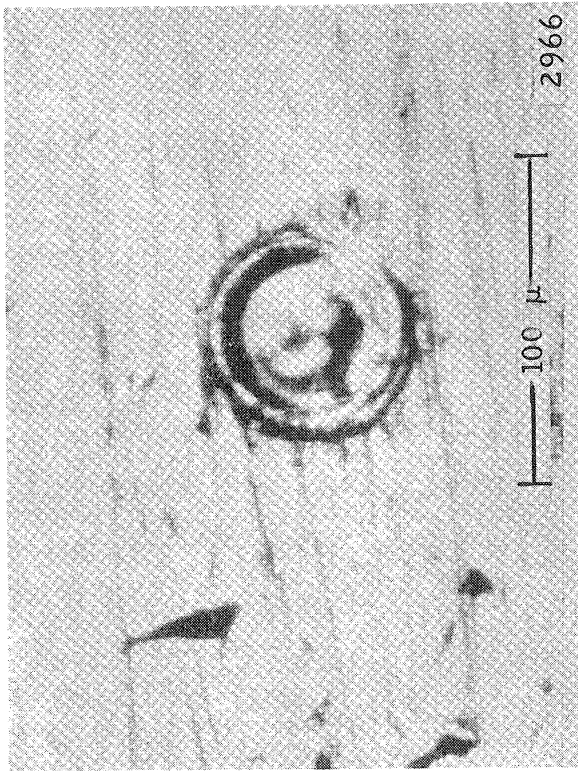


Figure 5.43 Photomicrograph of Damage Produced on the 0.5 mm Thick Aluminum Sheet by the Initiating Spark of a Spark Induced Cavitation Bubble with an Initial Normalized Wall Distance,  $b_o$ , of 1.15

the natural and spark generated bubbles are about the same size (compare Fig. 5.19 to Fig. 5.30). One reason may be that under the smaller hydrostatic pressures existing for the natural bubbles, a natural cavitation bubble must collapse through a larger volume ratio than a spark-induced bubble in order to achieve the same absolute wall velocity. If the natural cavitation bubble deformation were such that the jet did not form until such a smaller volume were reached, the jet would have the same velocity as the spark induced bubble jet but presumably smaller diameter. However, the natural cavitation bubble jet would be smaller, resulting in a smaller pit. These small pits also show a somewhat different form of damage failure, since the relative thickness of aluminum vs. pit diameter is increased; therefore, these pits may have characteristics lying between those of spark induced bubble pits produced on either thick aluminum foil or the 0.5 mm thick aluminum sheet. The pits all have the central damage area, and either a characteristic raised rim or circular damage ring.

Comparison between these pits produced by natural (Fig. 5.20) and spark-induced (Fig. 5.40 and 5.42) cavitation bubbles with the pits produced by the high speed water jet (Fig. 5.10 and 5.11) show several striking similarities. For the soft aluminum, the water jet pits (Fig. 5.10 and 5.11) show the same central damage area, the circular, damage ring, and the same type of central damage, and the same asymmetric raised rim.

## CHAPTER VI

### CONCLUSIONS

The theoretical and experimental evidence presented show the effects of a nearby solid boundary on the collapse of natural and spark-induced cavitation bubbles. The primary effect is an apparent "attraction" between the collapsing bubble and the solid boundary resulting in the movement of the centroid of the bubble toward this boundary. However, in many cases the distance between the bubble wall and the solid boundary remains approximately constant during collapse. For the bubbles sufficiently close to this boundary, the momentum produced during collapse causes the bubble to move toward it during rebound and eventually strike it.

Another effect of the solid boundary is to change drastically the collapse mode of the bubble. At maximum volume, all of the bubbles studied were nearly spherically symmetric. As the bubbles collapsed, the interference in the otherwise symmetrical fluid flow produced by the solid boundary first caused the bubble to elongate slightly along the axis perpendicular to the boundary (Fig. 5.38). Later the upper portion of the bubble collapsed more rapidly than the lower portion so that the bubble becomes flattened into a plane parallel to the boundary, the upper surface then threads its way through the bubble, forming a high speed "micro-jet" which strikes the boundary.

The damage produced by the collapsing bubbles on selected target materials appears very similar to the damage produced by both the impact of conventional high speed liquid jets and the impingement of a shock wave produced by initiation of the spark induced bubbles. However, the damage patterns produced by the

bubble collapse and conventional jet impingement were sometimes greatly asymmetric, depending presumably upon angle of impact, while in every case the damage pattern produced by the shock wave was very symmetrical. In addition, detailed analysis of the spark induced bubbles show that the minimum volumes achieved by bubbles collapsing near a solid surface are much greater than the minimum volumes achieved for collapse far from a boundary. This larger minimum volume resulted in maximum internal pressures that were far too low to cause damage to a nearby boundary. On the other hand, the water hammer pressure produced by the impact of the high speed jet was more than high enough to produce damage.

The damage potential produced by the collapse of a cavitation bubble is very sensitive to the position of the bubble relative to the solid boundary, and to the volume ratio of collapse before asymmetries cause formation of the high speed jet. Maximum damage potential is achieved when the jet does not form until minimum volume is reached, and when the bubble has migrated enough so that the jet immediately strikes the boundary. Possibly because of a large permanent gas or uncondensed vapor content in the spark induced bubbles, the minimum volumes reached were larger and the jet velocities achieved were smaller than for similar natural cavitation bubbles with little or no permanent gas. For this reason, natural cavitation bubbles collapsing under the same conditions should be able to produce a greater potential for damage.

The study of natural cavitation bubble collapse showed that flow conditions with pressure gradients parallel to the solid surface, divergent flow streamlines, separation wakes, or leading edges adversely affected the apparent attraction between the solid boundary and the collapsing bubble. In some cases, the bubble even moved away from the boundary during collapse, greatly reducing any damage

potential produced.

The spark bubble generator circuit coupled with the two-dimensional aluminum venturi provide a unique method for studying the damage produced by both shock waves and bubble collapse under controlled flow conditions. Future work with this equipment using more advanced photographic techniques such as laser-holography could provide greater detail of high speed jet formation, and could help clarify the similarity of shock wave and jet produced damage pits. In addition, a more detailed study of the effects of various flow conditions or surface preparations on bubble collapse could lead to general methods of reducing the damage potential of cavitation bubbles.

## REFERENCES

1. Euler, Leonhard, "Theorie plus complete des machines, qui sont mises en mouvement par la reaction de l'eau", *Historie de l'Academie Royale des Sciences et Belles Lettres, Classe de Philosophie Experimentale*, pp. 227-295, Mem 10, 1754, Berlin, 1756.
2. Bessant, W., A Treatise on Hydrodynamics, Cambridge University Press, Cambridge, (1859) 198.
3. Lord Rayleigh, "On the Pressure Developed in a Liquid During Collapse of a Spherical Cavity", Phil. Mag., 34, (1917) 94-98.
4. Burrill, L. C., "Sir Charles Parsons and Cavitation", Trans. Inst. Marine Engrs., 43, No. 8, (1951) 149-167.
5. Cole, R. H., Underwater Explosions, Princeton University Press, 1948.
6. Hammitt, F. G., "Collapsing Bubble Damage to Solids", Univ. of Michigan, January, 1969, presented at Cavitation State of Knowledge Symposium, ASME, June 1969.
7. Benjamin, T. B., 1954. Cavitation in Liquids. Doctoral Dissertation, Cambridge University.
8. Hickling, R. and Plesset, M. S., The Collapse of a Spherical Cavity in a Compressible Liquid, California Institute of Technology, Report No. 85-24, Pasadena, California, 1963.
9. Ivany, R. D., 1965. Collapse of a Cavitation Bubble in Viscous Compressible Liquid-Numerical and Experimental Analyses. Doctoral Dissertation, Nuclear Engineering Department, University of Michigan.
10. Forster, H. K., and Zuber, N., "Growth of a Vapor Bubble in a Superheated Liquid", *J. Applied Physics*, 25, 474 (1954).
11. Florschuetz, L. W., and Chao, B. T., On the Mechanics of Vapor Bubble Collapse - A Theoretical and Experimental Investigation, ME Technical Report 1069-2 Eng. Expt. Station, University of Illinois, 1963, also ASME Paper No. 64-HT-23.
12. Plesset, M. S., and Mitchell, T. P., 1956. On the Stability of the Spherical Shape of a Vapour Cavity in a Liquid. Quart. Appl. Math., Vol. 13, p. 419.

13. Birkhoff, G., and Zarantonello, E.H., Jets, Wakes and Cavities, Academic Press Inc., New York, (1957) 236.
14. Khoroshev, G. A., "Influence of a Wall on the Collapse of Cavitation Bubbles", Inzhenerno-fizicheskiy zhurnal, Vol. 6, no. 1, 1963, 59-65.
15. Korovkin, A.N., and Levkovskiy, Y. L., "Investigation of the Collapse of a Cavitating Bubble Near a Solid Wall", Inzhenerno-fizicheskiy zhurnal, Vol. 12, no. 2, 1967, 246-253.
16. Schmid, J., "Cinematographic Investigation of Single Bubble Cavitation", translated from ACUSTICA, Vol. 9, 1959.
17. Chang, Te-chun, and Wang, Ch'eng-hao, "Experimental High-Speed Photographic Investigation of the Motion of a Single Cavitation Bubble", Acta Acustica Sinica (Shenghsueh Hsueh-pao, Peiping, Communist China,) 7 March 1966, Vol. 3, No. 1, pp. 14-20.
18. Ellis, A. T., 1965. Parameters Affecting Cavitation and Some New Methods for their Study. Hydrodynamics Laboratory, California Institute of Technology, Report No. E-115-1.
19. Plesset, M. S., "Shock Waves from Cavitation Collapse," Paper presented at Royal Society Discussion, Deformation of Solids Due to Liquid Impact, London, May 27, 1965 (to be published in Proc. Roy. Soc.).
20. Olson, Hilding G., "High Speed Photographic Studies of Ultrasonically-Induced Cavitation and Detailed Examination of Damage to Selected Materials", Doctoral Dissertation, Dept. of Nuclear Engineering, University of Michigan, August, 1966.
21. Robinson, M. J., "On the Detailed Flow Structure and the Corresponding Damage to Test Specimens in a Cavitating Venturi," PhD Thesis, Department of Nuclear Engineering Laboratory of Fluid Flow and Heat Transport Phenomena, University of Michigan, 1965.
22. Naude, C. F., and Ellis, A. T., "On the Mechanism of Cavitation Damage by Non-Hemispherical Cavities Collapsing in Contact with a Solid Boundary", CIT Report No. E-108.7, 1960.



23. Shutler, N. D. and Mesler, R. B., "A Photographic Study of the Dynamics and Damage Capabilities of Bubbles Collapsing Near Solid Boundaries," Dept. of Chemical and Petrol. Engr. University of Kansas, 1964.
24. Benjamin, T. B., and Ellis, A. T., "The Collapse of Cavitation Bubbles and the Pressures They Produced Thereby Against Solid Boundaries", Phil. Trans. Roy. Soc., A, Vol. 260, p. 221, 1966.
25. Gibson, D. C., "The Collapse of Vapour Cavities", Doctoral Dissertation, Cambridge University, July, 1967.
26. Kozirev, S. P., "On Cumulative Collapse of Cavitation Cavities", ASME Paper No. 68-FE-2, November, 1967.
27. Chincholle, M. L., "Application de l'effet fusée a l'écoulement des bulles de gaz et de vapeur dans un pompe centrifuge", presented to Societe Hydrotechniques de France, Nov., 1967, Paris, France.
28. Shima, A. "The Behavior of a Spherical Bubble in the Vicinity of a Solid Wall"; Report 2, Journal of Basic Engr., Trans. of ASME, Ser. D, Vol. 20 (1968/1969), pp. 109/144.
29. Mitchell, T. M., PhD Thesis, in preparation, The University of Michigan.
30. Plesset, M. S., Personal Communication.
31. Hammitt, F. G., "Cavitation Damage and Performance Research Facilities", ASME Symposium on Cavitation Research Facilities and Techniques, May, 1964, pp. 175-184.
32. Koopman, R. P., C. L. Kling, and F. G. Hammitt, "High Velocity Fluid Impact Studies," University of Michigan, Technical Report No. 01077-3-T, July, 1968.
33. Robinson, M. J. and F. G. Hammitt, "Detailed Damage Characteristics in a Cavitating Venturi", Trans. ASME, J. Basic Engr., Vol. 89, D, No 1, March, 1967, pp. 161-173.
34. Martin, E. A., "The Underwater Spark: An Example of Gaseous Conduction at About  $10^4$  Atmospheres", PhD Thesis, University of Michigan, 1956.
35. Vorotnikova, M. I., "Effect of the Heat-Emission Rate in an Underwater Electric Explosion on the Distribution of the Explosion Energy", Zhurnal prikladnoy mekhaniki i tekhnicheskoy fiziki, No. 2, 1962, pp. 110-112.

36. Ahmed, O., PhD Thesis, in preparation, The University of Michigan.
37. Brunton, J. H., "High Velocity Liquid Impact", Phil. Trans. Roy. Soc., A, Vol. 260, July, 1966, pp. 79-85.
38. Lamb, H., "Hydrodynamics", 6th Edition, 1932.
39. Thomas, G. P., "The Initial Stages of Deformation in Metals Subjected to Repeated Liquid Impact", Phil. Trans., Roy. Soc., Series A, No. 1110, V. 260, pp. 73-315, July, 1966.
40. Chesterman, W. D., "The Photographic Study of Rapid Events," Oxford University Press, 1951.
41. Hyzer, W. G., "Engineering and Scientific High Speed Photography", (in Phoenix Library), University of Michigan.
42. Jones, G. A., "High-Speed Photography", Chapman and Hall, 1952.
43. Pressman, Z., "A Comparison of High-Speed Photographic Films with Different Vigorous Development Conditions," presented to the Fifth International Congress on High Speed Photography, Washington, D. C., 1960.
44. Green, N. W., R. B. Mesler, "An Experimental Study of Transient Pressures Accompanying Vapor Bubble Collapse in Water", to be presented at the Nucleation Symposium, May, 1970.
45. Harrison, M., "An Experimental Study of Single Bubble Cavitation Noise", J. Acoust. Soc. of America, 24, 6, Nov., 1952.

APPENDIX A  
SCIENTIFIC HIGH SPEED PHOTOGRAPHY

The major purpose of scientific photography is to broaden the interpretative powers of the human eye by time magnification or reduction and by increasing spatial resolution. The human eye responds to a wide range of natural phenomena, but it is limited in motion perception from a minimum of approximately 1 radian per hour to a maximum of approximately  $10^3$  radians per hour<sup>(40)</sup>. The maximum spatial resolution of the eye for natural phenomena is approximately 1 minute of arc. For viewing projected images these ranges and limitation of the eye are greatly reduced. Although the eye takes only 0.01 second to perceive a single stimulus, any motion which occurs must take place over at least 0.25 second in order to be perceived as motion<sup>(41)</sup>. These limitations of the human eye prescribe the time magnification or reduction and resolution required so that a given event can be analyzed. These limits are also used to provide the illusion of motion for the projected images of the event being analyzed. Experiments have shown that if reproductions of a given event are shown at a rate not less than 16 per second the eye perceives this reproduction as continuous motion<sup>(42)</sup>. Therefore, if series of pictures are taken at a rate of  $10^6$  frames per second and then projected at a rate of 16 frames per second, the time scale of the apparent rate of motion would be magnified by a factor of  $6.25 \times 10^4$ .

A motion picture camera consists of a lens, a method for exposure control, a photosensitive material, and a light-tight box to contain all of these components. Perhaps the simplest way to classify motion picture cameras is the technique by which they record images of a given event. A streak camera takes a small section

of the field of view and displays this slip continuously along the film so that an event is sampled with respect to space, while a framing camera produces complete images of the field of view at prescribed time intervals so that an event is sampled with respect to time. In a streak camera, the slit image is transported along the film either by having the film move past the focal plane of the lens or by a rotating mirror which sweeps the slit image around the interior of the camera. Because of the yield strength limitations of presently available film, the maximum transport rate is limited to approximately 100 m/s. This transport rate produces a writing rate of 0.1 mm/ $\mu$ s on the film. For streak cameras where the film is held stationary and the slit image is transported around the interior of the camera by a rotating mirror, the maximum writing rate presently available is approximately 10 mm/ $\mu$ s. Because streak cameras sample only a small segment of space, they are generally used to determine the motion of a discontinuity past a line in the field of view where a high degree of time resolution is required. This time resolution of a streak camera is given by

$$\text{time resolution} = \frac{1}{\text{camera resolution}} \times \frac{1}{\text{writing rate}} \quad (\text{A-1})$$

The important parameters of a motion picture camera used for the study of high-speed events are the time resolution, the spatial resolution, and the writing time. The time resolution which is a function of exposure time and framing or sweep rate must be great enough so that any motion in the projected image of the event being studied is within the limitations of the human eye. Spatial resolution which is a function of camera optics and film emulsion must be great enough so that the physical details of the event being photographed can be accurately defined. Finally, the

writing time,  $w$ , of the camera

$$w = F \cdot N \quad \begin{array}{l} F = \text{framing rate} \\ N = \text{total frames/sequence} \end{array} \quad (\text{A-2})$$

must be great enough to cover the critical part of the event being studied. Unfortunately these parameters are not independent of each other. If time resolution is too low because of a required long exposure time, spatial resolution will suffer because object motion during the exposure period will blur the image. Also if spatial resolution is limiting, the maximum usable framing rate is given by

$$F = V(\cos \theta) \cdot d \cdot M \quad \begin{array}{l} M = \text{magnification} \\ d = \text{resolution of system} \\ V = \text{maximum velocity of} \\ \quad \text{object being photographed} \\ \theta = \text{angle between velocity} \\ \quad \text{vector and film plane} \end{array} \quad (\text{A-3})$$

where  $d$  is the minimum distance on the image that can be measured accurately with a given resolution. The framing rate of a camera is related to the writing time by eq. B-2; therefore, in cameras having a fixed number of frames, once the duration of the event is known the maximum framing rate is also determined.

Framing cameras, because they require an additional device to transport the image to an unexposed portion of the film for the next frame, and must then compensate for the relative motion between the image and the film during the exposure period, have several more subclassifications than do streak cameras. The simplest device to reduce relative film-image motion uses an extremely short duration light pulse (less than  $1.0 \mu\text{s}$ ) produced by a short duration light source or a very fast electro-optic shutter (such as the Kerr cell) to reduce this motion to the minimum required to prevent blurring. Between exposures the image is

moved to an unexposed portion of the film by transport of the film (where stress limitations of film limit maximum framing rate to approximately 20,000 frames/second), by transport of the light beam using a rotating mirror (where minimum recycle times of the light source or electro-optic shutter limit the maximum framing rate to approximately  $10^6$  frames/second), or by effective transport of the light source and camera lens by using a separate camera lens and light source for each frame. This transport method, known as the Cranz-Schardin system, produces a slightly variable perspective for each image, and the framing rate is limited by the rate the separate light sources can be triggered (presently a maximum of approximately  $10^6$  frames/second).

Most low speed framing cameras rely on intermittent film transport to compensate for relative film image movement. The film is held stationary during the exposure time and moves the next frame between exposures. Because of the high stress exerted on the film, framing rates of over 300 frames/second generally result in failure of the film. Therefore, in cameras relying on film transport to achieve framing rates greater than 300 frames/second, the film moves continuously past a focal plane of the camera lens. Many methods are then used to compensate for the relative film image motion. Several camera lenses may be mounted on a wheel and then rotated so that the lens speed and the film speed are in synchronization. The dynamics of this system usually limits the framing rate to a maximum of 2,500 frames/second. A rotating prism may also be geared to the film. The refractive power of the prism is great enough to translate the image at the same speed as the film. In this case, the maximum framing rate is related to the maximum translational velocity of the film. With a maximum translational velocity of

100 m/s the framing rate is approximately 25,000 frames/second for 4 mm x 16 mm frames. In other cameras relying on film transport to achieve high framing rates short strips of film are positioned inside a rotating drum; thereby eliminating stresses in the film and achieving higher transport rates. These cameras use either a rotating mirror or a translating mirror to compensate for relative film-image motion, and have maximum framing rates ranging from 35,000 frames/second to 100,000 frames/second.

Finally there are several types of high speed motion picture cameras which hold the film stationary during a photographic sequence and move the image to an unexposed portion of the film by other methods. The Cranz-Schardin system which utilizes variable perspective to transport the image has already been discussed. Another method of image transport uses a rotating mirror which sweeps the image continuously around the interior of the camera. Spherical mirrors or relay lenses focus the image on the film track, while compensating for the continuous motion of the image and producing one frame/relay lens or mirror. The maximum framing rate of this type of camera (approximately  $5 \times 10^6$  frames/second) is limited by the stresses produced in the rotating mirror. The image may also be transported electronically, as in an image converter camera. In this device, the light beam is translated into an electron beam and then translated back into a light beam. As an electron beam, the image can be amplified by accelerating the electrons across a high voltage gap which increases their energy, and the image can be transported by using the electric field of deflector plates. Image converter cameras have extremely high framing rates ( $2 \times 10^7$  frames/second) and extremely short exposure time ( $10^{-8}$  seconds), and when used as a streak camera, extremely high sweep rates (100 millimeters/microsecond), but generally have low spatial resolution (8 to 16



lines/mm).

An important feature of any high speed camera is the required synchronization between the camera and the event being photographed. A camera which is always ready to take photographs (i. e. , has continuous access) requires only a detector of any event, and the photographs can be taken with nearly zero delay when the detector signal is used to activate the light source. A camera with limited access is not continuously ready to take photographs; therefore, the event must be triggered by a signal from the camera which synchronizes the event with the photographically active period of the camera. Limited access cameras cannot photograph random events unless the writing time of the camera is much larger than the average time between events, or several photographic sequences are made with the probability of a few of them coinciding with the event.

Because of the short exposures required in high speed photography and the emulsion speeds of commonly available films, ambient light generally does not have sufficient intensity to produce an image; therefore, special lighting techniques are required. The general requirements for a photographic light source are that it provide illumination of sufficient intensity to produce an image of the event being photographed on the film; and for the case of motion picture cameras, the illumination must be maintained at least as long as the writing time of the camera. In addition, depending on the type of camera used, the light source may require synchronization with a non-continuous access camera, or it may need to turn on and off rapidly, if the light source is used as the effective shutter. Light sources which produce intense short duration light pulses at a high repetition rate may be synchronized with motion picture cameras to effectively reduce exposure

time per frame to  $\sim 1 \mu\text{s}$ , thereby greatly reducing image blur. The maximum flash rate of this type of light source varies from 7,000 to 20,000 flashes/second and may be the limiting factor of a particular camera's framing rate. The majority of high intensity light sources are of the arc discharge type. Electrical energy is stored in a capacitor or a delay line, and then discharged across an air gap spark or across an enclosed gas tube containing an inert gas. This type of light source, simple in design, is one of the most efficient ways of converting electrical to light energy. The use of proper electronic switches and energy dumps allows for the precise control of the initiation and duration of light pulses.

Depending on the light intensity required to expose the photosensitive material used, and the light intensity which is available from the light sources at hand, a lighting technique must be chosen with the proper light economy to produce an image of acceptable density. "Light economy" in this sense means the light intensity which exposes the film relative to the intensity of the light source. Nearly all objects seen by the human eye are exposed to diffuse front lighting so that this type of lighting would produce the most naturally appearing image. For high-speed photography, this type of lighting is produced by placing the camera and the light source on the same side of the object plane, and no attempt is then made to concentrate the light on the object. Therefore only the extremely small amount of light which is reflected from the object into the objective lens of the camera exposes the film. This type of lighting is the least "economical" and may only be used when very high intensity light sources are available and/or the object to be photographed is highly reflective. Without having much deleterious effect on the type of image produced, the lighting economy may be improved by using focused front lighting. The light source still remains on the same side of the object plane as

the camera, but now lenses or mirrors are used to concentrate the light on the object being photographed. Still, only reflected light reaches the camera, so that the intensity which exposes the film is small compared with the initial intensity of the light source; however, for object planes that are opaque this type of lighting is the most economical. For object planes that are translucent or transparent, diffuse or focused backlighting may be used to improve light economy. In both cases the object plane is directly between the light source and the camera. For diffuse backlighting, a diffuser, which only slightly reduces the intensity of the light reaching the camera, is placed between the light source and the object plane. The resulting image of the object being photographed depends upon the object's opacity. If the object is translucent (as are cavitation bubbles), much of the surface and interior detail of the object is recorded on the image with this form of lighting. For lighting techniques requiring the highest light economy, focused back lighting is used. The diffuser is then replaced by a condensing lens which concentrates the light from the light source into the camera lens. Now the light which passes through the object plane is in a nearly parallel beam, and any object which interrupts the light or diffracts it out of the beam will not expose the film. Therefore, the majority of objects that can be photographed (including cavitation bubbles) appear only as silhouettes on the film image. Since density gradients (produced by shock waves, pressure pulses, temperature gradients, etc.) also will diffract light from a parallel beam, these gradients will appear as lines on the film image, thereby providing information about the object plane not available with other types of lighting.

The ultimate result of high-speed photography is displayed as an image on a photosensitive material. Photosensitive material contains an emulsion of suspended silver bromide particles, generally

supported on a flexible backing. These particles are sensitized by exposure to light and, with proper treatment in the developing process, produce a photographic image. The larger these particles, the more easily they are sensitized, and although all films contain a distribution of particles, films with greater sensitization have particles with greater average size. Particle distribution is regulated so that a plot of image density versus the log of exposure produces a straight line over a range called the latitude of the film. For any image exposed within this latitude, the tonal variations are directly related to the log exposure just as with an object viewed with the human eye. Emulsion sensitivity is more commonly called "film speed" with high sensitivity film being called "fast film". It should be noted that film speed can be altered somewhat by different developing processes thereby giving the experimenter a range in which to work. Another factor which adversely affects film speed is "reciprocity failure". As duration of the exposure approaches very short (less than  $10^{-5}$  seconds) or very long (greater than 10 seconds) times, efficiency of sensitization decreases so that higher speed films are required to achieve the same image density for a given exposure. As faster films are used, average grain size increases, limiting the ultimate spatial resolution of the film image. Since a good high-speed panchromatic film has an ultimate resolution of 40 lines/millimeter, <sup>(43)</sup> which is quite close to the ultimate resolution of high speed motion picture cameras, care must be taken to assure that film resolution is at least as good as the camera resolution.

Quantitative measurements made on the film image are subject to error due to the finite resolution of the film-camera combination, blurring due to object motion, movement of the object out of the depth of field of the camera, inaccuracies in monitoring

camera framing rate and film magnification, and changes in the film during the development process. Since the ultimate resolution of the camera-optic system is set by the manufacturer, the experimenter controls only the resolution of the film. To obtain the ultimate resolution possible for the photographic system, a film and developing process should be selected which matches or exceeds the camera's resolution. Then the magnification of the image should be adjusted so that the minimum measurement required is several times the ultimate resolution of the system. The amount of blur,  $b$ , due to object motion during the exposure period is given by

$$b = tMV\cos\theta$$

$t$  = exposure time  
 $M$  = magnification  $\left(\frac{\text{image}}{\text{object}}\right)$   
 $V$  = object velocity  
 $\theta$  = angle between velocity vector and film plane

(A-4)

Ideally the amount of blur should be equal to or less than the ultimate resolution achieved on the image. The depth of field,  $D$ , of an optical system for subjects close to the lens, is given by

$$D = \frac{2(M+1) c\Lambda}{M^2}$$

$M$  = magnification  
 $\Lambda$  = relative aperture  
 $c$  = circle of confusion

(A-5)

where the "circle of confusion" is again set equal to the ultimate resolution achieved on the film. In this equation the relative aperture,  $\Lambda$ , should not be confused with the value of effective aperture,  $\mathcal{A}$ , which is generally quoted for high-speed photographic equipment. The relative aperture, which is given by

$$\mathcal{A} = \frac{f}{d}$$

$f$  = focal length of lens  
 $d$  = diameter of lens aperture

(A-6)

applies only to the objective lens of the camera, while the effective aperture given by

$$A = \left( \frac{\text{object brightness}}{\text{film image brightness}} \right)^2 \quad (\text{A-7})$$

is a measure of the total light loss due to extra relay lenses and relay mirrors internal to the camera. Inaccuracies in measuring the camera framing rate are minimized by the placement of time marks along the film at precise time intervals or by the use of precision equipment which accurately determines framing rate.

Film magnification, M

$$M = \frac{f_e}{x - f_e} \quad \text{for } x \gg f_e$$

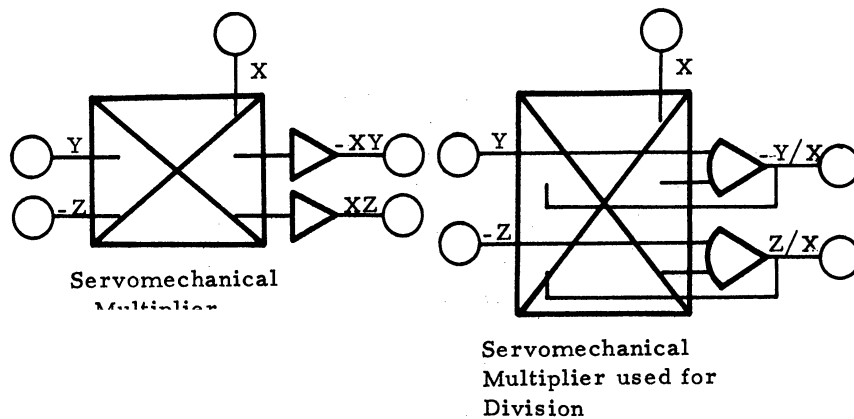
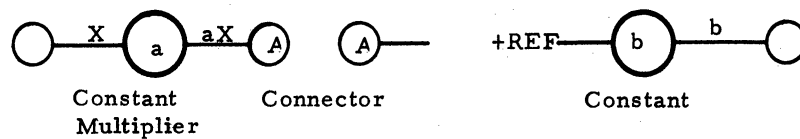
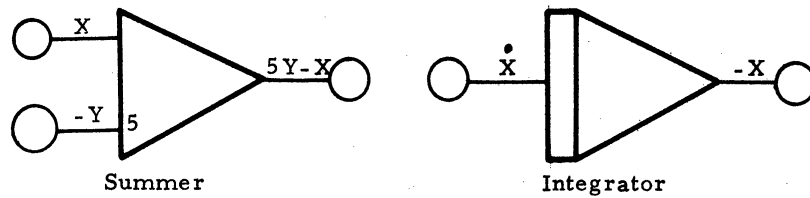
$f_e$  = effective focal length of camera system (A-8)  
 $x$  = object distance from camera lens

may be accurately determined by the precise measurement of the camera position with respect to the object. Changes in the dimension of the film during the developing process are minimized by strict adherence to prescribed darkroom procedure. The inclusion of a measurement standard in the plane of the object being photographed provides an excellent reference for measurements taken of the image.

## APPENDIX B

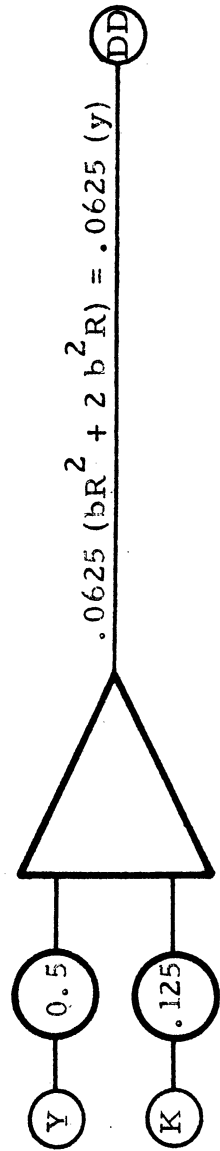
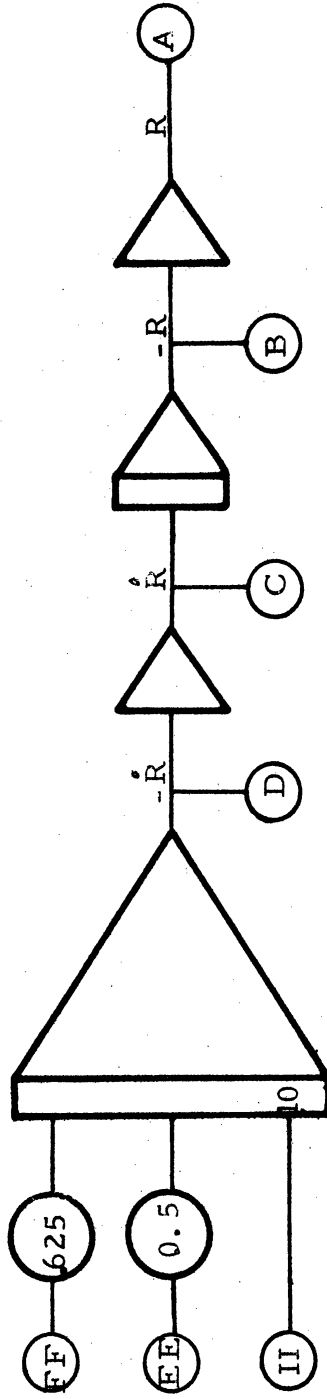
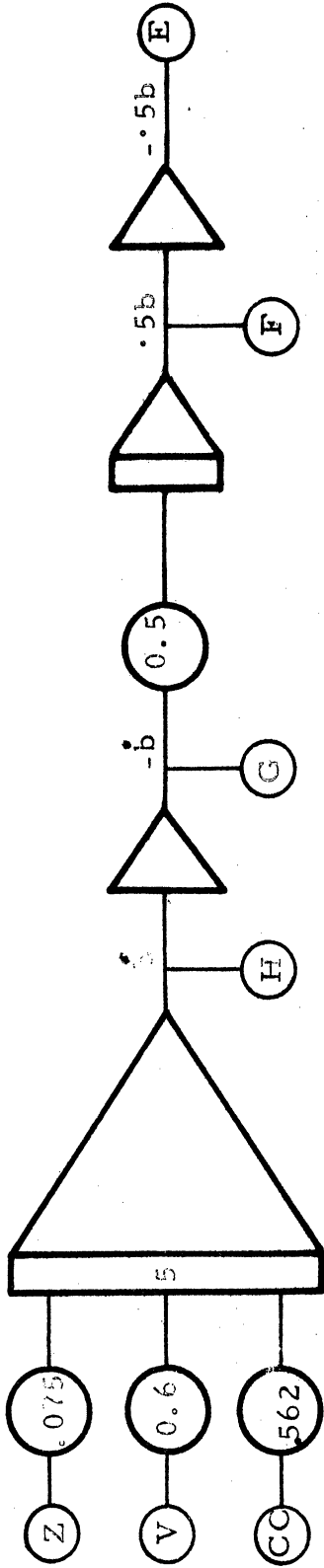
### ANALOG PROGRAM

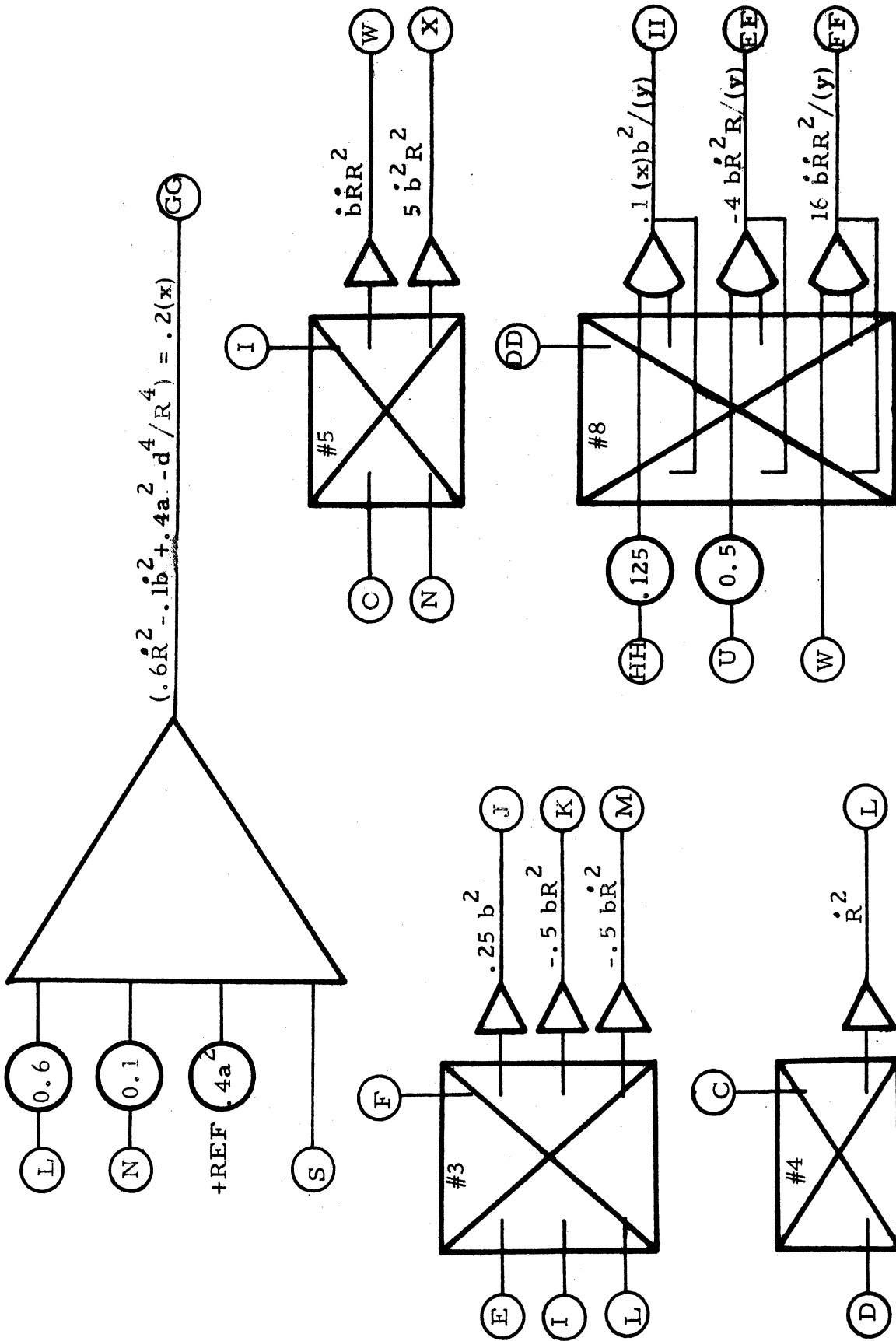
The basic component of an analog computer is a high gain amplifier which is used to sum variables, integrate them, and multiply them by a constant value. Voltage dividers are used to divide variables by a constant value and to provide constant factors. The servo-mechanical multiplier is used to multiply or divide variables. The symbols for these various components are given below. The analog program for equations 4.17 and 4.18 is given on the following pages.

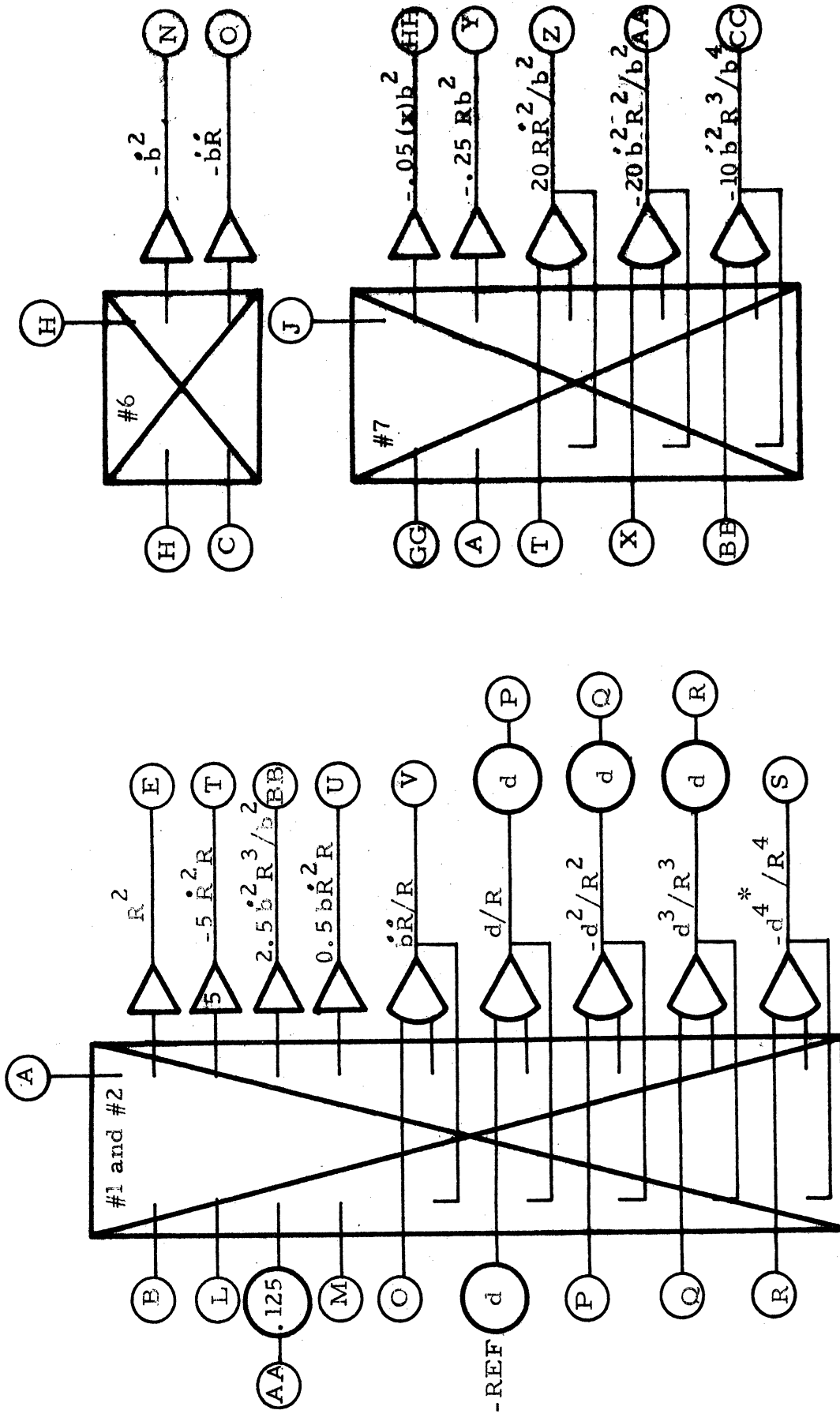


3010









3013

\*  $d^4 = .4Qa^2/\Delta P$

APPENDIX C

FORTRAN LISTING OF DIGITAL COMPUTER PROGRAM

```

0001      DIMENSION S(60,5),T(60),RA(60),WD(60),ECB(60),BVV(60),SVH(60),
          1WVB(60)
0002      REAL*8 B
0003      10 READ(5,11) B,RMAX,P,RHO,VF,RPS,N
0004      11 FORMAT(A5,F5.2,F6.3,F6.3,F6.2,F6.0,1X,I2)
0005      WD(1)=0.0
0006      SVH(1)=0.0
0007      BVV(1)=0.0
0008      WVB(1)=0.0
0009      T(1)=0.0
0010      ECB(1)=1.0
0011      DP=P*10.**6
0012      TN=SQRT(RHO/P)*RMAX*10.**2
0013      BE=4.189*DP*RMAX**3*10.**(-10)
0014      WVM=RMAX/(TN*10.**(-3))
0015      WRITE(6,12) B,RMAX,DP,BE,VF,WVM,TN
0016      12 FORMAT(1H1,'BUBBLE      ',A8,'//','MAX RADIUS  ',F7.2,' MM',/, 'PRESS
          1 DIFF',E15.4,' DYNES/CM2',/, 'BUBB ENER ',E15.4,' JOULES',/, 'FLUID
          1VEL ',F9.2,' M/S',/, 'NORM VEL  ',F9.2,' M/S',/, 'NORM TIME ',F9.2,
          1' MICROSEC',//)
0017      WRITE(6,13)
0018      13 FORMAT(' ',13X,'NORMALIZED  PROPERTIES',//,'TIME      MEAN',10X,
          1'RADIAL  VEL',11X,'WALL ',6X,'ECCEN',5X,'BUBBLE  VEL',11X,'SLIP',/,
          1'IOX','RADIUS  MEAN      HOR      VERT      DIST',15X,'HOR      VERT
          1  INST      AVE',/,65X,'(M/S)      (M/S)      (M/S)      (M/S)')
0019      READ(5,14) S(1,1),S(1,2),S(1,3),S(1,4),S(1,5)
0020      RA(1)=(S(1,2)**2*S(1,3)/4.):**((1./3.)/RMAX)
0021      DO 100 I=2,N
0022      READ(5,14) S(I,1),S(I,2),S(I,3),S(I,4),S(I,5)
0023      14 FORMAT(F4.0,3F5.2,F6.2)
0024      T(I)=S(I,1)/(1.24*RPS*TN*10.**(-3))
0025      WD(I)=S(I,4)/RMAX
0026      SVA=((S(I,5)-S(1,5))/(T(I)*TN*10.**(-3)))-VF
0027      IF(ABS(S(I,4)-0.01).GT.10E-6) GO TO 15
0028      RA(I)=(S(I,3)**2*S(I,2)/8.):**((1./3.)/RMAX)
0029      WD(I)=5.0
0030      GO TO 18
0031      15 IF(S(I,4)) 16,16,17
0032      16 RA(I)=(S(I,2)**2*S(I,3)/4.):**((1./3.)/RMAX)
0033      GO TO 18
0034      17 RA(I)=(S(I,2)**2*S(I,3)/8.):**((1./3.)/RMAX)
0035      18 Z=SQRT(ABS( S(I,2)**2-S(I,3)**2))
0036      ECA=Z/S(I,2)
0037      ECB(I)=Z/S(I,3)
0038      DT=(T(I)-T(I-1))*TN*10.**(-3)
0039      WVA=(RA(I-1)-RA(I))*RMAX/(DT*WVM)
0040      WVB(I)=(S(I-1,2)-S(I,2))/(2.*DT*WVM)
0041      WVC=(S(I-1,3)-S(I,3))/(2.*DT*WVM)
0042      IF(S(I,4)) 22,22,23
0043      22 WVC=2.*WVC
0044      23 BVH=(S(I,5)-S(I-1,5))/DT
0045      BVV(I)=(S(I-1,4)-S(I,4))/DT
0046      SVH(I)=BVH-VF
0047      IF(ECA-ECB(I)) 24,24,25
0048      24 ECB(I)=ECA

```

FORTRAN IV G COMPILER                    MAIN                    05-01-69                    18:25.47                    PAGE 0002

---

0049	25	IF(RPS-150.)	26,26,30
0050	26	BX=RVH	
0051		BVH=BVV(I)	
0052		BVV(I)=BX	
0053	30	WRITE(6,80) T(I),RA(I),WVA,WVR(I),WVC,WD(I),ECR(I),BVH,BVV(I),	
		ISVH(I),SVA	
0054		IF(ABS(WVB(I))-ABS(WVC))	42,42,100
0055	42	WVB(I)=WVC	
0056	80	FORMAT(' ',F5.3,5F9.3,F10.3,4F9.2)	
0057	100	CONTINUE	
0058		CALL BPLT(N,B,T,RA,WD,BVV,WVB)	
0059		GO TO 10	
0060		END	

---

FORTRAN IV G COMPILER	BPLT	05-01-69	18:26.08	PAGE 0001
0001	SUBROUTINE BPLT(N,BU,A,B,C,E,G)			
0002	DIMENSION A(60),B(60),C(60),E(60),G(60)			
0003	DIMENSION AA(3),BB(3)			
0004	REAL*8 BU			
0005	CALL PLTXMX(19.0)			
0006	AA(1)=10.0			
0007	AA(2)=10.5			
0008	AA(3)=11.0			
0009	DO 53 I=1,2			
0010	CALL PAXIS(2.0,1.0,4HTIME,-4,16.0,0.0,0.0,0.25,2.0)			
0011	CALL PSYMB(3.0,12.5,0.3,6HBUBBLE,0.0,6)			
0012	CALL PFNMBRT(5.5,12.5,0.3,BU,0.0,'C5*')			
0013	BB(1)=12.2			
0014	BB(2)=BB(1)			
0015	BB(3)=BB(1)			
0016	CALL PLINE(AA(1),BB(1),3,1, 1,0,0)			
0017	BB(1)=12.7			
0018	BB(2)=BB(1)			
0019	BB(3)=BB(1)			
0020	CALL PLINE(AA(1),BB(1),3,1, 1,2,0)			
0021	GO TO (52,54),I			
0022	52	CALL PSYMB(12.,12.5,-0.3,11HMEAN RADIUS,0.0,11)		
0023		CALL PSYMB(12.,12.0,-0.3,13HWALL DISTANCE,0.0,13)		
0024	CALL PAXIS(2.0,1.0,11HMEAN RADIUS,11,10.0,90.0,0.0,0.1,-2.0)			
0025	CALL PSCALE(10.0,2.0,CMIN,DC,C(1),N,1)			
0026	CALL PAXIS(1.0,1.0,13HWALL DISTANCE,13,10.0,90.0,CMIN,DC,-2.)			
0027	CALL PLTOFS(0.0,0.25,0.0,0.1,2.0,1.0)			
0028	CALL PLINE(A(1),B(1),N,1, 1,2,1)			
0029	CALL PLTOFS(0.0,0.25,CMIN,DC,2.0,1.0)			
0030	CALL PLINE(A(1),C(1),N,1, 1,0,1)			
0031	53	CALL PLTEND		
0032	54	CALL PSYMB(12.,12.0,-0.3,19HMAX RADIAL VELOCITY,0.0,19)		
0033		CALL PSYMB(12.,12.5,-0.3,17HVERTICAL VELOCITY, 0.0,17)		
0034	CALL PSCALE(10.0,2.0,EMIN,DE,E(1),N,1)			
0035	CALL PAXIS(2.0,1.0,24HVERTICAL VELOCITY(M/SEC),24,10.0,90.0,EMIN DE,-1.0)			
0036	CALL PSCALE(10.0,2.0,FMIN,DF,G(1),N,1)			
0037	CALL PAXIS(1.0,1.0,19HMAX RADIAL VELOCITY,19,10.0,90.0,FMIN,DF, 1-1.0)			
0038	CALL PLTOFS(0.0,.25,EMIN,DE,2.0,1.0)			
0039	CALL PLINE(A(1),E(1),N,1, 1,2,1)			
0040	CALL PLTOFS(0.0,.25,FMIN,DF,2.0,1.0)			
0041	CALL PLINE(A(1),G(1),N,1, 1,0,1)			
0042	CALL PLTEND			
0043	END			





UNIVERSITY OF MICHIGAN



3 9015 03023 8540